Structure-Property-Correlations in HfO_2 based Memristive Devices

Dissertation von Robert Winkler

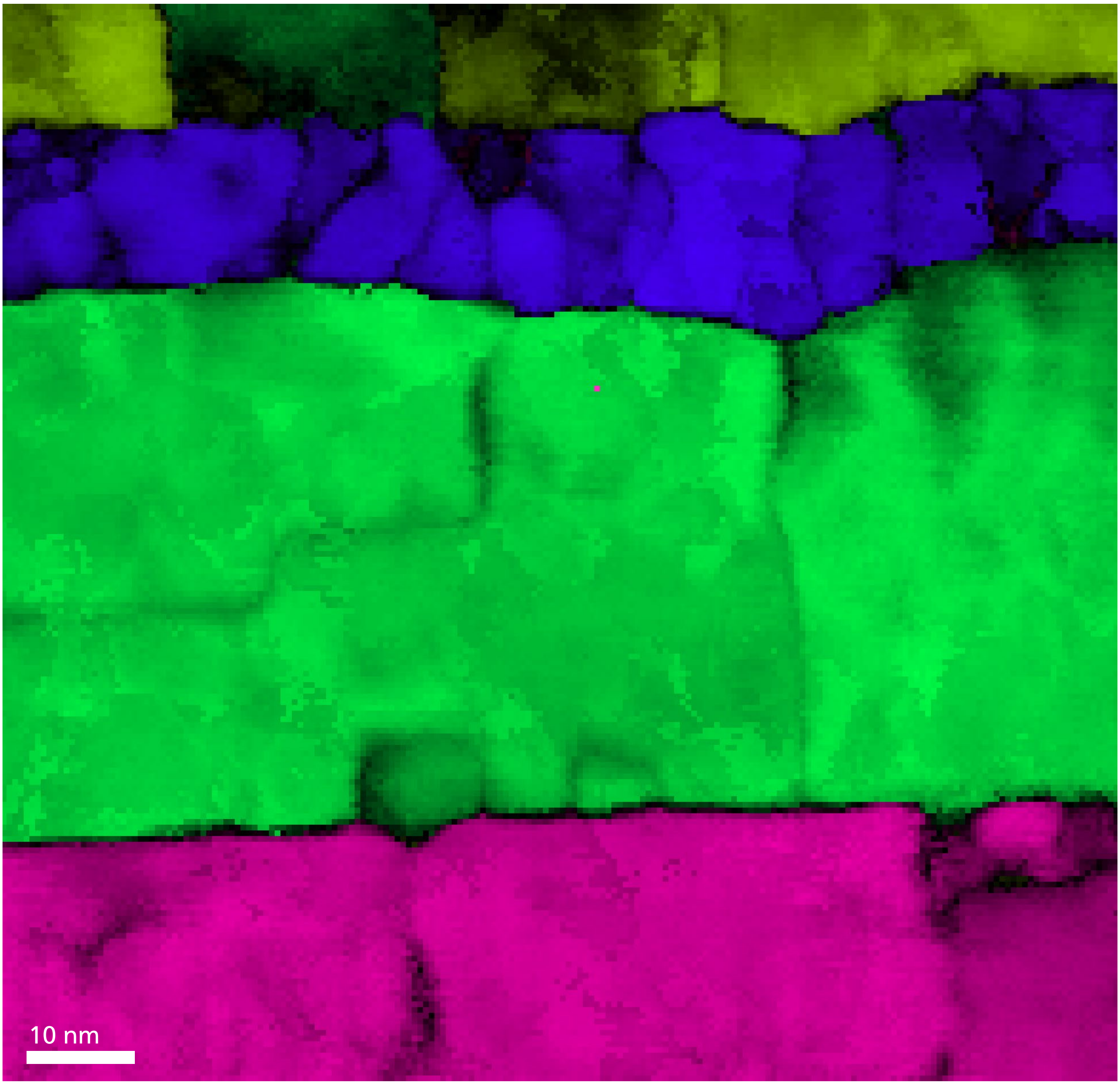

„Structure-Property-Correlations in HfO_2 based Memristive Devices“

Vom Fachbereich Material- und Geowissenschaften
der Technischen Universität Darmstadt

zur Erlangung des Grades

Doktor-Ingenieur
(Dr.-Ing.)

Dissertation
von M.Sc. Robert Winkler (geb. Eilhardt)

Erstgutachter: Prof. Dr. rer. nat. Leopoldo Molina-Luna

Zweitgutachter: Prof. Dr. Lambert Alff

Darmstadt 2024

Winkler, Robert: Structure-Property-Correlations in HfO_2 based Memristive Devices Darmstadt,

Technische Universität Darmstadt

Tag der Einreichung: 22. Mai 2024

Tag der mündlichen Prüfung: 9. Juli 2024

For my wife, Christine, with whom I would not have this wonderful life (and family), if I had not decided to do this doctorate.

1. Thesis Statement – Erklärung zur Dissertation

Thesis Statement pursuant to § 22 paragraph 7 of APB TU Darmstadt

I herewith formally declare that I, Robert Winkler (born Eilhardt), have written the submitted thesis independently pursuant to § 22 paragraph 7 of APB TU Darmstadt. I did not use any outside support except for the quoted literature and other sources mentioned. I clearly marked and separately listed all of the literature and all of the other sources which I employed when producing this academic work, either literally or in content. I state that all passages which have been taken from publications of all means or unpublished material either whole or in part, in words or ideas, have been marked as quotations. This thesis has not been handed in or published before in the same or similar form.

In the submitted thesis the written copies and the electronic version for archiving are pursuant to § 23 paragraph 7 APB identical in content.

Darmstadt, ____

(Robert Winkler (geb. Eilhardt), M.Sc.)

2. Curriculum Vitae

School teaching

08/2000-06/2004	Grundschule Bad Sachsa.
08/2004-06/2012	Internatsgymnasium Pädagogium Bad Sachsa, Abitur.

University study

10/2013-09/2016	Technische Universität Darmstadt, Bachelor of Science, Focus on Li-ion all solid state batteries.
10/2016-02/2019	Technische Universität Darmstadt, Master of Science, Focus on HfO_2 based memristive devices.
04/2019-05/2024	Technische Universität Darmstadt, Doctoral Thesis at the Advanced Electron Microscopy group. Supervisor: Prof. Dr. Leopoldo Molina-Luna

3. Acknowledgement

Quiero expresar mi especial agradecimiento a mi director de doctorado, el Prof. Dr. Molina-Luna, por ofrecerme la oportunidad de ocupar un puesto de doctorado mientras trabajaba en mi tesis de máster, oportunidad que acepté con gran entusiasmo. Su confianza y apoyo fueron fundamentales para que pudiera desarrollar plenamente mi potencial científico. Gracias a ello, tengo el privilegio de recordar años de intensa actividad científica, enriquecidos con numerosas participaciones en conferencias internacionales y valiosas colaboraciones internacionales.

Mein besonderer Dank gilt auch meinem Zweitgutachter, Herrn Prof. Dr. Lambert Alff, zum einen für die vielen produktiven Diskussionen und auch für das von ihm entgegengebrachte Vertrauen, welches mir ermöglicht hat, meine eigenen Dünnschichtproben herzustellen und zu charakterisieren.

I am also grateful to Prof. Keith Mckenna, who not only happily agreed to be my third examiner, but also for his indispensable scientific contribution.

Danken möchte ich auch Herrn Prof. Dr. Donner für die freundliche Übernahme des Viertgutachters.

Besonderer Dank gilt auch Herrn Dr. Alexander Zintler, welcher meinen wissenschaftlichen Werdegang durch seine beispiellose Hilfsbereitschaft maßgeblich nachhaltig beeinflusst hat.

Bedanken möchte ich mich auch bei

- Herrn Dr. Erwin Hildebrandt und Herrn Dr. Stefan Petzold, welche den Grundstein für meinen wissenschaftlichen Beitrag im Rahmen dieser Doktorarbeit gelegt haben.
- allen ehemaligen und aktuellen Mitarbeitern der ATFT Gruppe, besonders bei Herrn Dr. Tobias Vogel, Herrn Dr. Nico Kaiser, Frau Eszter Piros, Herrn Philipp Schreyer und Herrn Taewook Kim.
- allen ehemaligen und aktuellen Mitarbeitern der AEM Gruppe, besonders bei Herrn Oscar Recalde, Herrn Tianshu Jiang, Herrn Dr. Shuai Wang, Herrn Dr. Esmaeil Adabifiroozjaei und Herrn Dr. Tianmu Zhang.
- Frau Ulrike Kunz und Herrn Dr. Stefan Lauterbauch für Ihre technische Unterstützung im Bereich der Elektronenmikroskopie.
- bei meinen betreuten Masterstudierenden Frau Eléa Matheret und Herrn Alexander Fakiner für die Zusammenarbeit.

I am also grateful to Dr. Gennady Cherkashinin, who invited me to measure at several synchrotrons in Europe as part of his research.

Lastly, I am thankful to the European Research Council (ERC) who has funded my PhD through the “Horizon 2020” program under Grants 805359-FOXON and 957521-STARE.

4. Summary of Scientific Contribution

The present cumulative dissertation summarizes the essential scientific findings reported to the scientific community in the following peer-reviewed articles. Article reprints [1–3] are enclosed in the Chapter “Part II: Publications” at the end of this work.

1. Winkler, R., Zintler, A., Petzold, S., Piros, E., Kaiser, N., Vogel, T., Nasiou, D., McKenna, K.P., Molina-Luna, L., Alff, L.: Controlling the Formation of Conductive Pathways in Memristive Devices. Adv. Sci. 9, 2201806 (2022). https://doi.org/10.1002/advs.202201806

2. Zintler, A., Eilhardt, R., Petzold, S., Sharath, S.U., Bruder, E., Kaiser, N., Alff, L., Molina-Luna, L.: Enhanced Conductivity and Microstructure in Highly Textured TiN1–x/c-Al2O3 Thin Films. ACS Omega. 7, 2041–2048 (2022). https://doi.org/10.1021/acsomega.1c05505

3. Winkler, R., Zintler, A., Recalde-Benitez, O., Jiang, T., Nasiou, D., Adabifiroozjaei, E., Schreyer, P., Kim, T., Piros, E., Kaiser, N., Vogel, T., Petzold, S., Alff, L., Molina-Luna, L.: Texture Transfer in Dielectric Layers via Nanocrystalline Networks: Insights from in Situ 4D-STEM. Nano Lett. (2024). https://doi.org/10.1021/acs.nanolett.3c03941

In addition, publications 1 and 3 are accompanied by published cover arts designed by me, which are shown at the end of this PhD thesis.

5. List of Publications

(1) **Winkler, R** .; Zintler, A.; Recalde-Benitez, O.; Jiang, T.; Nasiou, D.; Adabifiroozjaei, E.; Schreyer, P.; Kim, T.; Piros, E.; Kaiser, N. Texture Transfer in Dielectric Layers via Nanocrystalline Networks: Insights from in Situ 4D-STEM. Nano Letters 2024.

(2) Recalde-Benitez, O.; Pivak, Y.; **Winkler,R** .; Jiang, T.; Adabifiroozjaei, E.; Perez-Garza, H. H.; Molina-Luna, L. Multi-Stimuli Operando Transmission Electron Microscopy for Two-Terminal Oxide-Based Devices. Microscopy and Microanalysis 2024, ozae023.

(3) Recalde-Benitez, O.; Pivak, Y.; Jiang, T.; **Winkler, R**.; Zintler, A.; Adabifiroozjaei, E.; Komissinskiy, P.; Alff, L.; Hubbard, W. A.; Perez-Garza, H. H. Weld-Free Mounting of Lamellae for Electrical Biasing Operando TEM. Ultramicroscopy 2024, 113939.

(4) Adabifiroozjaei, E.; Maccari, F.; Schäfer, L.; Jiang, T.; Recalde-Benitez, O.; Chirkova, A.; Shayanfar, N.; Dirba, I.; Kani, N. A.; Shuleshova, O. Martensitic Phase Transformation in Short-Range Ordered Fe50Rh50 System Induced by Thermal Stress and Mechanical Deformation. Acta Materialia 2024, 264, 119577.

(5) Yan, R.; Shen, C.; Widenmeyer, M.; Luo, T.; **Winkler, R**.; Adabifiroozjaei, E.; Xie, R.; Yoon, S.; Suard, E.; Molina-Luna, L. The Role of Interstitial Cu on Thermoelectric Properties of ZrNiSn Half-Heusler Compounds. Materials Today Physics 2023, 33, 101049.

(6) Recalde-Benitez, O.; Jiang, T.; **Winkler,R** .; Ruan, Y.; Zintler, A.; Adabifiroozjaei, E.; Arzumanov, A.; Hubbard, W. A.; van Omme, T.; Pivak, Y. Operando Two-Terminal Devices inside a Transmission Electron Microscope. Communications Engineering 2023, 2 (1), 83.

(7) Kim, T.; Vogel, T.; Piros, E.; Nasiou, D.; Kaiser, N.; Schreyer, P.; **Winkler, R**.; Zintler, A.; Arzumanov, A.; Petzold, S. Oxide Thickness-Dependent Resistive Switching Characteristics of Cu/HfO2/Pt ECM Devices. Applied Physics Letters 2023, 122 (2).

(8) Adabifiroozjaei, E.; Maccari, F.; Schäfer, L.; Jiang, T.; Recalde-Benitez, O.; Chirkova, A.; Shayanfar, N.; Dirba, I.; Kani, N. A.; Shuleshova, O. The Premartensite and Martensite in Fe50Rh50 System. arXiv preprint arXiv:2305.01351 2023.

(9) **Winkler, R.**; Zintler, A.; Petzold, S.; Piros, E.; Kaiser, N.; Vogel, T.; Nasiou, D.; McKenna, K. P.; Molina-Luna, L.; Alff, L. Controlling the Formation of Conductive Pathways in Memristive Devices (Adv. Sci. 33/2022). Advanced Science 2022, 9 (33), 2270212.

(10) **Winkler, R.**; Zintler, A.; Petzold, S.; Piros, E.; Kaiser, N.; Vogel, T.; Nasiou, D.; McKenna, K. P.; Molina-Luna, L.; Alff, L. Controlling the Formation of Conductive Pathways in Memristive Devices. Advanced Science 2022, 9 (33), 2201806.

(11) Vogel, T.; Zintler, A.; Kaiser, N.; Guillaume, N.; Lefèvre, G.; Lederer, M.; Serra, A. L.; Piros, E.; Kim, T.; Schreyer, P. Structural and Electrical Response of Emerging Memories Exposed to Heavy Ion Radiation. ACS nano 2022, 16 (9), 14463–14478.

(12) Vogel, T.; Zintler, A.; Kaiser, N.; Guillaume, N.; Lefèvre, G.; Lederer, M.; Serra, A. L.; Piros, E.; Kim, T.; Schreyer, P. Integration of Labeled 4D-STEM SPED Data for Confirmation of Phase Identification. 2022.

(13) Zintler, A.; **Eilhardt, R.**; Petzold, S.; Sharath, S. U.; Bruder, E.; Kaiser, N.; Alff, L.; Molina-Luna, L. Enhanced Conductivity and Microstructure in Highly Textured TiN1–x/c-Al2O3 Thin Films. ACS omega 2022, 7 (2), 2041–2048.

(14) Sharma, S.; Zintler, A.; Günzing, D.; Lill, J.; Meira, D. M.; **Eilhardt,R** .; Singh, H. K.; Xie, R.; Gkouzia, G.; Major, M. Epitaxy Induced Highly Ordered Sm_2Co_{17}–$SmCo_5$ Nanoscale Thin-Film Magnets. 2021.

(15) Recalde, O.; Jiang, T.; **Eilhardt, R.**; Zintler, A.; Ruan, Y.; Arzumanov, A.; van Omme, T.; Pivak, G.; Perez-Garza, H. H.; Komissinskiy, P. Effect of Induced Stimuli on the Leakage Current of Operative Oxide-Based Devices inside a TEM. Microscopy and Microanalysis 2022, 28 (S1), 820–821.

(16) Sharma, S.; Zintler, A.; Günzing, D.; Lill, J.; Meira, D. M.; **Eilhardt, R.**; Singh, H. K.; Xie, R.; Gkouzia, G.; Major, M. Epitaxy Induced Highly Ordered Sm2co17–Smco5 Nanoscale Thin-Film Magnets. ACS applied materials & interfaces 2021, 13 (27), 32415–32423.

(17) Kaiser, N.; Vogel, T.; Zintler, A.; Petzold, S.; Arzumanov, A.; Piros, E.; **Eilhardt, R.**; Molina-Luna, L.; Alff, L. Defect-Stabilized Substoichiometric Polymorphs of Hafnium Oxide with Semiconducting Properties. ACS Applied Materials & Interfaces 2021, 14 (1), 1290–1303.

(18) **Eilhardt,R.** ; Zintler, A.; Recalde, O.; Nasiou, D.; Petzold, S.; Alff, L.; Molina-Luna, L. Birth of a Grain Boundary: In Situ TEM Observation of the Microstructure Evolution in HfO2 Based Memristors. Microscopy and Microanalysis 2021, 27 (S1), 1238–1239.

(19) Cherkashinin, G.; **Eilhardt, R.**; Nappini, S.; Cococcioni, M.; Pis, I.; Dal Zilio, S.; Bondino, F.; Marzari, N.; Magnano, E.; Alff, L. Energy Level Alignment at the Cobalt Phosphate/Electrolyte Interface: Intrinsic Stability vs Interfacial Chemical Reactions in 5 V Lithium Ion Batteries. ACS Applied Materials & Interfaces 2021, 14 (1), 543–556.

(20) Zintler, A.; **Eilhardt, R.**; Wang, S.; Krajnak, M.; Schramowski, P.; Stammer, W.; Petzold, S.; Kaiser, N.; Kersting, K.; Alff, L. Machine Learning Assisted Pattern Matching: Insight into Oxide Electronic Device Performance by Phase Determination in 4D-STEM Datasets. Microscopy and Microanalysis 2020, 26 (S2), 1908–1909.

(21) Petzold, S.; Zintler, A.; **Eilhardt, R.**; Piros, E.; Kaiser, N.; Sharath, S. U.; Vogel, T.; Major, M.; McKenna, K. P.; Molina-Luna, L. Forming-Free Grain Boundary Engineered Hafnium Oxide Resistive Random Access Memory Devices (Vol 5, 1900484, 2019). ADVANCED ELECTRONIC MATERIALS 2020, 6 (3).

(22) Petzold, S.; Piros, E.; **Eilhardt, R.**; Zintler, A.; Vogel, T.; Kaiser, N.; Radetinac, A.; Komissinskiy, P.; Jalaguier, E.; Nolot, E. Neuromorphic Computing: Tailoring the Switching Dynamics in Yttrium Oxide-Based RRAM Devices by Oxygen Engineering: From Digital to Multi-Level Quantization toward Analog Switching (Adv. Electron. Mater. 11/2020). Advanced Electronic Materials 2020, 6 (11).

(23) Krajnak, M.; Blazit, J.-D.; Zintler, A.; **Eilhardt, R.**; Weiss, J.; Cosart, D.; Molina-Luna, L.; Tencé, M.; Gloter, A.; Allen, C. Transforming Transmission Electron Microscopy with MerlinEM Electron Counting Detector. Microscopy and Microanalysis 2020, 26 (S2), 1944–1945.

(24) Piros, E.; Petzold, S.; Zintler, A.; Kaiser, N.; Vogel, T.; **Eilhardt, R.**; Wenger, C.; Molina-Luna, L.; Alff, L. Enhanced Thermal Stability of Yttrium Oxide-Based RRAM Devices with Inhomogeneous Schottky-Barrier. Applied Physics Letters 2020, 117 (1).

(25) Piros, E.; Lonsky, M.; Petzold, S.; Zintler, A.; Sharath, S.; Vogel, T.; Kaiser, N.; **Eilhardt,R.** ; Molina-Luna, L.; Wenger, C. Role of Oxygen Defects in Conductive-Filament Formation in Y 2 O 3-Based Analog RRAM Devices as Revealed by Fluctuation Spectroscopy. Physical Review Applied 2020, 14 (3), 034029.

(26) Petzold, S.; Piros, E.; **Eilhardt, R.**; Zintler, A.; Vogel, T.; Kaiser, N.; Radetinac, A.; Komissinskiy, P.; Jalaguier, E.; Nolot, E. Tailoring the Switching Dynamics in Yttrium Oxide-

Based RRAM Devices by Oxygen Engineering: From Digital to Multi-Level Quantization toward Analog Switching. Advanced Electronic Materials 2020, 6 (11), 2000439.

(27) Petzold, S.; Zintler, A.; **Eilhardt, R.**; Piros, E.; Kaiser, N.; Sharath, S. U.; Vogel, T.; Major, M.; McKenna, K. P.; Molina-Luna, L. Resistive Switching: Forming-Free Grain Boundary Engineered Hafnium Oxide Resistive Random Access Memory Devices (Adv. Electron. Mater. 10/2019). Advanced Electronic Materials 2019, 5 (10), 1970054.

(28) Petzold, S.; Zintler, A.; **Eilhardt,R.** ; Piros, E.; Kaiser, N.; Sharath, S. U.; Vogel, T.; Major, M.; McKenna, K. P.; Molina-Luna, L. Forming-free Grain Boundary Engineered Hafnium Oxide Resistive Random Access Memory Devices. Advanced Electronic Materials 2019, 5 (10), 1900484.

(29) Cherkashinin, G.; Yu, Z.; **Eilhardt, R.**; Alff, L.; Jaegermann, W. Solid Electrolyte Interfaces: The Effect of Interfacial Charge Distribution on Chemical Compatibility and Stability of the High Voltage Electrodes (LiCoPO4, LiNiPO4)/Solid Electrolyte (LiPON) Interface (Adv. Mater. Interfaces 12/2020). Advanced Materials Interfaces 2020, 7 (12), 2070070.

(30) Zintler, A.; **Eilhardt,R.** ; Petzold, S.; Kaiser, N.; Ulhas, S.; Alff, L.; Molina-Luna, L. Correlation of Structural Modifications by Multiscale Phase Mapping in Filamentary Type HfO2-Based RRAM: Towards a Component Specific in Situ TEM Investigation. Microscopy and Microanalysis 2019, 25 (S2), 1842–1843.

(31) Cherkashinin, G.; Yu, Z.; **Eilhardt, R.**; Alff, L.; Jaegermann, W. The Effect of Interfacial Charge Distribution on Chemical Compatibility and Stability of the High Voltage Electrodes (LiCoPO4, LiNiPO4)/Solid Electrolyte (LiPON) Interface. Advanced Materials Interfaces 2020, 7 (12), 2000276.

(32) Petzold, S.; Miranda, E.; Sharath, S.; Muñoz-Gorriz, J.; Vogel, T.; Piros, E.; Kaiser, N.; **Eilhardt,R.** ; Zintler, A.; Molina-Luna, L. Analysis and Simulation of the Multiple Resistive Switching Modes Occurring in HfOx-Based Resistive Random Access Memories Using Memdiodes. Journal of applied physics 2019, 125 (23).

6. Conference Contributions (as Presenting Author) & Research Trips

MEMRISYS 2019 Dresden – Oral presentation - Control of Switching Modes in Grain Boundary Engineered HfO_2 based Memristor Devices

MC 2019 Berlin– Oral presentation - Impact of crystallinity on resistive switching properties of HfO_2 based Memristive Devices

MRS Fall 2019 Boston– Oral presentation - Temperature dependent study of microstructure evolution in HfO_2 based Memristive Devices

EMC 2020 Copenhagen – Accepted abstract – Canceled due to Covid

MEMRISYS 2020 Tsukuba – Accepted abstract – Postponed to 2021 due to Covid

MSE 2020 Darmstadt – Oral presentation - Watching a thin film crystallize: Microstructure Evolution in HfO2 Based Memristive Devices

MC 2021 Online – Poster presentation - Watching crystals grow: In situ TEM Observation of the Microstructure Evolution in HfO_2 Based Memristive Devices

M&M 2021 Online – Poster presentation - Birth of a grain boundary: In situ TEM Observation of the Microstructure Evolution in HfO_2 Based Memristors

MEMRISYS 2021 Online – Mini Conference, invited talks only due to Covid

MRS Spring 2022 Hawaii – Oral Presentation - In situ TEM studies of resistive switching in HfO2 based Memristors

MEMRISYS 2022 Boston – Oral Presentation - Impact of grain boundary atomic structure on the formation of conductive pathways in memristive devices

MC 2023 Darmstadt – Poster Presentation - Diffusion processes in HfO_2-based memristors investigated by in situ STEM and Atom Probe Tomography

MRS Spring 2024 Seattle – Oral Presentation - Unveiling Texture Transfer in Dielectric Thin Films via In Situ Electron Microscopy

MRS Spring 2024 Seattle – Oral Presentation - Bridging Thin Films Growth and Advanced Electron Microscopy to Uncover Structure-Property Correlations in Oxide Electronics

MRS Spring 2024 Seattle – Oral Presentation (Best Oral Presentation Award) - Breaking barriers in oxide nanoelectronics: Advancements in in situ TEM studies

M&M 2024 Cleveland – Oral Presentation - In Situ TEM Investigation of Conductive Bridge RAM devices

EMAT Antwerpen – 11.06.2019 – 21.06.2019

Elettra Sincrotrone Trieste – 22.11.2021-1.12.2021

EMATAntwerpen – 26.04.2022-27.04.2022

IOM Leipzig – 29.04.2022 – 30.04.2022

MIT Boston – 02.12.2022 – 11.12.2022

Diamond Light Source – 06.03.2023 – 10.03.2023

7. Index

8. Abbreviations

ABF	Annular Bright Field
ABSF	Average Background Subtraction Filter
ACOM	Automated Crystal Orientation Mapping
ADF	Annular Dark Field
ANN	Artificial Neural Network
BF	Bright Field
CBED	Convergent Beam Electron Diffraction
C-AFM	Conductive Atomic Force Microscopy
CMOS	Complementary Metal Oxide Semiconductor
CCD	Charge Coupled Device
CTF	Contrast Transfer Function
DED	Direct Electron Detector
DB	Dielectric Breakdown
DF	Dark Field
DFT	Density Functional Theory
DRAM	Dynamic Random Access Memory
EBIC	Electron Beam-Induced Current
ECM	Electro Chemical Metallization
EEPROM	Electrically Erasable Programmable Read-Only Memory
EPROM	Erasable Programmable Read-Only Memory
FEG	Field Emission Gun
FPGA	Field Programmable Gate Array
GPT	Generative Pre-trained Transformers
HAADF	High-Angle Annular Dark Field
HABF	High-Angle Bright Field
LABF	Low-Angle Bright Field
MABF	Medium-Angle Bright Field

MRAM	Magnetic Random Access Memory
NEM	Nanoelectromechinal
NVM	Non Volatile Memory
OTF	Optical Transfer Function
PAW	Projector Augmented Wave
PCI	Peripheral Component Interconnect
PCM	Phase Change Memory
PED	Precession Electron Diffraction
PROM	Programmable Read-Only Memory
RAM	Random Access Memory
ReRAM	Redox-based Resistive Random Access Memory
ROI	Region of Interest
RRAM	Resistive Random Access Memory
SAED	Selective Area Electron Diffraction
SCLC	Space-Charged Limited Conduction
SPED	Scanning Precession Electron Diffraction
SRAM	Static Random Access Memory
STEM	Scanning Transmission Electron Microscopy
STT	Spin Torque Transfer
TCM	Thermo Chemical Memory
TEM	Transmission Electron Microscopy
VCM	Valence Change Memory
FeFET	Ferroelectric Field Effect Transistor
ROM	Read Only Memory

Part I: Synopsis

9. Introduction and Motivation

With over 60 data centers (as of 2022), the Rhine-Main region adjacent to TU Darmstadt is one of the most important data processing locations in Europe (alongside London) [4]. Its electricity consumption is higher than that of Frankfurt Airport, which itself is one of the fourth-largest in Europe [5]. Due to the success of silicon semiconductor-based memories (DRAM, EEPROM, and Flash) in the 1980s, almost every computer today is equipped with this technology [6]. The increasing demand for data centers calls for technologies with enhanced performance, durability, and energy effectiveness [7]. Silicon-based technologies, particularly in the semiconductor and memory industries, are reaching their physical and technological limits for various reasons, including physical limitations in miniaturization or challenges in manufacturing technology [8]. As shown in Figure 9-1, the world's energy production will eventually be unable to support the power demands for computing (benchmark line). Therefore, novel computing technologies will be required, such as memristive systems [9].

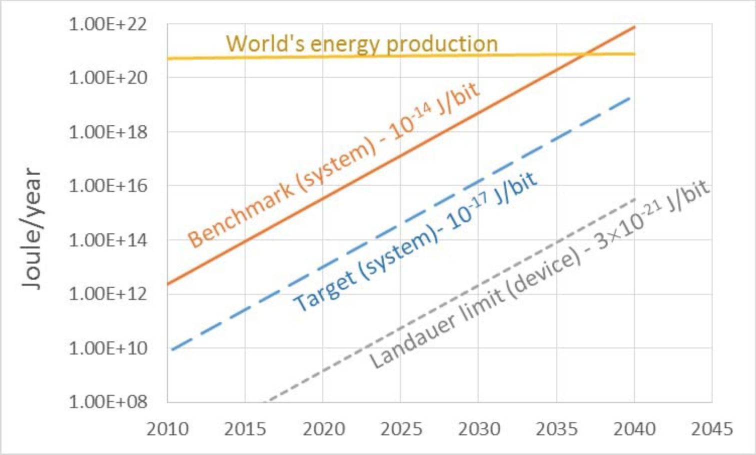

Figure 9-1: The energy consumption in computing for the current technology represented as “Benchmark” could surpass the world’s energy production. The targeted technologies (blue curve) should have an energy per bit conversion that is three orders of magnitude better. The theoretical physical limit known as Landauer limit is shown in grey [10], © 2015 Semiconductor Research Corporation.

In memristive systems, a logic state (0, 1) is related to the electrical resistance of a two-terminal device, which can be altered by resistive switching, or the so-called memristive phenomenon [11]. Since internal states are given by a stable physical value that remains even without power, memristive systems are typically considered for non-volatile memory (NVM) applications [12]. However, unlike Flash, which is also an NVM, memristive systems are more energy efficient, can be manufactured with a higher storage density, and are more easily scalable [13]. Aside from NVM applications, memristive systems can also be found in logic circuits with integrated memory, such as Field-Programmable Gate Arrays (FGPA) for in-memory computing or neuromorphic architectures like artificial neural networks (ANN) [14]. In-memory computing allows for direct communication between memory and computing, which is more efficient (energetically and computationally) than classical computing, which is based on the von Neumann architecture, where communication between memory and computing is limited by the PCI bus [15]. ANNs, on the other hand, are becoming more and more relevant with the use of artificial intelligence. For example, generative pre-trained transformers (GPTs) would benefit from the efficiency given by the transformer architecture of an ANN [16].

Despite the promising prospects of memristive systems for future computational tasks, it is intriguing as to why commercially functional redox-based resistive random access memory (ReRAM)-NVM was initially made available in 2013 [17] and complex neural networks are slated to be released in 2024 [18], although resistance switching in oxides was first discovered in the 1960s [19–21]. Looking at history, industry, and research could demonstrate several working ReRAM devices from the mid-1990s until 2004 [22, 23]; however, two major achievements led to the start of a megatrend in the semiconductor industry: first, a publication by Waser et al. in 2006 [24] that could clarify the underlying **microscopic mechanism** of the memristive phenomena in oxide ReRAM known by the name valence change memory (VCM) effect. Second, a publication by William's group in 2008 [25] which **proved** that the electrical characteristics can indeed be described in terms **of the theory** of memristive devices published by Kang and Chua in 1976 [26]. This highlights that a generic understanding of the **microscopic mechanism** and **a validation of the theoretical concept** were key to advancing an entire research field. With this in mind, this PhD research is realized with a similar objective: the information gained at the microscopic level, complemented, if possible, by theoretical calculations, provides the necessary insight to provide a true explanation of the device properties.

10. Related Work

10.1. The memristor and the memristive system

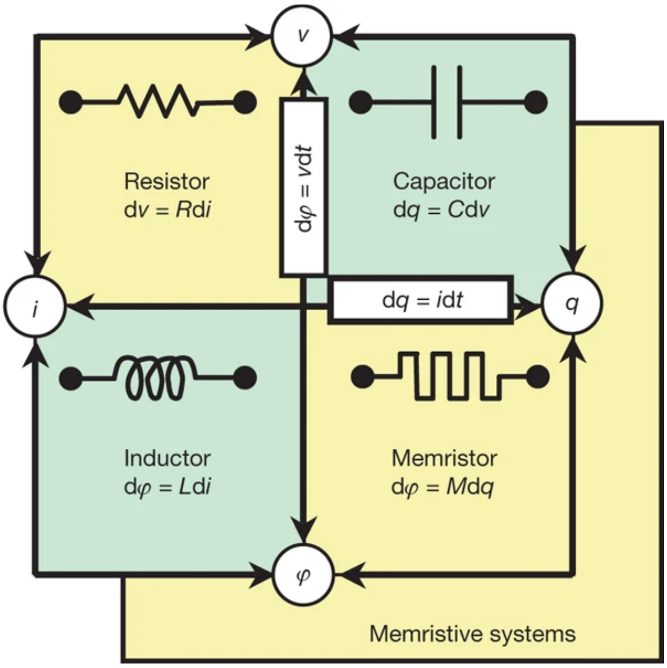

Figure 10-1: The four basic passive circuit elements (resistance *R*, capacitance *C*, inductance *L*, memristance *R*) given as functions of the four fundamental circuit variables voltage *v*, current *i*, charge *q* and flux *φ*. Reprinted with permission from [25], © 2008 Nature.

The memristor, as the fourth circuit element, was introduced in 1971 by Leon Chua [27] and is defined as a function of charge and flux, as shown in Figure 10-1. Nowadays, a memristor is typically expressed by the following equation [28], in which the resistance R depends on a dynamical state variable q (a state-dependent Ohm's law):

$$V = R(q) \cdot I \qquad \text{Equation 9-1}$$

The memristor state equation can thus be expressed by the following:

$$\dot{q} = I \qquad \text{Equation 9-2}$$

Based on this equation, it becomes clear why a memristor cannot be utilized for data storage applications. A NVM based on resistive switching can only work if the charge q is strongly non-proportional to the current, which is not the case with Equation 9-2 [29].
Therefore, two-terminal devices that are used for non-volatile resistive switching applications should not be called memristors. These devices should be named under the more general term memristive systems introduced by Chua and Kang [26]. The state-dependent Ohm's law has been refined accordingly, with x being an internal state variable:

$$V(t) = R(x, I, t) \cdot I(t) \qquad \text{Equation 9-3}$$

This complex state-dependent Ohm's law results in a strong non-linearity of R, as R now depends on the entire device history. In addition, to be representative of non-volatile resistive switching, the internal state variable must fulfill certain requirements, as shown by Strukov et al. [25].

10.2. Redox-based resistive random access memory (ReRAM)

Solid-state memory technologies are classified as read-only memories (ROM) and random access memories (RAM), as shown in Figure 10-2. Abbreviations of all the shown memory technologies are listed in Chapter 7. This PhD thesis will only cover data storage devices based on resistive switching. Information about the other memory technologies can be found elsewhere [8]. Data storage devices based on resistive switching are typically named under the umbrella term resistive random access memory (RRAM) or memristive RAM and are non-volatile solid-state memory technologies. Resistive switching can be based on three different effects: magnetic, electrostatic, or atomic configuration, while the underlying mechanism for resistive switching determines the device classification. This PhD thesis focuses on valence change memory (VCM). For VCM (and ECM and TCM), resistive switching is a result of redox effects, which is why these memristive devices are summarized by the term ReRAM.

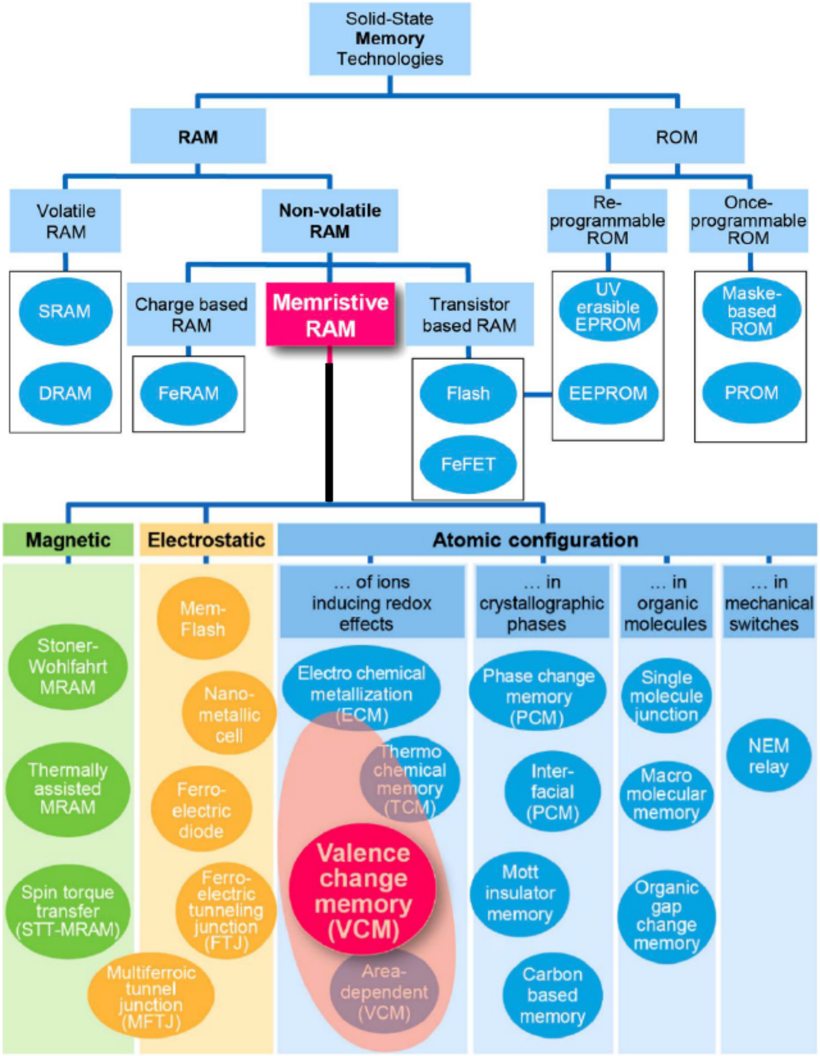

Figure 10-2: Solid-State Memories are classified as read-only memory (ROM) and random access memory (RAM). The memristive devices can be named under the umbrella term Memristive RAM, which is considered part of non-volatile RAM. Memristive RAM is further divided based on the effect that mediates resistive switching being either magnetic, electrostatic, or atomic configuration. Further differentiation is made based on the underlying mechanism of resistive switching, e.g., VCM or ECM. All acronyms are listed in Chapter 7. Reprinted with permission from [29], © 2021 Taylor & Francis.

A VCM cell is a two-terminal device that consists of a metal-insulator-metal (MIM) stack. As shown in Figure 10-3, a metal oxide dielectric layer like HfO_2 is sandwiched by a chemically inert but electronically active electrode like Pt and an ohmic counter electrode like TiN.

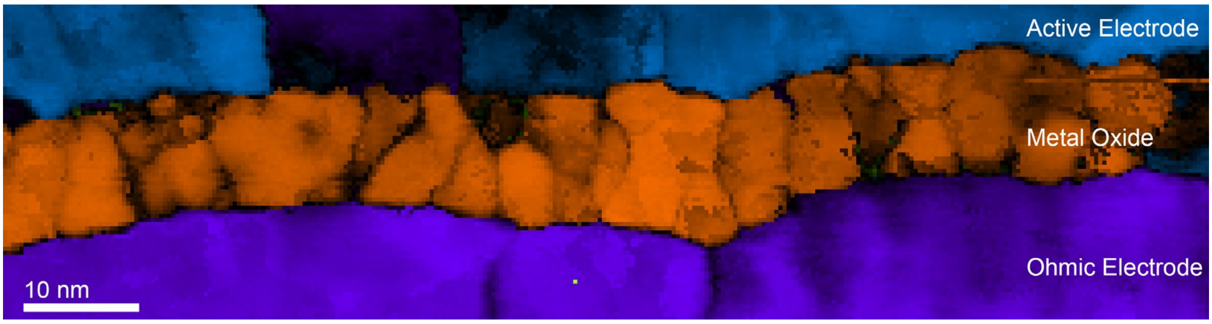

Figure 10-3: Phase map retrieved from a 4D-STEM dataset of a metal-insulator metal stack.

The choice of material and the associated work functions influence the metal-dielectric interface barriers, which impact the ionic phenomena during resistive switching operations [30]. Usually, the active electrode has a high work function to provide a Schottky contact, and the ohmic electrode has a low work function while being easily oxidizable [31]. A MIM cell is electronically considered a Schottky diode. However, Schottky emission fails to explain the conduction mechanisms of resistive switching in most VCM cells [32] because current is limited by the dielectric layer (bulk limited) and not by the metal electrodes (electrode limited). A brief summary of the different conduction mechanisms is shown in Figure 10-4, and respective schematic energy band diagrams are shown in Figure 10-5 and Figure 10-6 [33].

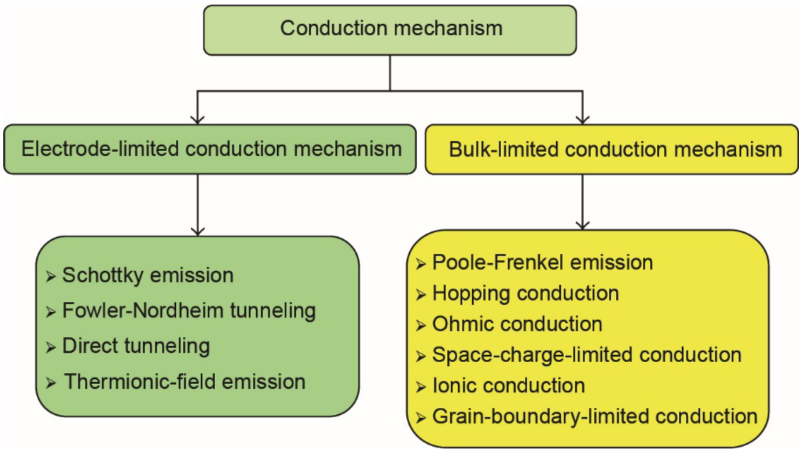

Figure 10-4: List of electrode-(green) and bulk-(yellow) limited conduction mechanisms. Reprinted under a CC BY NC ND from [33], © 2014 Elsevier.

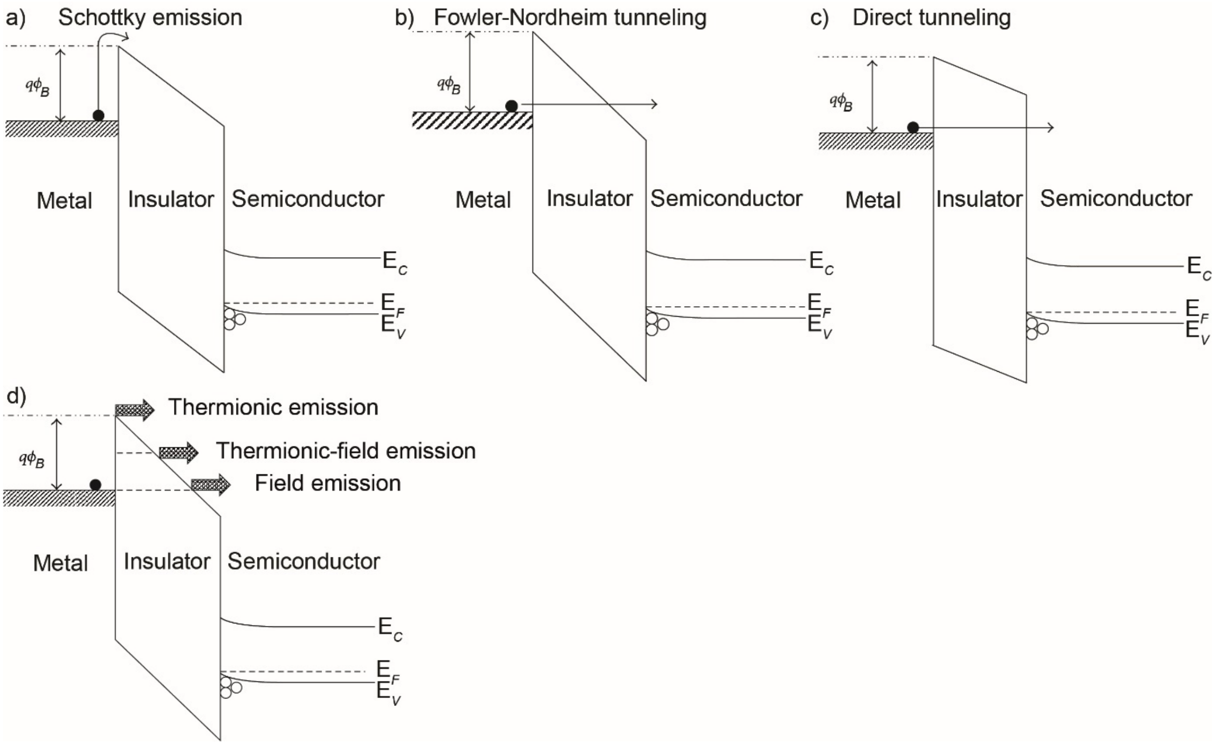

Figure 10-5: Schematic energy band diagrams of electrode-limited conduction mechanisms in metal-insulator semiconductor structures. $q\phi_B$ is the Schottky barrier height; E_C and E_V are the conduction and valence bands, respectively; and E_F is the Fermi level. Reprinted and modified under a CC BY NC ND from [33], © Elsevier.

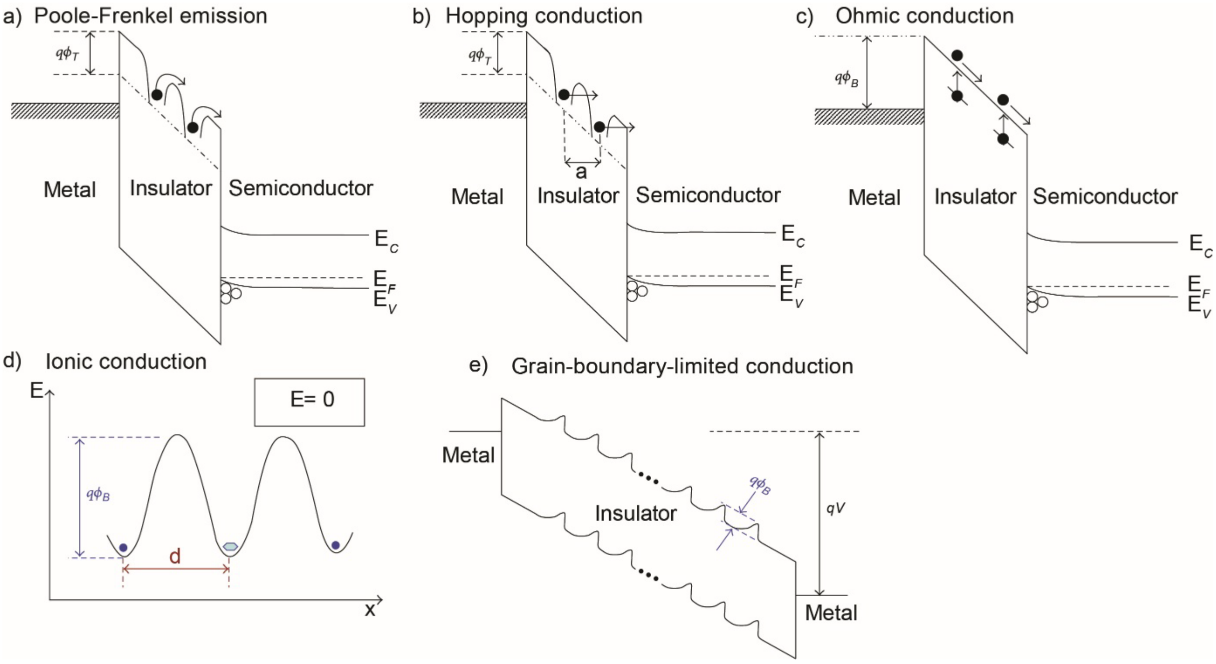

Figure 10-6: Schematic energy band diagrams of bulk-limited conduction mechanisms in metal-insulator-semiconductor structures. $q\phi_B$ is the Schottky barrier height in (c), the potential barrier height in (d), and the grain boundary potential energy barrier in (e); $q\phi_T$ is the trap energy level; *a* is the mean hopping distance; *d* is the spacing of two nearby jumping sites; E_C and E_V are the conduction and valence bands, respectively; and E_F is the Fermi level. Reprinted and modified under a CC BY NC ND from [33], © 2014 Elsevier.

For electrode-limited conduction, the barrier height $q\phi_B$ is one of the most important parameters. If electrons obtain enough energy to overcome the barrier, the resulting conduction mechanism is Schottky emission. For barriers thinner than 10 nm, electrons can tunnel through the barrier, which is Fowler-Nordheim tunneling, and for thin barriers (e.g., 3.5 nm for SiO_2), the conduction mechanism is direct tunneling. The current due to thermionic field emission is temperature-dependent and is located between (in terms of energy) Schottky emission and field emission.

Bulk-limited conduction is dependent on the trap energy level of the dielectric film $q\phi_T$. Poole-Frenkel emission is sometimes named “internal Schottky emission” due to its similarity, with the difference that electrons are thermally excited from traps inside the dielectric. Electrons from trap states can also tunnel and “hop” between trap sites, distanced by the mean hopping distance a, named hopping conduction. Ohmic conduction results from mobile electrons in the conduction band but is also influenced by charge carriers due to thermal excitation. Ion movement leads to ionic conduction, and polycrystalline dielectric layers can have grain boundaries with higher resistivity compared to the grain, thus limiting conduction, namely grain boundary-limited conduction.

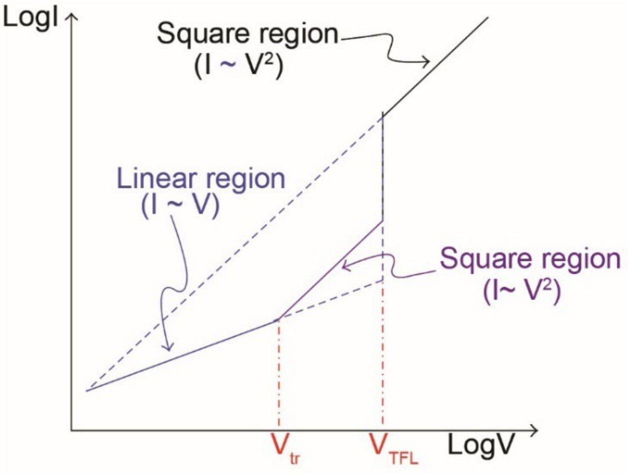

Figure 10-7: Schematic I-V (current-voltage) curve consistent of three regions showing space charge-limited conduction (SCLC). V_{tr} is the transition voltage, and V_{TFL} is the trap-filled limit voltage. Reprinted and modified under a CC BY NC ND from [33], © 2014 Elsevier.

A representative I-V (current-voltage) curve for space-charge-limited conduction (SCLC) of a MIM cell is shown in Figure 10-7 and consists of three regions with different slopes [34]. For the first region, current scales linearly with voltage, known as Ohm’s law. In the second region, from V_{tr} (transition voltage) to V_{TFL} (trap-filled limit voltage), current scales with the square of the voltage, which is also true for the third region but, as shown in the literature, can also be greater than two [35].

A brief summary of how to identify the most relevant conduction mechanisms based on I-V curves of leakage measurements is taken and modified from Chang et al. [36] and is given in Table 10-1. The power law can be used to identify several conduction mechanisms, e.g., SCLC. Depending on the conduction mechanism, resistive switching is either considered filamentary or area-dependent (non-filamentary) switching [37], as shown in Figure 10-8. An overview of filamentary resistive switching processes is shown in Figure 10-9. The pristine VCM cell shown in the bottom-left corner has an initial resistance state (IRS), and an electroforming step is required to allow for the resistive switching operations Set and Reset. A more general overview of possible processes in a memristive cell is summarized in Figure 10-10. The main driving forces are the electrochemical potential and temperature gradient. VCM cells with fully oxidized metal oxide layers usually require the creation of a conductive filament by applying relative high electric fields, which can damage the cell permanently, leading to device failure [38, 39], reduction of endurance and retention [40], and can also impede CMOS compatibility [41]. Therefore, different concepts of the insulating layer by oxygen [42–45] or grain boundary [1, 46] engineering are utilized to create usable VCM cells. Here, pre-existing oxygen vacancies facilitate CF formation, and in the case of grain boundary engineering, they can provide preferential pathways [47–50].

Table 10-1: Practical guide on how to determine the conduction mechanism based on I-V (current-voltage) curves. Reprinted and adapted with permission from [36], © AIP Publishing.

Chargetransport/Conductionmechanism	**Linearfittingplots**
Poole-Frenkel emission	$\ln(I/V)\ vs\ \sqrt{V}$
Fowler-Nordheim tunneling	$\ln(I/V^2)\ vs\ 1/V$
Schottky emission	$\ln(I)\ vs\ \sqrt{V}$
Hopping conduction	$\ln(I/V)\ vs\ V$
Power law	$\ln I\ \ vs\ \ln V$

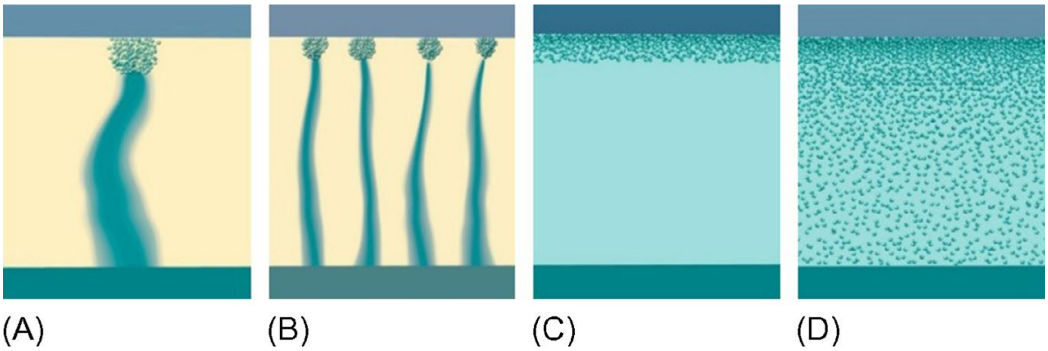

Figure 10-8: Metal (gray)-insulator (yellow)-metal (green) cell showing schematically (A) filamentary, (B) multi-filamentary, (C) area-dependent interface-type, and (D) area-dependent bulk resistive switching. Reprinted with permission from [51], © 2015 Elsevier.

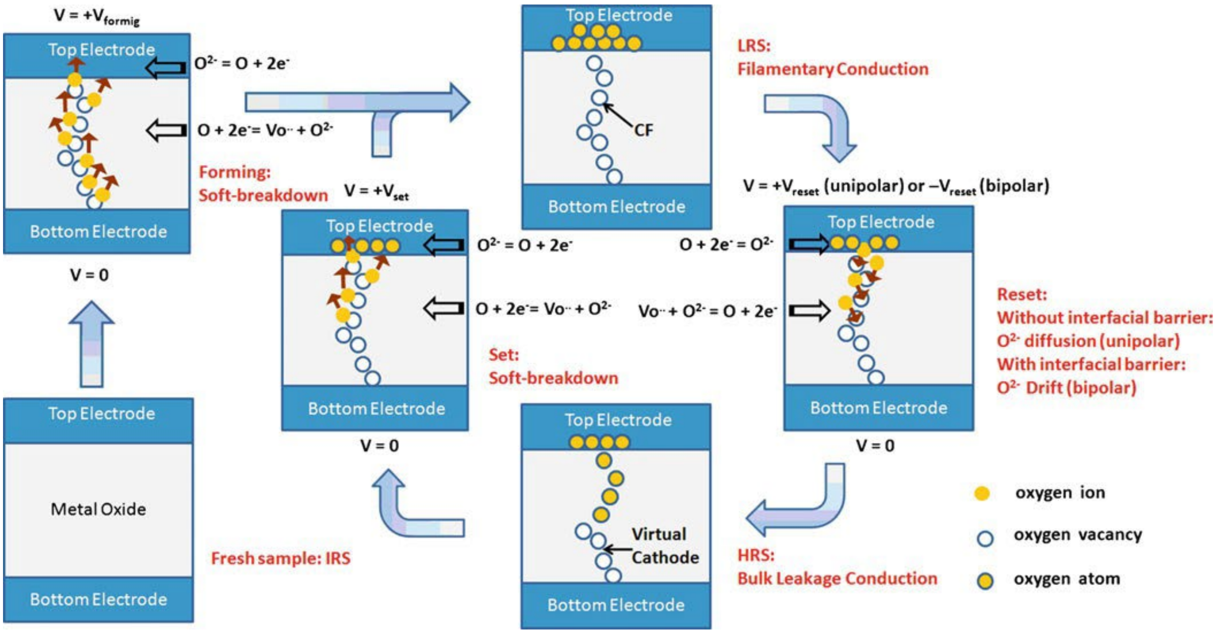

Figure 10-9: Resistive switching processes in a VCM cell. The pristine sample (Fresh sample, bottom-left corner) has an initial resistance state (IRS) due to the insulating properties of the metal oxide layer. Applying a positive voltage to the top electrode (+$V_{forming}$, top-left corner) results in the injection of electrons and a soft-breakdown that creates charged Frenkel defect pairs (Oxygen vacancies $V_O^{\cdot\cdot}$ and oxygen interstitials O_i'' (here O^{2-})). Due to the oxidizable top electrode, O_i'' will be incorporated and $V_O^{\cdot\cdot}$ will start to form a conductive filament (CF). Completing the electroforming step (top right) results in the VCM cell being in a low resistance state (LRS). Applying a sufficient voltage of the same polarity (+V_{reset}) or opposite polarity (-V_{reset}) will result in breakage or shrinkage (not shown) of the CF and, upon completion of the reset process, in an increase in resistance (high resistance state, HRS). Applying a voltage with the same polarity as the forming voltage is considered the set process and results in the growth of the CF and a reduction in resistance (LRS) upon completion. Reprinted with permission from [52], © 2012 Springer New York.

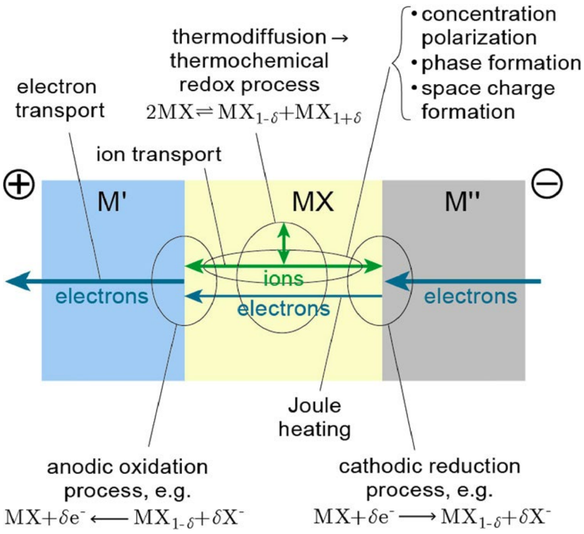

Figure 10-10: Supplying electrons to a metal (M’’)-insulator (MX)-metal (M’) can result in several redox reactions, including a local increase in temperature due to Joule heating and phase and space charge formation due to concentration polarization. Reprinted with permission from [29, 53], © 2012 John Wiley & Sons.

11. Methodology

11.1. Reactive molecular beam epitaxy (RMBE)

Molecular beam epitaxy (MBE) is a physical vapor deposition (PVD) technique to grow epitaxial or highly textured thin films by creating molecular beams of electron-evaporated high-purity materials onto a (heated) substrate in an ultra-high-vacuum (UHV) chamber. High-purity materials are loaded into a crucible and placed in an effusion cell, as shown in Figure 11-2 a). Electrons are targeted towards the crucible, as shown in Figure 11-2 b) to melt and evaporate the material. With the addition of radical beam-assisted evaporation (RBAE), elements can be in situ oxidized or nitridized before being deposited onto the substrate, as shown in Figure 11-3, which is known today as reactive molecular beam epitaxy (RMBE). A summary of the relevant parameters to create a thin film with the desired properties is shown in Figure 11-1. Impurities (low vacuum pressure, low purity materials or gases, dirty substrates, end plates, or RF discharge tubes) should be kept to an absolute minimum as device properties are strongly altered. The choice of substrate is the foundation for growing thin films. In-plane lattice spacings determine the lattice mismatch between substrate and thin film, which results in strain effects that can be utilized to grow epitaxial or textured thin films far beyond their thermodynamic equilibrium. The correct choice of substrate temperature can enhance thin film properties (crystallinity, surface roughness), but it can also cause unwanted phases. In addition, the evaporation rate relative to the amount of available radicals (optical output) finally determines not only the crystallinity but also the stoichiometry and phase. In principle, maximizing the optical output to have the most number of radicals available is best. The choice of end plate (aperture) determines the stable plasma power range for a certain partial pressure, which in turn influences the growing thin film stoichiometry. Moreover, a stable evaporation rate is crucial for high-quality thin films, which is not always possible for every evaporation rate.

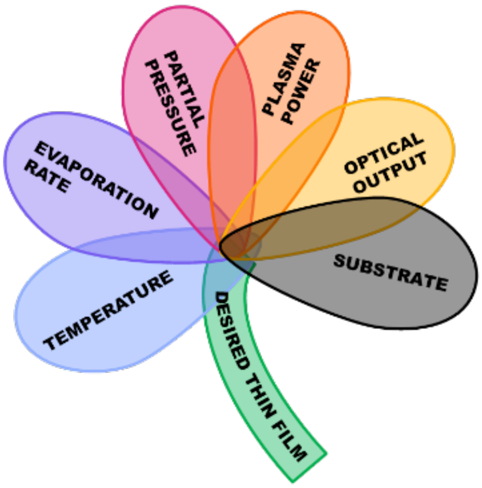

Figure 11-1: The bouquet of RMBE: Only careful selection of the shown growth parameters can yield a thin film with the desired properties.

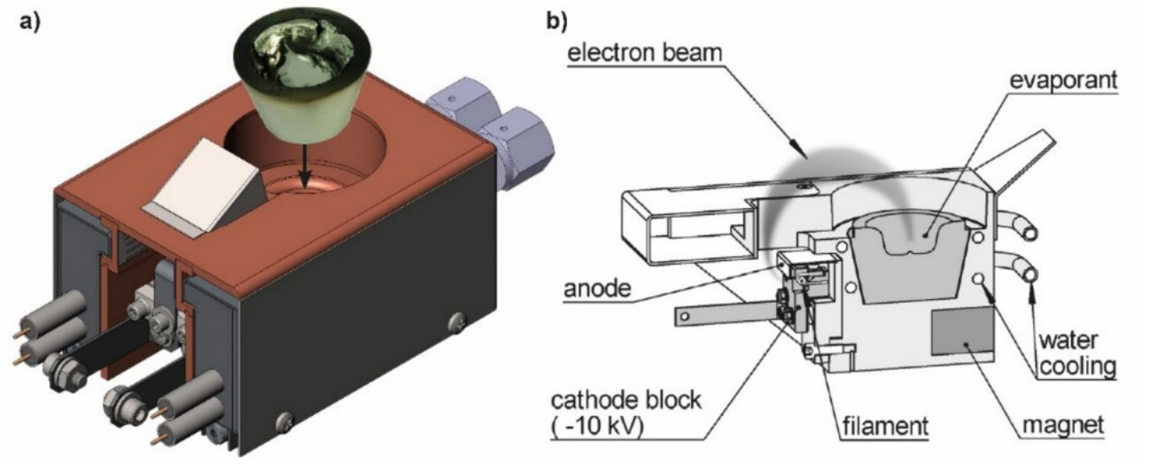

Figure 11-2: a) A tungsten crucible with melted Hf is placed in an effusion cell (Hanks HM^2 single-crucible e-gun). The picture of the crucible is taken from [54] and the technical drawing of the cell from [55], © 2020 thermionics laboratory, inc. b) Cross-sectional schematic view of an effusion cell. Electrons are deflected by 270° in a shielded compartment to avoid contamination from the material evaporation. Taken from [56], © 2024 Dr. Eberl MBE-Komponenten GmbH.

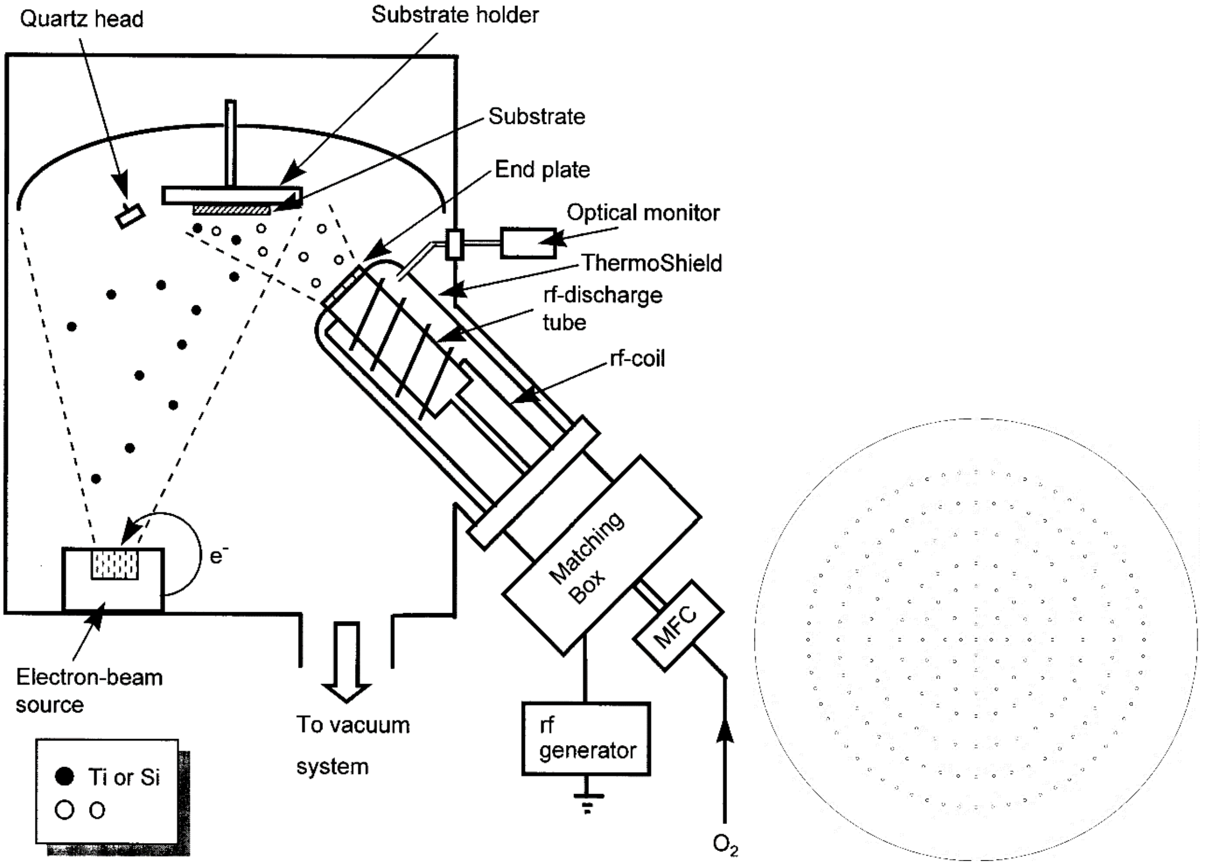

Figure 11-3: Left: Electron-beam evaporated materials like Ti or Si are in situ oxidized by O radicals before being deposited on the substrate. The evaporation rate is monitored by a quartz crystal microbalance (QCM, here quartz head) and the amount of O radicals by the optical monitor. Reprinted with permission from [57], © 2000 Elsevier. Right: Example of an end plate or aperture having 175 holes with a diameter of 200 µm.

11.2. Device fabrication and electrical characterization

PVD techniques like RMBE can produce continuous coatings on substrates. However, most semiconductor applications require a patterned coating, typically achieved via photolithography [58]. For this method, as shown in Figure 11-4, a sacrificial photoresist is deposited on a substrate via spin coating. This photoresist is exposed to ultraviolet (UV) light through a mask that creates a pattern on the surface. In the case of a negative photoresist, the illuminated sections will “harden” so that the unexposed parts can be removed via immersion in a developer solvent. In the case of a positive photoresist, illuminated parts become more soluble in the developer solvent. Thus, unexposed parts remain after immersion in the developer solvent. The pattern of the developed photoresist is then transferred to the substrate, either via etching or via lift-off. For the lift-off-process, an additional layer is deposited onto the patterned surface. This is typically achieved via sputtering as schematically shown in Figure 11-5. The substrate and desired coating material (target) are placed in a vacuum chamber. A working gas (e.g. argon) is ionized, which will create a plasma cloud. Supplying a negative potential to the target material will cause ions from the plasma to accelerate towards the target to dislodge and eject atoms. Some atoms will hit the substrate and recombine to form the coating, which generally has the same chemical composition as the target material. After sputter deposition, immersion in typically acetone will lift off the photoresist with the sputtered material, leaving only the desired sputtered material pattern on the surface. Most reliable pattern transfers with additive techniques (sputtering) that require a lift-off process, utilize a negative photoresist. As shown in Figure 11-6, the developed profile of a negative photoresist shows an undercut unlike the overcut profile of the positive photoresist. This undercut profile, usually called the lift-off profile, yields in gaps in the coating after sputter deposition facilitating the removal (lift-off) of material on top of the photoresist. The continued coating due to the overcut profile significantly complicates lift-off. Figure 11-7 shows an example of a patterned surface after lift-off of a VCM memristive device under test (DUT). The MIM structure is TiN/HfO_2/Pt, and the additional Au layer, is for protection against penetration when contacting with a probe, as schematically illustrated in Figure 11-8. One source meter unit (SMU) probe is placed on the Au layer and the other probe (the ground (Gnd) probe) is on the TiN layer. I-V measurements can be performed with a semiconductor characterization system (SCS).

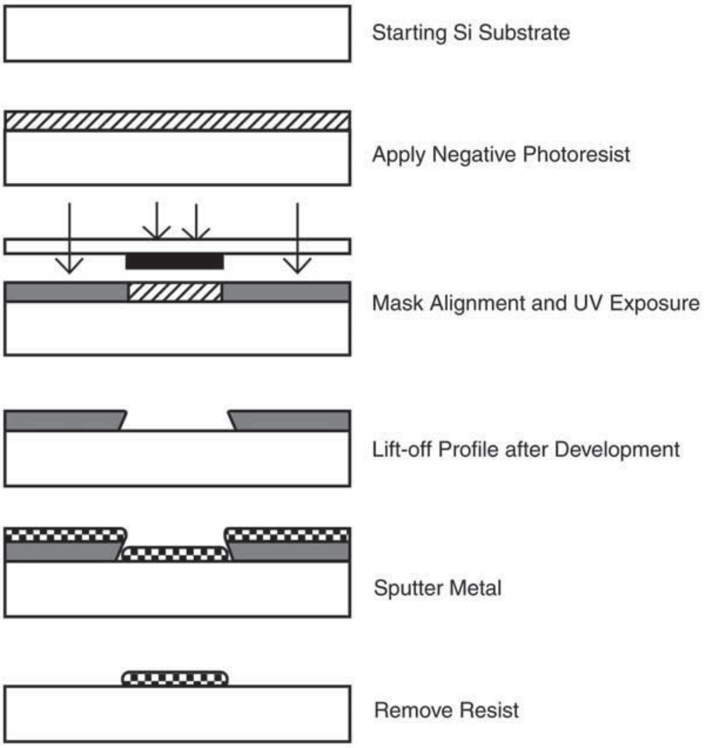

Figure 11-4. Selective surface coating is achieved via surface patterning: ultraviolet light (UV) shines through a mask onto a photoresist. For a negative photoresist, exposed parts "harden" so that unexposed parts can be removed after immersion in a developer solution. The sputtered material that is on top of the developed photoresist will be "lifted off" after immersion in acetone, completing the pattern transfer from the mask to the surface. Reprinted with permission from [59], © 2006 Springer.

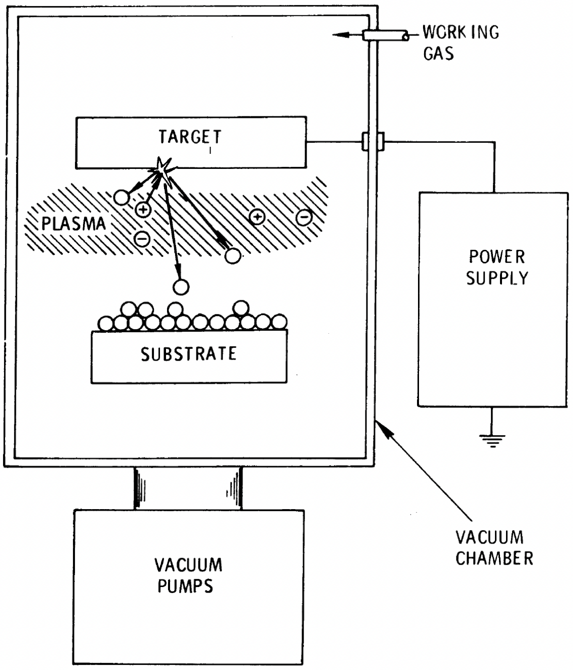

Figure 11-5: Sputter deposition is achieved by accelerating an ionized working gas in a vacuum chamber, known as plasma, to a target material to dislodge and eject atoms that will recombine on the substrate surface to form the coating. Reprinted with permission from [60], © 1973 SAE International.

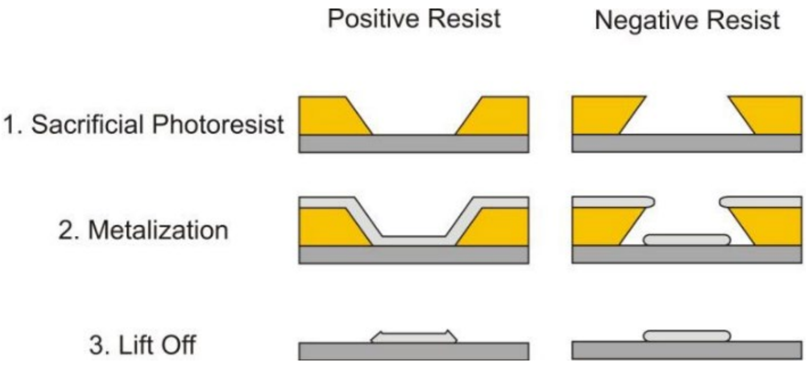

Figure 11-6: Schematic comparison of a lift-off process based on a positive (left) and negative (right) photoresist. Reprinted with permission for non-commercial purposes from [61], © 2014 University of Alberta Libraries.

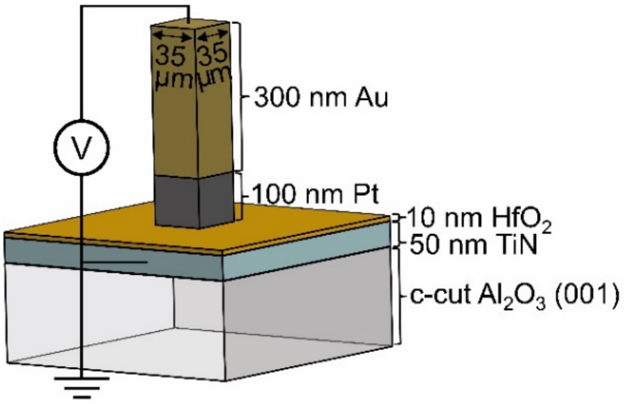

Figure 11-7: Illustration of a valence change memory (VCM) memristive device. The top electrode (Pt) is contacted, and the bottom electrode (TiN) is grounded. The additional Au layer protects the device from penetration during electrical testing. Reprinted with permission from [62], © 2021 Oxford University Press.

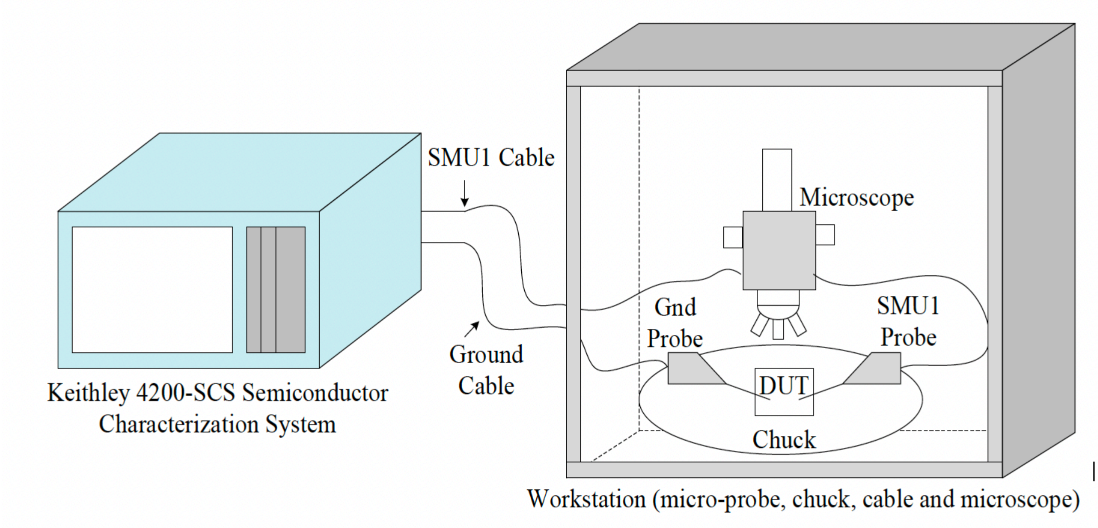

Figure 11-8: A device under test (DUT) is contacted by two source measure unit (SMU) probes, one for supplying voltage or current and the other for providing ground (Gnd), connected to an in this case Keithley 4200-SCS (Semiconductor Characterization System). Probes are usually micrometer sized. Thus, an optical microscope is required for precise positioning. Reprinted under a CC BY 4.0 from [63], © 2020 MDPI.

11.3. Thin film growth

The starting conditions for thin film growth via i.e. PVD (or chemical vapor deposition (CVD)) are shown in Figure 11-9 (a), where a metastable vapor (phase A) is adjacent to a substrate (s, phase $B^{(s)}$). To trigger the phase transition from vapor to solid so that nucleation and growth of the nuclei into a thin film can start, a steady state of supersaturation (or supercooling) needs to be achieved[64]. This is realized with a vapor phase that contains more material than can be sustained in equilibrium at a given temperature and pressure. This results in the adsorption of atoms from the vapor on the substrate, as schematically shown in Figure 11-9 (b), to form nuclei (either spontaneously or artificially induced). The growth of the nuclei into epitaxial or textured films is by definition related to atomic ordering and is influenced by the lattice misfit between substrate and film, thermal stress, but also the supersaturation (the flux), and the adhesion energy. The five most relevant growth modes are shown in Figure 11-10 and are systematically classified in terms of surface energies (SFE of substrate γ_B, SFE of film γ_A, and SFE of film-substrate interface γ^*)[65]. The growth mode and growth kinetics will impact the crystalline quality, i.e., surface morphology or microstructure, as shown in Figure 11-11. An ideally ordered single-crystalline thin film has no grain boundaries, with only one out-of-plane (growth) orientation and one in-plane (parallel to the interface) orientation. The opposite is an ideally disordered amorphous/polycrystalline film with no defined out- and in-plane orientation. Biaxially textured grown thin films can have a defined out-of plane, and, i.e. several defined in-plane orientations, usually named domains, and uniaxially textured films have only a defined out-of plane orientation.

.

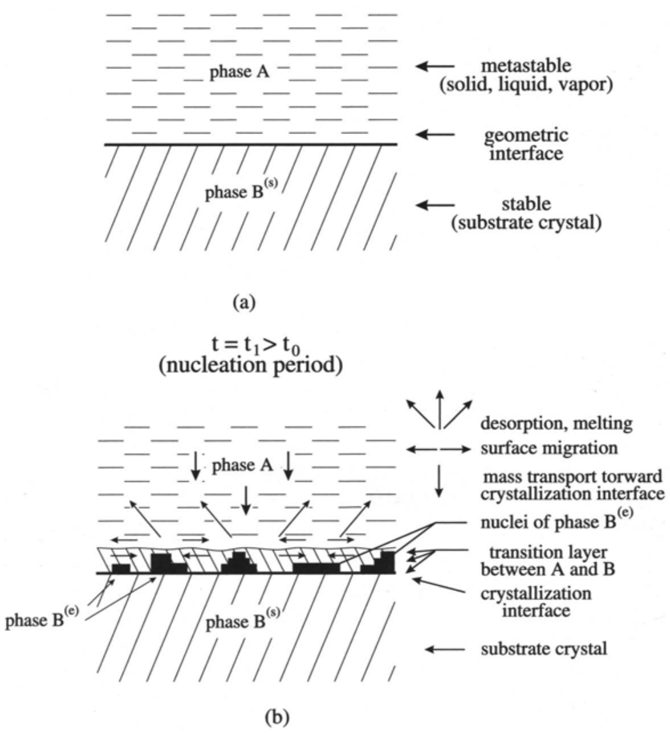

Figure 11-9: (a) A metastable phase A (i.e., vapor in the case of physical vapor deposition) is adjacent to a substrate (s) (phase $B^{(s)}$). b) If supersaturation is achieved, atoms from phase A are thermodynamically incorporated to the surface of phase $B^{(s)}$ and form nuclei of the new growing epilayer (e) of phase $B^{(e)}$. Surface atoms can diffuse across the surface and also desorb. Reprinted with permission from [66], © 2002 Springer.

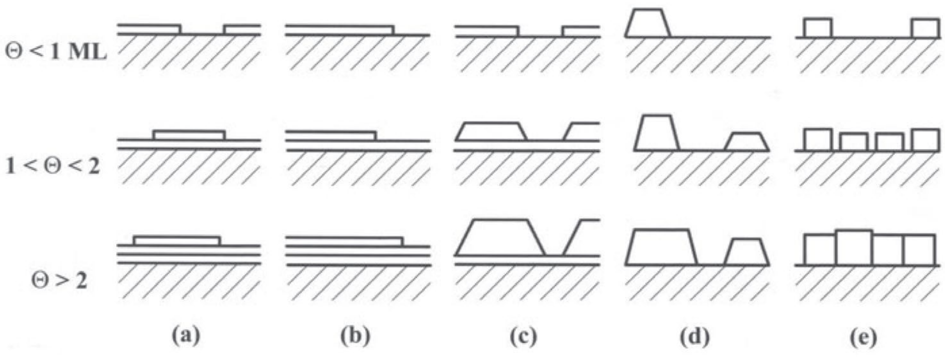

Figure 11-10: (a) A layer-by layer growth, known as two-dimensional Frank-van der Merwe (FM) growth mode, is achieved when the surface energy of the substrate γ_B is greater than the combined surface energy of the film γ_A and the interface energy of film-substrate γ^*. (d) If γ_B is smaller than $\gamma_A + \gamma^*$, the thin film will grow as islands, known as the three-dimensional Volmer-Weber (VW) growth mode. (c) A layer plus island growth, known as Stranski-Kstanov (SK) growth mode, occurs when γ^* increases with film thickness as a result of i.e. strain to match the lattices of film to substrate. (e) Columnar growth is similar to VW and SK growth but fundamentally different due to the lack of coalescence, where islands or columns do not fuse in a liquid-like fashion. (b) Step flow growth can be achieved for substrates with surface steps (i.e., monatomic terraces as a result of wafer miscut) at sufficiently high temperatures and low fluxes, respectively. Adatoms are directly incorporated in step edges (due to their mobility) and do not nucleate on terraces, which would result in FM growth. θ is the surface coverage in monolayers (ML). Reprinted with permission from [66], © 2004 Springer.

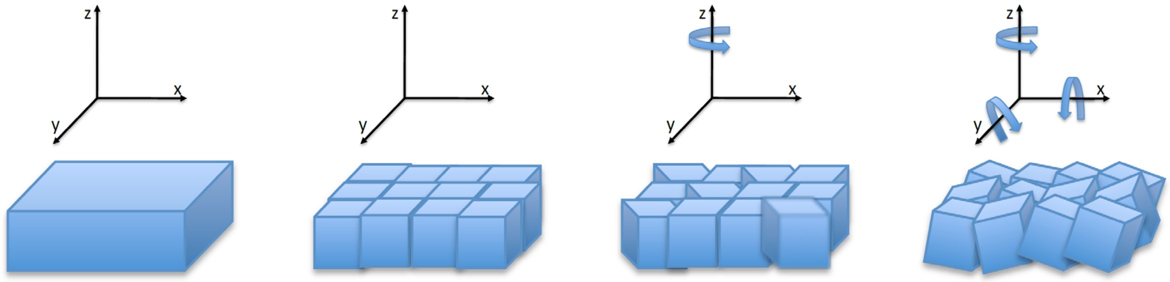

Single Crystal	
In-plane rotation	fixed
Out-of-plane rotation	fixed

Polycrystalline Biaxially textured	
In-plane rotation	fixed
Out-of-plane rotation	fixed

Polycrystalline Uniaxially textured	
In-plane rotation	not fixed
Out-of-plane rotation	fixed

Polycrystalline Randomly oriented	
In-plane rotation	not fixed
Out-of-plane rotation	not fixed

Figure 11-11: Different types of thin films are classified in terms of their out-(growth) and in-plane orientation. Reprinted under a CC BY-NC 3.0 US Deed from [67] © 2010 Stanford University.

11.4. X-ray diffraction techniques

X-ray diffraction (XRD) is typically used to investigate thin film quality. The essential components for investigating thin films are shown in Figure 11-12. The X-ray source is conditioned by a laterally graded multilayer (Göbel) mirror to form a parallel beam (parallel beam optics). This is essential as a divergent beam (Bragg Brentano optics), typically used for investigating powders, would cause errors that would falsely alter the results. The notation of angles in a diffractometer is shown in Figure 11-13 a). The angle between the incoming and scattered X-ray beam is known as 2θ analogous to the Bragg equation (Equation 9-4), which correlates lattice spacing (d) with constructive interference at certain Bragg angles based on the geometric considerations illustrated in Figure 9-23 b).

$$n\lambda = 2d\sin\theta \qquad \text{Equation 9-1}$$

At a tilt angle of $\psi = 0°$, lattice spacings of planes parallel to the surface, as depicted in Figure 11-14, can be measured with a 2θ-θ scan (mostly known as 2θ-ω scan in literature), yielding information about the out-of-plane orientation. To access in plane lattice spacings (and also asymmetric planes), samples are tilted (ψ, also known as χ) and rotated (ϕ) at a fixed 2θ value for the entire ϕ- ψ range, known as a pole figure, or at a fixed ψ value as a ϕ scan. 2θ-ω scans, as shown in Figure 11-15, near the total reflection critical angle can yield information about the thin film or a stack of thin films, i.e., roughness or thickness [68].

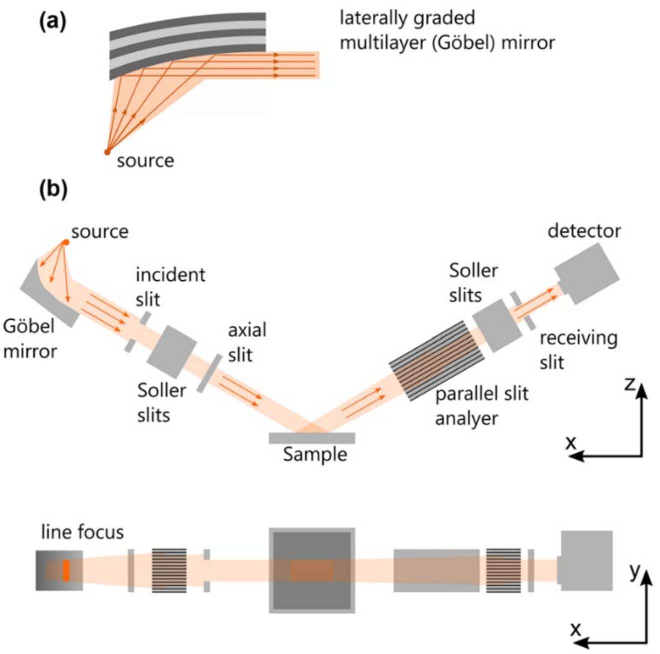

Figure 11-12: A parallel beam (PB) X-ray diffraction setup. (a) A Göbel mirror conditions rays from the source to form a parallel beam. (b) The incident and scattered beam is conditioned with optical arrangements consisting of slits. Reprinted with permission from [69] © 2021 Springer Nature.

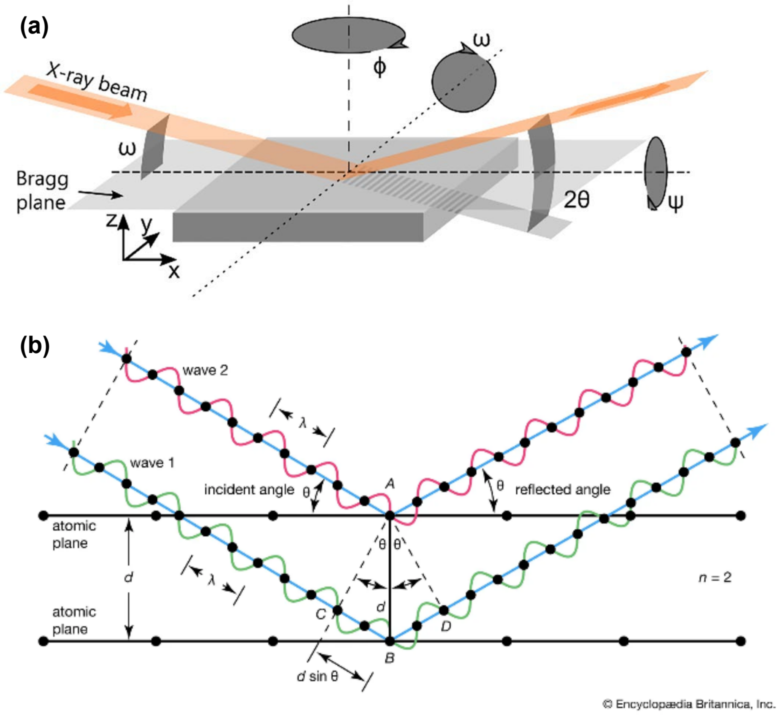

Figure 11-13: (a) The angle between the incoming beam and the sample is ω and between the diffracted beam and the sample is θ. The Sample tilt is given by ψ and the sample rotation with ϕ. Sample rotation along the rotation axis ω is typically performed for rocking curves. Reprinted with permission from [69] © 2021 Springer Nature. (b) Two X-rays with a wavelength λ are reflected by atoms of a lattice with the lattice spacing d. The incident angle θ is equivalent to the reflected angle, and in case that $n\lambda$ is equal to $2d\sin\theta$, both X-rays are reflected in phase, resulting in constructive interference. Reprinted from [70], © 1999 Encyclopedia Britannica, Inc.

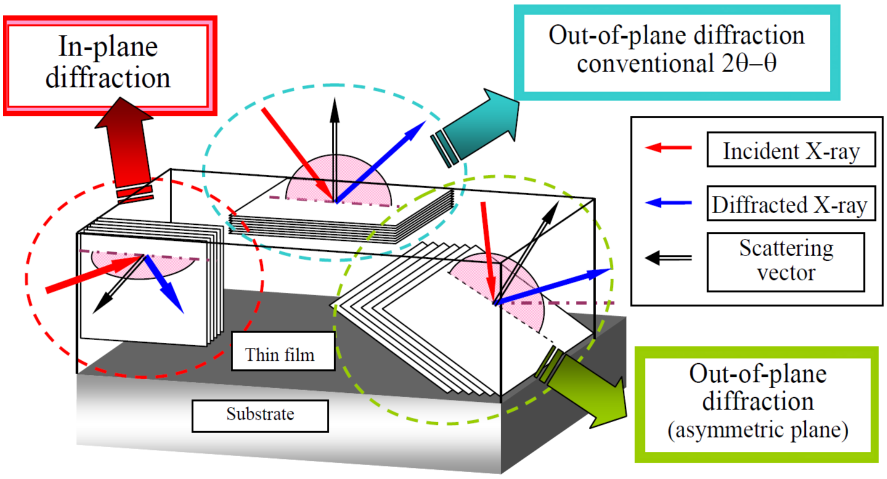

Figure 11-14: X-rays can only be diffracted at Bragg planes, which is why the growth orientation (out-of-plane) can be investigated without tilting the sample. In a textured thin film with defined out- and in-plane crystallographic planes, samples are tilted to investigate in-plane and asymmetric planes of interest so that the scattering vector is aligned to the incident and diffracted X-ray beam. Reprinted under a CC BY 4.0 Deed from [71], © 2013 Scientific Research.

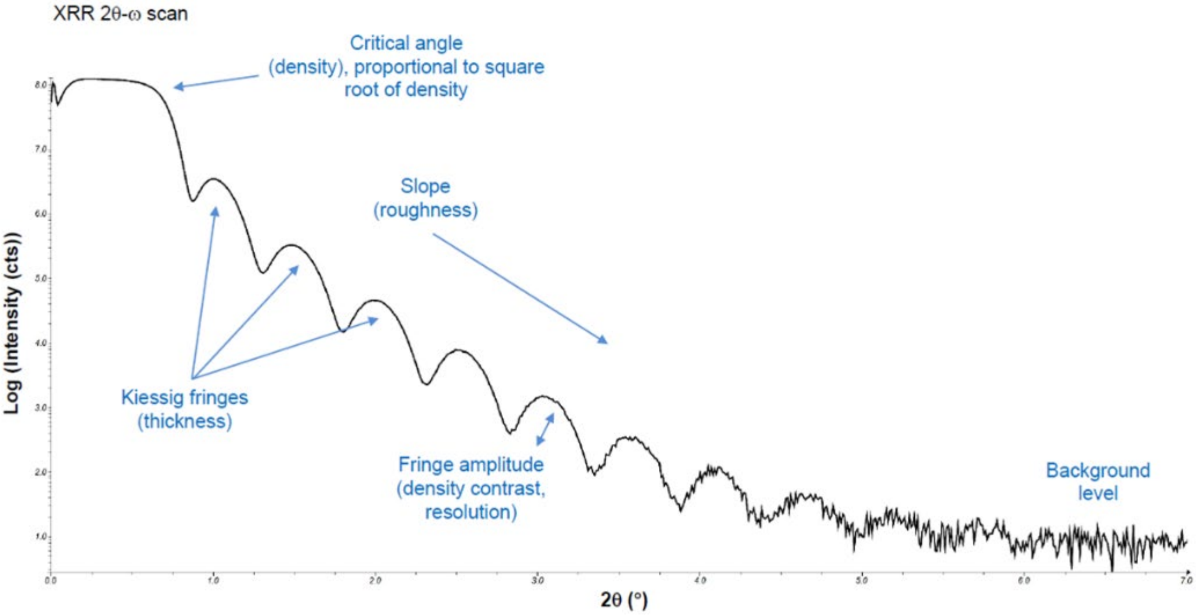

Figure 11-15: From $2\theta = 0°$ until the critical angle, all incident X-rays are reflected, resulting in a high intensity of the X-ray reflectivity (XRR) curve. At the critical angle, incident X-rays propagate along the sample surface, resulting in a decrease in the reflected intensity. Above the critical angle, incident X-rays penetrate the material and are refracted, resulting in a further decrease in the intensity of the reflected beam. From [72], © 2020 Covalent Metrology Corp.

Pole Figures or ϕ scans can provide information about the type of texture. A biaxially textured thin film can consist of two 60° in-plane rotated grains, as schematically shown by the cubic $TiN_{0.9}$ unit cells in Figure 11-16. The out-of-plane orientation is (111), thus a ϕ scan at a tilt angle of $\chi = 54°$ and a $2\theta = 42.62°$ would result in six peaks due to the six (200) planes as depicted by arrows. The microstructure and the arrangement of grains, however, cannot be investigated via XRD. One possibility to visualize grains, which is directly correlated with in-plane orientation, is ion channeling contrast imaging (ICCI). As schematically shown in Figure 11-17 (a), a low index crystal structure results in less secondary electron (SE, e^-) yield compared to (b) a high index crystal structure because gallium ions (Ga^+) can penetrate or channel deeper into the material. In the case of this biaxially textured thin film, aligning the (200) lattice vector with the ion beam would result in a low signal due to a low SE yield. The other grain type, as can be seen in Figure 11-16, would then be aligned along the $(\bar{1}22)$ axis. This high index orientation would result in a high SE yield.

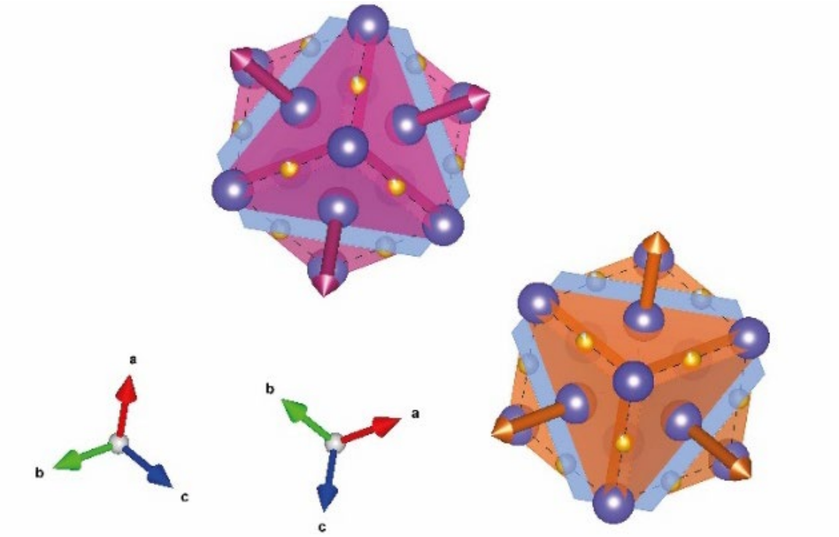

Figure 11-16: Two 60° in-plane rotated cubic $TiN_{0.9}$ unit cells along (111). Structure is taken from [73] and visualized with [74].

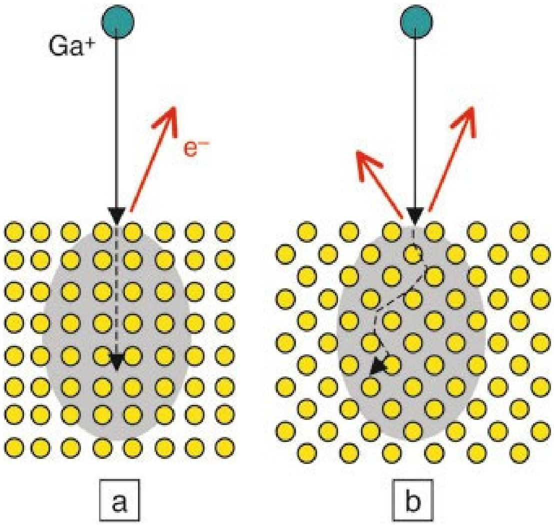

Figure 11-17: (a) Gallium ions (Ga^+) can penetrate or channel deeper into a material along low-index crystal planes, which results in less secondary electron (SE, e^-) yield compared to (b) high-index crystal planes. Reprinted with permission from [75], © 2007 Springer Nature.

11.5. Electron microscopy

The human eye can distinguish objects as small as ~29 μm in size [76], which is obviously insufficient to investigate the microstructural features of thin films in the range of nanometers. Even light microscopes can only resolve features as small as 0.2 μm due to the Abbe diffraction limit because the wavelength of the light limits the resolution. Therefore, electron microscopy techniques like scanning electron microscopy (SEM) or transmission electron microscopy (TEM) are employed, where an electron beam probes the material, which has a wavelength in the range of picometers (i.e., 2.5 pm), resulting in a suitable resolution for investigating thin films. As schematically shown in Figure 11-18, an SEM is a vacuum chamber where a focused electron beam is scanned across a sample generating, i.e., secondary electrons (SE) and backscattered electrons (BSE), which are collected and amplified by suitable detectors. All signals generated upon electron-matter interaction are summarized in Figure 11-19. The size of the shown excitation volume is proportional to the incident beam energy and anti-proportional to the atomic number Z of the material, which is why the amount of BSE scales with Z. SEs have a low kinetic energy and can only escape the sample within a few nanometers below the surface and thus are ideal to investigate the sample topology as a result of a difference in SE yield (resulting in a different image contrast), as schematically shown in Figure 11-20. To investigate thin film stacks and layer interfaces (exemplary as shown in Figure 11-21), usually precise cuts are performed via material removal with a high-energy focused ion beam (FIB), as schematically shown in Figure 11-22. The advantage of FIB technologies, compared to other micromachining technologies, is that a small feature resolution for various materials and geometries can be achieved. Hence, FIB is primarily used to prepare electron-transparent lamellae (samples) for TEM.

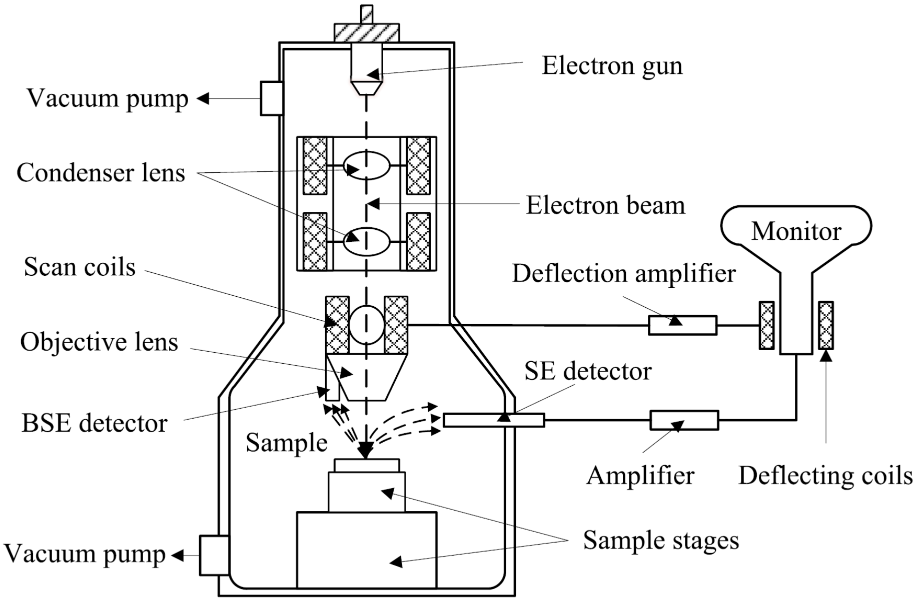

Figure 11-18: Example of a scanning electron microscope (SEM). Inside a vacuum chamber, an electron gun generates accelerated electrons, which have been emitted either from a thermionic emission filament like W or LaB_6, or a field emission filament like a field emission gun (FEG). The electromagnetic condenser and objective lenses form a fine electron probe, which is scanned via the scan coils across an area of interest in the form of a raster. Generated backscattered or secondary electrons (BSE and SE) are collected accordingly via, e.g., an Everhart-Thornley detector, which is primarily used to generate SE images of the sample surface. Reprinted under a CC BY-NC-ND 4.0 DEED from [77], © 2021 IEEE.

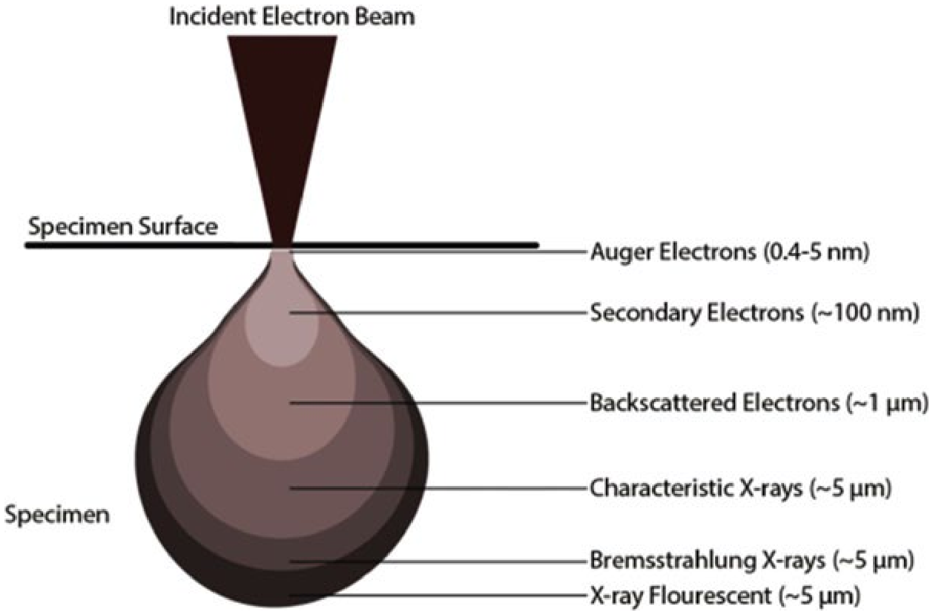

Figure 11-19: Electron-matter interaction generates numerous signals from different sample depths inside an excitation volume. Although the incident electron beam can be formed into a probe with a diameter in the range of nanometers, the spatial and analytical resolution are mostly limited by the size of the excitation volume, which can be several cubic micrometers (µm) in size. Reprinted with permission from [78], © 2018 Springer International Publishing.

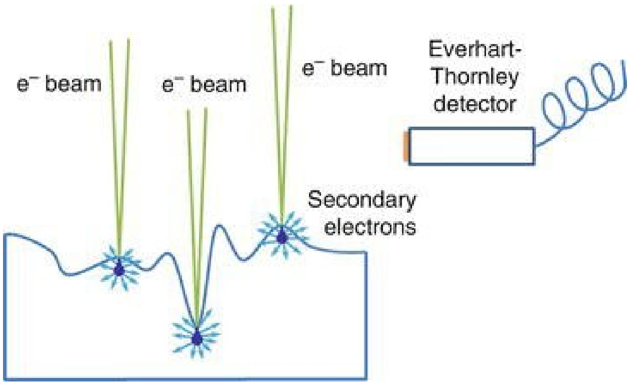

Figure 11-20: Secondary electron (SE) imaging can reveal information about the sample morphology and topography. SE yield and the resulting contrast are primarily due to edge effects: SEs are less absorbed and can exit more readily at surface bumps compared to flat areas. Hence, surface bumps can result in higher brightness due to a higher SE yield. Reprinted with permission from [79], © 2013 Springer Nature.

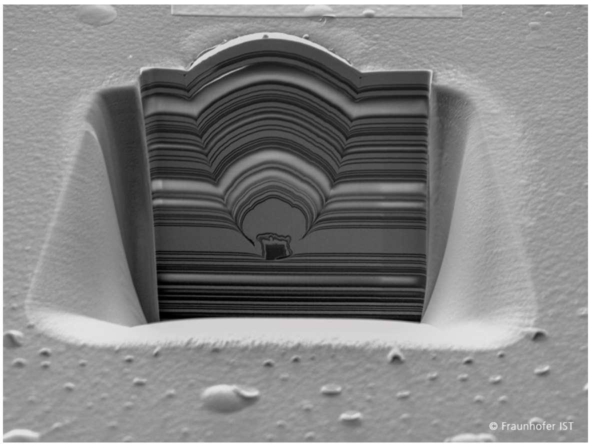

Figure 11-21: A cross-sectional view of a thin film stack was revealed via precise focused ion beam (FIB) milling. Taken from [80] © 2024 Dr. Kirsten Schiffmann, Frauenhofer IST.

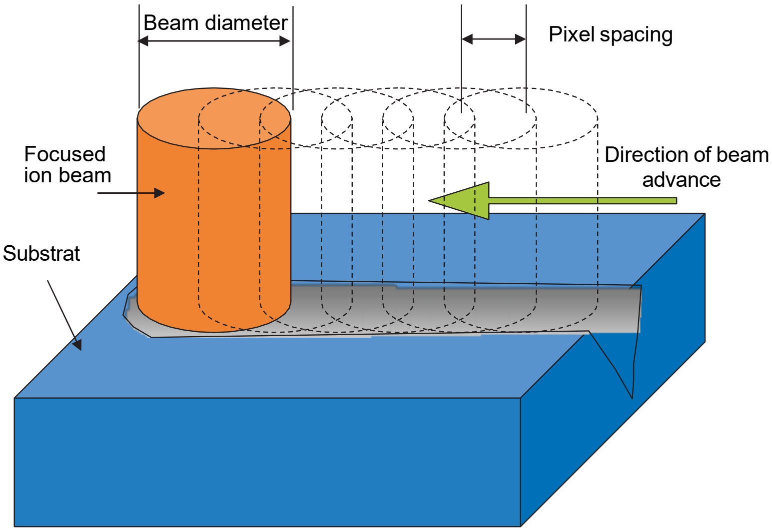

Figure 11-22: A focused ion beam (FIB) is scanned across a sample (substrate) via a precise pixel-by-pixel movement, resulting in material removal (milling). Dwell times (time per pixel) and pixel overlap (given by pixel spacing) must be adjusted for sufficient FIB milling. Reprinted with permission from [81], © 2004 Institute of Physics Publishing.

11.6. Electron transparent lamella preparation

Typical equipment to prepare electron-transparent lamellae is shown schematically in Figure 11-23. Such a FIB SEM dual-beam setup in combination with a lift-out (LO) system (probe/manipulator) is nowadays the standard tool and has replaced single- and dual-beam FIB-SEM systems (without LO) since their first usage in 1978, as shown in Figure 11-24. A modern FIB-SEM system where the FIB is based on Ga^+ with a LO system can produce lamella as thin as 50-100 nm, which can even be made thinner (resulting in higher-quality TEM images) by replacing Ga^+ ions with ions like He/Ar/N/O, known today as a plasma FIB (PFIB), and, in the future, with the addition of a laser beam.

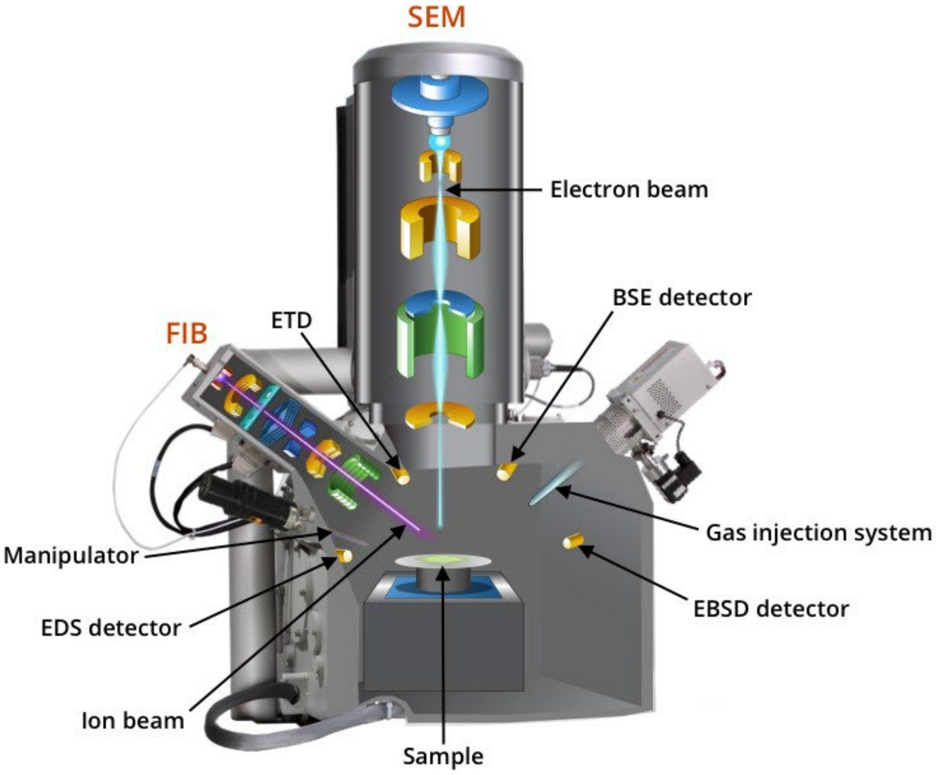

Figure 11-23: A modern dual beam system consists of a secondary electron microscope (SEM) and focused ion beam (FIB). To ensure that features of interest of a sample will not move out of field of view during tilting (required for lamella preparation), the sample must be placed at eucentric height which is the location where the electron beam of SEM intersects with the ion beam of FIB. Images are either created by collecting secondary electrons (SE) with an Everhart-Thornley detector (ETD) or by collecting backscattered electrons (BSE) with a BSE detector. An energy dispersive X-ray (EDS) detector allows to investigate the elemental composition of a sample and the electron backscatter diffraction (EBSD) detector can reveal information about the sample crystallinity. Signals (SE, BSE, characteristic X-rays) can either be generated by incident electrons or ions while EBSD can only be generated by incident electrons. The manipulator is used for the in situ lift-out technique and can be used in combination with a gas injection system (GIS) (to precisely deposit materials like C or Pt) and FIB milling to remove µm-sized lamellae from samples. Reprinted under a CC BY-SA 4.0 DEED from [82] © 2024 Microscopy Australia.

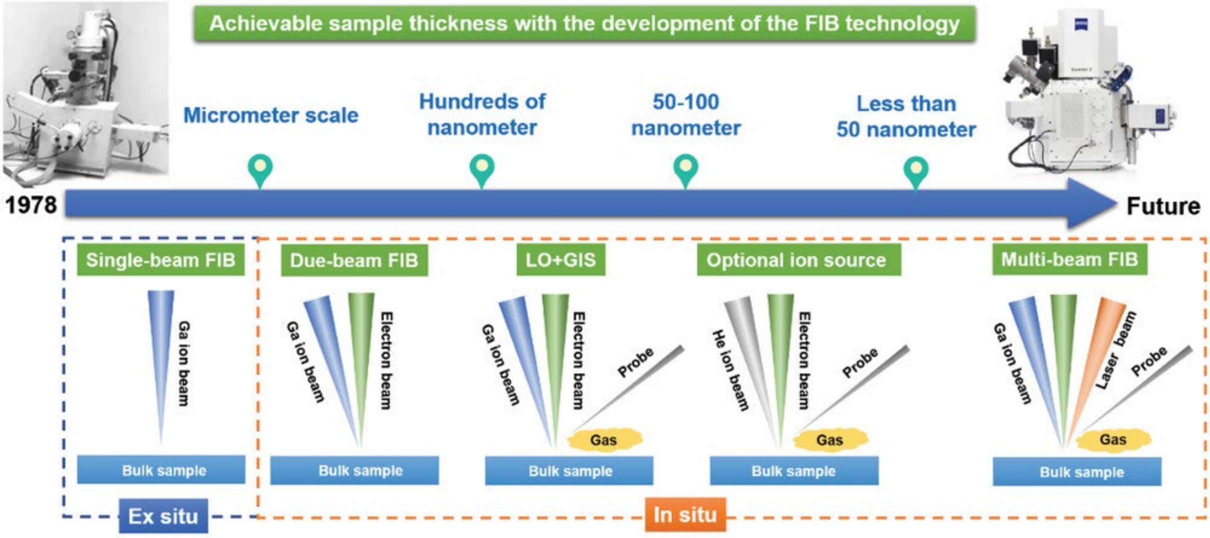

Figure 11-24: Electron-transparent lamella preparation using a focused ion beam (FIB) started in 1978. At that time, FIB was used to start the preparation; however, it could not finalize lamella preparation (to be usable for transmission electron microscopy (TEM)), which needed to be carried outside (ex situ) the FIB equipment. Nowadays, with the addition of a lift-out system (shown here by a probe) and a gas injection system (here denoted as “Gas”), all TEM lamella preparation steps can be performed inside (in situ). This development, with the addition of novel ion sources based on plasma (i.e., He), leads to TEM lamellae with a thickness less than 50 nm, which improves TEM imaging. Reprinted with permission from [83], © 2022 John Wiley and Sons.

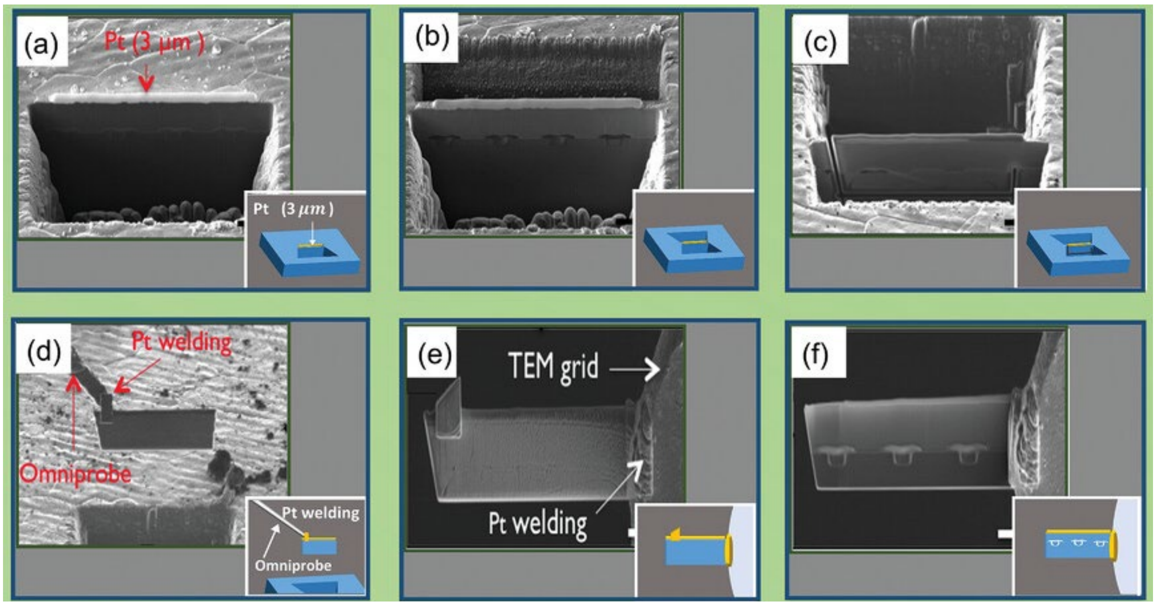

Figure 11-25: a) To protect the sample from ion beam radiation, a protective layer is deposited on the material at a desired location for the TEM lamella. The first 100 nm are usually deposited by using the electron beam. Then, deposition is continued by using the ion beam to accelerate this preparation step. (b, c) Trench cuts are placed at both sides of the TEM lamella. (d) The TEM lamella is then welded to a manipulator (Omniprobe) and lifted out of the trench by performing an undercut. A sufficiently sized lamella can only be guaranteed if the undercut can be performed at a suitable depth, which is influenced by properly sizing the trench cut width. The TEM lamella is then transferred to a TEM grid to mill and polish the TEM lamella to a desired thickness (typically less than 50 nm). Reprinted with permission from [83, 84], © 2015; 2022 John Wiley and Sons and Elsevier.

The LO system allows to in situ (inside the FIB-SEM system) lift-out a μm-sized lamella from a sample, which, compared to ex situ lift-out, increases precision and cleanliness and is the preferred preparation method since first introduced in 1993 by Overwijk et al. [85] due to the relative ease of use (as no initial specimen preparation is required and preparation can start from a bulk sample if compatible with FIB) [86]. The essential preparation steps are summarized in Figure 11-25.

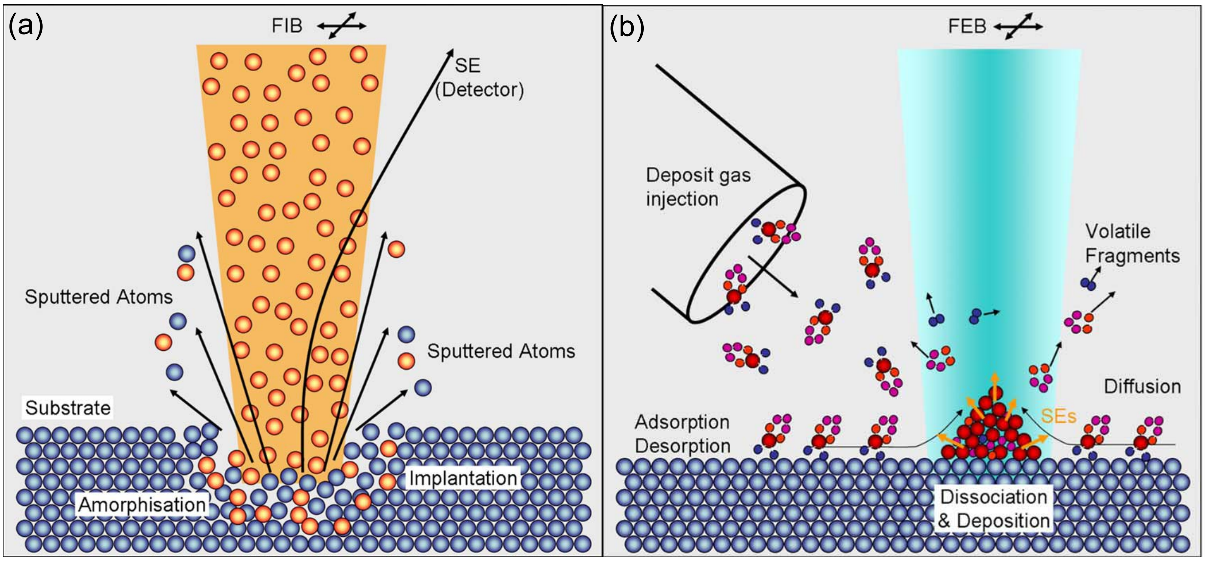

Figure 11-26: (a) Simplified illustration of atomic processes during focused ion beam (FIB) milling to remove material from the substrate. Please note that an incident angle of the ion beam of 90° results in less efficient milling, as the highest sputtering yield (the most amount of removed material) is between 70 and 80° [87]. In addition, such an incident angle typically results in more ions being implanted into the material, altering or damaging the substrate. (b) A desired material (atoms are represented by red circles) is supplied to the sample surface in the form of a precursor gas (purple and blue circles) through a gas injection system (GIS, here deposit gas injection). A focused electron beam (FEB) or FIB breaks up the precursor gas, resulting in the removal of the volatile precursor gas material and material deposition on the sample surface. Reprinted with permission from [88], © 2008 American Vacuum Society.

FIB milling can result in amorphization and, for example, Ga^+ implantation, as schematically shown in Figure 11-26 (a), which is why a ~1-3 μm thick protection layer is deposited at the area of interest to preserve the sample and the lamella (Figure 11-25 (a)). Typically, a gas injection system (GIS) is used to deposit material at specific sites. The essential processes are shown in Figure 11-26 (b). Similar to FIB milling, the ion or electron beam is scanned across the region of interest in a pixel-by-pixel movement. Dwell time (time per pixel) and pixel overlap (given by pixel spacing) must be adjusted so that the deposited material is not instantly removed (milled). The GIS is also used to weld the lamella to the manipulator (Omniprobe) [89] for lift-out and to the TEM grid (Figure 11-25 (d, e)). Typically, as schematically shown in Figure 11-27, TEM lamellae are attached to an Omniprobe lift-out grid. Moreover, as shown in Figure 11-28, TEM lamellae can be attached to a micro-electromechanical systems (MEMS)-based chip that allows to test a sample under stimuli like temperature or electric field.

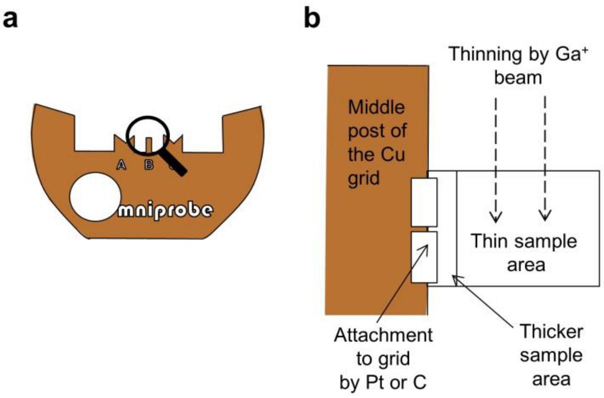

Figure 11-27: (a) Example of an Omniprobe lift-out grid made of copper. The grid has a diameter of 3 mm and is designed to fit standard transmission electron microscopy (TEM) holders. For this example, three posts labeled A, B, and C (not visible) with different shapes ("V"-shape and vertical bar) are available to securely attach TEM lamellae. (b) A TEM lamella is attached to the side of post B via Pt or C welding. This attachment allows thinning without recontamination from the copper grid. Reprinted under a CC BY 4.0 DEED from [90], © 2023 Juliane Weber.

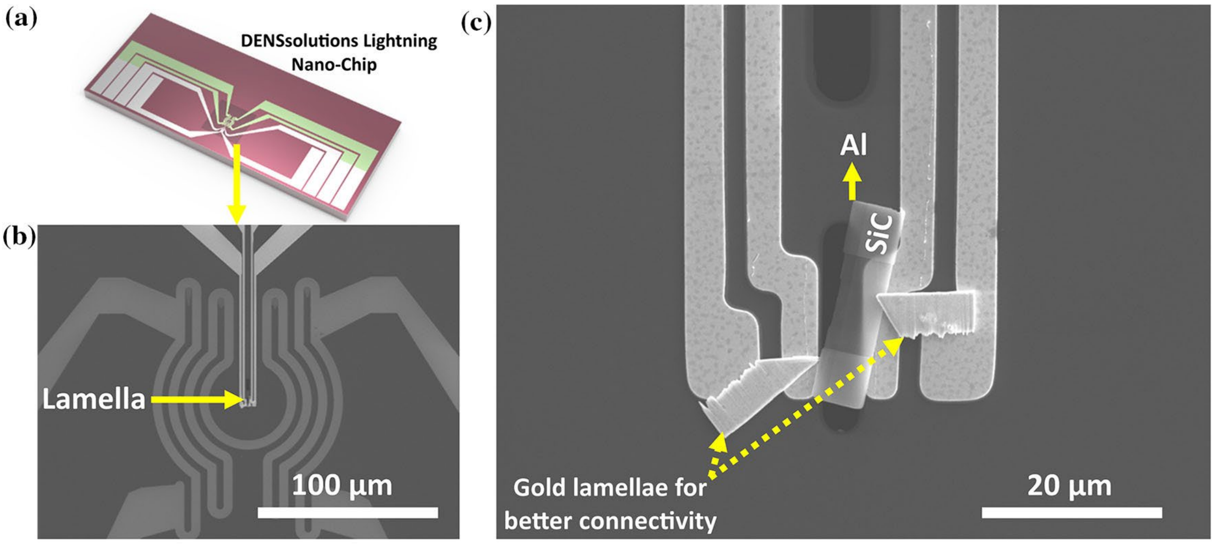

Figure 11-28: (a) A micro-electromechanical systems (MEMS)-based chip from DENSsolutions designed to fit sample holders for transmission electron microscopes (TEMs) from the manufacturer JEOL. Four contacts are available for electrical contact with attainable E-fields up to 300 kV/cm, and four contacts (colored green) are used for heating (up to 1300 °C for only heating and up to 900 °C when combined with biasing). The center of the chip is a thin membrane (colored differently). (b) Here, the lamella is placed at the center of the heater coils at the electrodes for biasing. (c) In this example, a SiC lamella is placed on top of the electrodes and additionally contacted with gold lamellae. Reprinted under a CC BY 4.0 DEED from [91], © 2023 Springer Nature.

11.6.1. Weld-free lamellae attachment for in situ biasing of two-terminal devices

Testing a two-terminal device, i.e., a memristive device, during an in situ biasing experiment necessitates that the applied current flows across the metal-insulator-metal (MIM) structure, ideally at the electron-transparent region of the MEMS-based chip. Previously, these TEM lamellae were attached to the MEMS-based chip via electron or ion beam-induced deposition, to ensure that the lamellae would remain on the chip when performing side cuts to guide the current flow and subsequent thinning to electron transparency. This deposition, however, as schematically shown in Figure 11-26 (b), contaminates the entire MEMS-based chip, leading to unintended stray leakage current pathways. Hence, current flow through the actual MIM is unlikely, which will prevent a proper current-voltage response from the device. A novel approach involves TEM lamellae attachment without deposition. This weld-free method requires a modification of the standard in-situ lift-out process, as shown in Figure 11-29 A-F: the side cuts (Figure 11-29 C) to guide the current across the MIM are placed before lift-out. The region of interest (ROI) is thinned to electron transparency at the manipulator and subsequently placed on the MEMS-based chip (Figure 11-29 G-I) via pushing, thereby affixing the lamella to the chip via van der Waals forces. Further, implementing electron beam induced current (EBIC) measurements into the preparation routine can help to validate that lamellae are properly electronically connected [92].

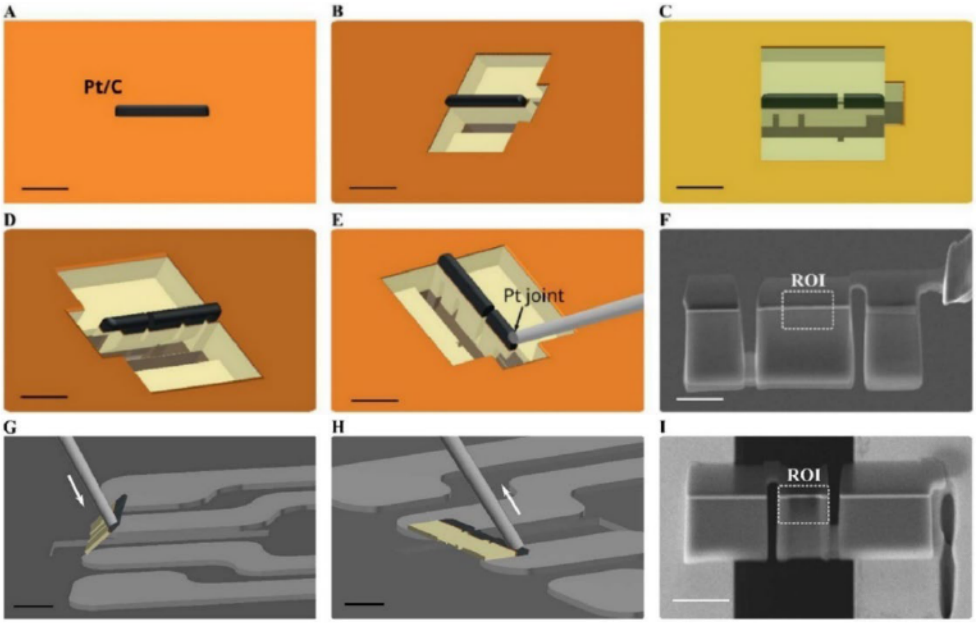

Figure 11-29: (A-E) A modified in situ lift-out focused ion beam preparation (see also Figure 11-25) to guide the current across a metal-insulator-metal structure of a two terminal device by placing side cuts (E). (F) Milling and polishing to a desired thickness is performed with the lamella attached to a manipulator. (G) The lamella is placed at the electrodes of the micro-electromechanical systems (MEMS)-based chip from DENSsolutions and pushed down. (H) The manipulator is detached, (I) leaving the region of interest (ROI) above the electron transparent window (shown in black). Reprinted under a CC BY 4.0 DEED from [93], © 2024 The Authors, published by Elsevier.

11.7. Transmission electron microscopy

High-energy electron beams (electrons accelerated to 80-300 kV) can be transmitted through electron-transparent lamellae (samples) with a thickness up to 1000 nm. As schematically shown in Figure 11-30, the electron-matter interaction can result in direct or unaltered transmission of electrons (direct beam), elastically or inelastically scattered electrons (if treated as particles), or in diffraction (if treated as waves).

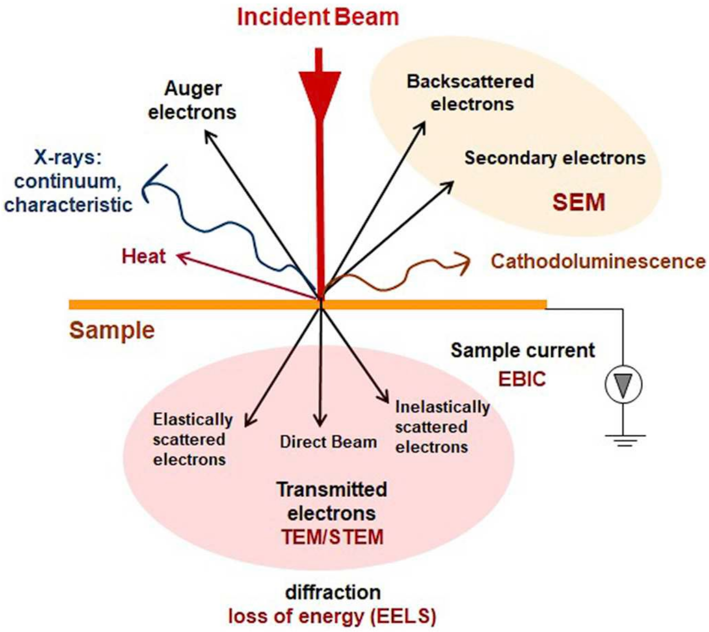

Figure 11-30: Electron-matter interaction for samples thinner than 1000 nm generates reflected (as shown in Figure 9-29) and transmitted signals, in addition to electron beam-induced current (EBIC). The amount of reflected signals (X-rays, secondary electrons, and backscattered electrons) is low due to the relatively thin sample thickness compared to the excitation volume. Most of the incident electrons are directly transmitted (direct beam). Elastically scattered electrons are used for imaging (transmission electron microscopy (TEM) and scanning transmission electron microscopy (STEM)) and inelastically scattered electrons for electron energy-loss spectroscopy (EELS). Reprinted with permission from [94], © 2019 Elsevier.

Electron diffraction can be explained by the same concept as for X-rays with Braggs law. However, the principle of obtaining diffraction information is different for XRD. In TEM, the incident angle of electrons is fixed to a few mrad ($10\ mrad \approx 0.5°$) and only limited lamella tilting (up to $\pm 30°$) can change the crystal orientation to fulfill the Bragg condition. In principle, this would limit the detection of crystallographic information. This, however, is circumvented by the comparatively high energy of electrons and the size of the lamellae. An intuitive explanation for why high-energy electrons can still result in constructive interference from several crystallographic planes with different lattice planes can be given by the introduction of the reciprocal space. In a crystalline material, atoms are periodically arranged in a three dimensional real space lattice distanced by the lattice spacing d. The lattice plane orientation is specified by the Miller indices *hkl*, which, as shown in Figure 11-31 (a), can be obtained by taking the reciprocals of the three intercepts on the axes (x, y, and z) in terms of the lattice constants a, b, c. The reciprocal lattice vector *G(*hkl) is normal to the planes {hkl}. Examples of lattice planes characterized by their (hkl) values are shown in Figure 11-31 (b).

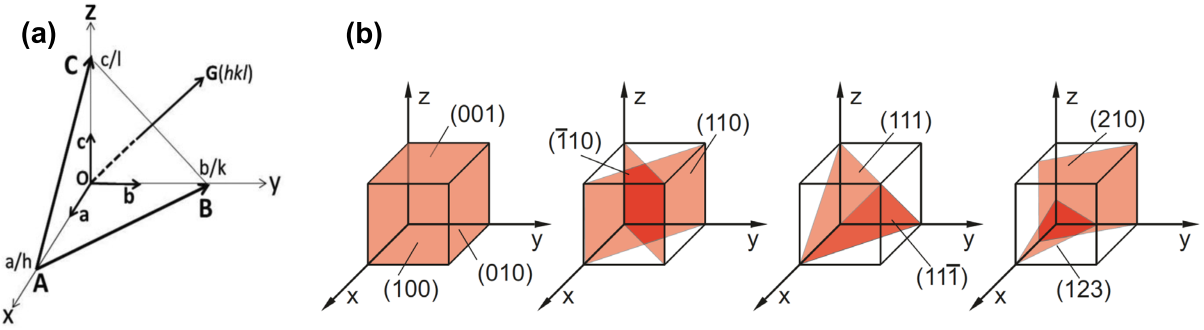

Figure 11-31: (a) Miller indices (hkl) are calculated by taking the reciprocals of the intercepts of the x-, y-, and z-axes in terms of the lattice constants a, b, and c. Reprinted with permission from [95], © 2014 Springer New York (b) Examples of cubic lattice planes. A (001) plane intercepts the x-, y-, and z-axes at ∞, ∞, and 1, respectively, hence $h = 1/\infty = 0$, $k = 1/\infty = 0$ and $l = 1/1 = 1$. Reprinted with permission from [96] © 2015 Springer Berlin Heidelberg.

Each of these lattice planes can be represented in a reciprocal lattice, which is basically just points with position coordinates h, k and l on a regular grid that represent diffraction possibilities. To visualize which points lead to diffraction (by satisfying the Bragg condition), an Ewald sphere with the diameter $1/\lambda$ is drawn on top of the reciprocal lattice. As can be seen in Figure 11-32, the about 61 times larger Ewald sphere for electrons intersects with several points, leading to several diffraction spots.

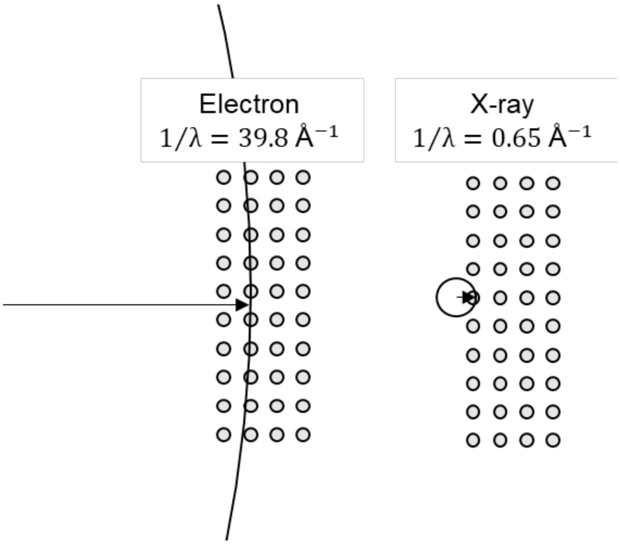

Figure 11-32: The Bragg condition is satisfied if the Ewald sphere intersects with reciprocal lattice points. Drawn after [97].

Moreover, because lamellae thickness is about three to four orders of magnitude smaller compared to its length and width, the reciprocal lattice points of lattice planes perpendicular to the thin direction are elongated, resulting in "relrods" (reciprocal lattice rods), as shown in Figure 11-33. Intersection of the Ewald sphere with a relrod can also lead to a diffraction spot, even though the Bragg condition is not satisfied.

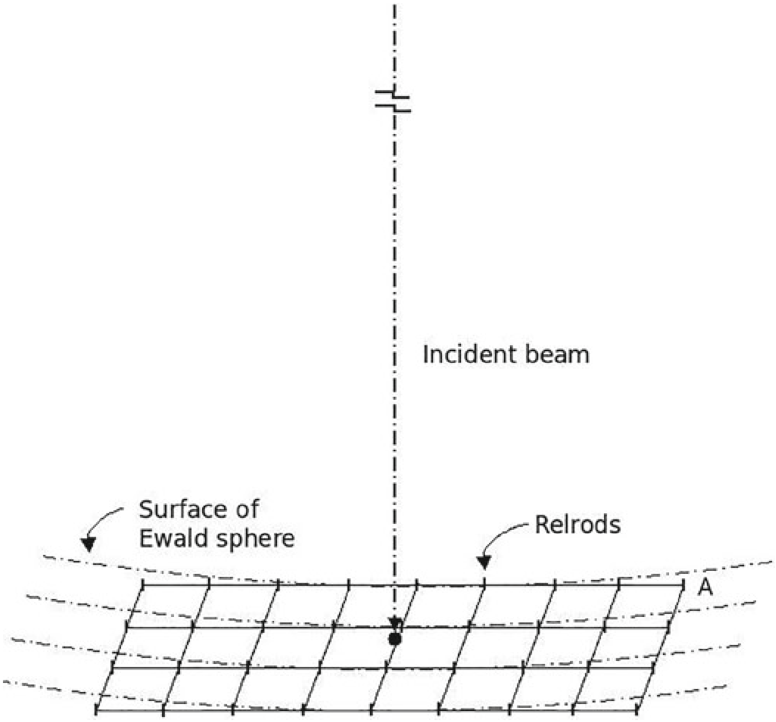

Figure 11-33: For thin electron-transparent lamellae, reciprocal lattice points are elongated normal to the thickness of the lamella (in this case, parallel to the incident beam) and are transformed into relrods thus relaxing the Bragg condition. Reprinted with permission from [98], © 2022 Springer Nature Singapore.

A typical selective-area electron diffraction (SAED) pattern of a polycrystalline material is shown in Figure 11-34 (b). Due to the random orientation of crystals, electrons are diffracted at respective lattice planes (labeled 1-5) in all possible directions, resulting in the formation of rings. The ring radius is proportional to the reciprocal lattice spacing d and can therefore be correlated with an XRD pattern where 2θ is also proportional to the reciprocal lattice spacing. In the case of a single crystal or a set of oriented grains, only specific diffraction spots in the diffraction image are possible and must be oriented with respect to the incident beam to achieve a highly symmetric diffraction pattern around the direct beam labeled (000), as shown in Figure 11-35 (b). The electron beam is aligned with a crystallographic direction named zone axis [HKL] determined from the zone axis criterion $hH + kK + lL = 0$. If not aligned, a random diffraction pattern with no specific relation among diffraction spots would be visible (Figure 11-36).

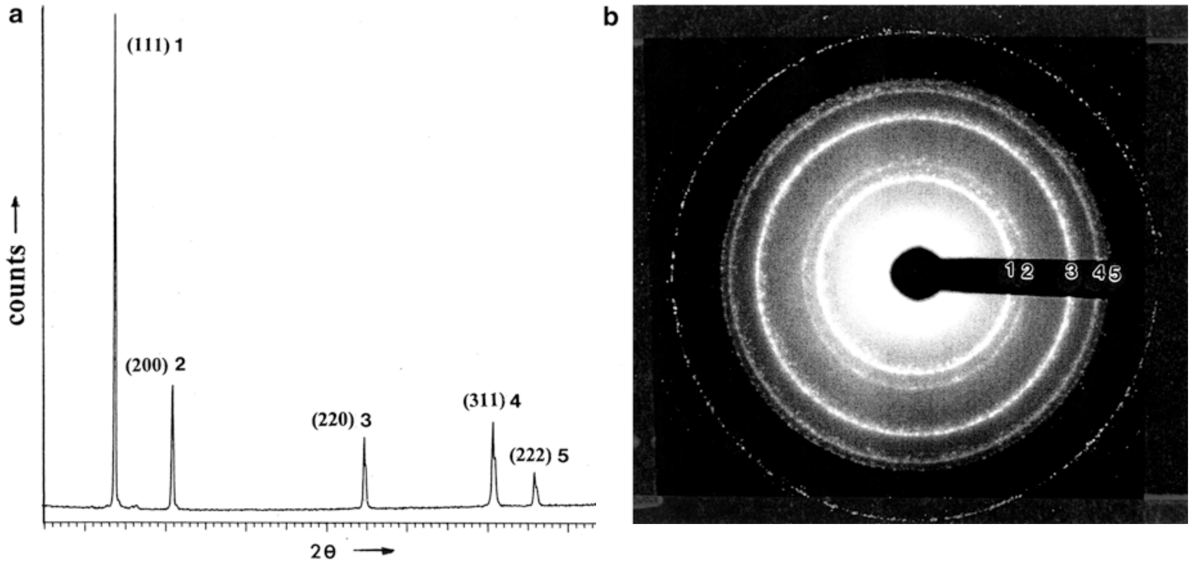

Figure 11-34: (a) X-ray diffraction pattern of a polycrystalline material with indexed diffraction peaks (hkl) labeled 1-5. (b) The corresponding selective-area diffraction pattern (SAED) shows rings with radii related to the spacing of the lattice planes (hkl). Reprinted with permission from [99] © 2014 Springer, Cham.

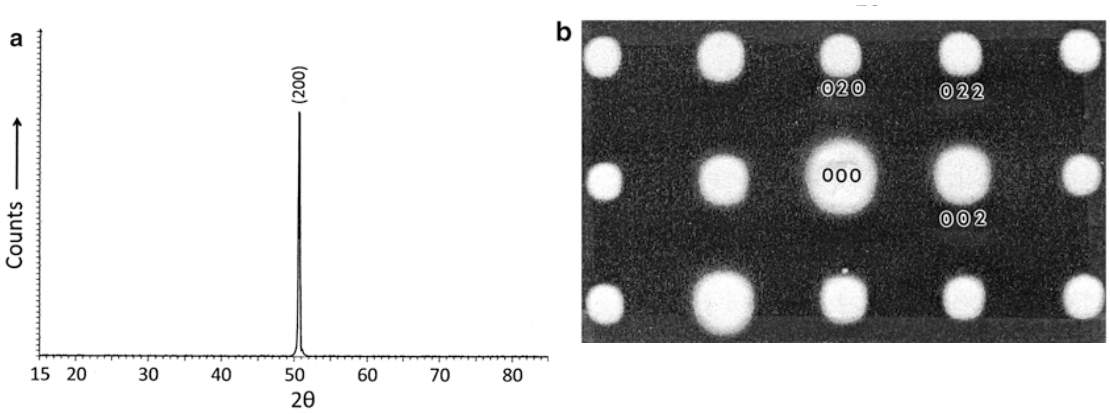

Figure 11-35: (a) The X-ray diffraction pattern of a single crystal shows only a single peak. (b) Such an oriented sample can produce a symmetric selective-area diffraction pattern (SAED) if the incident beam is aligned (parallel) to a material crystallographic axis. Reprinted with permission from [99] © 2014 Springer, Cham.

Figure 11-36: A randomly aligned crystal results in a asymmetric diffraction pattern with no relation among diffraction spots. Reprinted with permission from [98], © 2022 Springer Nature Singapore.

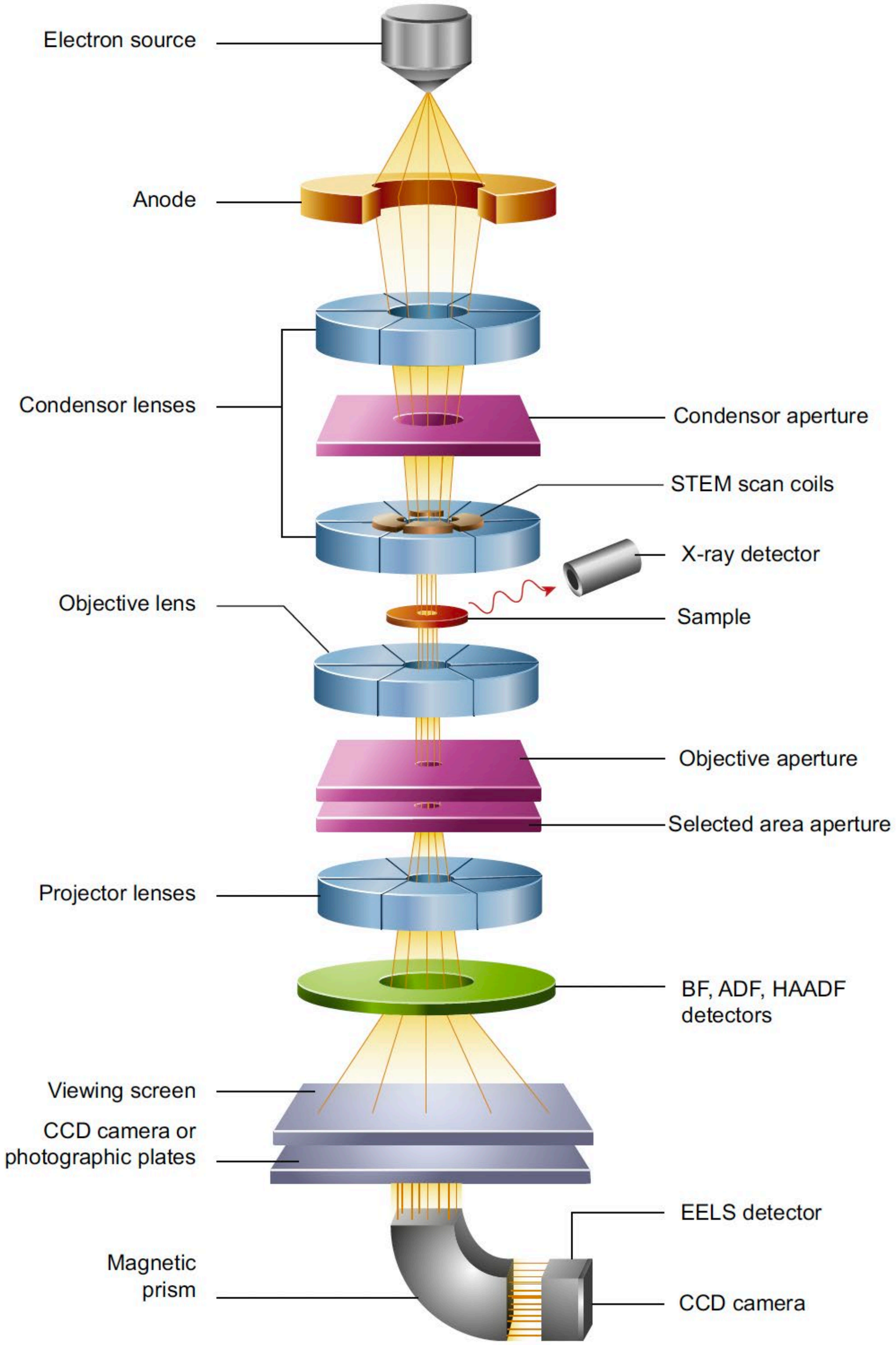

Figure 11-37: The electron source nowadays is typically a cold field emission gun (FEG) that generates electrons that are usually accelerated to 60-300 kV and are condensed on an electron transparent lamella (sample) either as a parallel beam (transmission electron microscopy, TEM) or probe (scanning transmission electron microscopy, STEM). The probe position can be controlled via STEM scan coils. The transmitted beam is treated by an imaging system (objective lens, objective aperture, selected area aperture, projector lenses) and can be collected either via bright field (BF), annular dark field (ADF), high-angle annular dark-field (HAADF) detectors, a CCD camera used for imaging, or for electron energy-loss spectroscopy (EELS). Reprinted with permission from [100], © 2016 Elsevier.

To perform TEM experiments (generating high-energy electrons and collecting generated signals due to electron-matter interaction), a schematic overview of the core components of a modern TEM microscope is shown in Figure 11-37. The TEM can be operated to generate either a diffraction pattern or an image, as schematically shown in Figure 11-38. In principle, a diffraction pattern and image are always produced by the objective lens at the focal and back focal planes (F), respectively, but only with a magnification of 20-50 times. Intermediate and projector lenses (as part of the imaging system) further magnify the image on the final image screen. With the addition of a diffraction lens between the objective and intermediate lenses, it becomes possible to image only the diffraction pattern.

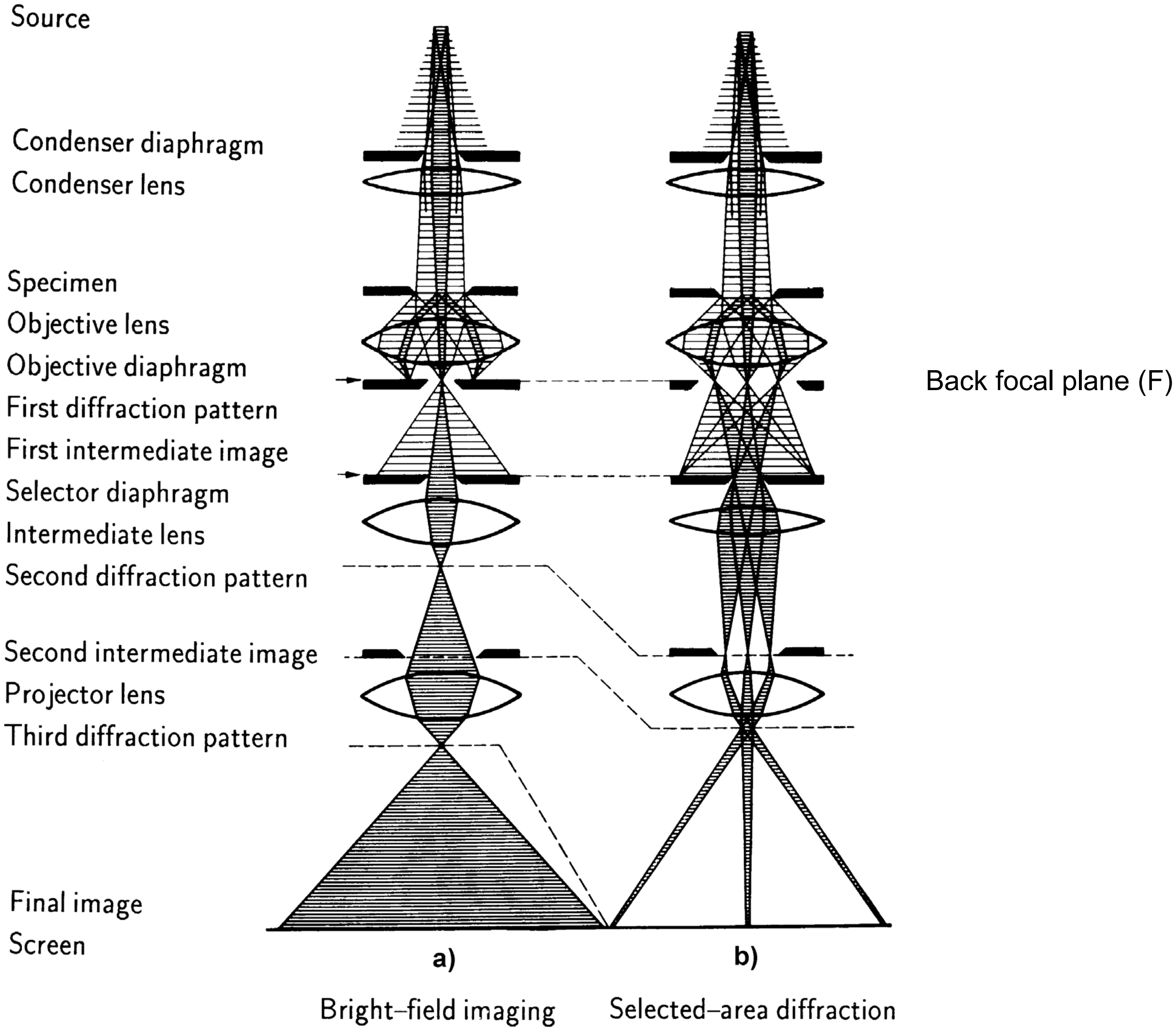

Figure 11-38: The transmission electron microscope can either be operated in (a) imaging or (b) diffraction mode. As shown by the ray diagrams, the transmitted beam is focused by the objective lens at the back focal plane (F). With the addition of a diffraction lens, the diffraction pattern can be magnified on the final image screen (selected-area diffraction); otherwise, as exemplary shown, by blocking diffracted waves with an objective diaphragm, a bright-field image is magnified. Reprinted with permission from [101], © 2008 Springer.

11.7.1. Diffraction contrast

Typically, an objective diaphragm is introduced at F either centered, resulting in bright-field (BF) mode, or to intercept the primary beam, resulting in dark-field (DF) mode, as shown in Figure 11-39. BF and DF modes are based on separating the primary beam (direct beam) from diffracted beams, yielding a diffraction contrast that produces the images. Figure 11-40 a) shows a BF TEM image of a thin film stack with only the direct beam used for contrast generation. The differences in brightness can map out crystallographic variations such as grain boundaries, dislocations, and other defects. For example, a grain boundary can be identified as a black vertical line in the TiN layer roughly in the center of the image. In this example, the TiN layer is grown with a biaxial texture (see also Figure 11-11) with two defined in-plane domains. Adjacent grains will generate different SAED patterns due to their 60° in plane rotation (see also Figure 11-16). The distinct in-plane orientation of grains can be visualized by DF TEM imaging as shown in Figure 11-40 b). The left grain in the TiN layer appears brightest because a diffracted beam, specific to the crystallographic orientation of this grain, has been utilized for contrast generation.

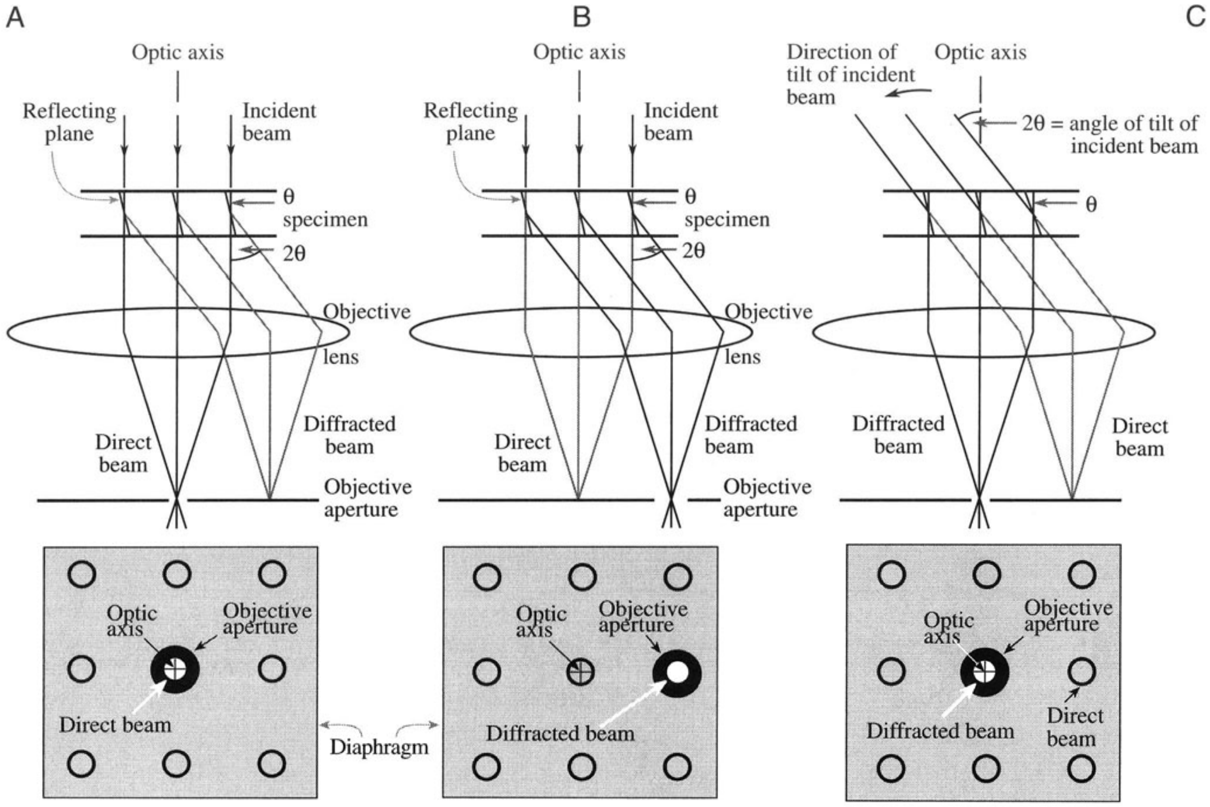

Figure 11-39: (a) In the bright-field (BF) imaging mode, only undiffracted transmitted waves are used for contrast generation. In dark-field (DF) mode, a diffraction spot is selected for contrast generation, which can be achieved either by (b) shifting the objective aperture or by (c) tilting the beam with a centered objective aperture (centered dark-field, CDF. Reprinted with permission from [102] © 1996 Springer Nature.

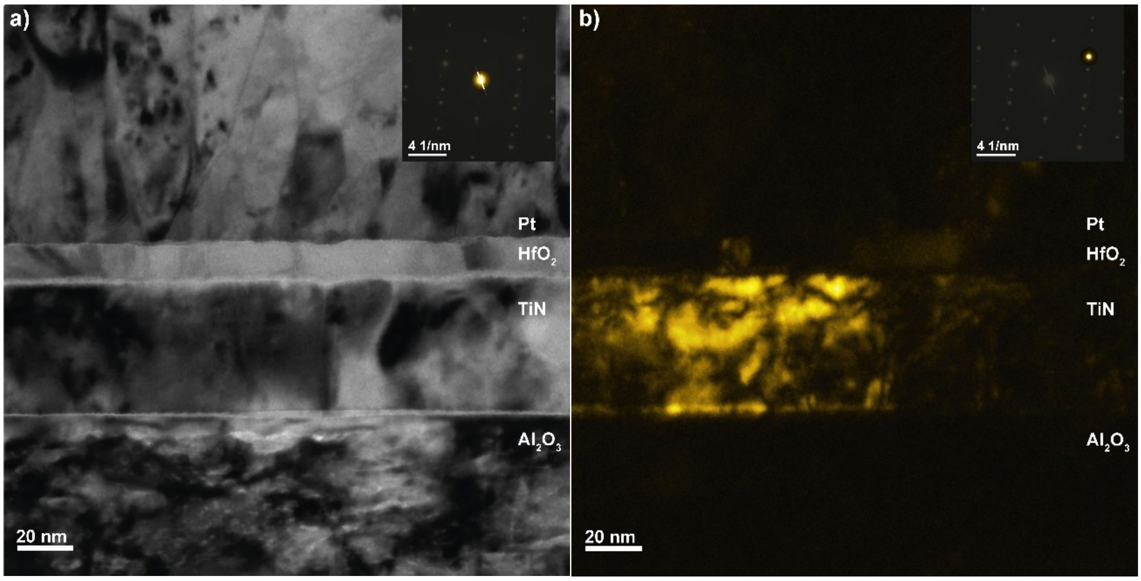

Figure 11-40: a) Bright-field (BF) transmission electron microscopy (TEM) image of a HfO_2 based memristive device. b) To visualize the different in-plane orientations of the TiN grains, the dark-field (DF) TEM image is generated by a diffracted beam of a specific (002) crystallographic orientation of the left grain. The insets show an exemplary selected area electron diffraction (SAED) pattern from both TiN grains at the grain boundary. For BF imaging, only the primary beam is selected for contrast generation, and for DF imaging, a diffracted beam. [103]

11.7.2. Phase contrast

The diameter of the objective diaphragm, which determines the objective aperture (angle), can also be selected in such a way that both the primary and either one or many diffracted beams are used for imaging. In principle, the interference due to a phase difference from scattering in the sample should generate a phase contrast in the image. However, the phase difference is relatively low, so that, as schematically shown in Figure 11-41 (a), waves of beams recombine in a focused image, leading to no discernible contrast (Figure 11-41 (b)). Introducing a phase shift, as schematically shown in Figure 11-41 (c), either due to spherical aberration (C_s) of the objective lens or defocus, will blur the image but also create a frequency-dependent interference that results in a defocus-dependent contrast (Figure 11-41 (d, e)). The resulting contrast is described in Fourier space by the (phase) contrast transfer function (CTF), as shown in Figure 11-41 (f). This Fourier transform (FT) is the calculated diffraction pattern of the TEM image. The FT differs from an actual diffraction pattern, as the TEM image is based on “double” interference. That is interference between diffracted and undiffracted waves and the diffracted waves, which are already a result of interference. The CTF is influenced by C_s, Scherzer defocus Δf and electron wavelength λ. Different frequencies can result in a reversal of contrast and also a loss of contrast (loss of information). Signal intensity decreases with frequency due to the effects of temporal and spatial coherence. However, sufficient contrast at higher frequencies is indispensable for high-resolution (HR)

TEM and as shown in Figure 11-41 (g), this can be cut off by a too small objective aperture (or insufficient temporal and spatial coherence), thus preventing HRTEM.

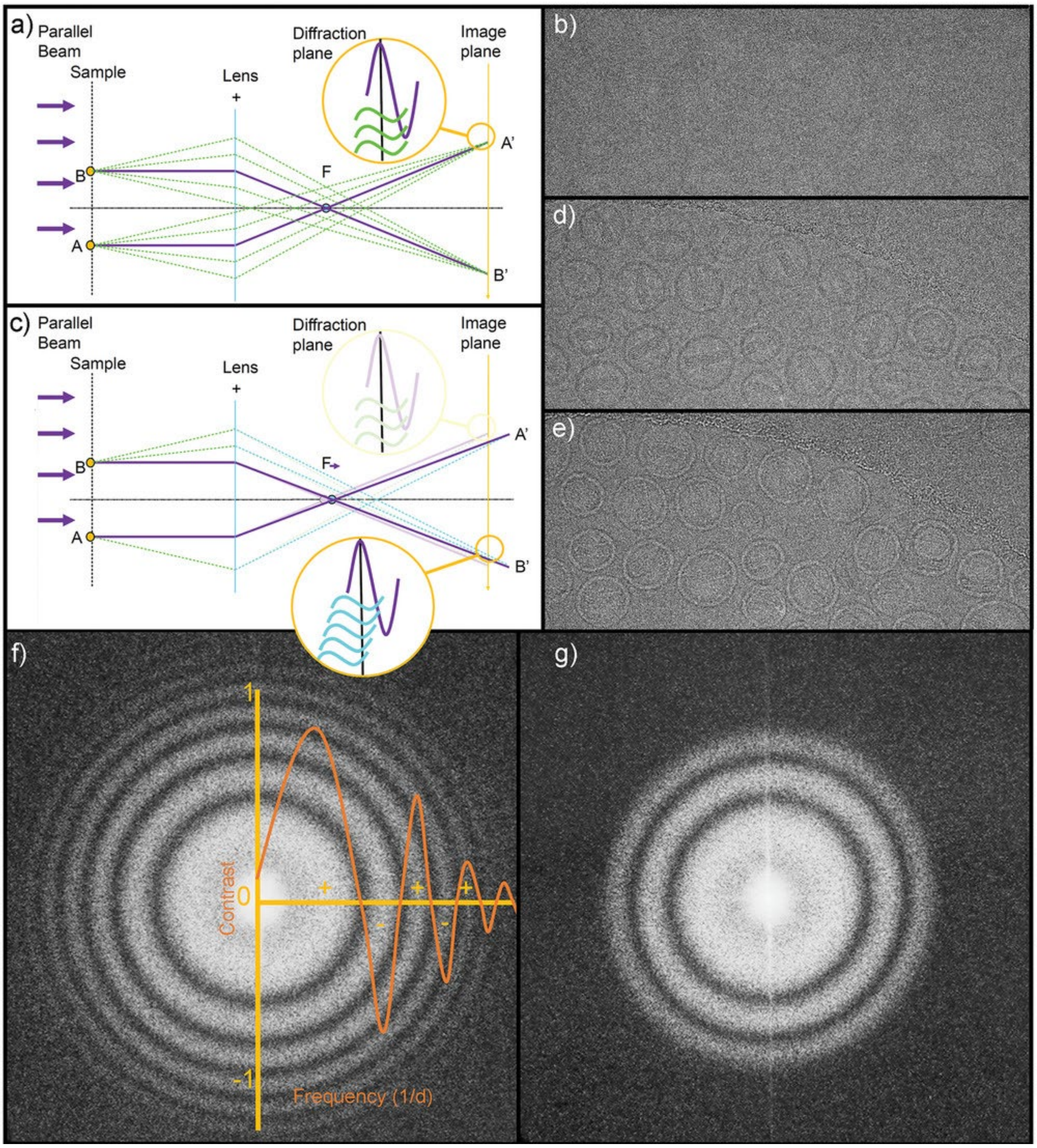

Figure 11-41: Phase-contrast imaging relies on the interference of scattered and unscattered waves. (a) In case of a focused image, the phase difference between the waves is insufficient for interference thus waves recombine. (b) This produces an image with no phase contrast and only some scattering contrast. (c) To achieve interference, a phase shift is introduced by defocusing and spherical abberation (C_S) of the objective lens, which results in a blurred image with a defocus-dependent contrast as shown by the (d) underfocused and (e) overfocused image. Underfocused images are easier to interpret as the scatter and phase contrast have the same amplitude at low frequencies. (f) The Fourier Transform highlights how contrast depends on frequency, which showcases the effect of the contrast transfer function (CTF) shown in orange. (g) A smaller objective aperture cuts off contrast at high frequencies, which prevents high-resolution imaging. Reprinted under a CC BY 4.0 DEED from [104], © 2020 Wiley.

In contrast to conventional TEM which relies on a highly parallel incident beam, it is also possible to focus the beam to ideally form an atomic-scale probe on the sample. As schematically shown in Figure 11-42, a convergent beam leads to broadening of the diffraction spots into diffraction disks because a focused beam consists of electron waves with different incident vectors that are scattered differently.

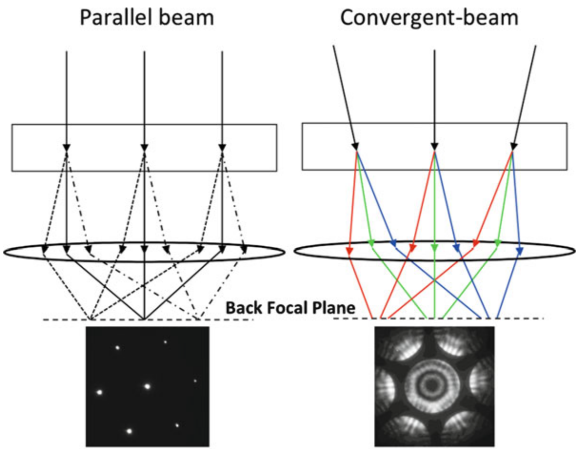

Figure 11-42: Diffraction from a nearly parallel beam results in distinct diffraction spots. A convergent beam contains a range of incident wave vectors; thus, diffraction spots are broadened to disks. Reprinted with permission from [105] © 2014 Springer Nature.

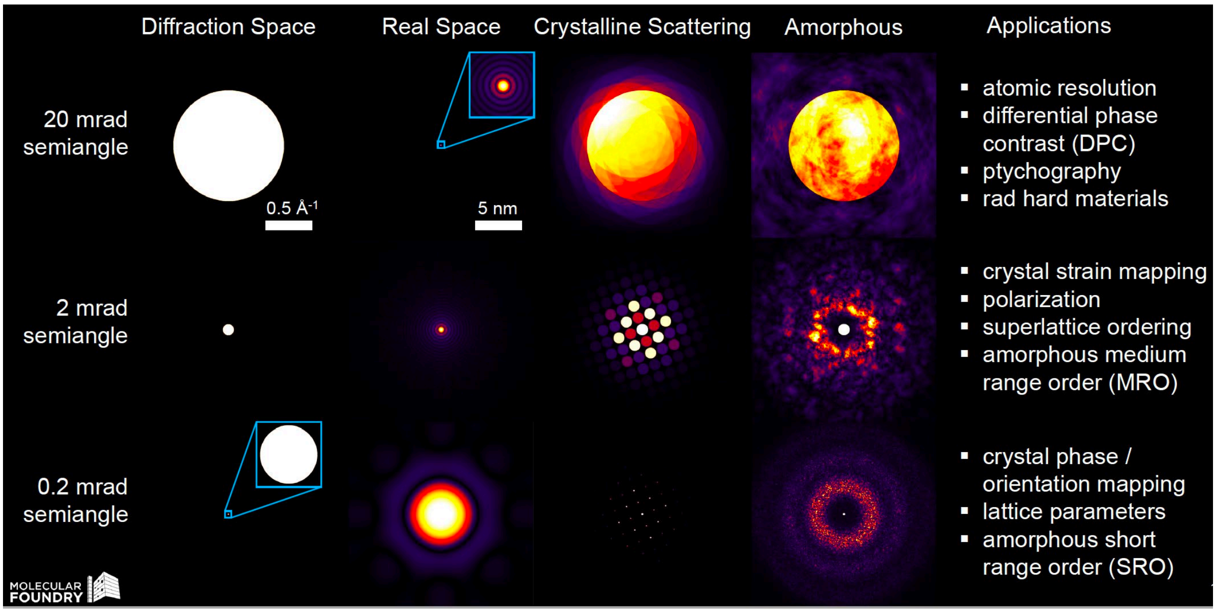

Figure 11-43: A small convergence semi angle (0.2 mrad) results in a several nanometer-sized probe, which is considered “quasi-parallel” as the resulting crystalline scattering consists of spots, which facilitates the investigation of crystallinity. An intermediate semiangle can result in crystalline scattering with non-overlapped diffraction discs and a nanometer sized probe. This Kossel-Möllenstedt pattern allows for the investigation of diffraction generated from minuscule regions, which is unique in comparison to other diffraction techniques. For larger semiangle, diffraction disks overlap creating a Kossel pattern. The probe size is in the range of atoms which allows to investigate with atomic resolution. Reprinted with permission from the author [106] © Colin Ophus.

The size of diffraction disks scales with the convergence angle, as shown in Figure 11-43. This can result in distinct spots for small convergence angles or an overlapped diffraction disk. The convergence angle also affects the probe size, while a large angle can yield probe sizes in the tens of picometer range, allowing to image atoms, and a small angle can yield a nanometer-sized probe useful to investigate crystal phases.

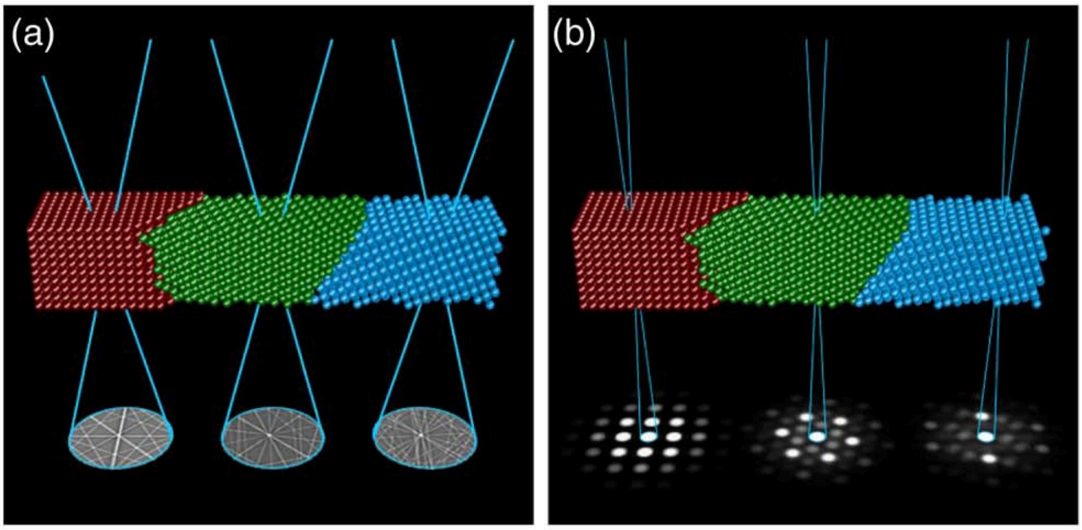

Figure 11-44: A probe scanned across an electron-transparent lamella can, i.e., generate (a) Kikuchi patterns or (b) Bragg disk diffraction, depending on the convergence semiangle. Reprinted under a CC BY from [107], © 2019 Oxford University Press.

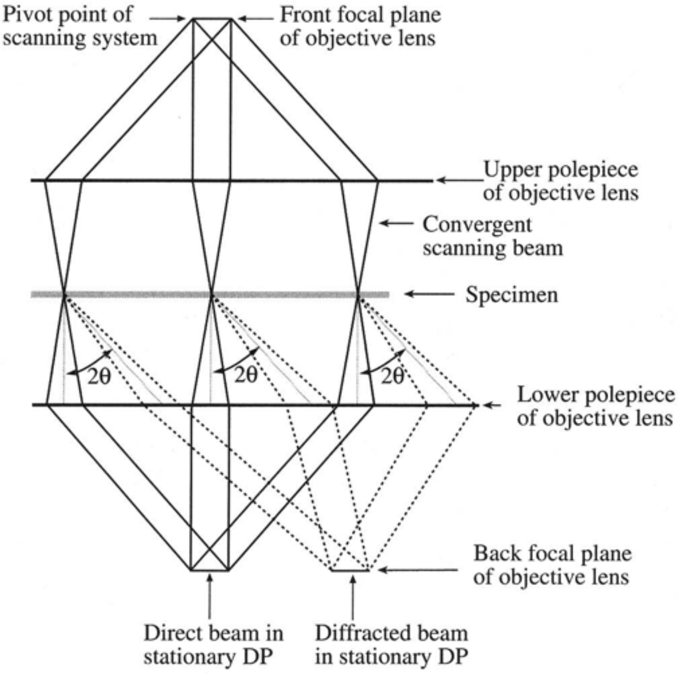

Figure 11-45: The direct and diffracted beam must stay stationary when the beam is scanned across the sample to generate a scanning transmission electron microscopy (STEM) image plane. Reprinted with permission from [102] © 1996 Springer Nature.

Unlike TEM, the probe must be scanned across the sample to generate an image. As schematically shown in Figure 11-44 different parts of the material result in different scattering. It should be noted that when the beam is scanned across the sample, the transmitted beam must stay stationary at the back focal plane, as schematically shown in Figure 11-45; otherwise, forming an image is not possible. Analogous to TEM, scanning transmission electron microscopy (STEM) can be performed in BF mode or DF mode.

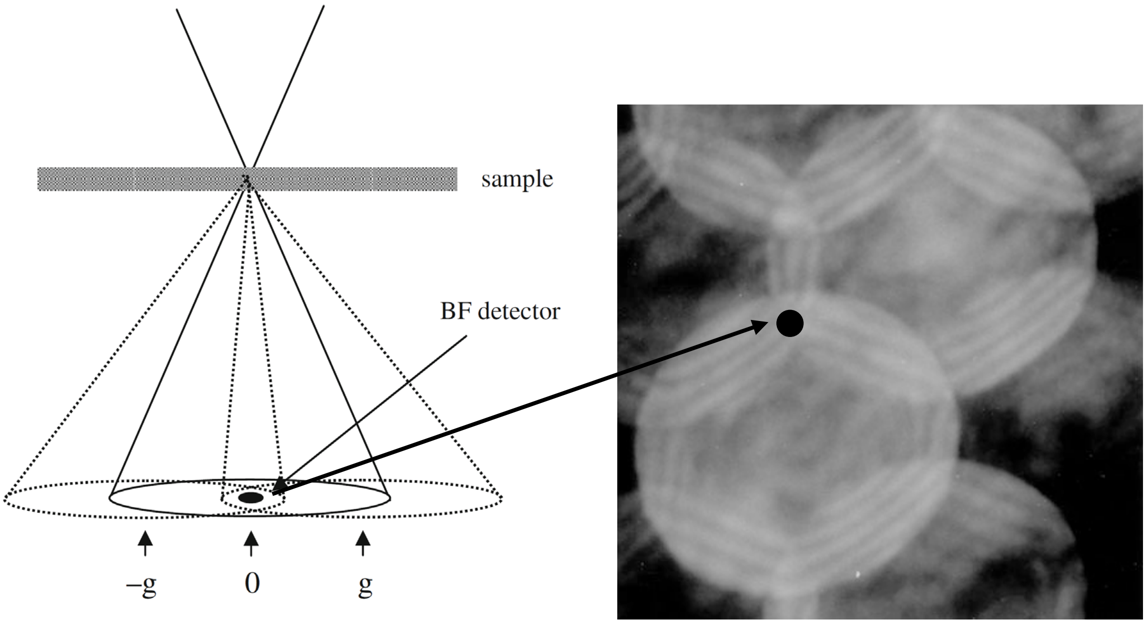

Figure 11-46: (a) Sufficiently large convergence angles and lattice spacings (smaller reciprocal lattice vector g) result in a triple overlap of the direct and diffracted beams. (b) The overlaps result in interference and can be used to generate a bright field (BF) scanning transmission electron microscopy (STEM) image by placing a BF detector at the triple overlap region. Reprinted with permission from [108], © 2011 Springer Nature.

The origin of contrast for BF STEM relies, similar to the origin of phase contrast, on interference between the direct beam and two opposite diffracted beams, and also on absorption. These interference features lead to contrast in BF STEM, which is why a BF detector is placed at this triple overlap region, as shown in Figure 11-46. Smaller lattice spacings (resulting in larger reciprocal lattice vectors g) could result in the absence of contrast due to missing diffraction disk overlap. This could be compensated by selecting a larger semiangle or could be resolved by using non-axial detector geometries. Nowadays, BF and DF STEM images can be obtained simultaneously, as the DF detector is typically a non-axial annular detector and the BF detector is an axial circular detector, as schematically shown in Figure 11-47 (c). The scattering semiangles (β) at which electrons are collected are defined by the detection range of the detectors. This can be adjusted by altering the camera length, which is the effective (not physical) distance between the specimen and the detector plane.

The different imaging modes are summarized in Figure 11-47 (a, b). High-angle annular dark field (HAADF) imaging collects scattered electrons at semiangles greater than 50 mrad according to [102]. However, nowadays, typically semiangles greater than 90 mrad are used for HAADF imaging. The generated contrast is free of Bragg effects and contains information about the atomic number Z (due to Rutherford scattering), since higher-angle scattering is caused by electron-nucleus interactions. Due to the absence of interference, as is the case for coherent imaging in BF, the contrast is no longer affected by the CTF. For this incoherent imaging as shown by the optical transfer function (OTF) in Figure 11-48, contrast is not reversed and decays monotonically with spatial frequency.

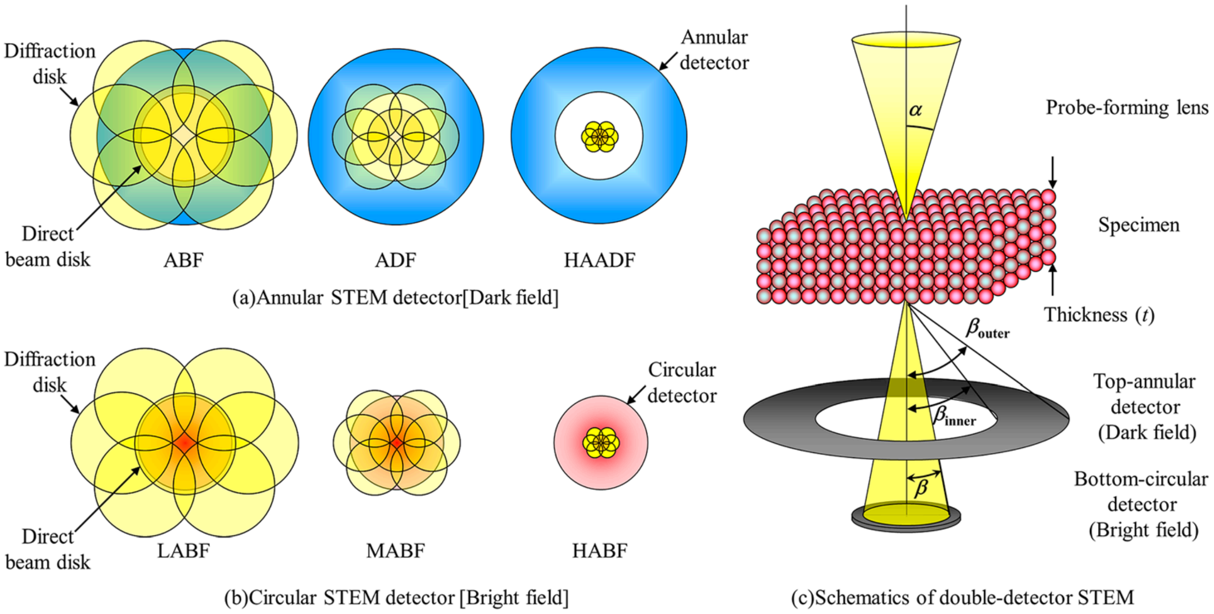

Figure 11-47: Different imaging modes lead to different atom contrast in atomically resolved scanning transmission electron microscopy (STEM) images. (a) Light and heavy atomic columns appear as dark spots in annular bright field (ABF) STEM. Annular dark field (ADF) STEM, typically differentiated into low-angle and medium-angle ADF, can be beneficial to investigate defects like grain boundaries, as Bragg effects are still included in the contrast. For high-angle ADF, heavy atomic columns appear as bright spots. (b) The inverse contrast of HAADF-STEM is visible in high-angle bright field (HABF) STEM images. For medium-angle bright field (MABF) STEM, light atomic columns appear as bright spots, while heavy atomic columns appear as dark spots. Low-angle bright field (LABF) STEM is similar to high-resolution transmission electron microscopy (TEM). (c) The annular and circular detectors are placed at different detection planes in a double-detector microscope. Reprinted with permission from [109], © 2012 AIP Publishing.

When acquiring images with a double-detector STEM, the imaging modes must be selected before imaging. This can be a disadvantage that can be circumvented nowadays by replacing the BF and DF detectors with a direct electron detector if the sample is investigated with a probe that has a semiangle greater than 20 mrad, as shown in Figure 11-49. A pixelated detector collects the entire Bragg (crystalline) scattering per probe position. Each pixel of the two-dimensional scanned image contains a two-dimensional convergent beam electron diffraction (CBED) pattern. For this reason, this imaging is referred to as 4D-STEM. The 4D-STEM dataset allows for the generation of conventional STEM images by applying a mask to the 4D dataset, i.e., permits scattered electrons in the range of 90-360 mrad to generate contrast for a HAADF STEM image.

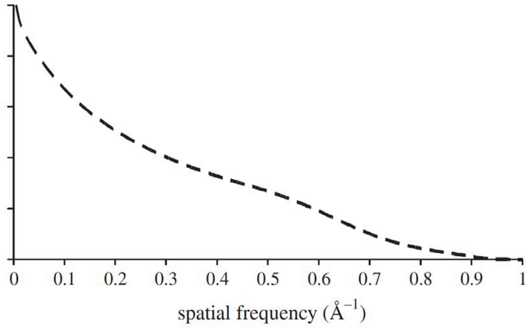

Figure 11-48: The optical transfer function (OTF), which is the Fourier transform of the electron probe intensity, shows a contrast decrease for high spatial frequencies. Reprinted with permission from [108], © 2011 Springer Nature.

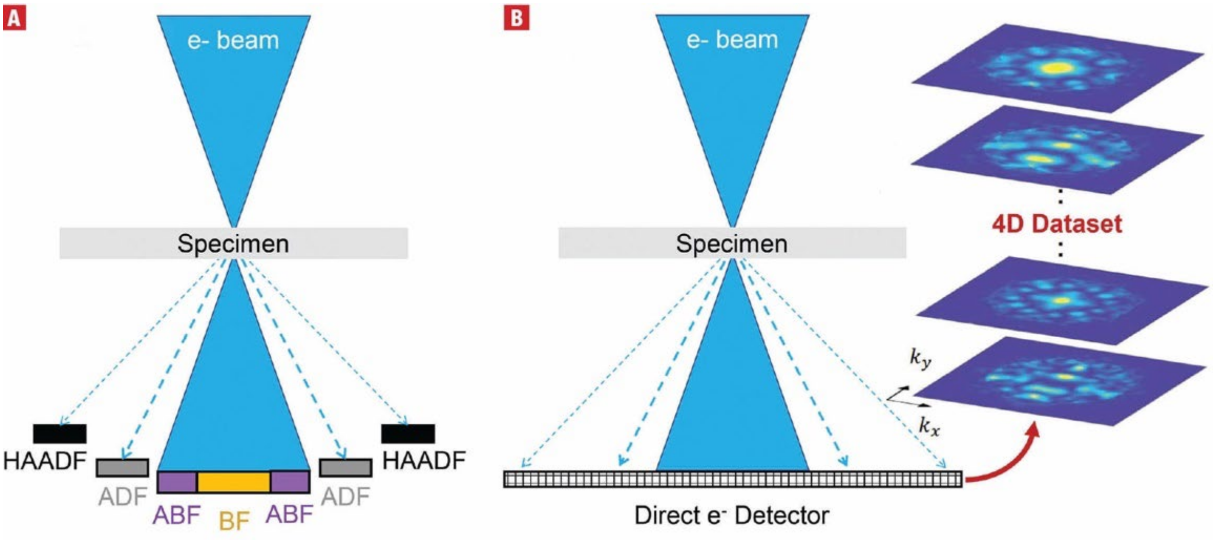

Figure 11-49: (a) A conventional scanning transmission electron microscopy (STEM) image is produced by collecting signal intensities from a fixed angular region either with an annular detector (high-angle annular dark field (HAADF) or annular dark field (ADF)) or a circular detector (bright field (BF) or annular bright field (ABF)). (b) A direct electron detector, on the other hand, detects a large angular region of the diffraction plane. Each probe position contains a 2D image of the diffraction plane. When the probe is scanned across the sample, a 4D dataset will be created, which is why this imaging technique is referred to as 4D-STEM. Reprinted with permission from the author. Original figure in Microscopy and Analysis at [110].

A 4D STEM dataset acquired with a probe semiangle smaller than 2 mrad cannot be used to generate conventional STEM images, however, can be used to generate, i.e., grain orientation or phase maps. A schematic workflow for automated crystal orientation mapping (ACOM) is shown in Figure 11-50. Tilting the beam continuously around the optical axis, known as precession, can improve the quality of the available diffraction data for analysis. This precession electron diffraction-assisted (PED) 4D-STEM is usually referred to as scanning precession electron diffraction (SPED).

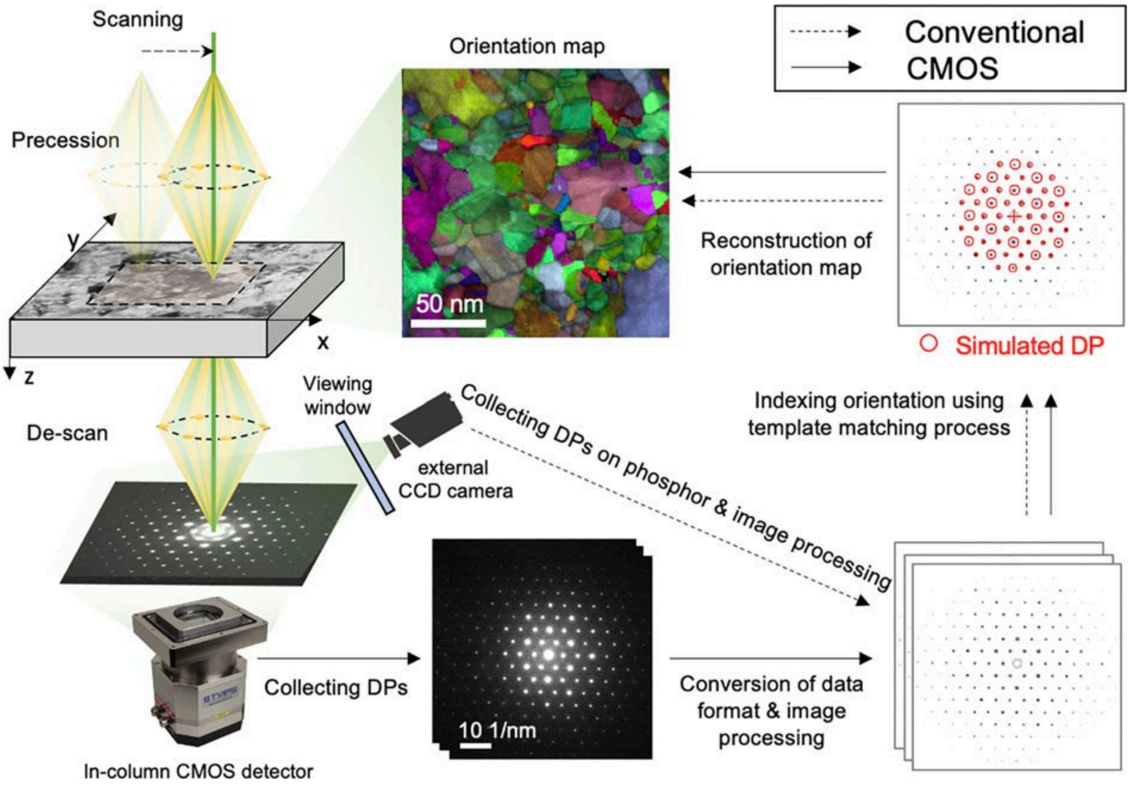

Figure 11-50: Recent developments allow to acquire 4D-STEM datasets with a direct electron detector (DED, here in-column complementary metal oxide semiconductor (CMOS)) detector. The installation of our special dedicated 4D-STEM setup is documented by Dr. Alexander Zintler in his PhD thesis [103]. In comparison to collecting diffraction patterns (DPs) from a phosphorus screen with an external CCD (charge coupled device) camera, a DED offers a faster readout with less noise and little radiation damage. With software like ASTAR from Nanomegas [111], DPs are analyzed by using template matching. Simulated DPs are compared to measured DPs. The result can be used to generate, i.e., an orientation map. Reprinted under a CC BY from [112] © Oxford University Press.

12. Cumulative Part

12.1. Grain boundaries and resistive switching

McKenna et al. in 2011 [113] and Lanza et al. in 2012 [114] showed by using conductive atom force microscopy (C-AFM) that grain boundaries (GBs) are beneficial pathways for CF formation in highly textured insulating thin films. Ab initio calculations based on density functional theory (DFT) relaxed structures further supported this idea [115–118]. However, research on metal-oxide based memristive devices with $SrTiO_3$ bicrystals [119] or CeO_2 thin films [120] as the insulating layer could not provide evidence that GBs act as preferential pathways. Surprisingly, the samples investigated in the first publication [1] showed very different resistive switching behavior in terms of electroforming voltage, although the microstructure, especially the grain boundary layout of the insulating layer, was identical. Based on the C-AFM results in the literature, a grain boundary layout of textured insulating thin films, where threading GBs bridge the adjacent metal layer, should improve electroforming voltage. However, only memristive devices with $(11\bar{1})$ textured HfO_2 layers have improved electroforming voltage, while the devices with (010) textured HfO_2 have not. Hence, a goal was set to answer this in principle simple question of why these memristive devices behave differently in the first publication [1].

This section is published in: Winkler, R., Zintler, A., Petzold, S., Piros, E., Kaiser, N., Vogel, T., Nasiou, D., McKenna, K.P., Molina-Luna, L., Alff, L.: Controlling the Formation of Conductive Pathways in Memristive Devices. Adv. Sci. 9, 2201806 (2022).
https://doi.org/10.1002/advs.202201806

12.1.1.Summary and discussion

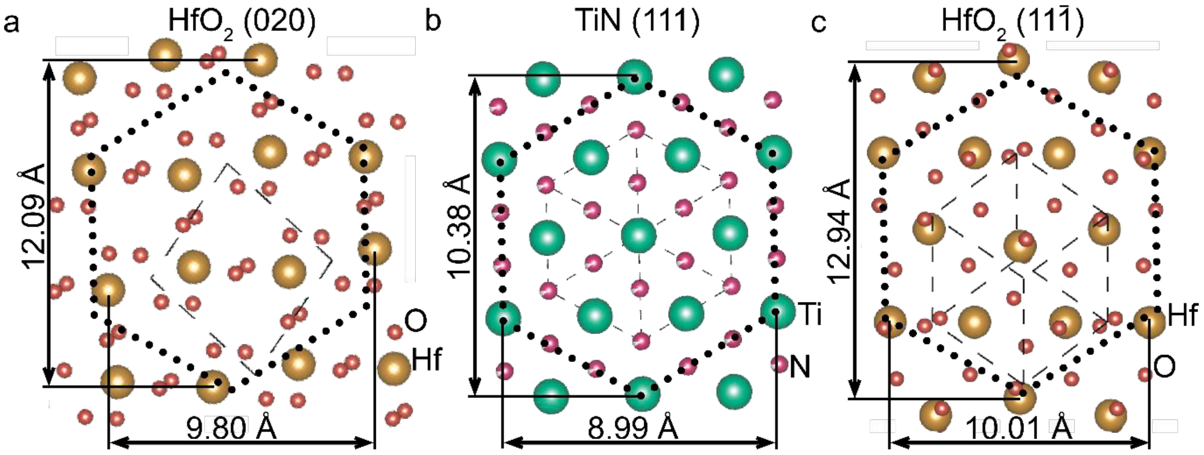

Figure 12-1: Growing a $(11\bar{1})$ oriented HfO$_2$ on top of (111) TiN can result in larger strain effects in comparison to (020) oriented HfO$_2$ due to the larger lattice mismatch as shown by the in-plane lattice spacings of the common structure (dotted line). Single atomic planes are visualized along the respective growth orientation with VESTA [74]. Unit cell (hatched lines) structures for TiN and HfO$_2$ are taken from [73, 121], respectively. Reprinted under a CC BY 4.0 from [1], © 2022 Wiley.

Growing HfO$_2$ based memristive devices with distinct HfO$_2$ crystallinities has been achieved by utilizing texture transfer during RMBE growth (more information on RMBE in Chapter 11.1). First, a (111) textured TiN layer has been grown on *c*-cut sapphire (Al$_2$O$_3$) substrates continued by in situ growth of (020) and $(11\bar{1})$ textured HfO$_2$, respectively. For $(11\bar{1})$ textured HfO$_2$, a relatively large lattice mismatch of ~25% relative to the TiN layer, as highlighted by the common structure shown by dotted lines in Figure 12-1, needed to be compensated. This was possible by careful adjustment of RMBE growth parameters, however, most significantly influenced by the choice of rf-source endplate (aperture). An endplate with fewer holes allowed to operate the plasma with a high optical output (a high amount of O* radicals) at 200 W resulting in $(11\bar{1})$, while another endplate, that allowed to operate at 280 W with a high optical output resulted in (020) textured hafnia. O flow and Hf evaporation rate have been the same (1 sccm and 0.7 Å s^{-1}) with only a temperature difference of 60 °C (020 grown at 460 °C, $(11\bar{1})$ grown at 520 °C).

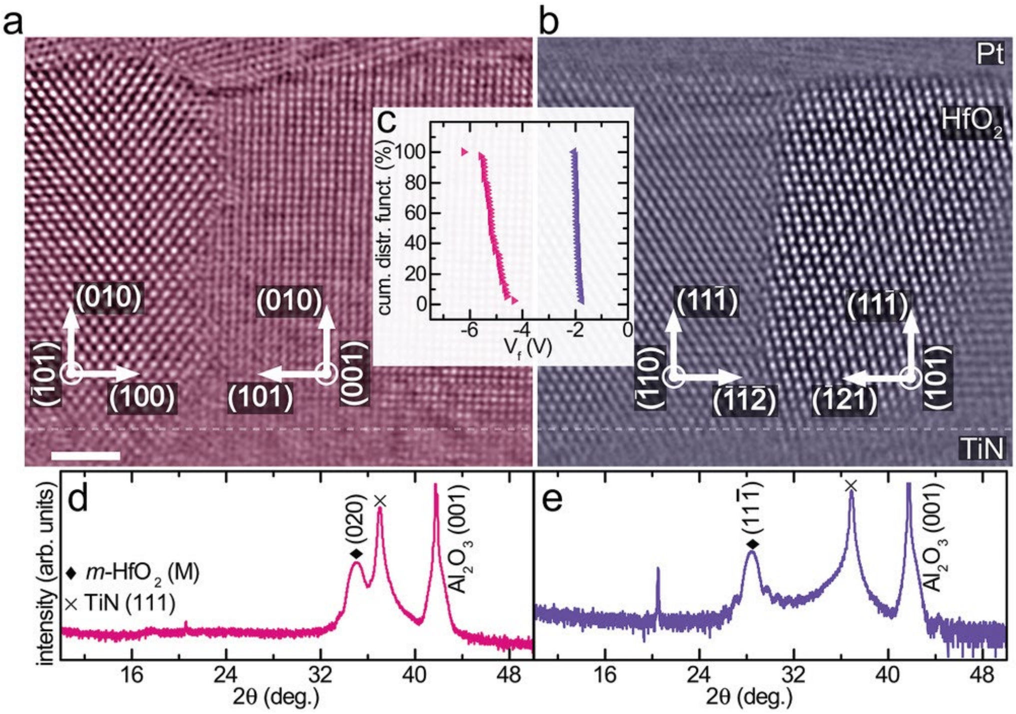

Figure 12-2: (a, b) Atomically resolved cross-sectional high-angle annular dark-field (HAADF) scanning transmission electron microscopy (STEM) images of metal-insulator-metal stacks reveal, that the textured monoclinic (*m*)-HfO$_2$ thin film growth, either with a (020), (pink) or $(11\bar{1})$, (purple) texture (single peaks in respective X-ray diffraction patterns (d, e)), results in an insulating layer with threading grain boundaries. (c) Despite the same grain boundary layout, only devices with $(11\bar{1})$ HfO$_2$ have a reduced average forming voltage of $\overline{V_F} = -1.9\ V$ unlike devices with (020) HfO$_2$ with $\overline{V_F} = -5.3\ V$. The cumulative distribution function (cum. distr. funct.) shows 50 data points for each type of texture, representing 50 memristive devices. HAADF STEM images were filtered by an average background subtraction filter (ABSF), a Butterworth filter and a STEM crosshair filter to improve the visibility of atomic columns [122, 123]. Dashed lines show the HfO$_2$/TiN interface. The length of the scale bar in the HAADF STEM image is 2 nm. Reprinted under a CC BY 4.0 from [1], © 2022 Wiley.

XRD patterns of HfO$_2$/TiN/Al$_2$O$_3$ directly acquired after RMBE growth, shown in Figure 12-2 (d, e), confirmed the growth of highly textured HfO$_2$ thin films. The MIM structure has been complemented by surface patterning via optical lithography and sputter deposition of Pt and Au (more information about device fabrication is in Chapter 10.2). The cross-sectional HAADF STEM images shown in Figure 12-2 (a, b) highlighted that the HfO$_2$ layers consist of GBs that thread the entire thin film. This, according to C-AFM measurements [113, 114], should therefore yield memristive devices with improved RS performance. However, as shown in Figure 12-2 (c) by the cumulative distribution function of forming voltages (V_F) collected from 50 devices, only the devices with $(11\bar{1})$ textured HfO$_2$ have reduced V_F. Examples of electroforming are shown in Figure 12-3 (b).

Analysis of the conduction mechanism as shown in Figure 12-3 (c, d), which is based on the leakage measurements shown in Figure 12-3 (a), revealed that both memristive devices have bulk-limited conduction. Because GBs are considered preferential pathways for filament formation, the local atomic configuration of GBs, influenced by the thin film texture, should therefore be related to the required forming voltages. For this purpose, density function theory (DFT) relaxed atomic structure models have been retrieved from the atomic resolution images of grain boundaries, as shown in Figure 12-4 and Figure 12-5.

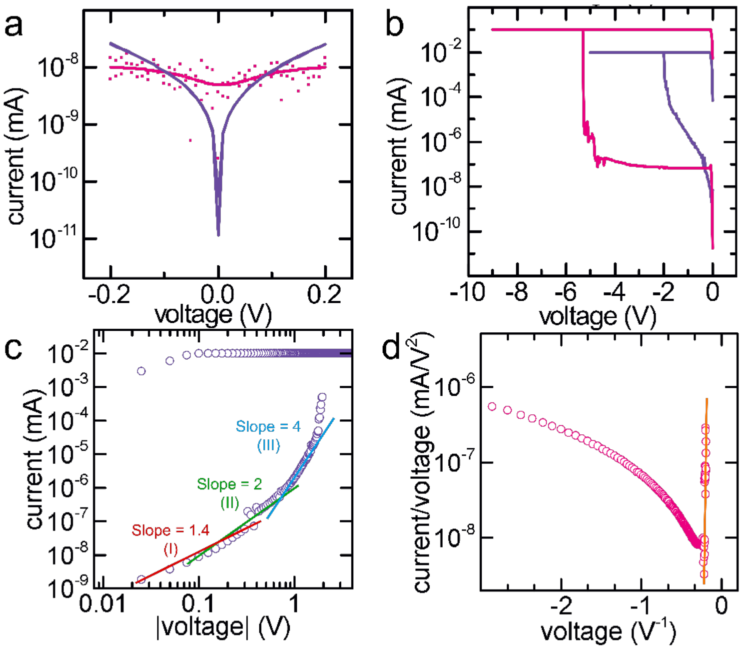

Figure 12-3: (a) The leakage current of memristive devices with (020), pink, and $(11\bar{1})$, purple HfO$_2$ was used to investigate the conduction mechanism by changing current-voltage (I-V) plots (see Table 9-1). Data points from the leakage measurement of the device with (020) HfO$_2$ are fitted with a Lorentzian function for better visibility. (c) The device with $(11\bar{1})$ shows space-charged limited conduction (SCLC), and the device with (020) shows Fowler-Nordheim tunneling. (b) The device with (020) requires a higher voltage for electroforming, but also a higher compliance current (maximum allowed current) to reliably switch from the initial low resistance state to the formed high resistance state. Reprinted under a CC BY 4.0 from [1], © 2022 Wiley.

The cross-sectional HAADF STEM images are shown in (a), and the DFT relaxed atomic structures are shown in (b). The GB of $(11\bar{1})$ textured HfO$_2$ is composed of high-indexed terminated grains $(\overline{112}|\bar{1}21)$, and the GB of (020) textured HfO$_2$ is composed of low-indexed terminated grains (100|101). To validate that the calculated structures match with atomic images, the DFT relaxed atomic structures were used as the basis to simulate HAADF-STEM images shown in (c) by using the multislice method [124]. The construction of the $(\overline{112}|\bar{1}21)$ GB structure for $(11\bar{1})$ textured HfO$_2$ could only be achieved by applying significant strain parallel to the GB.

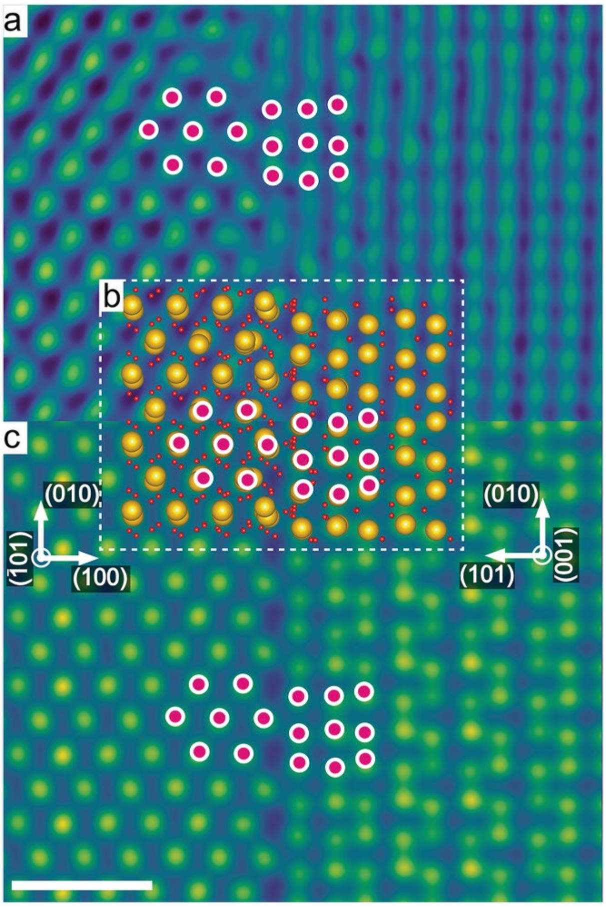

Figure 12-4: To understand how the grain boundary atomic structure impacts electroforming, (a) the atomically resolved high-angle annular dark-field (HAADF) scanning transmission electron microscopy (STEM) images were used to construct realistic density functional theory (DFT) relaxed atomic structures, which were used to simulate (c) HAADF STEM images. The DFT relaxed atomic structure is overlaid on the real and simulated image to highlight the congruence, in addition to the drawn, periodically occurring structural units (pink circles). Atomic bonds are not shown in the DFT relaxed structure for better visibility. Experimental HAADF-STEM images are filtered by an average background subtraction filter (ABSF) and a Butterworth filter [122, 123]. Both HAADF STEM images are colored with the GEM-16 LUT. The scale bar is 1 nm. Reprinted under a CC BY 4.0 from [1], © 2022 Wiley.

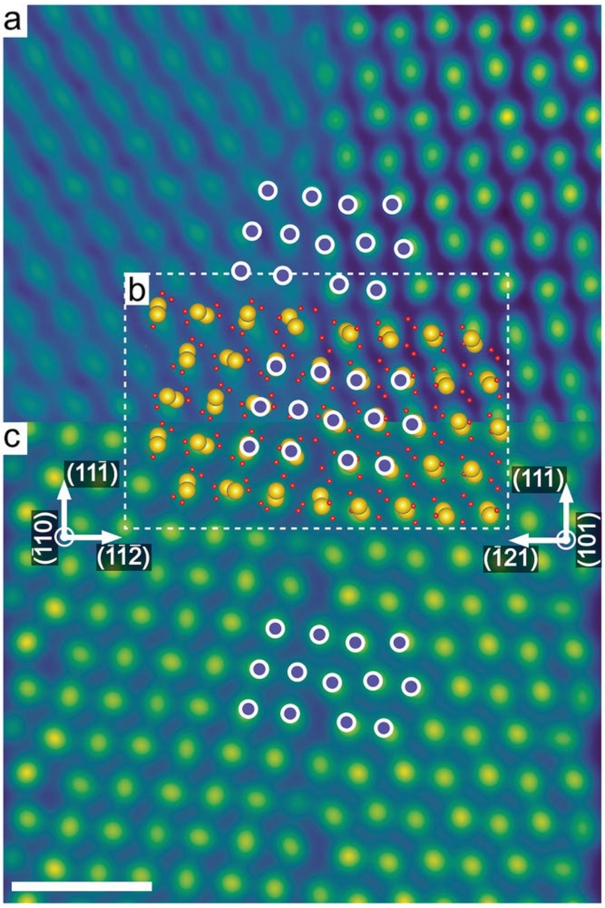

Figure 12-5: See description of Figure 7-4. Reprinted under a CC BY 4.0 from [1], © 2022 Wiley.

The realistic models of the grain boundary atomic structure were used to investigate neutral oxygen vacancy (V_O) interactions by first principles calculations. The calculated segregation energies (E_{seg}) in the vicinity of the GBs are shown in Figure 12-6 (a). For a low V_O concentration of 1 nm^{-2}, the E_{seg} of the $(\overline{112}|\overline{1}21)$ GB is significantly more negative compared to the (100|101) GB. A negative E_{seg} results in segregation of V_O at the GB [125], which could explain the low V_F for devices based on $(11\overline{1})$ textured HfO_2, as preexisting oxygen vacancies are known to lower V_F [126]. For higher V_O concentrations above 2 nm^{-1}, as shown by the average E_{seg} per V_O in Figure 12-6 (b) the E_{seg}/V_O of both types of GBs is comparable. In principle, a low V_O concentration below 2 nm^{-1} should be representative of these memristive devices, as HfO_2 has been grown with a close to ideal 2:1 stoichiometry. Therefore, any anisotropy in V_O distribution cannot be the reason for a reduced V_F. Moreover, as shown by the density of states (DOS) projected onto the GB region in Figure 12-6 (c-f), a higher V_O concentration of 4 nm^{-1} results in the formation of a conductive sub-band [127, 128]. Because this sub-band deteriorates the insulating properties, the investigated pristine, non-formed memristive devices, which are insulating, must have a low V_O concentration, as a V_O concentration of 1 nm^{-1} shows a clear gap state between the valence and conduction bands.

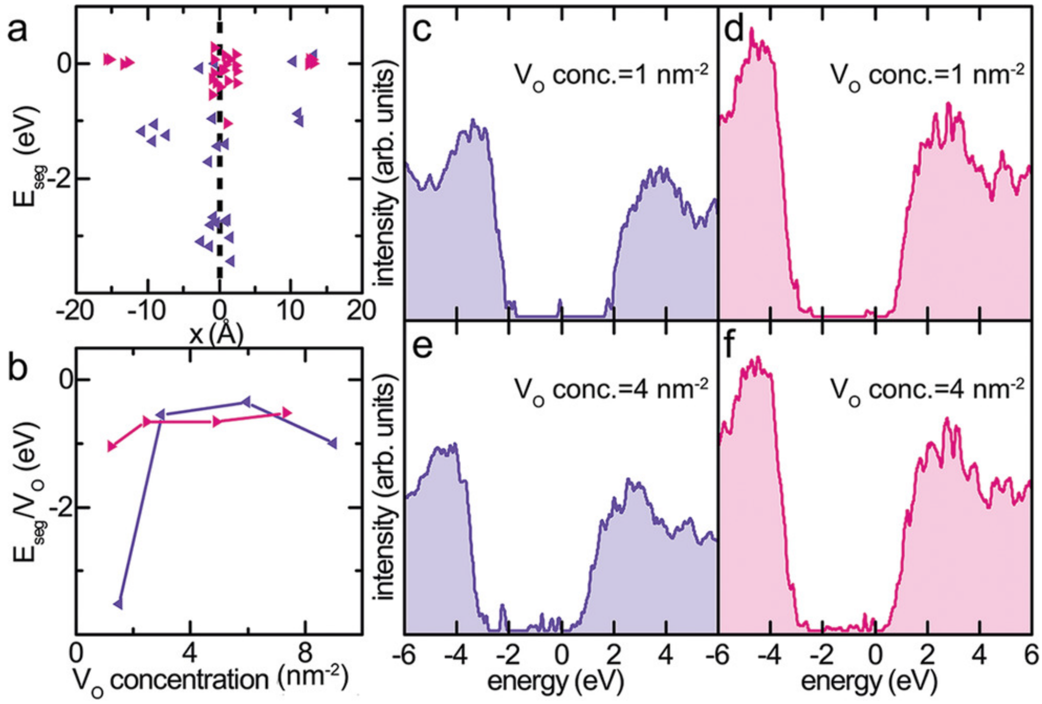

Figure 12-6: Oxygen vacancy (V_O) segregation energies (E_{seg}) (a) near the grain boundary for (020), (pink) and $(11\overline{1})$, (purple) for and (b) averaged for different initial V_O concentrations. The density of states (DOS) are calculated using the projector augmented wave (PAW) for a low (c, d) and higher (e, f) V_O concentration. Reprinted under a CC BY 4.0 from [1], © 2022 Wiley.

Although only a single GB per texture has been investigated, the type of investigated GB (high-indexed terminated grains for $(11\bar{1})$, low-indexed terminated grains for (020)), can be considered representative as the HfO_2 layer is grown with a biaxial texture. As shown by the pole figure measurements in Figure 12-7 (a, b), both $(11\bar{1})$ and (020) textured HfO_2 thin films have six allowed in-plane directions. As emphasized by the unit cells of (out-of-plane oriented) $(11\bar{1})$ and (020) HfO_2 in Figure 12-7 (c, d), respectively, the majority of GBs in (020) textured HfO_2 must therefore be composed of low-indexed terminated grains, contrary to GBs in $(11\bar{1})$ HfO_2, which are primarily composed of high-indexed terminated grains.

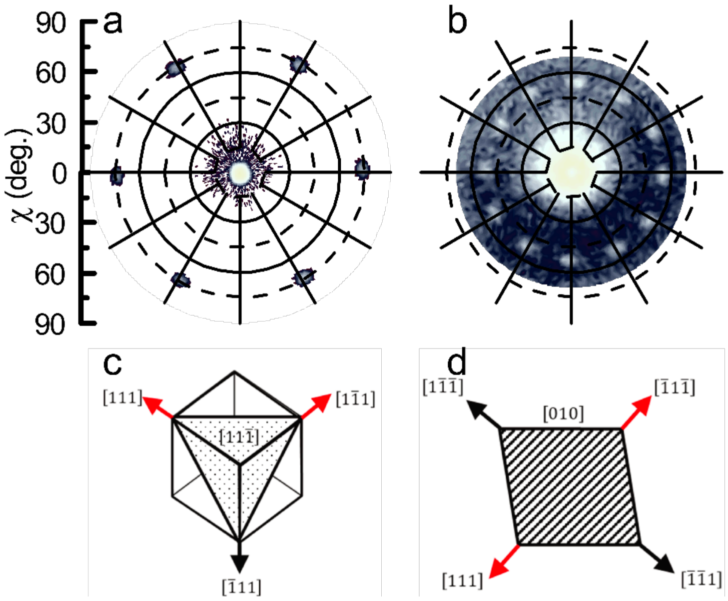

Figure 12-7: Pole figure (PF) measurements at a fixed 2θ of (a) 28.35° and (b) 36.64° for the $(11\bar{1})$ and (020) textured HfO_2, respectively. (c) A $(11\bar{1})$ out-of-plane oriented monoclinic HfO_2 single crystal would produce a single in-plane peak in a (11-1) PF measurement (due to the monoclinic nature of the unit cell). (d) In the case of a (020) crystallinity, two in-plane peaks are expected. Reprinted under a CC BY 4.0 from [1], © 2022 Wiley.

12.1.2. Presentation of own contribution

Successive RMBE growth of the $(11\bar{1})$ HfO_2 and (111) TiN thin films on *c*-cut sapphire was carried out by Dr. Stefan Petzold, while I have grown the thin film stack with (020) HfO_2. The entire macroscopic analysis, including surface patterning, electrical measurements and XRD, was performed by me. The HAADF-STEM image of the memristive device with $(11\bar{1})$ HfO_2 was acquired by Dr. Alexander Zintler, and the HAADF-STEM image of the device with (020) was acquired by me. Rough structural models of the $(11\bar{1})$ and (020) grain boundaries were made by Dr. Alexander Zintler and me, which were given to Prof. Dr. Keith McKenna. He calculated the DFT-relaxed atomic structures and performed the first-principles calculations.

Eszter Piros, Dr. Nico Kaiser, Dr. Tobias Vogel, and Déspina Nasiou contributed to the discussion of results and proofreading of the manuscript. Prof. Dr. Leopoldo Molina-Luna provided support for all results related to electron microscopy, and Prof. Dr. Lambert Alff provided support for all results related to electrical characterization.

12.2. Grain boundaries and texture transfer

Grain boundary engineering of the dielectric layer in memristive devices, as in the case of this PhD research, has been based on growing highly textured thin films via texture transfer during thin film growth. These optimized dielectric films, however, are grown at elevated temperatures, which could be more challenging to integrate in a complementary metal oxide semiconductor (CMOS) back-end-of-line (BEOL) process [129]. Usually, in a CMOS BEOL process, thermal annealing is used to activate dopants or remove defects [130], and in the case of RRAM to alter the polycrystallization or texture of the dielectric [131, 132]. According to literature, annealing temperatures increase with decreasing film thickness [131, 133–140], and about 300 °C is required to crystallize amorphous HfO_2, while crystallization for layers thinner than 6 nm can be suppressed [141]. Striking about these experimental data is the fact that the chosen deposition technique resulted in different annealing temperatures, which are higher for films grown by atomic layer deposition (ALD), a low-kinetic deposition method [142], and lower for films grown by pulsed laser deposition (PLD), a high-kinetic technique [143]. This could affect the atomic coordination of the amorphous films. A study by Luo and Demkov [144] investigated different atomically coordinated amorphous hafnia and calculated a crystallization temperature of 146 °C, lower than the experimentally determined crystallization temperatures. This difference could be related to a higher surface-to-interface ratio (thinner film), but it could also be related to the fact that HfO_2 films are always grown on a substrate or underlying layer that can alter the Gibbs free energy by accommodating strain, which impacts the crystallization temperature texture. Therefore, the third publication [3] was meant to answer the question of at which temperature amorphous HfO_2, grown on textured TiN, starts to crystallize, and whether the adjacent layers influence the crystallinity, and if the resulting crystallinity improves resistive switching performance.

This section is published in: Winkler, R., Zintler, A., Recalde-Benitez, O., Jiang, T., Nasiou, D., Adabifiroozjaei, E., Schreyer, P., Kim, T., Piros, E., Kaiser, N., Vogel, T., Petzold, S., Alff, L., Molina-Luna, L.: Texture Transfer in Dielectric Layers via Nanocrystalline Networks: Insights from in Situ 4D-STEM. Nano Lett. (2024). https://doi.org/10.1021/acs.nanolett.3c03941

12.2.1.Summary and discussion

An electron-transparent lamella of a MIM device with the layer configuration TiN (111)/amorphous HfO_2/Pt was prepared on a MEMS-based heating chip from DENSSolutions (see also Figure 11-28).

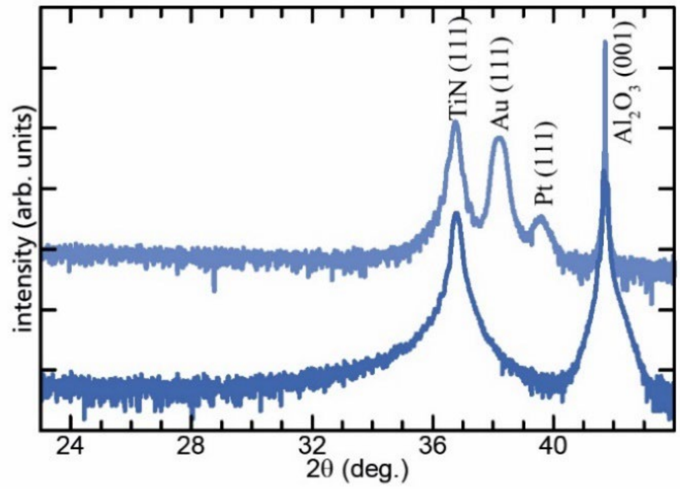

Figure 12-8: The darker blue X-ray diffraction pattern of the reactive molecular beam epitaxy (RMBE) grown amorphous HfO_2/TiN (111)/Al_2O_3 (001) stack shows, in addition to the expected crystalline peaks, a low-intense broad feature between 32° and 34° related to amorphous HfO_2. Surface patterning and subsequent sputter coating result in the additional Au and Pt peaks in the lighter blue XRD pattern. Reprinted with permission from [3], © 2024 American Chemical Society.

The thin film stack was created by using RMBE. TiN (111) was grown on *c*-cut sapphire, followed by in situ growth of amorphous HfO_2. Figure 12-8 shows the corresponding XRD pattern (darker blue color). To ensure that HfO_2 is grown with an amorphous structure, the RMBE chamber was cooled down overnight after TIN (111) deposition. The Pt layer was added via sputter coating after surface patterning via optical lithography, yielding a similar device structure as shown in Figure 11-7. The corresponding XRD pattern is shown in light blue in Figure 12-8.

The crystallization temperature was determined by investigating microstructural changes during in situ heating. High-resolution (HR)-TEM images of the heating experiment are shown in Figure 12-9. To facilitate identification of crystallization, FFTs of two selected areas, named here as “grain I” and “grain II”, are shown next to the respective TEM images. Further, arrows indicate the direction of crystallization and are placed on the crystalline phase, while colored lines indicate the boundary between the crystalline and amorphous phases. The difference between a crystalline area and an amorphous or nanocrystalline area is relatively difficult to assess from the HR-TEM images. To properly recognize which part of the HfO_2 is already crystalline and which is not, inverse FFTs were retrieved by bandpass filtering the amorphous ring of the HR-TEM images, and, as shown in Figure 12-10, amorphous parts therefore appear brighter compared to crystalline parts. In the pristine state (t=0 min), both the HR-TEM and iFFT images show that the HfO_2 layer is mostly amorphous. However, some nanocrystallinity is already present, as shown by spots in the FFT of grain I. Within 30 minutes, the temperature was carefully increased until noticeable changes were visible at 160 °C. For the investigated section, two grains start to grow from the corners of the image toward each other, parallel to the interface. Continuous heating at 160 °C for another 30 minutes (t=60 minutes) resulted in the formation of a grain boundary (shown by a white line in Figure 11-9 (d)). To investigate the crystallization in more detail, azimuthal integration (AI) plots were calculated for the entire in situ heating experiment by using the PASAD tools [145]. As exemplary shown in Figure 12-11 (a-c) for the pristine (t=0 min), intermediate (t=69 min) and the annealed (t=90 min) states, the 2D FFTs can be represented by a 1D plot, the azimuthal integration (AI). Intensities are collected from radial segments (rings) for each radius given by 1/d. The AIs were then used to visualize the entire in situ heating experiment as a 2D waterfall plot shown in Figure 12-12 (d). The amorphous ring shown in the FFT of the pristine state (Figure 12-12 (a)) is visible as a broad peak ranging from 3 to 4 nm^{-1}, as shown in the corresponding AI (Figure 11-12 (c)). This feature disappears after 60 minutes of continuous heating, and instead, two distinct peaks appear at 3 and 4 nm^{-1}. The peak at 3 nm^{-1} can be identified as $(11\bar{1})$ HfO_2. The peaks close to 4 nm^{-1}, as indicated in the FFT (Figure 12-12 (b)) and the corresponding AI (Figure 12-12 (e)), can be identified as (200) HfO_2 and TiN (111). It should be noted, that a peak at 3 nm^{-1} is not visible in the AI of the annealed state. This could be related to loss of high resolution as a consequence of drift resulting in defocus. Bandpass filtering the feature at 3 nm^{-1} to retrieve an iFFT as shown in Figure 12-11 (d) indicates that this feature is related to the HfO_2 layer, as the highest intensities originate from the HfO_2 layer close to the layer interfaces. The close positioning of the HfO_2 (200) and TiN (111) peaks, as emphasized by the overlaid simulated diffraction patterns in Figure 12-13, indicates a texture relation between both layers.

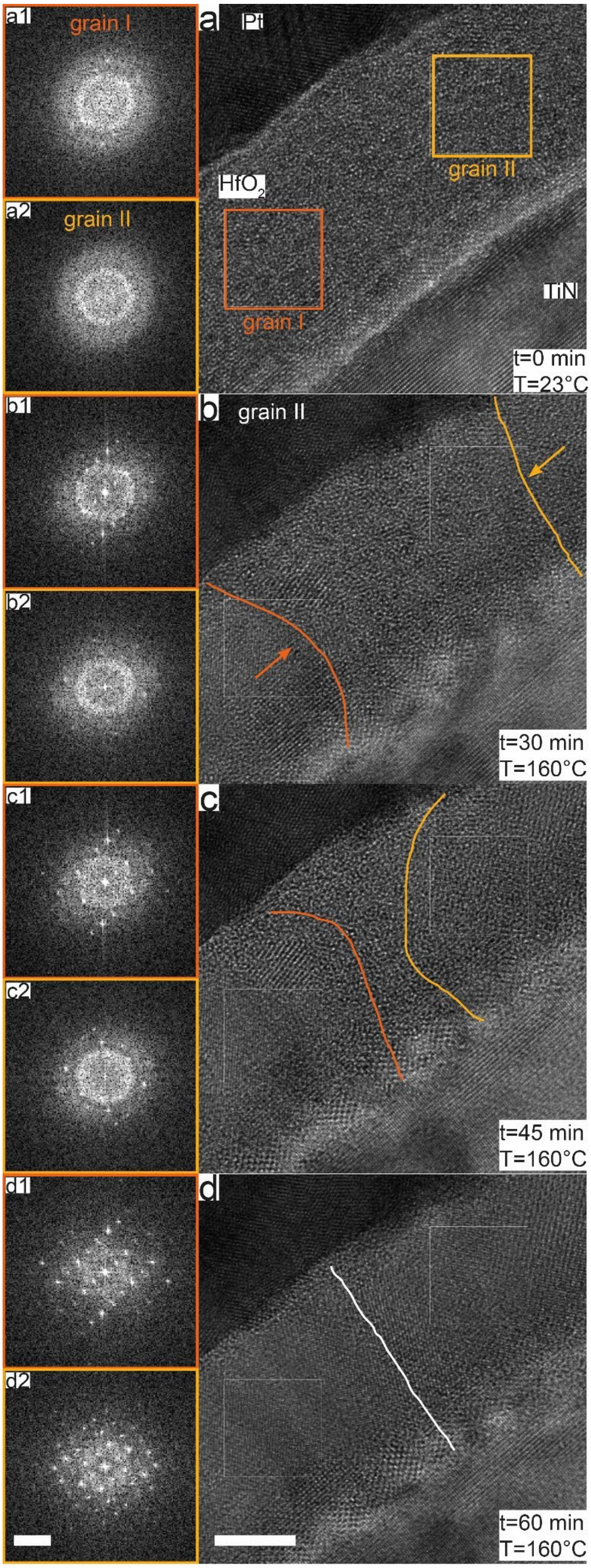

Figure 12-9: (a1), (a2) – (d1), (d2) Fast Fourier transforms (FFTs) of selected areas, named grain I and II, are presented next to (a-d) the respective high-resolution transmission electron microscopy (HR-TEM) images to illustrate crystallization at a temperature of 160 °C of amorphous HfO_2 sandwiched between Pt and highly textured (111) TiN during in situ TEM. Arrows indicate the growth direction of developing grains. Colored lines indicate the boundary between crystalline and amorphous HfO_2, and a white line indicates the formed grain boundary. The HR-TEM scale bar is 5 nm, and the FFT scale bar is 5 1/nm. Reprinted with permission from [3], © 2024 American Chemical Society.

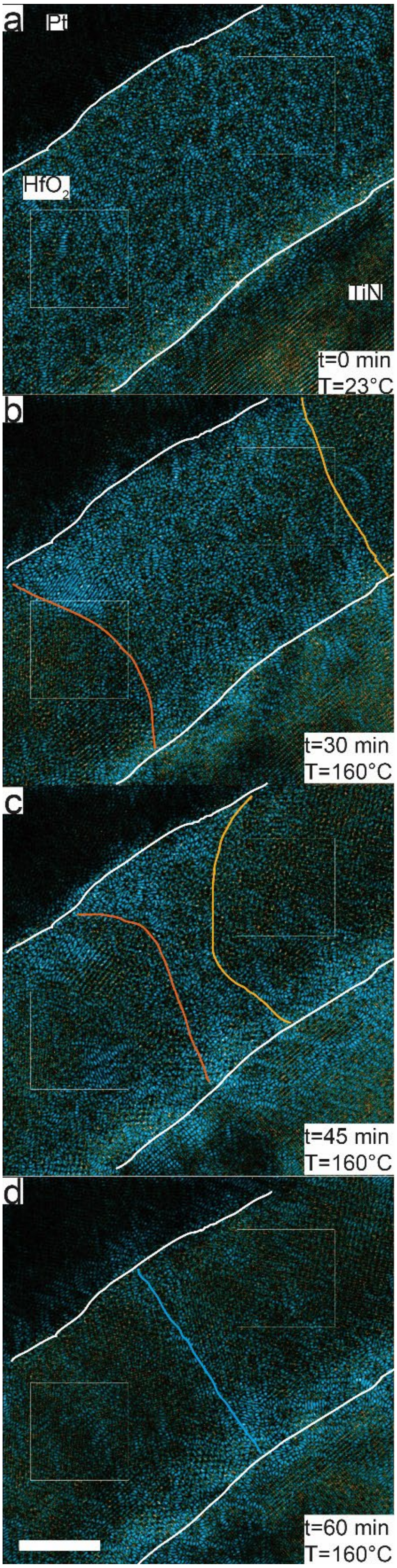

Figure 12-10: (a-d) Inverse Fast Fourier Transforms (iFFTs) were retrieved from bandpass filtering the amorphous ring of the high-resolution transmission electron microscopy (HR-TEM) images (shown in Figure 11-8) to highlight the noncrystalline parts of the HfO_2 layer shown in blue. To facilitate identification of the layer interfaces, shown by white lines, the iFFTs are overlaid on the HR-TEM images. Phase boundaries (amorphous|crystalline) are shown as orange and yellow lines. The formed grain boundary is shown as a blue line. The scale bar is 5 nm. Reprinted with permission from [3], © 2024 American Chemical Society.

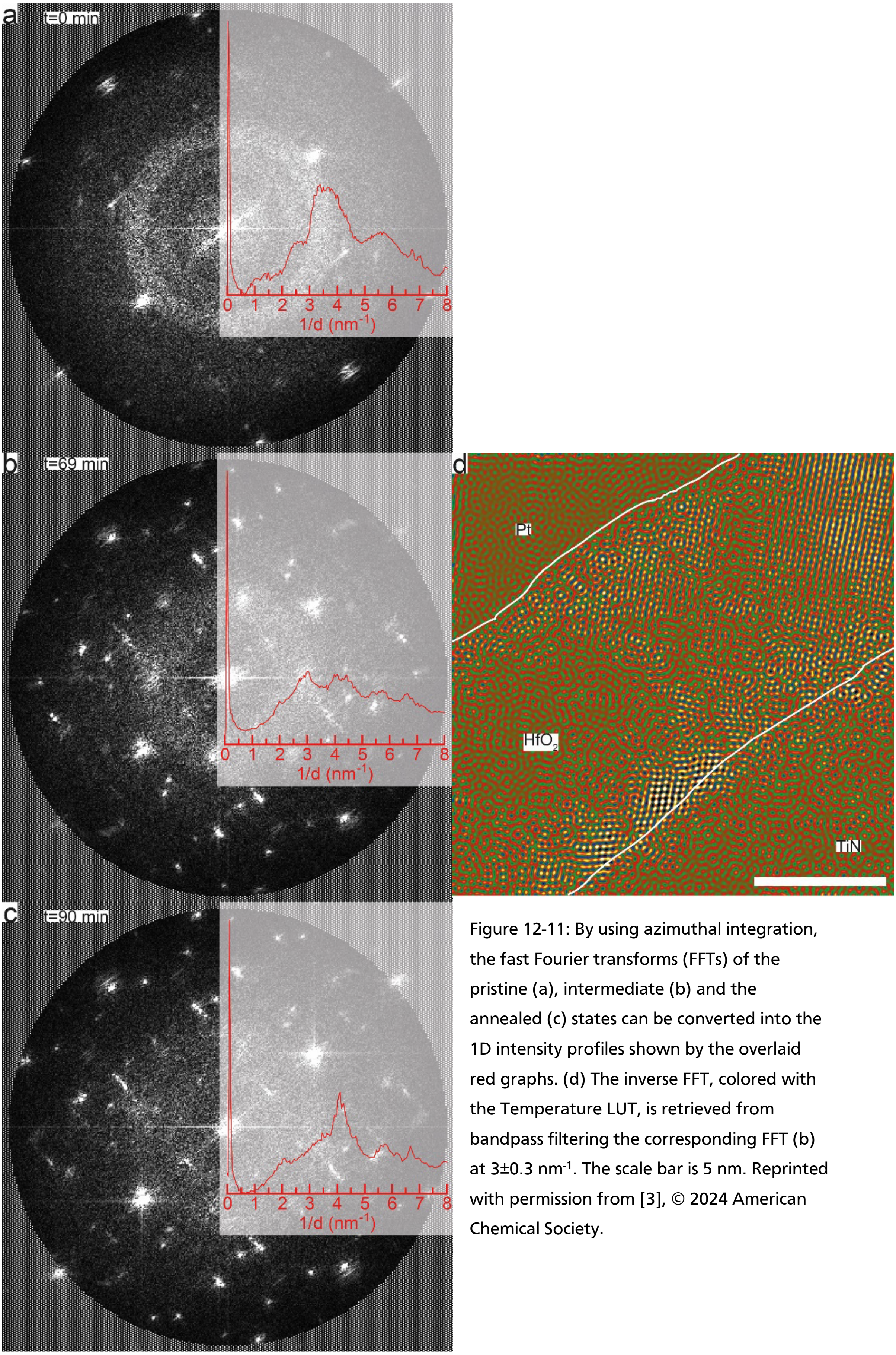

Figure 12-11: By using azimuthal integration, the fast Fourier transforms (FFTs) of the pristine (a), intermediate (b) and the annealed (c) states can be converted into the 1D intensity profiles shown by the overlaid red graphs. (d) The inverse FFT, colored with the Temperature LUT, is retrieved from bandpass filtering the corresponding FFT (b) at 3±0.3 nm^{-1}. The scale bar is 5 nm. Reprinted with permission from [3], © 2024 American Chemical Society.

Although these HR-TEM images already showed information about crystallinity and grain orientation, the relatively small field of view did not allow for a clear insight into grain growth origins and dynamics. To investigate a larger field of view while still being able to obtain precise information about the microstructure evolution, a second in situ heating experiment was performed using 4D-STEM. The acquired dataset was analyzed by the software ASTAR utilizing ACOM (more details in Chapter 11.7) to generate phase and orientation maps. To include the quality of template matching, the phase maps are superimposed by the phase reliability, as shown in Figure 12-14 right, and the orientation maps are superimposed by the index (Figure 12-14 left).

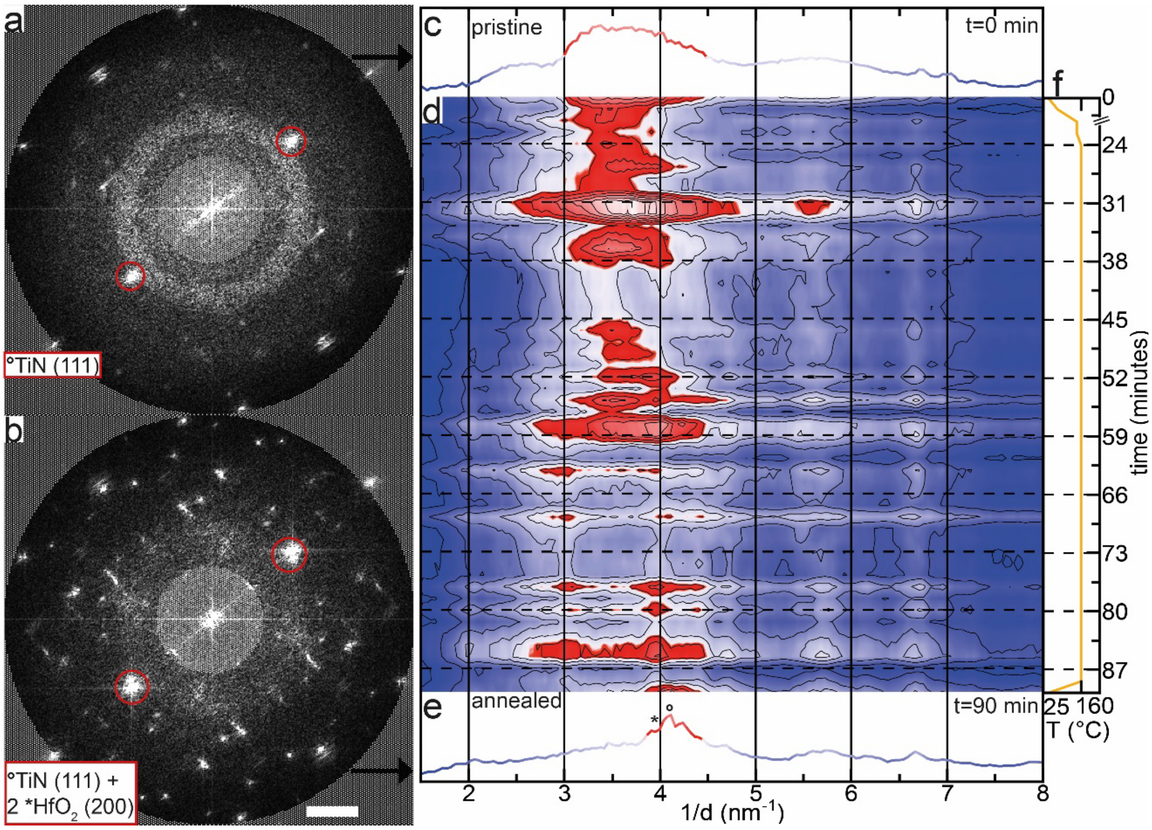

Figure 12-12: The Fast Fourier Transforms of the (a) pristine and (b) annealed states are shown to indicate the range (non-grayed-out part) of the (c, e) respective azimuthal integrations (Ais). (d) The 2D waterfall plot of AIs is shown as a function of time and temperature (f) The peaks (corresponding spots) around 4 nm^{-1} are attributed to TiN (111) and HfO_2 (200). The scale bar is 2 1/nm. Reprinted with permission from [3], © 2024 American Chemical Society.

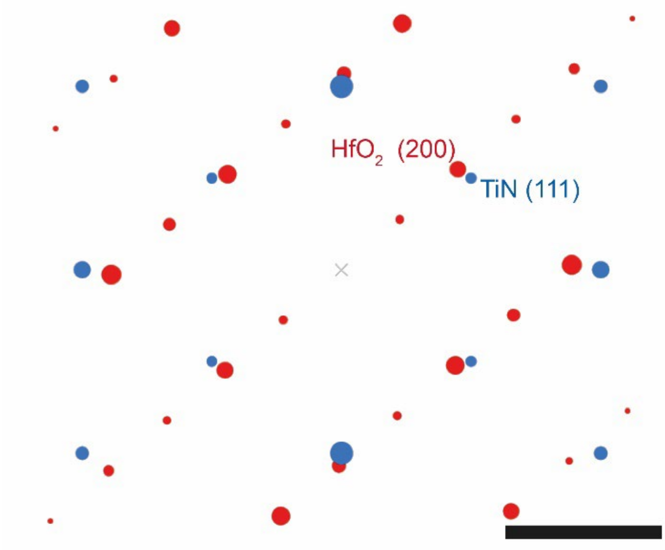

Figure 12-13: Diffraction patterns of TiN (blue) with a $(\bar{1}01)$ zone axis and of HfO_2 ((010) zone axis) are simulated with the software ReciPro [146]. The overlaid diffraction patterns are representative of HfO_2 that adapts a growth orientation of (200) due to a possible texture transfer from an underlying TiN (111), which, in addition to a similar d spacing of HfO_2 (200) and TiN (111), results in close positioning of the HfO_2 (200) and TiN (111) spots. The scale bar is 4 1/nm. Reprinted with permission from [3], © 2024 American Chemical Society.

As visible in the phase map of the pristine state (Figure 12-14, right first row), every layer is identified by the expected phase (top layer = cubic-Pt, middle layer = amorphous-HfO_2, bottom layer=cubic-TiN). Similar to the pristine state shown in the HR-TEM image (Figure 12-9(a)), a grain seed is also already present inside the amorphous HfO_2 matrix. It should be noted that proper phase identification was challenging for this 4D STEM dataset. The map of the annealed state (last row) shows Pt inside HfO_2. This identified Pt is, however, darker compared to the color at the Pt layer. A darker color is related to lower phase reliability. The shown Pt phase inside the HfO_2 should therefore be related to an identification error. To investigate grain growth in more detail, selected orientation+index maps of the pristine, two intermediate and the final annealed states are shown in Figure 12-15. The bright yellow color, representing amorphous HfO_2, which is covering the entire HfO_2 of the pristine state (Figure Figure 12-15 (a)), changes to a darker, indistinct mix of yellow and red when the temperature is set to at least 180 °C. As shown in Figure 12-15 (b), the pre-existing grain grows, and new grains are formed. Intriguingly, the newly formed grains do not have a distinct crystallinity and continue to grow without a distinct crystallinity (Figure 12-15 (c). Only when grains are sufficiently in contact with an adjacent layer does a distinct crystallinity become present.

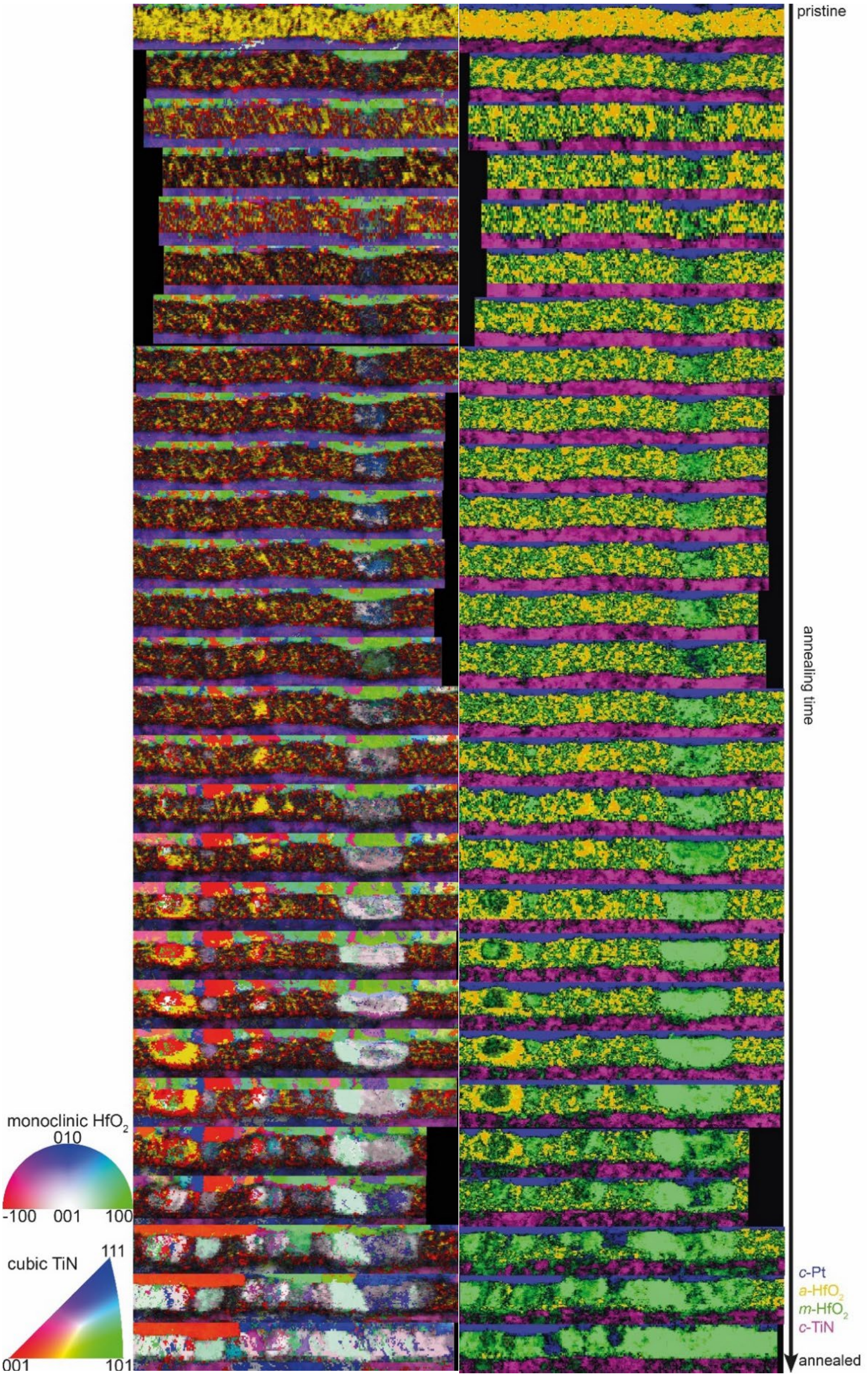

Figure 12-14: Overview of the entire crystallization process by analyzing the in situ heating 4D-scanning transmission electron microscopy (STEM) dataset with automated crystal orientation mapping (ACOM). Left: superimposed orientation+index maps. Right: superimposed phase+phase reliability maps. Reprinted with permission from [3], © 2024 American Chemical Society.

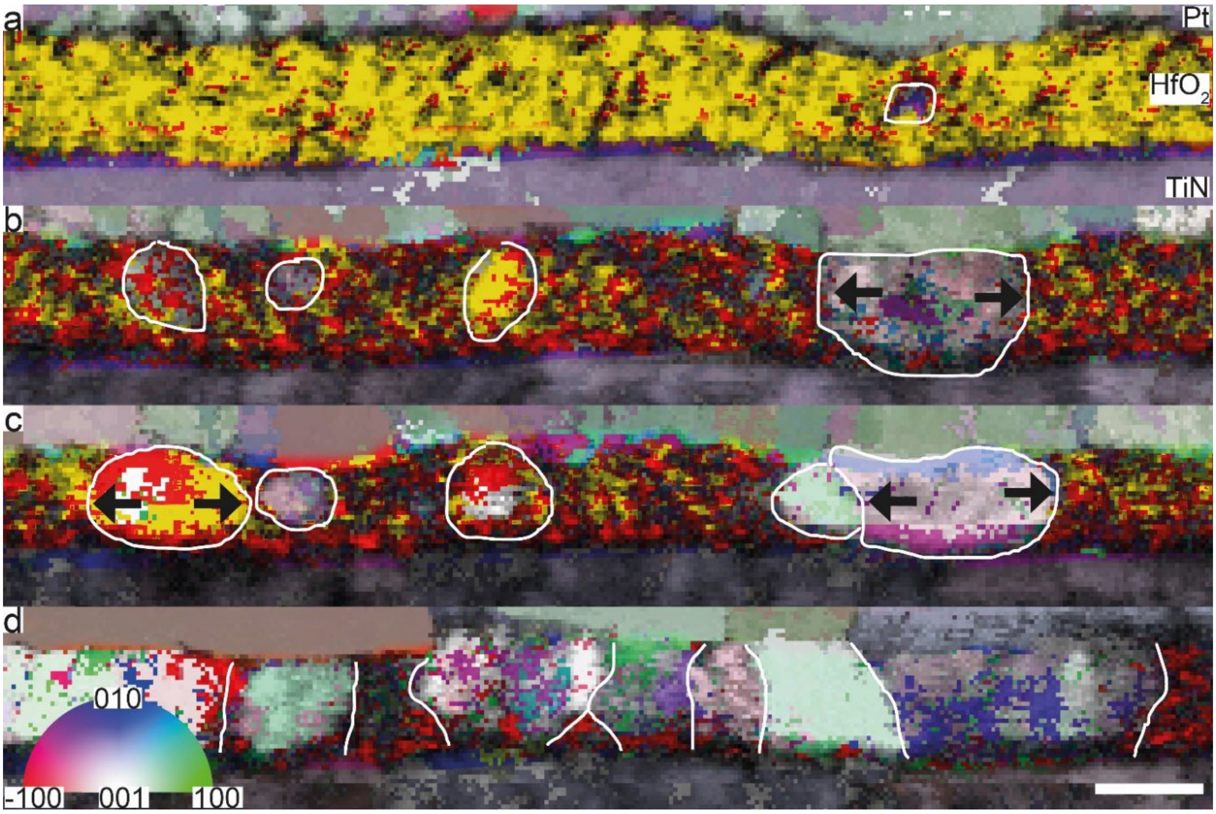

Figure 12-15: Superimposed orientation+index maps from automated crystal orientation mapping (ACOM) of the 4D scanning transmission electron microscopy (STEM) data set. The saturation of the Pt and TiN layers is reduced, growing grains are encircled and formed grain boundaries are represented by lines. (a) The pristine state contains primarily amorphous HfO_2, as shown by the bright yellow color. Some pixels, however, are shown by a darker yellow color or a black color resulting from a lower index (darker pixel) or inadequate indexing (no orientation, black pixel). (b, c) Heating to at least 180 °C results in the formation of new grains, which are primarily amorphous or nanocrystalline (yellow in color) and in the growth of the pre-existing grain. (d) The annealed state shows grain boundaries that thread the HfO2 layer. The coloring of the grains shows a mixed (001), (100), and $(11\bar{1})$ orientation. Reprinted with permission from [3], © 2024 American Chemical Society.

The in situ TEM results were verified by annealing another bulk memristive sample. Figure 12-16 (a) shows the XRD pattern after RMBE growth (orange) and after annealing (pink). Surface patterning was performed before annealing. Like in situ TEM annealing, the HfO_2 layer crystallizes at 180 °C into a mixed $(200)+(11\bar{1})$ texture. The forming voltages (Figure 12-16 (c)) collected from 50 devices with amorphous and annealed HfO_2, respectively, show that the average forming voltage improves from $V_F = -6.1\ V$ to $V_F = -4.2V$. Exemplary electroforming is shown in Figure 12-16 (b).

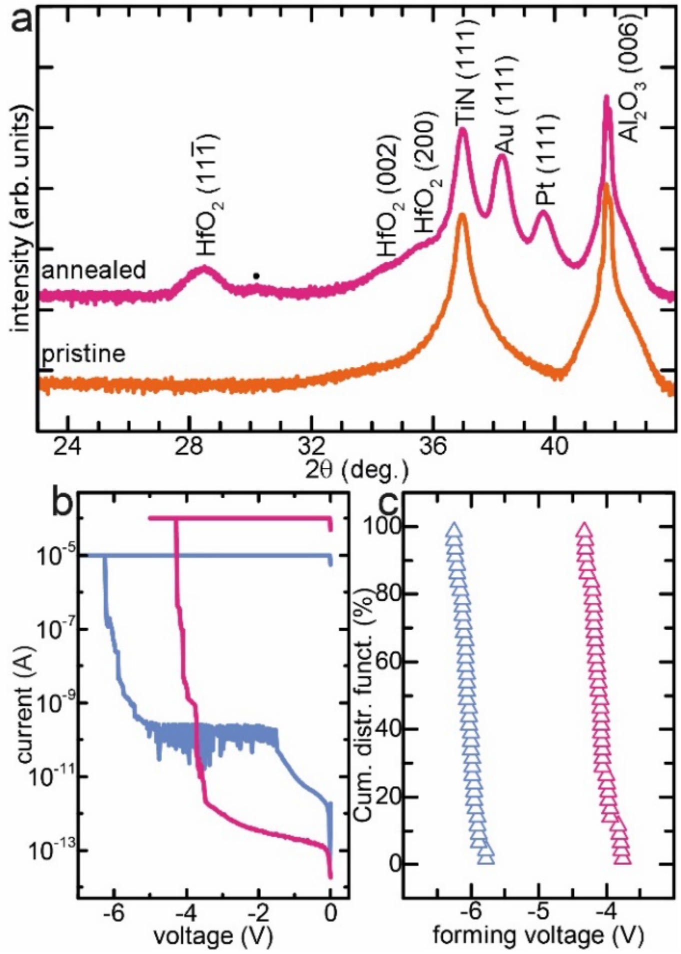

Figure 12-16: (a) The reactive molecular beam epitaxy (RMBE) grown amorphous HfO$_2$/TiN (111)/Al$_2$O$_3$ thin film stack (shown by the orange X-ray diffraction) was patterned by optical lithography and sputter coated with Au and Pt. Annealing at 180 °C results in a mixed $(11\bar{1})$+(002) HfO$_2$ texture, as shown by the pink XRD pattern. (b) Compared to a device with amorphous HfO$_2$ (blue), the electroforming voltages for a device with annealed HfO$_2$ (pink) are lower. (c) The average forming voltage retrieved from 50 devices, shown by the cumulative distribution function (cum. distr. funct.) is lowered from $V_F = -6.1\ V$ (blue) to $V_F = -4.2V$ (pink). Reprinted with permission from [3], © 2024 American Chemical Society.

12.2.2.Presentation of own contribution

Successive RMBE growth of the amorphous HfO$_2$ and (111) TiN thin films on *c*-cut sapphire was carried out by me. The entire macroscopic analysis, including surface patterning, electrical measurements, and XRD, was performed by me. Dr. Alexander Zintler and I have acquired the HR-TEM images and 4D-STEM dataset. One in situ lamella was prepared by Mr. Oscar Recalde with assistance from Dr. Letian Li, and another in situ lamella by Dr. Alexander Zintler. I have calculated all AIs and performed ACOM. Dr. Shuai Wang was responsible for the calculation of the iFFT retrieved by bandpass filtering the amorphous ring of the HR-TEM images. Tianshu Jiang, Déspina Nasiou, Esmaeil Adabifiroozjaei, Philipp Schreyer, Taewook

Kim, Eszter Piros, Dr. Nico Kaiser, Dr. Tobias Vogel, and Dr. Stefan Petzold contributed to the discussion of results and proofreading of the manuscript. Prof. Dr. Leopoldo Molina-Luna provided support for all results related to electron microscopy, and Prof. Dr. Lambert Alff provided support for all results related to electrical characterization.

12.3. Grain boundaries and conductivity

Texture transfer in dielectric layers is an intricate part of the investigated memristive systems in this PhD research and is strongly influenced by the underlying layers. The foundation on which every investigated textured layer is grown is a *c*-cut sapphire substrate (Al_2O_3), which has been selected to grow highly textured TiN thin films. This layer is one of the metal electrodes in the VCM cell and acts as the ohmic electrode. Usually, fully stoichiometric TiN is inert and cannot be used as the ohmic electrode as it is not oxidizable. In principle, TiN could be grown as a substoichiometric nitride. However, this would result in undesirable surface oxidation during the subsequent growth of the HfO_2 layer, as these layers are grown through the addition of radical beam-assisted evaporation (RBAE) of oxygen. Ab initio simulations based on DFT relaxed structures have shown that defects (e.g., vacancies) increase the oxygen affinity of initially internet electrodes [147, 148], but also extended defects (e.g., grain boundaries) can significantly increase oxygen diffusion [149, 150]. Having an electrode that is usable for texture transfer while being oxidizable is crucial, as oxygen is released during resistive switching operations from the metal oxide layer and can lead to bubble formation, causing deformation or delamination, ultimately resulting in device failure if not incorporated into the electrode [151, 152]. Therefore, the second publication [2] investigates how nitrogen deficiency in similarly textured TiN layers affects the microstructure and type of evolving grain boundary with the intent in mind of identifying an ideal stoichiometry, regarding conductivity, to be used as an ohmic electrode for a VCM cell.

This section is published in: Zintler, A., Eilhardt, R., Petzold, S., Sharath, S.U., Bruder, E., Kaiser, N., Alff, L., Molina-Luna, L.: Enhanced Conductivity and Microstructure in Highly Textured TiN1–x/c-Al2O3 Thin Films. ACS Omega. 7, 2041–2048 (2022). https://doi.org/10.1021/acsomega.1c05505

12.3.1. Summary and discussion

TiN thin films were grown on *c*-cut sapphire (Al_2O_3 (001)) using RMBE. One TiN thin film was grown with a Ti evaporation rate of 0.6 Å/s and a nitrogen flow of 1.0 sccm at 750 °C. The corresponding XRD pattern is shown in Figure 12-17 #1. In addition, a sample series was grown with a constant Ti evaporation rate of 0.2 Å/s and a constant nitrogen flow of 1.0 sccm at different substrate temperatures. The resulting thin film crystallinity is shown by the XRD patterns (#2-#5) in Figure 12-17. Please note that the patterns are ordered by the thin film stoichiometry (and not primarily by temperature), as the 2θ peak position of the TiN_{1-x} peak is influenced by the amount of nitrogen deficiency. Sample #1 is less nitrogen deficient due to the growth with a higher Ti evaporation rate. In addition, samples #1 and #5, grown at 750 °C, show an additional peak related to an interface layer (Ti_3AlN (111)). Samples #2-#4, show a decrease in nitrogen deficiency with higher growth temperatures, except sample #5, which is most nitrogen deficient.

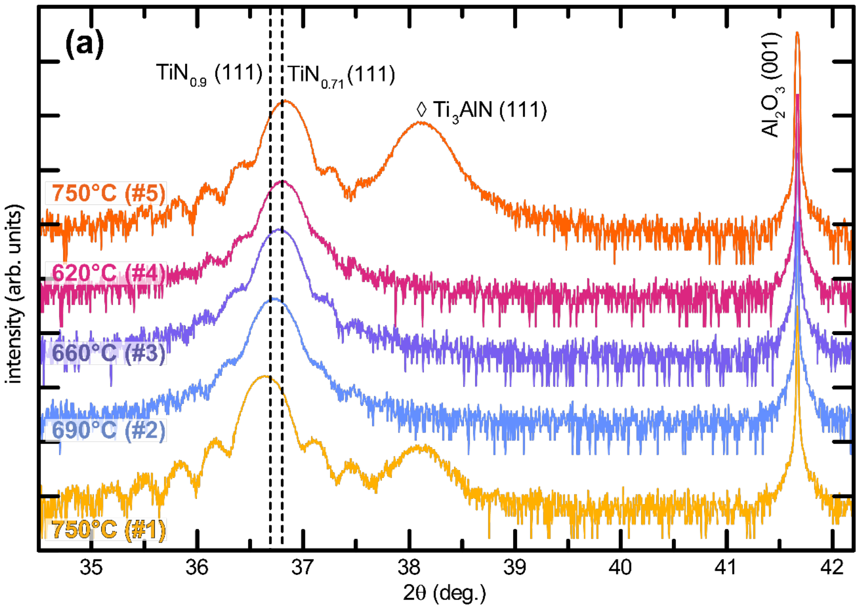

Figure 12-17: TiN thin films grown on *c*-cut sapphire (Al_2O_3 (001)) using reactive molecular beam epitaxy (RMBE) show higher nitrogen deficiencies at higher growth temperatures (samples #2-#5) which can be counteracted by increasing the Ti evaporation rate (sample #1). Growth at 750 °C results in the creation of an interfacial layer (Ti_3AlN) between TiN and *c*-cut sapphire. Literature values for $TiN_{0.71}$ and $TiN_{0.9}$ are taken from [153] and [73], respectively, and are shown as dashed lines. Reprinted under a CC-BY-NC-ND 4.0 from [2], © 2022 American Chemical Society.

A decrease in nitrogen deficiency for sample #2-#4 is also visible in the XRR curves shown in Figure 12-18 by a shift of the critical angle. The dashed line, as a guide, highlights, that the critical angle shifts towards higher 2θ values because of an increase in density (higher nitrogen content). For samples #1 and #5, the additional Ti_3AlN layer dampens the oscillations near the critical angle. In addition, growth at 750 °C (sample #1 and #5) results in low surface roughness as oscillations are still present for high 2θ values.

The type of texture (see also Figure 11-11) of the TiN_{1-x} thin films was investigated by performing ϕ-scans shown in Figure 12-19. The presence of six in-plane peaks indicates a biaxial texture with two 60° in-plane rotated domains. This is because in a cubic phase like TiN_{1-x}, a (111) out-of-plane orientation should result in three {111} in-plane peaks for each in-plane locked crystal orientation (see also Figure 11-16).

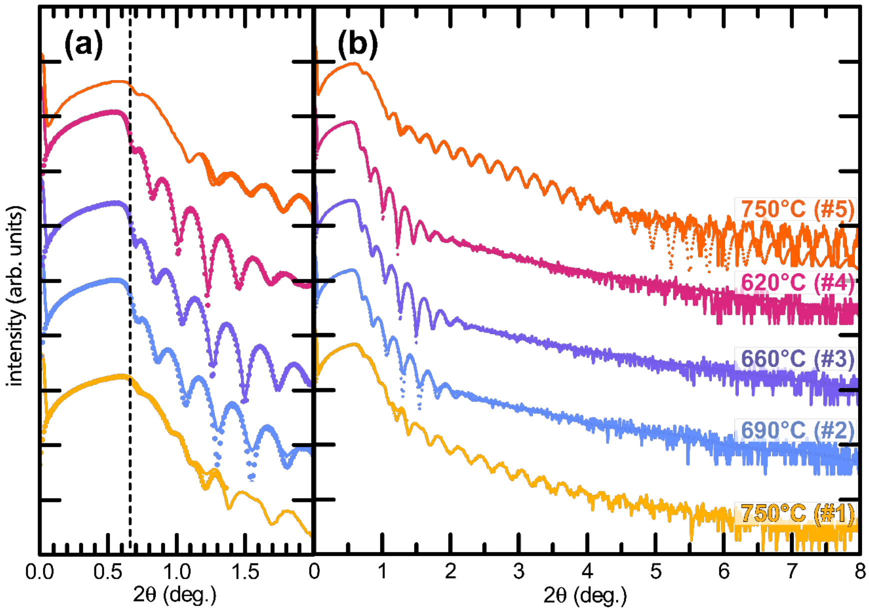

Figure 12-18: (a) A decrease in nitrogen deficiency, as a result of an increase in growth temperature (samples #2-#4), shifts the critical angle (indicated by the dotted line), shown by the X-ray reflectivity (XRR) curves, towards higher 2θ values. (b) XRR curves of samples grown at the highest growth temperature (#1 and #5) show oscillations up to 6° and 8°, respectively, due to low surface roughness. Reprinted under a CC-BY-NC-ND 4.0 from [2], © 2022 American Chemical Society.

To examine how these TiN_{1-x} {111}in-plane orientations align with the in-plane orientations of the substrate, an additional ϕ-scan of the substrate is shown in Figure 12-19. This ϕ-scan is performed at a fixed 2θ of the Al_2O_3 $\{\bar{1}02\}$ and not of the Al_2O_3 {001} present in the 2θ/ω scan (81). This is because then the sample can be tilted to χ = ~57° (and not to χ = ~90°) to access the $\{\bar{1}02\}$ in-plane orientations with a detectable XRD signal. As depicted in Figure 12-20, *c*-cut Al_2O_3 has six R-planes. The lattice planes in this hexagonal system are given by the hexagonal Miller-Bravais notation (hkil), which in principle is $(\bar{1}02)$. The ϕ-scan, however, only shows three peaks of the $\{\bar{1}02\}$ lattice planes and not six. This is because, i.e., a (102) lattice plane is 180° rotated along the c-axis to the $(\bar{1}02)$ which is why at a tilt of χ =

~ + 57° only one of each plane can be detected. If the sample were tilted to $\chi = \sim -57°$ (or turned upside-down), the other respective lattice plane could be detected. The three Al_2O_3 $\{\bar{1}02\}$ in-plane peaks are offset by ±30° with respect to the TIN_{1-x} {111} in-plane peaks. Because the three Al_2O_3 are representative of the edges of the hexagonal unit cell, the TiN_{1-x} {111} in-plane orientations align with the corners (i.e., a_1, a_2, a_3, Figure 12-20).

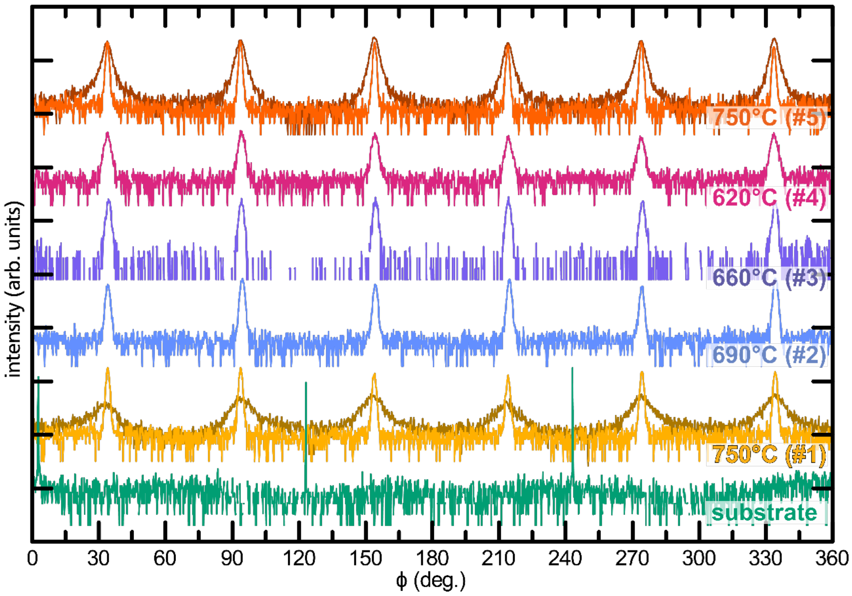

Figure 12-19: The ϕ-scans at a fixed 2θ value of the (111) TiN_{1-x} peak ($\chi = \sim 71°$) show six peaks as a result of two 60° in-plane rotated domains (schematically shown in Figure 9-16). For samples #1 and #5, additional phi scans shown in a darker color were acquired for the additional peak (Ti_3AlN (111)) in the XRD patterns (Figure 11-16). As shown by the six peaks, this Ti_3AlN interface layer has a similar biaxial texture as the TiN layer. The phi scan of the substrate (shown in green, 2θ value fixed to Al_2O_3 (-102), $\chi = \sim 57°$) shows three peaks that are offset by ±30°. Reprinted under a CC-BY-NC-ND 4.0 from [2], © 2022 American Chemical Society.

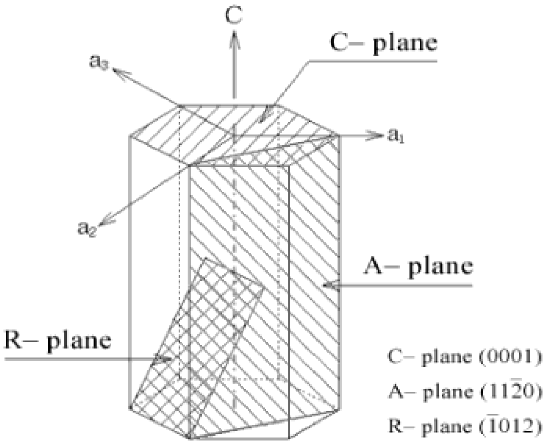

Figure 12-20: The rhombohedral crystal structure of sapphire (Al_2O_3) can be cut along different planes (C, A, and R), resulting in, i.e., *c*-cut sapphire, which is a hexagonally symmetric lattice. Reprinted under a CC BY 4.0 DEED from [154], © 2021 Kai Trepka.

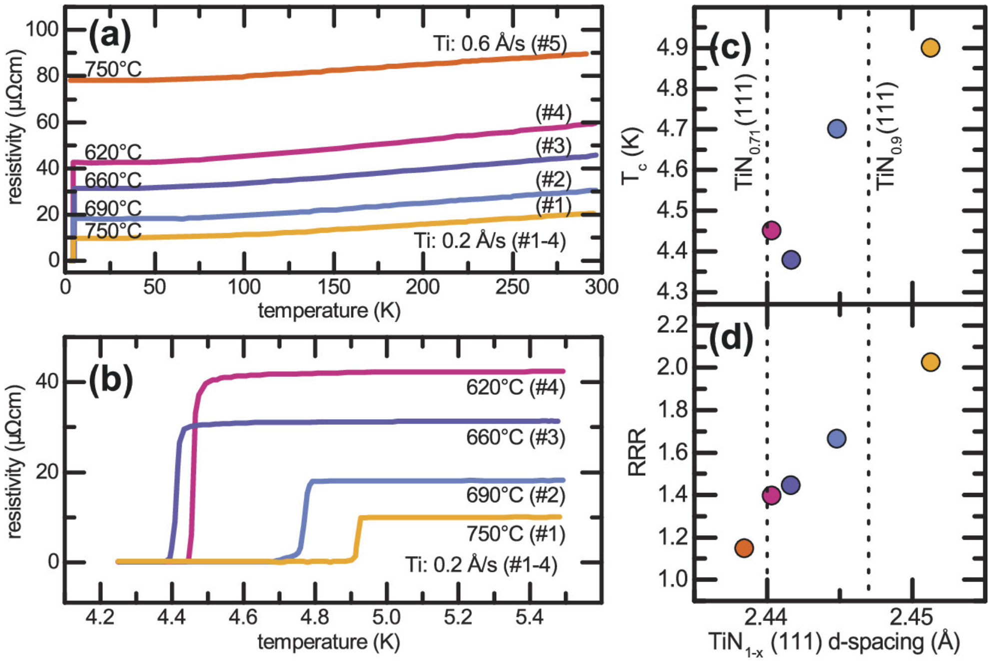

Figure 12-21: (a) Four-probe resistivity measurements during cooling with liquid He. (b) Selected temperature range to reveal the critical temperature (T_c). (c) T_c's and (d) residual resistance ratios ($RRR = \rho(300\ K)/\rho(10\ K)$) are plotted as a function of the TiN_{1-x} (111) d-spacing calculated from TiN_{1-x} (111) 2θ peak positions retrieved from the X-ray diffraction patterns shown in Figure 12-17. Reprinted under a CC-BY-NC-ND 4.0 from [2], © 2022 American Chemical Society.

To investigate the conductivity of the samples, four gold patches were sputtered onto the surface to measure the resistivity by using the four-probe method. Because TiN is also used in superconducting applications, the resistivity was not only measured at room temperature, but also as a function of temperature to investigate the critical temperature. Figure 12-21 (a) shows the entire temperature range, and Figure 12-21 (b) shows the range around the transition. To correlate the stoichiometry to the conductivity, Figure 12-21 (c) shows the critical temperature (T_c) and Figure 12-21 (d) the residual resistance ratio (RRR), both as a function of the TiN_{1-x} (111) d-spacing retrieved from the 2θ peak positions. RRR is calculated by dividing the resistance at 300 K with the resistance at 10 K ($RRR = \rho(300\ K)/\rho(10\ K)$). Both T_c and RRR scale linearly with stoichiometry: the most stoichiometric film (#1, yellow) has the highest T_c of 4.9 K and the highest RRR of 2.0. The most deficient thin film (#5, orange) has the lowest RRR and shows no T_c (or a T_c below the temperature of liquid helium (used for cooling), which is 4.2 K). In addition to the loss of superconductivity, the most deficient film has a resistivity at 10 K that is twice as high compared to sample #4. At this temperature, (thermal) phonon scattering is greatly reduced [155]; thus, conductivity is an indirect measure of the defect density, which, in this case, should be governed by the nitrogen deficiency. However, unlike sample #1-#4, where $\rho(10\ K)$ changes ~10 $\mu\Omega$cm per sample, the doubling in resistivity for sample #5 compared to #4 does not reflect the relatively minor change in stoichiometry. Therefore, the introduced volume defects cannot be the only source of defects that impact conductivity.

Another source of defects are GBs, which should be present in the TiN$_{1-x}$ thin films due to the biaxial texture. According to the out- and in-plane XRD measurements, all samples should have a similar microstructure. However, when investigating GBs by backscatter electron (BSE) imaging, as shown in Figure 12-22, only the most deficient thin film (sample #5) shows GBs as meandering dark lines. In general, a GB should result in less BSE due to defects, and all samples should have grain boundaries. Therefore, ICCI (see also Chapter 11.4) was used to visualize the microstructure, as shown in Figure 12-23. For these images, the TiN$_{1-x}$ {200} in-plane lattice planes were used for two reasons: first, a low index plane, i.e., (200) planes of grain I, would be simultaneously imaged with i.e., $(\bar{1}22)$ planes of grain II, which yields a high SE contrast. Second, accessing the TiN$_{1-x}$ {111} planes would not be possible because of the tilt limitations of the JEOL JIB-4600F. Due to the 53° tilt of the FIB column, the incidence angle at a stage tilt of 0° is already 53°. To achieve the required incident angle of 71° (similar to χ in XRD), the sample stage must be tilted to -18°, which exceeds the limit (-10°).

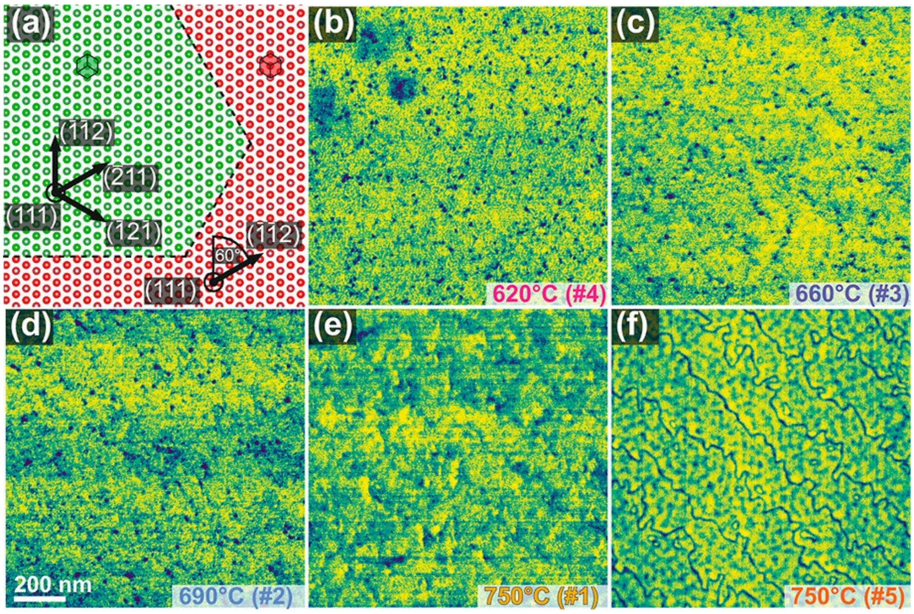

Figure 12-22: (b-f) The surface (top view) of the TiN$_{1-x}$ layers is imaged by backscattered electron (BSE) microscopy. A BSE signal contains atomic number and crystallographic (orientation contrast electron channeling) contrast [156]. Because all thin films are textured (every grain has the same out-of-plane orientation), the BSE contrast should only contain information about the local stoichiometry. Defects, which are present at grain boundaries (GBs), lower the BSE yield and are only visible in the most nitrogen-deficient sample (f, #5). The "meandering" of these GBs follow a set of three dominant orientations that correspond to the twin boundaries ((a), dashed lines). Samples #2-#4 show dark spots due to a higher surface roughness. Reprinted under a CC-BY-NC-ND 4.0 from [2], © 2022 American Chemical Society.

The ICC images shown in Figure 12-23 (b-c) reveal that all samples indeed have a similar microstructure with elongated grains. The anisotropy of grain size (100 nm in one direction, several cm in the other direction) is a result of step flow growth (see also Figure 11-10) due to surface steps, which can even be present in nominally 0° miscut substrates [157]. These initial surface steps (due to miscut), schematically augmented for visualization in Figure 12-24, will bunch because of sample heating during RMBE growth before deposition of the TiN_{1-x} layer. The uniform step widths and heights affect the seeding condition [158] and thus the final grain boundary density. Although the microstructure and the GB density are virtually the same for all samples, only the GBs in the most deficient sample (#5) are visible by BSE imaging. To investigate a difference in the type of GB, cross-sectional TEM lamellae across a GB were prepared from sample #5 and the most stoichiometric sample (#1), as schematically shown by red lines in Figure 12-23 (e, f). The corresponding atomic HAADF-STEM images are shown in Figure 11-25. Both images show a $\{\bar{1}2\bar{1}\}$ twin boundary. For sample #1 (Figure 12-25 (a)), defects are located at the boundary itself. However, for sample #5 (Figure 11-25 (b)), an extended defect structure is visible, as emphasized by blue arrows as a result of stacking faults along the growth direction ((111) direction). These stacking faults extend up to the surface of the thin film, causing the observed change in BSE contrast.

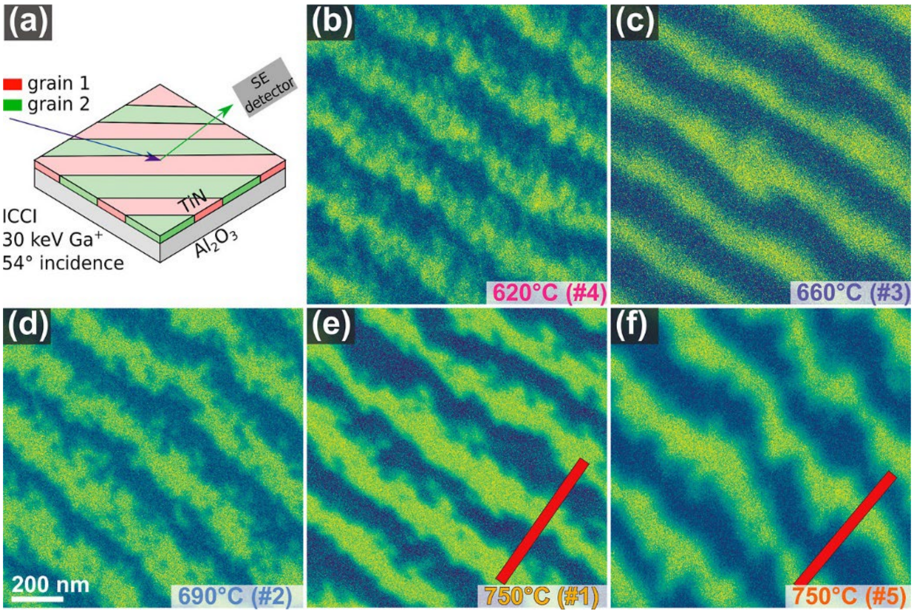

Figure 12-23: (a) Ion channeling contrast (ICC) images were acquired with an incidence angle of 54°. (b-f) All ICC images show a similar grain structure with comparable grain sizes. (e, f) To investigate the GBs, cross-sectional electron transparent lamellae were prepared across the GBs (represented by red lines) for transmission electron microscopy. Reprinted under a CC-BY-NC-ND 4.0 from [2], © 2022 American Chemical Society.

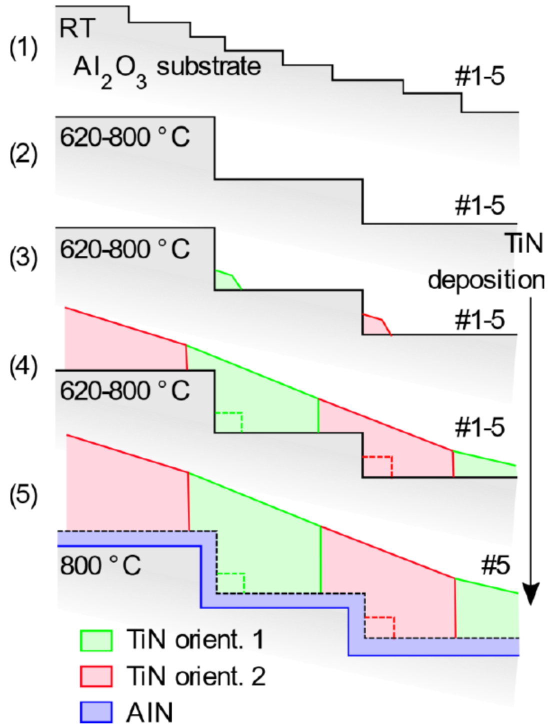

Figure 12-24: (1) Al_2O_3 substrate miscut can create small surface steps, which can bunch (2) during annealing. (3) These terraces affect the seeding during TiN thin film growth. (4) The uniform step width and height lead to a consistent alteration of in-plane orientations (green and red). (5) Annealing at or above 800 °C leads to the formation of an AlN interface layer. Reprinted under a CC BY-NC-SA 4.0 DEED from [103], © 2022 Alexander Zintler.

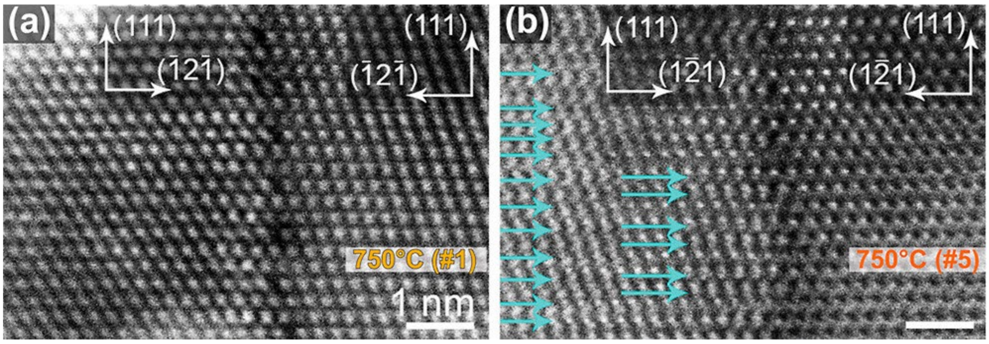

Figure 12-25: High-angle annular dark-field scanning transmission electron microscopy (HAADF-STEM) images of grain boundaries of the (a) most stoichiometric and (b) most nitrogen-deficient TiN_{1-x} thin film. Blue arrows denote the extended defect structure shown by the split atomic columns. Reprinted under a CC-BY-NC-ND 4.0 from [2], © 2022 American Chemical Society.

12.3.2. Presentation of own contribution

TiN thin film growth, 2θ/ω scans, and temperature-dependent resistivity measurements were carried out by Dr. Sankaramangalam Ulhas Sharath. Dr. Enrico Bruder, in the presence of Dr. Alexander Zintler and me, acquired the BSE maps. I have acquired the ϕ-scans and suggested investigating the microstructure via ICCI (analogous to in-plane XRD measurements), which Dr. Alexander Zintler and I have acquired. Dr. Alexander Zintler prepared the electron-transparent lamellae and acquired the HAADF-STEM images. Dr. Alexander and I prepared the manuscript. Dr. Stefan Petzold and Dr. Nico Kaiser contributed to the discussion of the results and proofreading of the manuscript. Prof. Dr. Leopoldo Molina-Luna provided support for all results related to electron microscopy, and Prof. Dr. Lambert Alff provided support for all results related to electrical characterization.

13. Conclusion

This PhD work has aimed to combine synthesis, macroscopic and microscopic investigation, and device characterization to bridge the information gaps required to further oxide electronics. Reactive Molecular Beam Epitaxy (RMBE), among other Physical Vapor Deposition (PVD) techniques, can precisely fabricate high-quality semiconductor heterostructures necessary for complex oxide electronics. Typically, RMBE is used to grow epitaxial thin films, yet textured thin films with defects might be more promising. Their composition and crystallinity can be engineered through careful selection of growth parameters; however, they are subject to the underlying layer. Here, miscut, composition, and lattice mismatch impact texture transfer and thus the resulting microstructure. Analogous to building a house, a poorly engineered foundation will ultimately prevent the consecutively built floors from being perfect. In a memristive system, where a device consists of a metal-insulator-metal (MIM) structure, the developed texture of the first metal layer, impacted by the substrate, will subsequently impact the texture of the next insulator layer. Therefore, it is indispensable to inspect how texture develops in each layer and how the developed texture impacts the device's performance.

The first metal layers with potential use in MIM structures of memristive devices were 23 nm TiN_{1-x} thin films grown on *c*-cut sapphire with varying nitrogen deficiencies. All thin films developed a biaxial texture with a (111) out-of-plane and two in-plane orientations. Ion channeling contrast imaging (ICCI) revealed a similar microstructure and grain boundary

(GB) density for all thin films with an elongated grain structure. This anisotropy of grain size can be attributed to the miscut of the substrate (*c*-cut sapphire). Only the TiN_{1-x} thin film with the highest nitrogen deficiency ($TiN_{0.71-x}$) resulted in GB dissociation by stacking faults (extended defect structure). Such TiN_{1-x} thin films are advantageous as an ohmic bottom electrode in a valence change memory memristive device, as the dissociated GBs with a localized high density of defects can incorporate oxygen necessary for device operation.

These types of TiN_{1-x} layers were the foundation for engineering textures in stoichiometric HfO_2 thin films, which are used as the insulating layer in MIM structures of memristive devices.

First, HfO_2 thin films were grown at elevated temperatures using RMBE. By changing the oxidation conditions, these thin films can be grown with either a distinct (001) or $(11\bar{1})$ texture on (111) textured TiN_{1-x}. The texture transfer induces a specific type of GB, which impacts the V_F of the memristive devices. Devices with (001) textured HfO_2 show relatively high V_F, unlike devices with $(11\bar{1})$ HfO_2. The $(11\bar{1})$ HfO_2 devices are considered forming-free, as the required V_F is in the range of the standard operational voltages. First-principles calculations based on density functional theory (DFT) relaxed atomic structures retrieved from atomic images of the different types of GB were used to correlate the GB atomic structure to the difference in V_F. Negative neutral oxygen vacancy (V_O) segregation energies (E_{seg}) at high-index GBs present in $(11\bar{1})$ HfO_2 indicate that this type of GB acts as a sink for V_O. Therefore, this type of GB can be identified as the preferential pathway for conductive filament formation due to the presence of pre-existing V_O, which explains the observed low V_F.

Second, HfO_2 thin films were grown at room temperature on (111) textured TiN_{1-x} using RMBE to observe the microstructure evolution of amorphous HfO_2 during in situ transmission electron microscopy (TEM) and 4D-scanning TEM (4D-STEM) annealing. This allowed us to investigate the exact transition temperature and origins of grain growth with nanometer precision. The in-between Pt and TiN_{1-x} sandwiched amorphous HfO_2 layer started to crystallize into the monoclinic phase at 180 °C, non-adjacent to an interface. Only when growing grains are adjacent to an interface does a distinct crystallinity (texture) develop. The developed mixed monoclinic $(11\bar{1} + 001)$ texture was confirmed by annealing a macroscopic device at 180 °C. The developed texture improves the device's performance by lowering the forming voltage (V_F) from -6.1 V, for a memristive device with amorphous HfO_2, to -4.2 V.

14. Outlook

14.1. Grain boundary density

The ideal lateral size of a memristive device is a balance between the technological capabilities, the desired memory density, and the specific application requirements [159, 160], which typically ranges from a few tens of nanometers to about 50 nm. In the case of VCM RRAM devices, the ohmic electrode must be oxidizable, which can be achieved by having GBs with an extended defect structure. For this PhD work, the TiN_{1-x} thin films that are used as the ohmic electrode were grown with a grain boundary density of ~ 100 nm. The investigated devices with a lateral size in the range of several micrometers (see also Figure 11-7) would therefore cover several TiN_{1-x} GBs. However, nanometer-sized devices could be positioned above a TiN_{1-x} grain and not a GB, which should negatively impact the device's resistive switching performance. The first results indicated that the GB density can be altered by changing the growth temperature. But also the choice of substrate batch, which might have different miscuts, can impact the GB density [103]. Therefore, optimizing TiN_{1-x} thin film growth should not only be based on the stoichiometry, the texture, and the roughness, but also on the resulting grain arrangement and GB density.

14.2. Impact of adjacent electrodes on microstructure evolution

Although in situ TEM and 4D-STEM could provide insights into how the microstructure develops, it is still unclear why a mixed $(11\bar{1} + 001)$ HfO_2 texture develops and why grain growth does not start adjacent to an interface layer. Understanding how to alter the development of a certain texture, either by changing the layer thickness or stoichiometry of the insulating layer, by changing the adjacent electrodes (different material, different stoichiometry, different texture), by having a distinct annealing profile (within the temperature budget of the CMOS BEOL process), by annealing in a certain atmosphere, or by using a different PVD method for thin films, could provide more insights into how to engineer a texture. Moreover, understanding how the developed texture impacts the device's performance could lead to more reliable and efficient devices.

14.3. Confining conductive filament formation during in situ biasing

Investigating the fundamental working mechanism of RRAM devices is still one of the greatest challenges. The most prominent examples that claim to have visualized the conductive filament during resistive switching operations are from 2012 [161] and 2013 [162], which are also included in several review articles [163–166]. However, these experimental findings could not be reproduced. A progress report written by numerous relevant contributors to the RRAM community has concluded: "*During the past ten years a large number of RS studies have been reported. Unfortunately, we observed that many of them: i) do not provide enough information to reproduce the experiments, ii) use device structures that are not relevant/realistic from a technological point of view, iii)omit essential figures of merit, or iv) make claims that are not well supported by rigorous experimental or computational data.*" [167]

The formation of a conductive filament is a result of a dielectric breakdown (DB). A novel approach to visualize this DB is in situ STEM electron beam-induced current (EBIC) imaging. Collecting the electronic signature allows for local detection of changes in the conductivity (with high spatial resolution) [168] and, in combination with standard STEM imaging, provides the necessary support when observing the RS mechanism.

In this example, the CF formation is confined by using a slant vertical device structure which is different to the cross-sectional lamellae investigated in this PhD work. For these devices, CF formation is, in principle, not confined to a specific location and could appear random without being able to visualize the RS phenomena. Only locally confining the CF formation in a realistic RRAM device and identifying the most likely location for CF formation would allow investigating CF during in situ TEM biasing. With the knowledge that the GB density of TiN can be tuned by the *c*-cut sapphire misfit (and temperature) and that distinct GB types can be engineered by texture transfer during growth or in situ annealing, we would be able to engineer an ideal thin film structure as schematically depicted in Figure 12-1. Deliberately creating a HfO_2 GB on top of a TiN GB should therefore confine the CF formation.

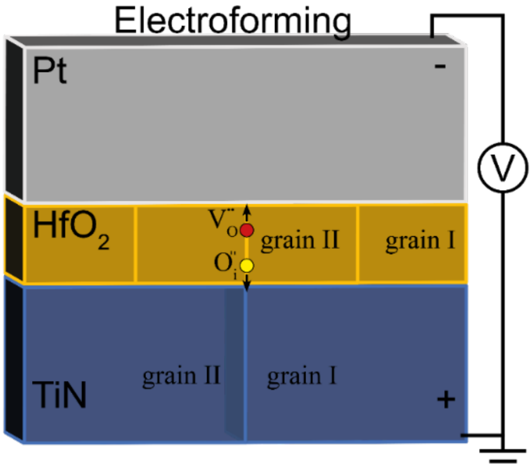

Figure 14-1: Conductive filament formation (consisting of oxygen vacancies (V_O)) in a valence change memory (VCM) memristive device should occur at a HfO_2 grain boundary (GB), which is located on top of a TIN GB that can incorporate the oxygen interstitials (O_i).

15. References

1. Winkler R, Zintler A, Petzold S, et al (2022) Controlling the Formation of Conductive Pathways in Memristive Devices. Adv Sci 9:2201806. https://doi.org/10.1002/advs.202201806

2. Zintler A, Eilhardt R, Petzold S, et al (2022) Enhanced Conductivity and Microstructure in Highly Textured TiN1–x/c-Al2O3 Thin Films. ACS Omega 7:2041–2048. https://doi.org/10.1021/acsomega.1c05505

3. Winkler R, Zintler A, Recalde-Benitez O, et al (2024) Texture Transfer in Dielectric Layers via Nanocrystalline Networks: Insights from in Situ 4D-STEM. Nano Lett. https://doi.org/10.1021/acs.nanolett.3c03941

4. deutschlandfunkkultur.de Rechenzentren - Riesiges Potenzial für Abwärmenutzung. In: Dtschl. Kult. https://www.deutschlandfunkkultur.de/rechenzentrum-abwaerme-nutzung-100.html. Accessed 8 Mar 2024

5. Winter T, Frankfurt (2016) Stromverbrauch: Data-Center hängen Airport ab. FAZ.NET

6. Schroeder U, Cho K, Slesazeck S (2015) Materials for DRAM Memory Cell Applications. In: Thin Films on Silicon. WORLD SCIENTIFIC, pp 369–401

7. Ahmed KMU, Bollen MHJ, Alvarez M (2021) A Review of Data Centers Energy Consumption and Reliability Modeling. IEEE Access 9:152536–152563. https://doi.org/10.1109/ACCESS.2021.3125092

8. Meena JS, Sze SM, Chand U, Tseng T-Y (2014) Overview of emerging nonvolatile memory technologies. Nanoscale Res Lett 9:526. https://doi.org/10.1186/1556-276X-9-526

9. Jeong DS, Kim KM, Kim S, et al (2016) Memristors for Energy-Efficient New Computing Paradigms. Adv Electron Mater 2:1600090. https://doi.org/10.1002/aelm.201600090

10. dcadmin (2015) Rebooting the IT Revolution: A Call to Action. In: Semicond. Ind. Assoc. https://www.semiconductors.org/resources/rebooting-the-it-revolution-a-call-to-action-2/. Accessed 19 Feb 2024

11. Huang Y, Li S, Yang Y, Chen C (2023) Progress on Memristor-Based Analog Logic Operation. Electronics 12:2486. https://doi.org/10.3390/electronics12112486

12. Chen A (2016) A review of emerging non-volatile memory (NVM) technologies and applications. Solid-State Electron 125:25–38. https://doi.org/10.1016/j.sse.2016.07.006

13. Im IH, Kim SJ, Jang HW (2020) Memristive Devices for New Computing Paradigms. Adv Intell Syst 2:2000105. https://doi.org/10.1002/aisy.202000105

14. Yu Y, Xiao M, Fieser D, et al (2024) Nanoscale memristor devices: materials, fabrication, and artificial intelligence. J Mater Chem C. https://doi.org/10.1039/D3TC04510B

15. Bao H, Zhou H, Li J, et al (2022) Toward memristive in-memory computing: principles and applications. Front Optoelectron 15:23. https://doi.org/10.1007/s12200-022-00025-4

16. Aguirre F, Sebastian A, Le Gallo M, et al (2024) Hardware implementation of memristor-based artificial neural networks. Nat Commun 15:1974. https://doi.org/10.1038/s41467-024-45670-9

17. Liu T-Y, Yan TH, Scheuerlein R, et al (2013) A 130.7mm2 2-layer 32Gb ReRAM memory device in 24nm technology. In: 2013 IEEE International Solid-State Circuits Conference Digest of Technical Papers. pp 210–211

18. AG IT 32-bit TriCore^{TM} AURIX^{TM}– TC4x | Infineon's AURIX^{TM} TC4x family of microcontrollers - a leader in real-time safety and security performance is coming! - Infineon Technologies. https://www.infineon.com/cms/en/product/microcontroller/32-bit-tricore-microcontroller/32-bit-tricore-aurix-tc4x/. Accessed 8 Mar 2024

19. Dearnaley G, Stoneham AM, Morgan DV (1970) Electrical phenomena in amorphous oxide films. Rep Prog Phys 33:1129–1191. https://doi.org/10.1088/0034-4885/33/3/306

20. Oxley DP (NaN/NaN/NaN) Electroforming, Switching and Memory Effects in Oxide Thin Films. Act Passive Electron Compon 3:217–224. https://doi.org/10.1155/APEC.3.217

21. Pagnia H, Sotnik N (1988) Bistable switching in electroformed metal–insulator–metal devices. Phys Status Solidi A 108:11–65. https://doi.org/10.1002/pssa.2211080102

22. Asamitsu A, Tomioka Y, Kuwahara H, Tokura Y (1997) Current switching of resistive states in magnetoresistive manganites. Nature 388:50–52. https://doi.org/10.1038/40363

23. Beck A, Bednorz JG, Gerber Ch, et al (2000) Reproducible switching effect in thin oxide films for memory applications. Appl Phys Lett 77:139–141. https://doi.org/10.1063/1.126902

24. Szot K, Speier W, Bihlmayer G, Waser R (2006) Switching the electrical resistance of individual dislocations in single-crystalline SrTiO3. Nat Mater 5:312–320. https://doi.org/10.1038/nmat1614

25. Strukov DB, Snider GS, Stewart DR, Williams RS (2008) The missing memristor found. Nature 453:80–83. https://doi.org/10.1038/nature06932

26. Chua LO, Kang SM (1976) Memristive devices and systems. Proc IEEE 64:209–223. https://doi.org/10.1109/PROC.1976.10092

27. Chua L (1971) Memristor-The missing circuit element. IEEE Trans Circuit Theory 18:507–519. https://doi.org/10.1109/TCT.1971.1083337

28. Chua L (2011) Resistance switching memories are memristors. Appl Phys A 102:765–783. https://doi.org/10.1007/s00339-011-6264-9

29. Dittmann R, Menzel S, Waser R (2021) Nanoionic memristive phenomena in metal oxides: the valence change mechanism. Adv Phys 70:155–349. https://doi.org/10.1080/00018732.2022.2084006

30. Jabeen S, Ismail M, Rana AM, Ahmed E (2017) Impact of work function on the resistive switching characteristics of M/ZnO/CeO2/Pt devices. Mater Res Express 4:056401. https://doi.org/10.1088/2053-1591/aa6dec

31. Waser R (2012) Redox-Based Resistive Switching Memories. J Nanosci Nanotechnol 12:7628–7640. https://doi.org/10.1166/jnn.2012.6652

32. Yu S, Guan X, Wong H-SP (2011) Conduction mechanism of TiN/HfOx/Pt resistive switching memory: A trap-assisted-tunneling model. Appl Phys Lett 99:063507. https://doi.org/10.1063/1.3624472

33. Chiu F-C (2014) A Review on Conduction Mechanisms in Dielectric Films. Adv Mater Sci Eng 2014:e578168. https://doi.org/10.1155/2014/578168

34. Fu YJ, Xia FJ, Jia YL, et al (2014) Bipolar resistive switching behavior of La0.5Sr0.5CoO3−σ films for nonvolatile memory applications. Appl Phys Lett 104:223505. https://doi.org/10.1063/1.4881720

35. Lim EW, Ismail R (2015) Conduction Mechanism of Valence Change Resistive Switching Memory: A Survey. Electronics 4:586–613. https://doi.org/10.3390/electronics4030586

36. Chang Y-F, Fowler B, Chen Y-C, et al (2014) Intrinsic SiOx-based unipolar resistive switching memory. II. Thermal effects on charge transport and characterization of multilevel programing. J Appl Phys 116:043709. https://doi.org/10.1063/1.4891244

37. Wang C, Wu H, Gao B, et al (2018) Conduction mechanisms, dynamics and stability in ReRAMs. Microelectron Eng 187–188:121–133. https://doi.org/10.1016/j.mee.2017.11.003

38. Salaoru I, Khiat A, Li Q, et al (2013) Pulse-induced resistive and capacitive switching in TiO2 thin film devices. Appl Phys Lett 103:233513. https://doi.org/10.1063/1.4840316

39. Acharyya D, Hazra A, Bhattacharyya P (2014) A journey towards reliability improvement of TiO2 based Resistive Random Access Memory: A review. Microelectron Reliab 54:541–560. https://doi.org/10.1016/j.microrel.2013.11.013

40. Pan T-M, Lu C-H (2013) Structural properties and electroforming-free resistive switching characteristics of GdOx, TbOx, and HoOx memory devices. Mater Chem Phys 139:437–442. https://doi.org/10.1016/j.matchemphys.2013.01.015

41. Hermes C, Bruchhaus R, Waser R (2011) Forming-Free TiO_2-Based Resistive Switching Devices on CMOS-Compatible W-Plugs. IEEE Electron Device Lett 32:1588–1590. https://doi.org/10.1109/LED.2011.2166371

42. Sharath SU, Bertaud T, Kurian J, et al (2014) Towards forming-free resistive switching in oxygen engineered HfO_{2-x}. Appl Phys Lett 104:063502. https://doi.org/10.1063/1.4864653

43. Sharath SU, Kurian J, Komissinskiy P, et al (2014) Thickness independent reduced forming voltage in oxygen engineered HfO2 based resistive switching memories. Appl Phys Lett 105:073505. https://doi.org/10.1063/1.4893605

44. Sharath SU, Joseph MJ, Vogel S, et al (2016) Impact of oxygen stoichiometry on electroforming and multiple switching modes in TiN/TaOx/Pt based ReRAM. Appl Phys Lett 109:173503. https://doi.org/10.1063/1.4965872

45. Sharath SU, Vogel S, Molina-Luna L, et al (2017) Control of Switching Modes and Conductance Quantization in Oxygen Engineered HfOx based Memristive Devices. Adv Funct Mater 27:1700432. https://doi.org/10.1002/adfm.201700432

46. Petzold S, Zintler A, Eilhardt R, et al (2019) Forming-Free Grain Boundary Engineered Hafnium Oxide Resistive Random Access Memory Devices. Adv Electron Mater 5:1900484

47. Gao DZ, Strand J, Munde MS, Shluger AL (2019) Mechanisms of Oxygen Vacancy Aggregation in SiO2 and HfO2. Front Phys 7:. https://doi.org/10.3389/fphy.2019.00043

48. Bradley SR, Shluger AL, Bersuker G (2015) Electron-Injection-Assisted Generation of Oxygen Vacancies in Monoclinic ${\mathrm{HfO}}_{2}$. Phys Rev Appl 4:064008. https://doi.org/10.1103/PhysRevApplied.4.064008

49. Bersuker G, Yum J, Iglesias V, et al (2010) Grain boundary-driven leakage path formation in HfO2 dielectrics. In: 2010 Proceedings of the European Solid State Device Research Conference. pp 333–336

50. Young-Fisher KG, Bersuker G, Butcher B, et al (2013) Leakage Current-Forming Voltage Relation and Oxygen Gettering in HfOx RRAM Devices. IEEE Electron Device Lett 34:750–752. https://doi.org/10.1109/LED.2013.2256101

51. Bäumer C, Dittmann R (2018) 20 - Redox-based memristive metal-oxide devices. In: Pryds N, Esposito V (eds) Metal Oxide-Based Thin Film Structures. Elsevier, pp 489–522

52. Yu S, Lee B, Wong H-SP (2012) Metal Oxide Resistive Switching Memory. In: Wu J, Cao J, Han W-Q, et al (eds) Functional Metal Oxide Nanostructures. Springer, New York, NY, pp 303–335

53. Waser R (2012) Nanoelectronics and Information Technology: Advanced Electronic Materials and Novel Devices. John Wiley & Sons

54. Hildebrandt EM (2012) Oxygen Engineered Hafnium Oxide Thin Films grown by Reactive Molecular Beam Epitaxy. Dissertation, Technische Universität

55. HM2 Series Single Pocket e-Gun$^{\mathrm{TM}}$ – Thermionics Laboratory Incorporated. https://thermionics.com/product/the-hanks-hm2-single-crucible-single-emitter-e-gun/. Accessed 19 Mar 2024

56. Electron Beam Evaporator EBV - Dr. Eberl MBE-Komponenten GmbH. https://www.mbe-komponenten.de/products/mbe-components/e-beam-evaporators/ebv.php. Accessed 19 Mar 2024

57. Yamada Y, Harada T, Uyama H, et al (2000) Low-temperature deposition of optical films by oxygen radical beam-assisted evaporation. Thin Solid Films 377–378:92–96. https://doi.org/10.1016/S0040-6090(00)01390-0

58. Madou MJ (2018) Fundamentals of Microfabrication and Nanotechnology, Three-Volume Set, 3rd ed. CRC Press, Boca Raton

59. Zaouk R, Park BY, Madou MJ (2006) Introduction to Microfabrication Techniques. In: Minteer SD (ed) Microfluidic Techniques: Reviews and Protocols. Humana Press, Totowa, NJ, pp 5–15

60. Thornton JA (1973) Sputter Coating-Its Principles and Potential. p 730544

61. Lueke JS (2014) A MEMS-based Fixed-Fixed Folded Spring Piezoelectric Energy Harvester. In: ERA. https://era.library.ualberta.ca/items/77543089-2d79-4a4f-8ea0-4be21217f210. Accessed 19 Mar 2024

62. Eilhardt R, Zintler A, Recalde O, et al (2021) Birth of a grain boundary: In situ TEM Observation of the Microstructure Evolution in HfO2 Based Memristors. Microsc Microanal 27:1238–1239. https://doi.org/10.1017/S1431927621004645

63. Mohamad Hadis NS, Manaf AA, Rahman MFA, et al (2020) Fabrication and Characterization of Simple Structure Fluidic-Based Memristor for Immunosensing of NS1 Protein Application. Biosensors 10:143. https://doi.org/10.3390/bios10100143

64. Dhanaraj G, Byrappa K, Prasad V, Dudley M (2010) Springer Handbook of Crystal Growth. Springer Berlin Heidelberg, Berlin, Heidelberg

65. Kaiser N (2002) Review of the fundamentals of thin-film growth. Appl Opt 41:3053–3060. https://doi.org/10.1364/AO.41.003053

66. Herman MA, Richter W, Sitter H (2004) Epitaxy: Physical Principles and Technical Implementation. Springer Berlin Heidelberg, Berlin, Heidelberg

67. Groves JR, Clemens BM, Nix WD, Salleo A (2010) Ion-beam texturing at nucleation: investigation of the fundamental mechanism of biaxial texture development in ion beam assisted deposition and applications

68. X-ray thin-film measurement techniques V. X-ray reflectivity measurement | Rigaku Global Website. https://www.rigaku.com/journal/summer-2010-volume-26-no-2/01-09. Accessed 2 Apr 2024

69. Harrington GF, Santiso J (2021) Back-to-Basics tutorial: X-ray diffraction of thin films. J Electroceramics 47:141–163. https://doi.org/10.1007/s10832-021-00263-6

70. (2024) Bragg law | Definition, Equation, Diagram, & Facts | Britannica. https://www.britannica.com/science/Bragg-law. Accessed 3 Apr 2024

71. Inaba K, Kobayashi S, Uehara K, et al (2013) High Resolution X-Ray Diffraction Analyses of (La,Sr)MnO3/ZnO/Sapphire(0001) Double Heteroepitaxial Films. Adv Mater Phys Chem 3:72–89. https://doi.org/10.4236/ampc.2013.31A010

72. X-ray Reflectometry | Covalent Metrology. https://covalentmetrology.com/service/x-ray-reflectometry-xrr/. Accessed 2 Apr 2024

73. Christensen A, An C (1978) The Temperature Factor Parameters of Some Transition Metal Carbides and Nitrides by Single Crystal X-ray and Neutron Diffraction. Temp Factor Parameters Some Transit Met Carbides Nitrides Single Cryst X-Ray Neutron Diffr

74. Momma K, Izumi F (2011) VESTA 3 for three-dimensional visualization of crystal, volumetric and morphology data. J Appl Crystallogr 44:1272–1276. https://doi.org/10.1107/S0021889811038970

75. Volkert CA, Minor AM (2007) Focused Ion Beam Microscopy and Micromachining. MRS Bull 32:389–399. https://doi.org/10.1557/mrs2007.62

76. AliceD (2014) Answer to "What's the smallest size a human eye can see?" Biol. Stack Exch.

77. Yao S, Li H, Pang S, et al (2021) A Review of Computer Microvision-Based Precision Motion Measurement: Principles, Characteristics, and Applications. IEEE Trans Instrum Meas 70:1–28. https://doi.org/10.1109/TIM.2021.3065436

78. Ul-Hamid A (2018) A Beginners' Guide to Scanning Electron Microscopy. Springer International Publishing, Cham

79. Ni C (2013) Scanning Electron Microscopy (SEM). In: Wang QJ, Chung Y-W (eds) Encyclopedia of Tribology. Springer US, Boston, MA, pp 2977–2982

80. Focussed Ion Beam FIB. In: Fraunhofer-Inst. Für Schicht- Oberflächentechnik IST. https://www.ist.fraunhofer.de/de/kompetenzen/analytik-prueftechnik/fib.html. Accessed 5 Apr 2024

81. Tseng AA (2004) Recent developments in micromilling using focused ion beam technology. J Micromechanics Microengineering 14:R15. https://doi.org/10.1088/0960-1317/14/4/R01

82. Whiting J, Yen L, Stanford N (2022) MyScope: Free online microscopy training resource – continuing development to reflect the current microscopy landscape. Micron 160:103319. https://doi.org/10.1016/j.micron.2022.103319

83. Zhang Z, Wang W, Dong Z, et al (2022) The Trends of In Situ Focused Ion Beam Technology: Toward Preparing Transmission Electron Microscopy Lamella and Devices at the Atomic Scale. Adv Electron Mater 8:2101401. https://doi.org/10.1002/aelm.202101401

84. Ruffilli R, Berkani M, Dupuy P, et al (2015) In-depth investigation of metallization aging in power MOSFETs. Microelectron Reliab 55:1966–1970. https://doi.org/10.1016/j.microrel.2015.06.036

85. Overwijk MHF, van den Heuvel FC, Bulle-Lieuwma CWT (1993) Novel scheme for the preparation of transmission electron microscopy specimens with a focused ion beam. J Vac Sci Technol B Microelectron Nanometer Struct Process Meas Phenom 11:2021–2024. https://doi.org/10.1116/1.586537

86. Giannuzzi LA, Kempshall BW, Schwarz SM, et al (2005) FIB Lift-Out Specimen Preparation Techniques. In: Giannuzzi LA, Stevie FA (eds) Introduction to Focused Ion Beams: Instrumentation, Theory, Techniques and Practice. Springer US, Boston, MA, pp 201–228

87. Mahne N, Čekada M, Panjan M (2022) Total and Differential Sputtering Yields Explored by SRIM Simulations. Coatings 12:1541. https://doi.org/10.3390/coatings12101541

88. Utke I, Hoffmann P, Melngailis J (2008) Gas-assisted focused electron beam and ion beam processing and fabrication. J Vac Sci Technol B Microelectron Nanometer Struct Process Meas Phenom 26:1197–1276. https://doi.org/10.1116/1.2955728

89. Lekstrom M, McLachlan MA, Husain S, et al (2008) Using the in situ lift-out technique to prepare TEM specimens on a single-beam FIB instrument. J Phys Conf Ser 126:012028. https://doi.org/10.1088/1742-6596/126/1/012028

90. Weber J, Roth G, Bosbach D (2017) Fundamental insights into the radium uptake into barite by atom probe tomography and electron microscopy. Forschungszentrum Jülich GmbH, Zentralbibliothek

91. Adabifiroozjaei E, Rastkerdar E, Nemoto Y, et al (2023) In-situ scanning transmission electron microscopy study of Al-amorphous SiO2 layer-SiC interface. J Mater Sci 58:2456–2468. https://doi.org/10.1007/s10853-023-08186-z

92. Hubbard WA (2023) Making Connections: Challenges and Opportunities for In Situ TEM Biasing. EDFA Tech Artic 25:4–8. https://doi.org/10.31399/asm.edfa.2023-1.p004

93. Recalde-Benitez O, Pivak Y, Jiang T, et al (2024) Weld-free mounting of lamellae for electrical biasing operando TEM. Ultramicroscopy 260:113939. https://doi.org/10.1016/j.ultramic.2024.113939

94. Kwiecińska B, Pusz S, Valentine BJ (2019) Application of electron microscopy TEM and SEM for analysis of coals, organic-rich shales and carbonaceous matter. Int J Coal Geol 211:103203. https://doi.org/10.1016/j.coal.2019.05.010

95. Wang G-C, Lu T-M (2014) Crystal Lattices and Reciprocal Lattices. In: RHEED Transmission Mode and Pole Figures. Springer New York, New York, NY, pp 7–22

96. Roos E, Maile K, Seidenfuß M (2022) Atomarer Aufbau kristalliner Stoffe. In: Werkstoffkunde für Ingenieure. Springer Berlin Heidelberg, Berlin, Heidelberg, pp 7–35

97. Electron vs. X-ray Diffraction: https://www.eng.uc.edu/~beaucag/Classes/XRD/Labs/Keithhtml/Keith.html. Accessed 9 Apr 2024

98. Sastry GVS (2022) Electron Diffraction. In: Microstructural Characterisation Techniques. Springer Nature Singapore, Singapore, pp 41–98

99. Murr LE (2014) Crystallography Principles. In: Handbook of Materials Structures, Properties, Processing and Performance. Springer International Publishing, Cham, pp 1–8

100. Inkson BJ (2016) 2 - Scanning electron microscopy (SEM) and transmission electron microscopy (TEM) for materials characterization. In: Hübschen G, Altpeter I, Tschuncky R, Herrmann H-G (eds) Materials Characterization Using Nondestructive Evaluation (NDE) Methods. Woodhead Publishing, pp 17–43

101. Reimer L, Kohl H (2008) Transmission electron microscopy: physics of image formation, 5th ed. Springer, New York, NY

102. Williams DB, Carter CB (1996) The Transmission Electron Microscope. In: Transmission Electron Microscopy. Springer US, Boston, MA, pp 3–17

103. Zintler A (2022) Investigating the influence of microstructure and grain boundaries on electric properties in thin film oxide RRAM devices – A component specific approach. Dissertation, Technische Universität Darmstadt

104. Franken LE, Grünewald K, Boekema EJ, Stuart MCA (2020) A Technical Introduction to Transmission Electron Microscopy for Soft-Matter: Imaging, Possibilities, Choices, and Technical Developments. Small 16:1906198. https://doi.org/10.1002/smll.201906198

105. Wen JG (2014) Transmission Electron Microscopy. In: Sardela M (ed) Practical Materials Characterization. Springer New York, New York, NY, pp 189–229

106. Ophus C, Savitzky B, Zeltmann S, et al Guidelines for Performing 4D-STEM Characterization from Atomic to Micrometer Scales: Experimental Considerations, Data Analysis and Simulation

107. Ophus C (2019) Four-Dimensional Scanning Transmission Electron Microscopy (4D-STEM): From Scanning Nanodiffraction to Ptychography and Beyond. Microsc Microanal 25:563–582. https://doi.org/10.1017/S1431927619000497

108. Nellist PD (2011) The Principles of STEM Imaging. In: Pennycook SJ, Nellist PD (eds) Scanning Transmission Electron Microscopy: Imaging and Analysis. Springer, New York, NY, pp 91–115

109. Kotaka Y (2012) Direct visualization method of the atomic structure of light and heavy atoms with double-detector Cs-corrected scanning transmission electron microscopy. Appl Phys Lett 101:133107. https://doi.org/10.1063/1.4756783

110. 4D STEM with a direct electron detector - 2020 - Wiley Analytical Science. https://analyticalscience.wiley.com/do/10.1002/was.00010003/. Accessed 31 Aug 2023

111. Darbal AD, Gemmi M, Portillo J, et al (2012) Nanoscale Automated Phase and Orientation Mapping in the TEM. Microsc Today 20:38–42. https://doi.org/10.1017/S1551929512000818

112. Jeong J, Cautaerts N, Dehm G, Liebscher CH (2021) Automated Crystal Orientation Mapping by Precession Electron Diffraction-Assisted Four-Dimensional Scanning Transmission Electron Microscopy Using a Scintillator-Based CMOS Detector. Microsc Microanal 27:1102–1112. https://doi.org/10.1017/S1431927621012538

113. McKenna K, Shluger A, Iglesias V, et al (2011) Grain boundary mediated leakage current in polycrystalline HfO2 films. Microelectron Eng 88:1272–1275. https://doi.org/10.1016/j.mee.2011.03.024

114. Lanza M, Bersuker G, Porti M, et al (2012) Resistive switching in hafnium dioxide layers: Local phenomenon at grain boundaries. Appl Phys Lett 101:193502. https://doi.org/10.1063/1.4765342

115. Xue K-H, Blaise P, Fonseca LRC, et al (2013) Grain boundary composition and conduction in HfO2: An *abinitio* study. Appl Phys Lett 102:201908. https://doi.org/10.1063/1.4807666

116. Xue KH, Traore B, Blaise P, et al (2014) A Combined Ab Initio and Experimental Study on the Nature of Conductive Filaments in Pt/HfO_2/Pt Resistive Random Access Memory. IEEE Trans Electron Devices 61:1394–1402. https://doi.org/10.1109/TED.2014.2312943

117. McKenna KP (2014) Optimal stoichiometry for nucleation and growth of conductive filaments in HfOx. Model Simul Mater Sci Eng 22:025001. https://doi.org/10.1088/0965-0393/22/2/025001

118. Bersuker G, Gilmer DC, Veksler D, et al (2011) Metal oxide resistive memory switching mechanism based on conductive filament properties. J Appl Phys 110:124518. https://doi.org/10.1063/1.3671565

119. Metlenko V, Ramadan AHH, Gunkel F, et al (2014) Do dislocations act as atomic autobahns for oxygen in the perovskite oxide SrTiO3? Nanoscale 6:12864–12876. https://doi.org/10.1039/C4NR04083J

120. Waldow SP, Statham BJ, Wardenga HF, et al (2020) Oxygen Surface Exchange and Tracer Diffusion in Differently Oriented Thin Films of Gd-Doped CeO2. ACS Appl Mater Interfaces 12:36768–36777. https://doi.org/10.1021/acsami.0c09605

121. Ruh R, Corfield PWR (1970) Crystal Structure of Monoclinic Hafnia and Comparison with Monoclinic Zirconia. J Am Ceram Soc 53:126–129. https://doi.org/10.1111/j.1151-2916.1970.tb12052.x

122. Rosenauer A, Kaiser S, Reisinger T, et al (1996) Digital analysis of high resolution transmission electron microscopy lattice images. Digit Anal High Resolut Transm Electron Microsc Lattice Images 102:63–69

123. Kilaas R (1998) Optimal and near-optimal filters in high-resolution electron microscopy. J Microsc 190:45–51. https://doi.org/10.1046/j.1365-2818.1998.3070861.x

124. Cowley JM, Moodie AF (1957) The scattering of electrons by atoms and crystals. I. A new theoretical approach. Acta Crystallogr 10:609–619. https://doi.org/10.1107/S0365110X57002194

125. Bean JJ, Saito M, Fukami S, et al (2017) Atomic structure and electronic properties of MgO grain boundaries in tunnelling magnetoresistive devices. Sci Rep 7:45594. https://doi.org/10.1038/srep45594

126. Sharath SU, Vogel S, Molina-Luna L, et al (2017) Control of Switching Modes and Conductance Quantization in Oxygen Engineered HfOx based Memristive Devices. Adv Funct Mater 27:1700432. https://doi.org/10.1002/adfm.201700432

127. Radamés RM, Mendoza JG, Z AV, et al (2016) Structural and Optical Properties of Co-doped HfO2 Multi-layer Deposited by Spray Pyrolysis Technique. MRS Online Proc Libr OPL 1817:imrc2015abs245. https://doi.org/10.1557/opl.2016.50

128. Hildebrandt E, Kurian J, Müller MM, et al (2011) Controlled oxygen vacancy induced p-type conductivity in HfO2−x thin films. Appl Phys Lett 99:112902. https://doi.org/10.1063/1.3637603

129. Schmitz J (2018) Low temperature thin films for next-generation microelectronics (invited). Surf Coat Technol 343:83–88. https://doi.org/10.1016/j.surfcoat.2017.11.013

130. Lanza M (2014) A Review on Resistive Switching in High-k Dielectrics: A Nanoscale Point of View Using Conductive Atomic Force Microscope. Materials 7:2155–2182. https://doi.org/10.3390/ma7032155

131. Gusev EP, Cabral C, Copel M, et al (2003) Ultrathin HfO2 films grown on silicon by atomic layer deposition for advanced gate dielectrics applications. Microelectron Eng 69:145–151. https://doi.org/10.1016/S0167-9317(03)00291-0

132. Lanza M, Porti M, Nafria M, et al (2007) Influence of the manufacturing process on the electrical properties of thin (<4nm) Hafnium based high-k stacks observed with CAFM. Microelectron Reliab 47:1424–1428. https://doi.org/10.1016/j.microrel.2007.07.045

133. Nishitani K, Yabuhara H, Endou A, et al (2009) Prediction of Crystallization Temperature for HfO_2 Thin Film in High Temperature Annealing Process by Reaction Time Accelerating Molecular Dynamics. In: Extended Abstracts of the 2009 International Conference on Solid State Devices and Materials. The Japan Society of Applied Physics, Sendai Kokusai Hotel, Miyagi, Japan

134. Lysaght PS, Woicik JC, Sahiner MA, et al (2008) Incipient amorphous-to-crystalline transition in HfO2 as a function of thickness scaling and anneal temperature. J Non-Cryst Solids 354:399–403. https://doi.org/10.1016/j.jnoncrysol.2007.07.050

135. Triyoso D, Liu R, Roan D, et al (2004) Impact of Deposition and Annealing Temperature on Material and Electrical Characteristics of ALD HfO2. J Electrochem Soc 151:F220. https://doi.org/10.1149/1.1784821

136. Khan SB, Zhang Z, Lee SL (2020) Annealing influence on optical performance of HfO2 thin films. J Alloys Compd 816:152552. https://doi.org/10.1016/j.jallcom.2019.152552

137. Ho M-Y, Gong H, Wilk GD, et al (2003) Morphology and crystallization kinetics in HfO2 thin films grown by atomic layer deposition. J Appl Phys 93:1477–1481. https://doi.org/10.1063/1.1534381

138. Vinod A, Rathore MS, Srinivasa Rao N (2018) Effects of annealing on quality and stoichiometry of HfO2 thin films grown by RF magnetron sputtering. Vacuum 155:339–344. https://doi.org/10.1016/j.vacuum.2018.06.037

139. Park MH, Chung C-C, Schenk T, et al (2018) Effect of Annealing Ferroelectric HfO2 Thin Films: In Situ, High Temperature X-Ray Diffraction. Adv Electron Mater 4:1800091. https://doi.org/10.1002/aelm.201800091

140. Balogh-Michels Z, Stevanovic I, Borzi A, et al (2021) Crystallization behavior of ion beam sputtered HfO2 thin films and its effect on the laser-induced damage threshold. J Eur Opt Soc-Rapid Publ 17:3. https://doi.org/10.1186/s41476-021-00147-w

141. Ushakov SV, Navrotsky A, Yang Y, et al (2004) Crystallization in hafnia- and zirconia-based systems. Phys Status Solidi B 241:2268–2278. https://doi.org/10.1002/pssb.200404935

142. Shih H-Y, Lee W-H, Kao W-C, et al (2017) Low-temperature atomic layer epitaxy of AlN ultrathin films by layer-by-layer, in-situ atomic layer annealing. Sci Rep 7:39717. https://doi.org/10.1038/srep39717

143. Aziz MJ (2008) Film growth mechanisms in pulsed laser deposition. Appl Phys A 93:579–587. https://doi.org/10.1007/s00339-008-4696-7

144. Luo X, Demkov AA (2015) Structure, thermodynamics, and crystallization of amorphous hafnia. J Appl Phys 118:124105. https://doi.org/10.1063/1.4931157

145. Gammer C, Mangler C, Rentenberger C, Karnthaler HP (2010) Quantitative local profile analysis of nanomaterials by electron diffraction. Scr Mater 63:312–315. https://doi.org/10.1016/j.scriptamat.2010.04.019

146. Seto Y, Ohtsuka M (2022) ReciPro: free and open-source multipurpose crystallographic software integrating a crystal model database and viewer, diffraction and microscopy simulators, and diffraction data analysis tools. J Appl Crystallogr 55:397–410. https://doi.org/10.1107/S1600576722000139

147. Cho D-Y, Luebben M, Wiefels S, et al (2017) Interfacial Metal–Oxide Interactions in Resistive Switching Memories. ACS Appl Mater Interfaces 9:19287–19295. https://doi.org/10.1021/acsami.7b02921

148. Cottom J, Bochkarev A, Olsson E, et al (2019) Modeling of Diffusion and Incorporation of Interstitial Oxygen Ions at the TiN/SiO2 Interface. ACS Appl Mater Interfaces 11:36232–36243. https://doi.org/10.1021/acsami.9b10705

149. Bradley SR, McKenna KP, Shluger AL (2013) The behaviour of oxygen at metal electrodes in HfO2 based resistive switching devices. Microelectron Eng 109:346–350. https://doi.org/10.1016/j.mee.2013.03.132

150. McKenna KP (2018) Structure, electronic properties, and oxygen incorporation/diffusion characteristics of the Σ 5 TiN(310)[001] tilt grain boundary. J Appl Phys 123:075301. https://doi.org/10.1063/1.5016626

151. Hwan Lee M, Seong Hwang C (2011) Resistive switching memory: observations with scanning probe microscopy. Nanoscale 3:490–502. https://doi.org/10.1039/C0NR00580K

152. Yang JJ, Miao F, Pickett MD, et al (2009) The mechanism of electroforming of metal oxide memristive switches. Nanotechnology 20:215201. https://doi.org/10.1088/0957-4484/20/21/215201

153. Holmberg B, Yhland M, Dahlbom R, et al (1962) Structural Studies on the Titanium-Nitrogen System. Acta Chem Scand 16:1255–1261. https://doi.org/10.3891/acta.chem.scand.16-1255

154. Trepka K (2021) Quantifying epitaxial growth using a purely topographical signal

155. Wilson AH (1937) The second order electrical effects in metals. Math Proc Camb Philos Soc 33:371–379. https://doi.org/10.1017/S0305004100019757

156. Lloyd GE (1987) Atomic number and crystallographic contrast images with the SEM: a review of backscattered electron techniques. Mineral Mag 51:3–19. https://doi.org/10.1180/minmag.1987.051.359.02

157. Cuccureddu F, Murphy S, Shvets IV, et al (2010) Surface morphology of *c*-plane sapphire (α-alumina) produced by high temperature anneal. Surf Sci 604:1294–1299. https://doi.org/10.1016/j.susc.2010.04.017

158. Lee H-J, Fujii K, Goto T, et al (2011) Effects of controlled ambidirectional nucleation on the heteroepitaxial growth of m-GaN on m-sapphire. Appl Phys Lett 98:071904. https://doi.org/10.1063/1.3553019

159. Zahoor F, Hussin FA, Isyaku UB, et al (2023) Resistive random access memory: introduction to device mechanism, materials and application to neuromorphic computing. Discov Nano 18:36. https://doi.org/10.1186/s11671-023-03775-y

160. Yoon JH, Song Y-W, Ham W, et al (2023) A review on device requirements of resistive random access memory (RRAM)-based neuromorphic computing. APL Mater 11:090701. https://doi.org/10.1063/5.0149393

161. Yang Y, Gao P, Gaba S, et al (2012) Observation of conducting filament growth in nanoscale resistive memories. Nat Commun 3:732. https://doi.org/10.1038/ncomms1737

162. Chen J-Y, Hsin C-L, Huang C-W, et al (2013) Dynamic Evolution of Conducting Nanofilament in Resistive Switching Memories. Nano Lett 13:3671–3677. https://doi.org/10.1021/nl4015638

163. Wang H, Yan X (2019) Overview of Resistive Random Access Memory (RRAM): Materials, Filament Mechanisms, Performance Optimization, and Prospects. Phys Status Solidi RRL – Rapid Res Lett 13:1900073. https://doi.org/10.1002/pssr.201900073

164. Sun W, Gao B, Chi M, et al (2019) Understanding memristive switching via in situ characterization and device modeling. Nat Commun 10:3453. https://doi.org/10.1038/s41467-019-11411-6

165. Sun K, Chen J, Yan X (2021) The Future of Memristors: Materials Engineering and Neural Networks. Adv Funct Mater 31:2006773. https://doi.org/10.1002/adfm.202006773

166. Zhang Y, Wang C, Wu X (2022) Review of electrical stimulus methods of in situ transmission electron microscope to study resistive random access memory. Nanoscale 14:9542–9552. https://doi.org/10.1039/D2NR01872A

167. Lanza M, Wong H-SP, Pop E, et al (2019) Recommended Methods to Study Resistive Switching Devices. Adv Electron Mater 5:1800143. https://doi.org/10.1002/aelm.201800143

168. Hubbard WA, Lodico JJ, Chan HL, et al (2022) Imaging Dielectric Breakdown in Valence Change Memory. Adv Funct Mater 32:2102313. https://doi.org/10.1002/adfm.202102313

16. Figure Listing

17. Equation Listing

18. Table Listing

Part II: Publications

Controlling the Formation of Conductive Pathways in Memristive Devices

Robert Winkler, Alexander Zintler, Stefan Petzold, Eszter Piros, Nico Kaiser, Tobias Vogel, Déspina Nasiou, Keith P. McKenna, Leopoldo Molina-Luna, and Lambert Alff**

Resistive random-access memories are promising candidates for novel computer architectures such as in-memory computing, multilevel data storage, and neuromorphics. Their working principle is based on electrically stimulated materials changes that allow access to two (digital), multiple (multilevel), or quasi-continuous (analog) resistive states. However, the stochastic nature of forming and switching the conductive pathway involves complex atomistic defect configurations resulting in considerable variability. This paper reveals that the intricate interplay of 0D and 2D defects can be engineered to achieve reproducible and controlled low-voltage formation of conducting filaments. The author find that the orientation of grain boundaries in polycrystalline HfO_x is directly related to the required forming voltage of the conducting filaments, unravelling a neglected origin of variability. Based on the realistic atomic structure of grain boundaries obtained from ultra-high resolution imaging combined with first-principles calculations including local strain, this paper shows how oxygen vacancy segregation energies and the associated electronic states in the vicinity of the Fermi level govern the formation of conductive pathways in memristive devices. These findings are applicable to non-amorphous valence change filamentary type memristive device. The results demonstrate that a fundamental atomistic understanding of defect chemistry is pivotal to design memristors as key element of future electronics.

1. Introduction

A memristor is based on the controlled (digital or analog)[1–4] change of the resistance of a conductive pathway. In complementary metal oxide semiconductor (CMOS) relevant materials such as Hf–O or Ta–O, the conductive pathways consist of a local enrichment of oxygen vacancies.[5–8] Preexisting oxygen vacancies allow for low-voltage and thickness independent electroforming as only a reshuffle of vacancies is required.[9–14] However, the oxygen vacancy distribution itself is still a random process associated with forming and operating voltage variability.[15–17] Defect engineering to reduce the device variability has been investigated in several works using dislocations and nanocomposites.[18–20] The introduction of threading grain boundaries (GBs) via GB engineering results in highly reproducible low-voltage electroforming.[17] Here, we show that the complete materials picture is disclosed only when taking into account the intricate interplay between point-defects (oxygen vacancies) and 2D defect planes (grain boundaries). The specific atomic configurations of the grain boundaries including strain effects result in enhanced or suppressed attraction between both types of defects. As a consequence, the selection of the proper GB allows us to create a predefined region of increased oxygen vacancy concentration which is associated with electronic defect states close to the Fermi level. These defect states, in turn, are the nuclei for the soft dielectric breakdown via formation of a defined conducting filament. This insight into the materials defect chemistry suggests new experimental methods of controlling the conducting

---

R. Winkler, S. Petzold, E. Piros, N. Kaiser, T. Vogel, L. Alff
Advanced Thin Film Technology Division
Institute of Materials Science
Technical University of Darmstadt
Alarich-Weiss-Straße 2, 64287 Darmstadt, Germany
E-mail: lambert.alff@tu-darmstat.de

R. Winkler, A. Zintler, D. Nasiou, L. Molina-Luna
Advanced Electron Microscopy Division
Institute of Materials Science
Technical University of Darmstadt
Alarich-Weiss-Straße 2, 64287 Darmstadt, Germany
E-mail: leopoldo.molina-luna@aem.tu-darmstadt.de

K. P. McKenna
Department of Physics
The University of York
York YO10 5DD, UK

The ORCID identification number(s) for the author(s) of this article can be found under https://doi.org/10.1002/advs.202201806

DOI: 10.1002/advs.202201806

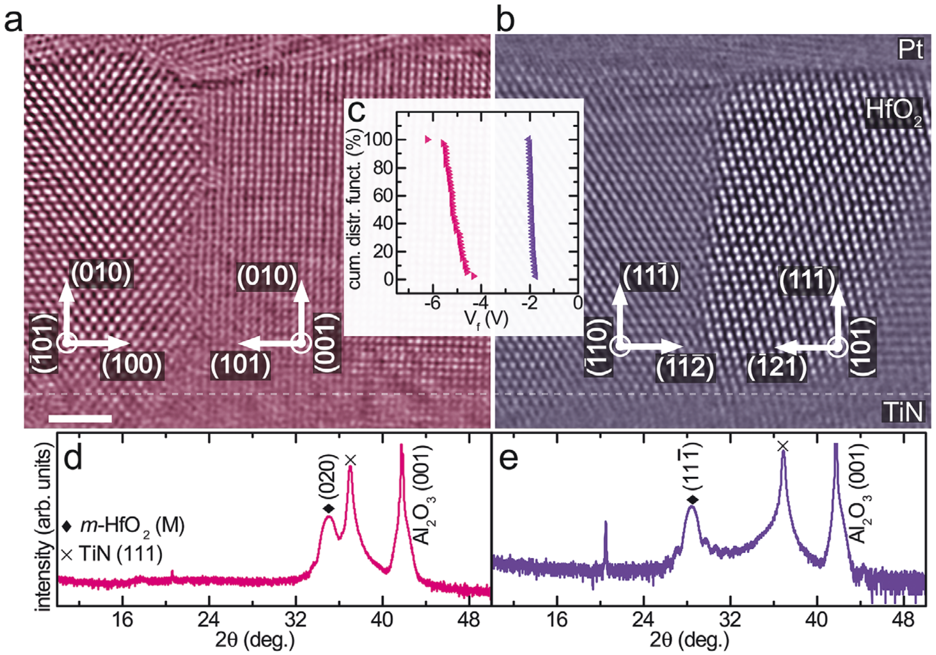

Figure 1. Cross-sectional high-angle annular dark-field (HAADF) scanning transmission electron microscopy (STEM) image of the metal-insulator-metal stack with a) (010) and b) (11$\bar{1}$) textured HfO_2. Scale bar is 2 nm. The TiN-HfO_2 interface is indicated by a faint dashed line. Images were filtered by an average background subtraction filter (ABSF), a Butterworth filter and a STEM crosshair filter to reduce image noise.[25,26] Titanium nitride (TiN) and hafnium oxide (HfO_2) have been grown on (001) oriented Al_2O_3 by using RMBE. The X-ray diffraction (XRD) pattern reveals that a change in the growth temperature and rf-power for HfO_2 results in d) (11$\bar{1}$), (purple) and e) (020), (pink) when grown at 520 °C, 200 W and 460 °C, 280 W, respectively. c) Devices with (010) textured HfO_2 (pink) have an increased average forming voltage of $\overline{V_f} = -5.3$ V compared to devices with (11$\bar{1}$) HfO_2 having $\overline{V_f} = -1.9$ V as shown by the cumulative distribution function measured from 50 30 × 30 µm² devices. The purple XRD pattern, purple cumulative distribution of V_f and the purple colored high-resolution scanning transmission electron microscopy image is adapted from Petzold et al.[17]

filament, and thus also serves as a valuable guideline for future memristor designs.[21–34]

2. An Intriguing Observation: Electroforming Voltages Depend on Texture

The starting point of this investigation is the discovery of clearly distinct electroforming voltages in memristive model devices with different crystal orientation of the HfO_2 layer. The devices consist of a 50 nm TiN bottom electrode, followed by a 10 nm thin HfO_2 layer covered with Pt (100 nm) and gold (300 nm) grown on c-cut sapphire. When choosing the appropriate growth conditions either a (11$\bar{1}$) or (010) texture of the HfO_2 dielectric is achieved (**Figure 1**d,e and Figure S1, Supporting Information). We have verified the oxygen content by X-ray photoelectron spectroscopy revealing that the HfO_2 layers are homogeneously stoichiometric. Electroforming voltages were collected from 50 devices for each texture and reveal a clear correlation to the respective growth direction of HfO_2. For the (010) texture an average forming voltage of $\overline{V_f} = -5.3$ V was observed as compared to $\overline{V_f} = -1.9$ V for the (11$\bar{1}$) texture (see Figure 1c and Figure S2, Supporting Information). Both devices have a similar leakage current level at +/− 200 mV (see Figure S2a, Supporting Information). In addition to the very distinct quantitative voltage levels, the device-to-device variability is considerably reduced for the low voltage devices which are formed already at standard operation voltages (see Figure 1c).

2.1. Texture Defines Specific Grain Boundaries

Transmission electron microscopy revealed that the two types of textured HfO_2 layers are fully threaded by grain boundaries belonging to well-defined crystallographic equivalent sets of orientations (see Figure 1a,b). Such grain boundaries display characteristic periodic structure units that repeat themselves along the grain boundary plane (see purple and pink circles in **Figures 2**a and **3**a). So far, grain boundaries have been discussed as a source of variability.[27] Here we show that a smart use of grain boundaries may lead to the opposite, reduced, and more uniformly distributed forming voltage at negative bias. It is plausible to assume that grain boundaries in general provide a predefined pathway for filament formation.[27] What is unexpected, however, is that there is a pronounced correlation of crystallographic directions and forming voltages, the latter ones being related to the electronic structure of the grain boundary. In the next step, therefore, we have used high-resolution imaging of atomic sites to model the real nanostructure of both grain boundary types using density functional theory (DFT). The DFT relaxed atomic structure for the (11$\bar{1}$) textured HfO_2 (see Figure 2b) is composed of one grain terminated by (11$\bar{2}$) and the other by ($\bar{1}$21). For (020) HfO_2 (Figure 3b), grains terminate at (100) and (101). The complete unit cells of these structures are shown in Figure S3, Supporting Information. The same periodically occurring structural units are again marked by purple and pink circles. The DFT calculation of the ($\overline{112}$)|($\bar{1}$21) grain boundary revealed two possible stable

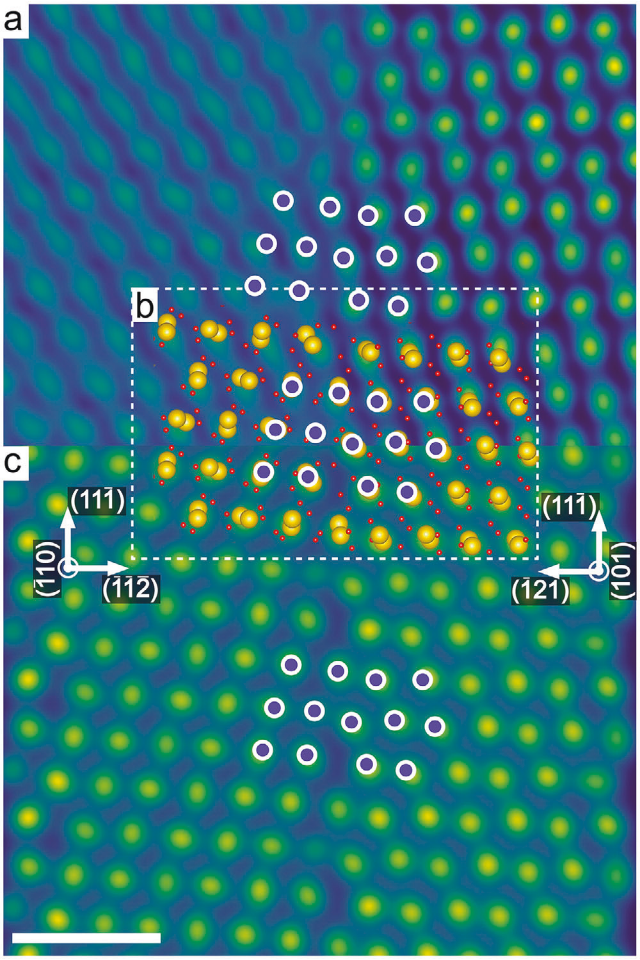

Figure 2. a) Cross-sectional high-angle annular dark-field (HAADF) scanning transmission electron microscopy (STEM) images of a grain boundary in $(11\bar{1})$ textured HfO_2. The image was used as basis to simulate the b) DFT relaxed atomic structure model which were then used to simulate the HAADF-STEM image (c). Periodically occurring structural units at the grain boundaries are indicated by purple circles. Scale bar is 1 nm. Experimental HAADF-STEM images were filtered by an average background subtraction filter (ABSF) and a Butterworth filter to reduce image noise.[25,26] All STEM images are colored with the GEM-16 LUT to improve visibility of atomic columns.

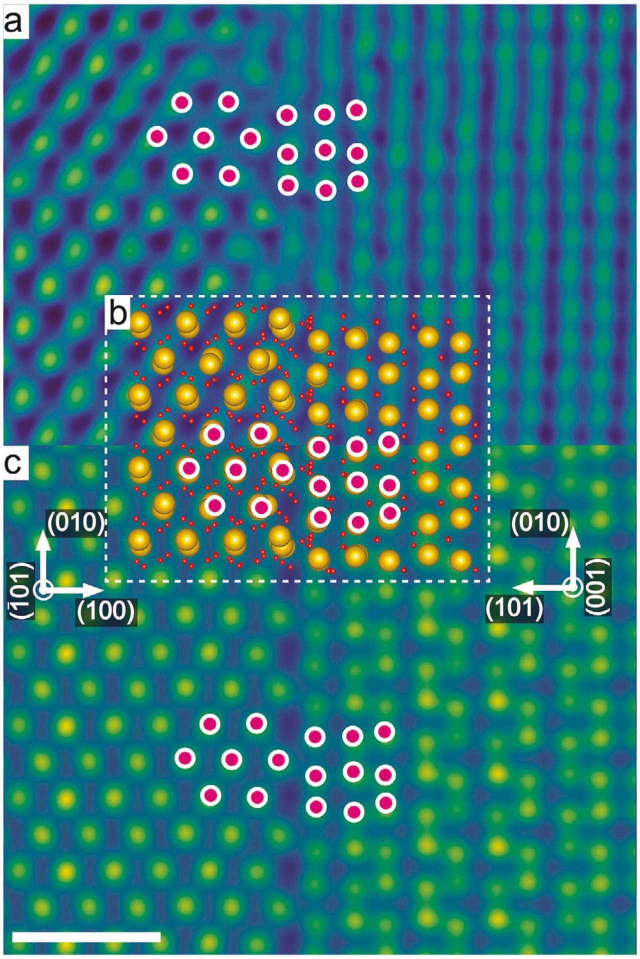

Figure 3. a) Cross-sectional high-angle annular dark-field (HAADF) scanning transmission electron microscopy (STEM) images of a grain boundary in (020) textured HfO_2. The image was used as basis to simulate the b) DFT relaxed atomic structure model which was then used to simulate the HAADF-STEM image (c). Periodically occurring structural units at the grain boundaries are indicated by pink circles. Scale bar is 1 nm. Experimental HAADF-STEM images were filtered by an average background subtraction filter (ABSF) and a Butterworth filter to reduce image noise.[25,26] All STEM images are colored with the GEM-16 LUT to improve visibility of atomic columns.

structures differing only by a rigid translation of one grain with respect to each other (Figure S4, Supporting Information). To validate if these models replicate the real complex atomic structures, multislice-based electron microscopy image simulations were performed (Figures 2c and 3c). The results match with high accuracy the atomically resolved HAADF-STEM data. This result shows that imaging of defect processes at grain boundaries can be obtained not only on well-defined bicrystals,[28,29] but can be extended to realistic CMOS materials.

It is important to note that for $(11\bar{1})$ textured HfO_2, construction of the $(\overline{112})|(\bar{1}21)$ GB was only possible by applying significant strain parallel to the grain boundary. In contrast, the construction of the (100)|(101) grain boundary for (020) HfO_2 requires no strain most likely due to the semi-coherent nature of this grain boundary.[30] Strain effects by lattice mismatch or dopants are being routinely used in semiconductor technology to modify electronic properties and transistor performance.[31] Here we show that texture transfer induced strain in coherent grain boundaries have a strong effect on electronic properties in memristive devices.

2.2. Grain Boundary Influence on Oxygen Segregation Energies and Electronic Structure

Having properly modelled the grain boundary defect nanostructures of realistic memristive model devices gives us the possibility to investigate neutral oxygen vacancy (V_O) interactions with GBs by first principles calculations. Note that we are not using a model grain boundary of higher symmetric (cubic) HfO_2 but are taking the real atomic positions of the grain boundary within

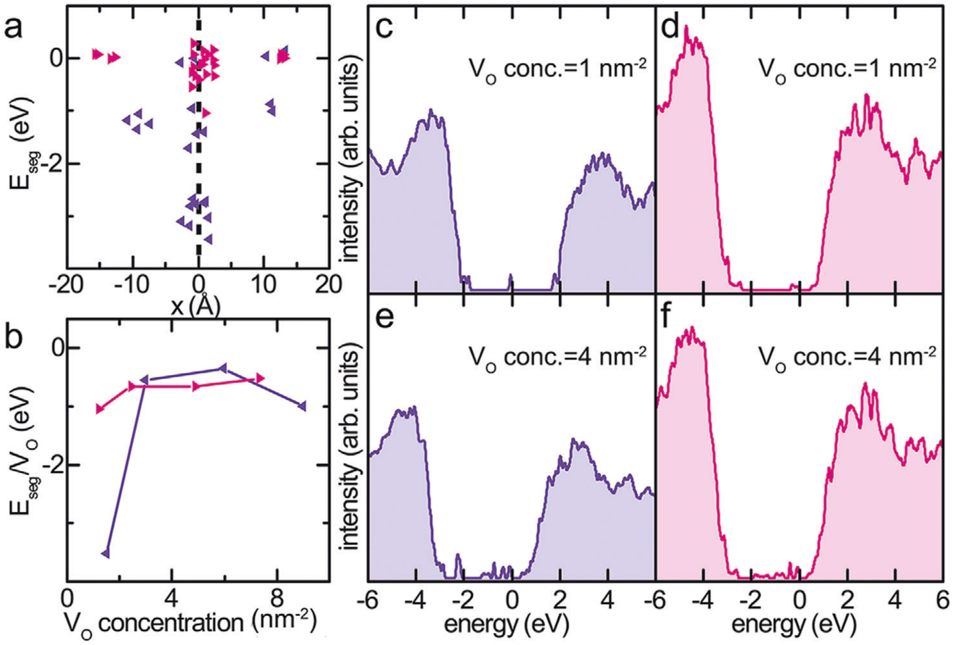

Figure 4. Oxygen vacancy segregation energies were calculated from the DFT relaxed atomic structure models as a function of a) distance from the grain boundary (marked by dotted line) and b) oxygen vacancy concentration for $(11\bar{1})$, (purple) and (020), and (pink) textured HfO_2. The density of states (DOS) at grain boundaries for c,e) $(11\bar{1})$ and d,f) (020) HfO_2 were calculated using the projector augmented wave (PAW) method and are shown as a function of oxygen vacancy concentration (V_O conc.).

the monoclinic phase. The variation of segregation energy E_{seg} in the vicinity of the GBs (**Figure 4**a) shows that oxygen vacancy segregation is more favorable at the $(\overline{112})|(\bar{1}21)$ GB (purple) than at the (100)|(101) GB (pink). However, as the concentration of vacancies increases beyond 2 nm^{-2} the average segregation energy per vacancy (E_{seg}/V_O) for the two GBs becomes comparable (Figure 4b). The electronic properties investigated by the density of states (DOS) projected onto the GB regions (Figure 4c) as a function of V_O concentration reveal a larger band gap for the $(\overline{112})|(\bar{1}21)$ GB (purple) than the (100)|(101) GB (pink). The magnitude of the band gaps is comparable to previous reports[32,33] and in the presence of V_O the bandgaps are significantly smaller as compared to bulk *m*-HfO_2.[34,35] For low V_O concentration (below 2 nm^{-2}) the DOS of both GBs show a deep and narrow gap state associated with the vacancies.[34]

For the $(\overline{112})|(\bar{1}21)$ GB, the gap state is positioned mid-gap, while for the (100)|(101) GB the gap state is positioned closer to the conduction band. With increase in V_O concentration the DOS shows the formation of a conductive sub-band as suggested in literature.[33,35] DOS for V_O concentration equal to 0, 2, and 6 nm^{-2} are shown in Figure S5, Supporting Information.

The electronic properties investigated by the DOS from the DFT relaxed structures of the $(\overline{112})|(\bar{1}21)$ GB and the (100)|(101) GB were comparable and the introduction of oxygen vacancies resulted in a similar change of the intermediate bandgap states of the DOS. The formed conductive sub-band for V_O concentration above 2 nm^{-2} is a percolation path for the current and deteriorates the insulating properties of HfO_2. The oxygen vacancy concentration can be driven even to a state where the insulator transitions to a semiconducting or even metallic state.[35] The presence of preexisting oxygen vacancies is known to reduce the required forming voltages for a conductive filament in HfO_{2-x}.[12] For the here discussed samples, the stoichiometry of the HfO_2 matrix is close to the ideal 1:2. It can, therefore, be excluded that any anisotropy in oxygen vacancy distribution inside the nanocrystals is the reason for the difference in forming voltages. Therefore, the V_O concentration below 2 nm^{-2} is representative for a pristine non-formed resistive switching device, which is insulating. Our results show that at low vacancy concentrations the V_O segregation energy in $(\overline{112})|(\bar{1}21)$ GBs (in comparison to the (100)|(101) GBs) are more negative. The $(\overline{112})|(\bar{1}21)$ GB therefore acts as a sink for oxygen vacancies, thereby, driving the surrounding matrix closer to perfect stoichiometry by the depletion of vacancies, while the grain boundary plane itself is enriched in vacancies. As a consequence, this type of grain boundary is the perfect percolation path for electron transport initiating the formation of a conducting filament.

Due to the monoclinic structure of the HfO_2 thin films, imaging a grain boundary with both grains being atomically resolved was highly challenging. Moreover, finding a high resolved GB did not guarantee that the construction of a DFT relaxed supercell was possible due to the non-commensurate nature of adjacent monoclinic grains. Therefore, only one GB of each HfO_2 texture is shown. However, the textured growth of the $(11\bar{1})$ and (020) HfO_2 thin films results in six allowed in-plane directions each (Figure S6a,b, Supporting Information) limiting the possible orientations and resultant GB types. According to Figure S6c,d, Supporting Information, the majority of GBs in (020) textured HfO_2 are therefore composed of grains terminated by low-index orientations (e.g., (100)), contrary to GBs in $(11\bar{1})$ HfO_2 which have high-indexed terminated grains. Construction of the GB with high-indexed terminated grains ($(\overline{112})|(\bar{1}21)$ GB) required application of strain. In the near future, we plan to probe local stress fields of GBs with high- and low-indexed terminating grains to investigate the effect on local ionic mobility.[36–41]

3. Conclusion

Our combined experimental and ab initio study reveals that an intricate interplay of defects with different dimensionality plays the key role in predefining the formation path of the conducting filament. The controlled induction of a specific grain boundary type by texture transfer is a promising way to overcome present limitations set by the variability of forming voltages and is likely to be favorable for improved device endurance and cycle stability. For the sake of this study we have used MBE growth parameters outside the CMOS temperature budget. However, the favorable combination of a (111) oriented TiN electrode with a (11-1) oriented HfO_2 functional layer can also be achieved with industrial relevant methods such as atomic layer deposition. The here suggested method of grain boundary and defect engineering is scalable well below 10 nm as the grain size is comparable to the thickness of the dielectric layer.

4. Experimental Section

Sample Preparation: Reactive molecular beam epitaxy (RMBE) was used to grow TiN on *c*-cut sapphire followed by in situ growing HfO_2 in a custom designed ultra-high vacuum chamber (base pressure ≈ 10^{-9} mbar).[42] For the TiN layers, the substrate was heated to 800 °C. Ti from Lesker (4.5 N purity) was evaporated at a rate of 0.3 Å s^{-1} with in situ nitridation by using a radio frequency (rf)-source with an rf-power of 350 W and a flow of 0.6 sccm nitrogen (5 N purity). Growth of hafnia layers with defined textures were achieved by using distinct temperatures and rf-powers. Hf from MaTeck (3 N purity) was evaporated at a rate of 0.7 Å s^{-1} and in situ oxidized by a rf-source with a flow of 1 sccm oxygen (5 N purity). For the $(11\bar{1})$ textured hafnia, the rf-source was operated at 200 W and the substrate was heated to 520 °C. The (020) textured hafnia was grown at a substrate temperature of 460 °C with the rf-source operating at 280 W. The film thickness and surface crystallinity were in situ monitored by using quartz crystal microbalance (QCM) and reflection high energy electron diffraction (RHEED), respectively. To complement the metal–insulator–metal (MIM) structure, first a standard lithography step was carried out to pattern the surface followed by sputtering 100 nm Pt and 300 nm Au with a Quorum sputter cutter. The lift-off process resulted in 30 × 30 μm^2 MIM devices.

X-Ray Measurements: Before completing the MIM structure, texture quality of the reactive molecular beam epitaxy (RMBE)-grown TiN and HfO_2 thin films were examined with X-ray diffractometry (XRD). A Rigaku SmartLab diffractometer were used in parallel beam geometry with a copper K_α X-ray source.

Electroforming: Initialization of resistive switching for a device under test (DUT) was achieved by a DC-negative voltage sweep using a Keithley 4200 semiconductor characterization system (SCS). The top electrode of the device under test (DUT) was biased while electrically grounding the bottom electrode. To prevent a hard dielectric breakdown during electroforming, the internal current compliance (CC) of the semiconductor characterization system (SCS) was limited to 10 and 100 µA.

Electron Microscopy: From the MIM devices, TEM lamellae were prepared by using in situ lift-out focused ion beam (FIB) microscopy (JEOL JIB-4600F). Aberration corrected STEM images were acquired with a convergence angle of 36 mrad by using a field-emission (S)TEM (JEOL ARM-200F) at an acceleration voltage of 200 kV. Detection angles of the HAADF detector ranged from 90 to 370 mrad. Growth direction and zone axis of the HfO_2 thin films were identified by using the diffractGUI of CrysTBox developed by Klinger and Jäger[43] with the FFTs of individual grains and a reference structure from Christensen and An[44] as the material input.

Density Functional Theory Methodology: Calculations of the structure and electronic properties of *m*-HfO_2 GBs were performed using the projector augmented wave (PAW) method as implemented in the Vienna Ab-initio Simulation Package (VASP).[45,46] The approach was the same as that described in the authors' previous paper which focused on a single GB type observed in $(11\bar{1})$ textured films.[17] Here a second GB type observed in (020) textured films was also considered as well as V_O segregation to both GB models was considered in order to provide insight into the origin of the difference in V_F. The generalized gradient approximation of Perdew, Burke, and Ernzerhof (PBE)[47] and standard Hf and soft oxygen projector augmented wave (PAW) potentials was employed. Using a 400 eV plane wave cut-off and a Monkhorst–Pack k-point grid of 11 × 11 × 11 lattice constants for bulk *m*-HfO_2 within 0.5% of experimental values were obtained.

The GB in the $(11\bar{1})$ textured films could be formed by joining a $(\bar{1}\bar{1}\bar{2})$ terminated *m*-HfO_2 grain to a $(\bar{1}21)$ terminated grain. To make a commensurate supercell in this case one must apply strain to both grains parallel to the interface (<10%). The grain boundary in the (020) textured films could be formed by joining a (100) terminated *m*-HfO_2 grain to a (101) terminated grain. In this case, it was possible to form a commensurate supercell with very little strain (<0.1%). For both GB models, a vacuum gap of 10 Å was included to separate the two free surfaces in the periodic supercell such that only one GB interface was present. This was necessary in this case as the low symmetry of the GB makes it impossible to construct two equivalent GB interfaces in the supercell as is usually possible for higher symmetry GBs.[48–51] To determine the most stable configuration, a gamma-surface scan of GB translation states was carried out (in steps of ≈1 Å in both directions parallel to the grain boundary).

To assess the tendency of V_O to segregate to the GBs, vacancy formation energies for all inequivalent oxygen sites in the region between the centers of each grain were calculated. The formation energy was computed relative to half the energy of an oxygen molecule. For the (020) textured GB (which had negligible in-plane strain applied), the formation energies in the bulk of each grain were very similar and in good agreement with previous calculations of V_O in bulk *m*-HfO_2 (6.57 eV for three-coordinated sites and 6.64 eV for four-coordinated sites). Because the $(11\bar{1})$ textured grain boundary had significant strain applied, the absolute formation energies in the bulk of each grain were modified (≈1.2 eV lower in energy). To allow comparison and assess general trends in defect segregation, a segregation energy (E_{seg}) is defined relative to the bulk formation energy in each GB model. In both models, vacancy segregation was favorable both in the dilute limit and, as the concentration of vacancies segregated to the grain boundaries, was increased. To assess the effect this has on electronic properties, the electronic DOS both for the pristine stoichiometric GB and the GB with increasing concentrations of V_O were computed.

Multislice Simulations: To correlate experimental high-resolution data to the developed supercells from density functional calculations, STEM images were simulated with the software Dr. Probe[52] using the multislice method.[53] Within the software, the microscope parameters were set to an acceleration voltage of 200 kV, a convergence angle of 25 mrad, a source size of 0.08 nm, and a HAADF detection range of 90 to 370 mrad with all aberrations set to zero. Cell sizes for equidistant slice creation along *z* with applied Debye–Waller factors for the $(\overline{112})|(\bar{1}21)$ and the (100)|(101) GB were 10.49 × 1.90 × 14.03 nm, 4800 pixel × 864 pixel × 80 slices, 19 200 atoms and 11.77 × 1.03 × 15.87 nm, 5400 pixel × 480 pixel × 180 slices, 13 920 atoms (x × y × z), respectively. Centered calculation windows were set to 5.24 × 0.95 nm, 524 × 95 pixels and 5.89 × 0.52 nm, 589×52 pixels (x × y) with a sampling of 0.01 nm/pix for the $(\overline{112})|(\bar{1}21)$ and the (100)|(101) GB, respectively. Computational time for a "Scan image" type with a thickness of ≈10 nm (56 and 113 slices, respectively) took ≈2 h 30 min and ≈2 h for the $(\overline{112})|(\bar{1}21)$ and the (100)|(101) GB, respectively, using 30 threads of an AMD Ryzen 9 3950X CPU overclocked to 4.15 GHz assisted by a GeForce RTX 3070 GPU (128 GB 2666 MHz RAM and 500 GB Samsung SSD 970 EVO Plus).

Supporting Information

Supporting Information is available from the Wiley Online Library or from the author.

Acknowledgements

This work was supported by the European Research Council (ERC) "Horizon 2020" Program under Grant No. 805359-FOXON and Grant No. 957521-STARE and the Deutsche Forschungsgemeinschaft (DFG) under projects MO 3010/3-1 and AL 560/21-1. The work was supported by the framework of the WAKeMeUP and StorAIge project which received funding from the Electronic Components and Systems for European Leadership Joint Undertaking in collaboration with the European Union's H2020 Framework Programme (H2020/2014-2020) and National Authorities, under grant agreement No. 783176 and No. 101007321, respectively. Funding by the Federal Ministry of Education and Research (BMBF) under contract 16ESE0298 and 16MEE0154 are gratefully acknowledged. E.P. acknowledges funding from the Deutscher Akademischer Austauschdienst (DAAD). K.P.M. acknowledges support from EPSRC (EP/P023843/1) and access to the Viking Cluster, which is a high-performance computing facility provided by the University of York. All data relating to the density functional theory calculations are available by request from the University of York Research database.

Open Access funding enabled and organized by Projekt DEAL.

Conflict of Interest

The authors declare no conflict of interest.

Author Contributions

L.A. and S.P. started and suggested the study. L.A., L.M.-L. supervised and steered the ongoing project. R.W., N.K., S.P., and T.V. were responsible for sample synthesis and electrical characterization. R.W., D.N., and A.Z. performed the TEM measurements and multislice simulations. K.P.M. performed the DFT calculations. L.A., R.W., L.M.-L., E.P., S.P., and A.Z. wrote the manuscript. All authors discussed the results and provided constructive comments on the manuscript.

Data Availability Statement

The data that support the findings of this study are available from the corresponding author upon reasonable request.

Keywords

first principle calculation, grain boundary atomic structures, hafnium oxide, resistive switching memory, scanning transmission electron microscopy

Received: March 28, 2022
Revised: June 21, 2022
Published online: September 8, 2022

---

[1] Z. Wang, H. Wu, G. W. Burr, C. S. Hwang, K. L. Wang, Q. Xia, J. J. Yang, *Nat. Rev. Mater.* **2020**, *5*, 173.
[2] D. Ielmini, S. Ambrogio, *Nanotechnology* **2019**, *31*, 092001.
[3] International Roadmap for Devices and Systems (IRDSTM) 2020 Edition - IEEE IRDSTM, https://irds.ieee.org/editions/2020 (accessed: December 2021).
[4] D. Marković, A. Mizrahi, D. Querlioz, J. Grollier, *Nat. Rev. Phys.* **2020**, *2*, 499.
[5] D. Ielmini, R. Waser, *Resistive Switching: From Fundamentals of Nanoionic Redox Processes to Memristive Device Applications*, Wiley-VCH, Weinheim **2015**.
[6] B. Govoreanu, G. S. Kar, Y. Y. Chen, V. Paraschiv, S. Kubicek, A. Fantini, I. P. Radu, L. Goux, S. Clima, R. Degraeve, N. Jossart, O. Richard, T. Vandeweyer, K. Seo, P. Hendrickx, G. Pourtois, H. Bender, L. Altimime, D. J. Wouters, J. A. Kittl, M. Jurczak, 2011 Int. Electron Devices Meet, IEEE, Piscataway, NJ **2011**, pp. 31.6.1-31.6.4.
[7] Y. Hayakawa, A. Himeno, R. Yasuhara, W. Boullart, E. Vecchio, T. Vandeweyer, T. Witters, D. Crotti, M. Jurczak, S. Fujii, S. Ito, Y. Kawashima, Y. Ikeda, A. Kawahara, K. Kawai, Z. Wei, S. Muraoka, K. Shimakawa, T. Mikawa, S. Yoneda, 2015 Symp. VLSI Technol. (VLSI Technol.) IEEE, Piscataway, NJ **2015**, pp. T14-T15.
[8] Z. Wei, T. Takagi, Y. Kanzawa, Y. Katoh, T. Ninomiya, K. Kawai, S. Muraoka, S. Mitani, K. Katayama, S. Fujii, R. Miyanaga, Y. Kawashima, T. Mikawa, K. Shimakawa, K. Aono, 2011 Int. Electron Devices Meet IEEE, Piscataway, NJ **2011**, pp. 31.4.1-31.4.4.
[9] S. U. Sharath, T. Bertaud, J. Kurian, E. Hildebrandt, C. Walczyk, P. Calka, P. Zaumseil, M. Sowinska, D. Walczyk, A. Gloskovskii, T. Schroeder, L. Alff, *Appl. Phys. Lett.* **2014**, *104*, 063502.
[10] S. U. Sharath, J. Kurian, P. Komissinskiy, E. Hildebrandt, T. Bertaud, C. Walczyk, P. Calka, T. Schroeder, L. Alff, *Appl. Phys. Lett.* **2014**, *105*, 073505.
[11] S. U. Sharath, M. J. Joseph, S. Vogel, E. Hildebrandt, P. Komissinskiy, J. Kurian, T. Schroeder, L. Alff, *Appl. Phys. Lett.* **2016**, *109*, 173503.
[12] S. U. Sharath, S. Vogel, L. Molina-Luna, E. Hildebrandt, C. Wenger, J. Kurian, M. Duerrschnabel, T. Niermann, G. Niu, P. Calka, M. Lehmann, H.-J. Kleebe, T. Schroeder, L. Alff, *Adv. Funct. Mater.* **2017**, *27*, 1700432.
[13] S. Petzold, E. Miranda, S. Sharath, J. Muñoz-Gorriz, T. Vogel, E. Piros, N. Kaiser, R. Eilhardt, A. Zintler, L. Molina-Luna, *J. Appl. Phys.* **2019**, *125*, 234503.
[14] S. Petzold, E. Piros, R. Eilhardt, A. Zintler, T. Vogel, N. Kaiser, A. Radetinac, P. Komissinskiy, E. Jalaguier, E. Nolot, C. Charpin-Nicolle, C. Wenger, L. Molina-Luna, E. Miranda, L. Alff, *Adv. Electron. Mater.* **2020**, *6*, 2000439.
[15] C. Baeumer, R. Valenta, C. Schmitz, A. Locatelli, T. O. Menteş, S. P. Rogers, A. Sala, N. Raab, S. Nemsak, M. Shim, C. M. Schneider, S. Menzel, R. Waser, R. Dittmann, *ACS Nano* **2017**, *11*, 6921.
[16] S. Ambrogio, S. Balatti, A. Cubeta, A. Calderoni, N. Ramaswamy, D. Ielmini, *IEEE Trans. Electron Devices* **2014**, *61*, 2920.
[17] S. Petzold, A. Zintler, R. Eilhardt, E. Piros, N. Kaiser, S. U. Sharath, T. Vogel, M. Major, K. P. McKenna, L. Molina-Luna, *Adv. Electron. Mater.* **2019**, *5*, 1900484.
[18] W. Banerjee, Q. Liu, H. Hwang, *J. Appl. Phys.* **2020**, *127*, 051101.
[19] S. Choi, S. H. Tan, Z. Li, Y. Kim, C. Choi, P.-Y. Chen, H. Yeon, S. Yu, J. Kim, *Nat. Mater.* **2018**, *17*, 335.
[20] M. N. Martyshov, A. V. Emelyanov, V. A. Demin, K. E. Nikiruy, A. A. Minnekhanov, S. N. Nikolaev, A. N. Taldenkov, A. V. Ovcharov, M. Y. Presnyakov, A. V. Sitnikov, A. L. Vasiliev, P. A. Forsh, A. B. Granovsky, P. K. Kashkarov, M. V. Kovalchuk, V. V. Rylkov, *Phys. Rev. Appl.* **2020**, *14*, 034016.
[21] A. Sebastian, M. L. Gallo, R. Khaddam-Aljameh, E. Eleftheriou, *Nat. Nanotechnol.* **2020**, *15*, 529.
[22] K. Sun, J. Chen, X. Yan, *Adv. Funct. Mater.* **2021**, *31*, 2006773.
[23] D. Ielmini, H.-S. P. Wong, *Nat. Electron.* **2018**, *1*, 333.
[24] M. A. Zidan, Y. Jeong, J. Lee, B. Chen, S. Huang, M. J. Kushner, W. D. Lu, *Nat. Electron.* **2018**, *1*, 411.

[25] A. Rosenauer, S. Kaiser, T. Reisinger, J. Zweck, W. Gebhardt, D. Gerthsen, *Optik* **1996**, *102*, 63.
[26] R. Kilaas, *J. Microsc.* **1998**, *190*, 45.
[27] M. Lanza, *Materials* **2014**, *7*, 2155.
[28] J. Wei, B. Feng, R. Ishikawa, T. Yokoi, K. Matsunaga, N. Shibata, Y. Ikuhara, *Nat. Mater.* **2021**, *20*, 951.
[29] E. Tochiga, Y. Kezuka, A. Nakamura, N. Shibata, Y. Ikuhara, *Nano Lett.* **2017**, *17*, 2908.
[30] G. B. Olson, M. Cohen, *Acta Metall.* **1979**, *27*, 1907.
[31] Y. Sun, S. E. Thompson, T. Nishida, *J. Appl. Phys.* **2007**, *101*, 104503.
[32] K.-H. Xue, P. Blaise, L. R. C. Fonseca, G. Molas, E. Vianello, B. Traoré, B. De Salvo, G. Ghibaudo, Y. Nishi, *Appl. Phys. Lett.* **2013**, *102*, 201908.
[33] G. Bersuker, J. Yum, V. Iglesias, M. Porti, M. Nafría, K. McKenna, A. Shluger, P. Kirsch, R. Jammy, 2010 Proc. Eur. Solid State Device Res. Conf. **2010**, pp. 333-336.
[34] K. H. Xue, B. Traore, P. Blaise, L. R. C. Fonseca, E. Vianello, G. Molas, B. D. Salvo, G. Ghibaudo, B. Magyari-Kope, Y. Nishi, *IEEE Trans. Electron Devices* **2014**, *61*, 1394.
[35] E. Hildebrandt, J. Kurian, M. M. Müller, T. Schroeder, H.-J. Kleebe, L. Alff, *Appl. Phys. Lett.* **2011**, *99*, 112902.
[36] J. A. Kilner, *Nat. Mater.* **2008**, *7*, 838.
[37] R. Pornprasertsuk, P. Ramanarayanan, C. B. Musgrave, F. B. Prinz, *J. Appl. Phys.* **2005**, *98*, 103513.
[38] A. Kushima, B. Yildiz, *J. Mater. Chem.* **2010**, *20*, 4809.
[39] B. Yildiz, *MRS Bull.* **2014**, *39*, 147.
[40] C. Jiang, N. Swaminathan, J. Deng, D. Morgan, I. Szlufarska, *Mater. Res. Lett.* **2014**, *2*, 100.
[41] N. Chen, L.-L. Niu, Y. Zhang, X. Shu, H.-B. Zhou, S. Jin, G. Ran, G.-H. Lu, F. Gao, *Sci. Rep.* **2016**, *6*, 36955.
[42] A. Buckow, R. Retzlaff, J. Kurian, L. Alff, *Supercond. Sci. Technol.* **2012**, *26*, 015014.
[43] M. Klinger, A. Jäger, *J. Appl. Crystallogr.* **2015**, *48*, 2012.
[44] R. Ruh, P. W. R. Corfield, *J. Am. Ceram. Soc.* **1970**, *53*, 126.
[45] G. Kresse, J. Hafner, *Phys. Rev. B* **1993**, *47*, 558.
[46] G. Kresse, J. Hafner, *Phys. Rev. B* **1994**, *49*, 14251.
[47] J. P. Perdew, K. Burke, M. Ernzerhof, *Phys. Rev. Lett.* **1996**, *77*, 3865.
[48] J. J. Bean, M. Saito, S. Fukami, H. Sato, S. Ikeda, H. Ohno, Y. Ikuhara, K. P. McKenna, *Sci. Rep.* **2017**, *7*, srep45594.
[49] K. P. McKenna, *ACS Energy Lett.* **2018**, *3*, 2663.
[50] C. J. Tong, K. P. McKenna, *J. Phys. Chem. C* **2019**, *123*, 23882.
[51] J. A. Quirk, V. K. Lazarov, K. P. McKenna, *Adv. Theory Simul.* **2019**, *2*, 1900157.
[52] J. Barthel, *Ultramicroscopy* **2018**, *193*, 1.
[53] J. M. Cowley, A. F. Moodie, *Acta Crystallogr.* **1957**, *10*, 609.

ACS OMEGA

http://pubs.acs.org/journal/acsodf

Article

Enhanced Conductivity and Microstructure in Highly Textured $TiN_{1-x}/c\text{-}Al_2O_3$ Thin Films

Alexander Zintler, Robert Eilhardt, Stefan Petzold, Sankaramangalam Ulhas Sharath, Enrico Bruder, Nico Kaiser, Lambert Alff, and Leopoldo Molina-Luna*

Cite This: *ACS Omega* 2022, 7, 2041−2048

Read Online

ACCESS | Metrics & More | Article Recommendations | Supporting Information

ABSTRACT: Titanium nitride thin films are used as an electrode material in superconducting (SC) applications and in oxide electronics. By controlling the defect density in the TiN thin film, the electrical properties of the film can achieve low resistivities and a high critical temperature (T_c) close to bulk values. Generally, low defect densities are achieved by stoichiometric growth and a low grain boundary density. Due to the low lattice mismatch of 0.7%, the best performing TiN layers are grown epitaxially on MgO substrates. Here, we report for the first time a T_c of 4.9 K for ultrathin (23 nm), highly textured (111), and stoichiometric TiN films grown on 8.75% lattice mismatch *c*-cut Al_2O_3 (sapphire) substrates. We demonstrate that with the increasing nitrogen deficiency, the (111) lattice constant increases, which is accompanied by a decrease in T_c. For highly N deficient TiN thin films, no superconductivity could be observed. In addition, a dissociation of grain boundaries (GBs) by the emission of stacking faults could be observed, indicating a combination of two sources for electron scattering defects in the system: (a) volume defects created by nitrogen deficiency and (b) defects created by the presence of GBs. For all samples, the average grain boundary distance is kept constant by a miscut of the *c*-cut sapphire substrate, which allows us to distinguish the effect of nitrogen deficiency and grain boundary density. These properties and surface roughness govern the electrical performance of the films and influence the compatibility as an electrode material in the respective application. This study aims to provide detailed and scale-bridging insights into the structural and microstructural response to nitrogen deficiency in the *c*-Al_2O_3/TiN system, as it is a promising candidate for applications in state-of-the-art systems such as oxide electronic thin film stacks or SC applications.

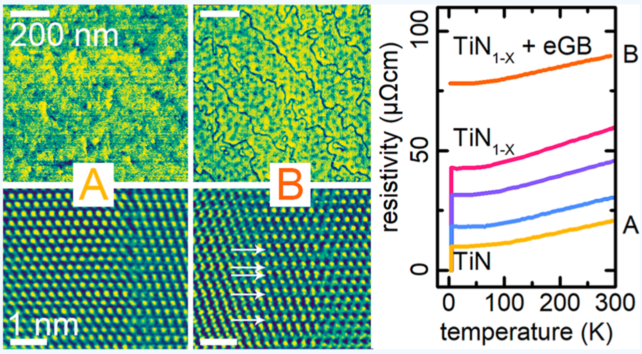

1. INTRODUCTION

Titanium nitride (TiN) is an intensely studied electrode material for oxide and superconducting (SC) electronics. For example, the successful combination of TiN and dielectric materials has been demonstrated on hafnium oxide (HfO_2) in complementary metal-oxide-semiconductor field-effect transistors and next-generation Hafnia-based resistive random access memories (RRAM).[1−3] Ferroelectric RAM (FeRAM), which requires symmetric electrodes, can also be realized with TiN as a bottom and top electrode.[4−8] In addition, TiN is a strong candidate as an electrode material in Josephson junctions and SC coplanar waveguides[9] with bulk transition temperature (T_c) of up to 6.0 K[10−12] and exhibits low losses at microwave frequencies.[13] In the search for the highest possible T_c, extensive research including machine learning-based growth parameter prediction is applied.[14] TiN has also gained significant interest in plasmonic and metamaterial applications in the visible and near-infrared wavelength range.[15] The fabrication of TiN electrodes is generally based on thin film deposition by either physical vapor deposition techniques, such as radio frequency (RF) sputtering, chemical vapor deposition (CVD) techniques like inorganic CVD or metal organic CVD (MOCVD), or by sol−gel based approaches.

These films exhibit resistivity values ranging from 14 to 1000 μΩcm for film thicknesses above 40 nm.[9,16−18] Sol−gel based approaches of depositing a TiO_2 film with subsequent nitridation achieved 40 nm TiN films with a 1510 μΩcm resistivity.[19] In most cases, these TiN thin films exhibit a polycrystalline microstructure with a columnar grain growth[20−22] and grain boundaries (GBs) that run along the entire thin film thickness.[23] This microstructure is commonly discussed as the source for reduced conductivity in TiN thin films.[24] The use of highly epitaxial TiN thin films would be

Received: October 4, 2021
Accepted: December 10, 2021
Published: January 3, 2022

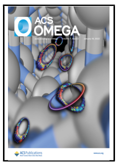

https://doi.org/10.1021/acsomega.1c05505

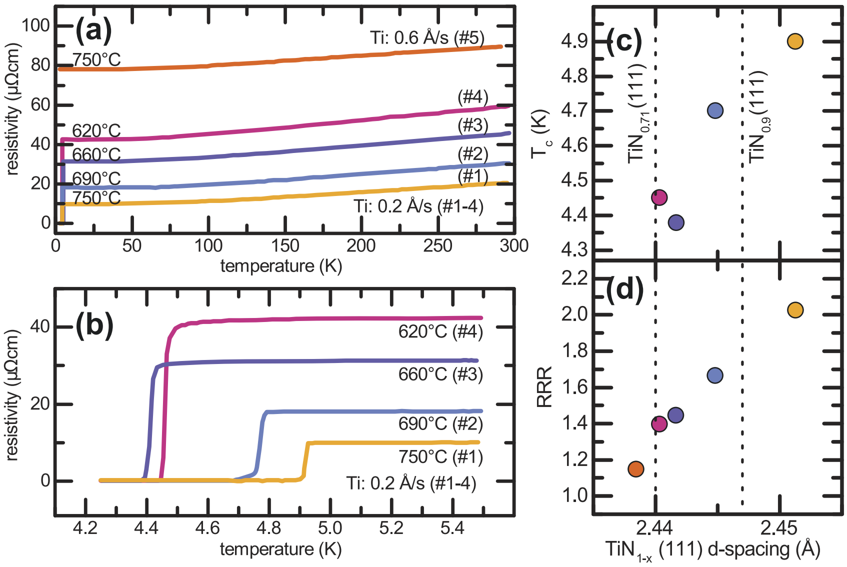

Figure 1. With an increase in growth temperature, the room temperature resistivity ρ(300 K) decreases (a) while T_c increases (b), which is associated with an increase in the residual resistance ratio (RRR = ρ(300 K)/ρ(10 K)), and (c) increase in the TiN_{1-x} (111) *d*-spacing (d); dashed lines indicate literature references for N-deficient and stoichiometric TiN_{1-x} compositions.

advantageous for thin film electronic applications.[25] Epitaxial or single-orientation growth of TiN has been previously reported in the literature using DC reactive sputtering,[26] pulse laser deposition (PLD),[27] atomic layer deposition (ALD),[28,29] and reactive molecular beam epitaxy (RMBE) methods.[9,30] High-quality epitaxy leads to very smooth thin film surfaces and low-defect densities. In the work by Krockenberger et al., TiN grown on MgO substrates by RMBE yields T_c of up to 5.25 K and resistivity in the range of 10−15 $\mu\Omega$cm at 40 nm film thickness.[9] The highest surface quality with a T_c of 5.25 K was obtained for thin films grown at 720 °C. Superconductivity was found to disappear at lower growth temperatures due to a decrease in the nitrogen content of the thin films. As demonstrated by Torgovkin et al., this can be reversed by annealing deficient TiN_{1-x} layers in a nitrogen atmosphere.[12] Chen et al. achieved RMBE-based quasi-epitaxial growth[31] TiN thin films on Si and Al_2O_3 substrates at elevated temperatures, resulting in T_c as high as 5.9 K for 130 nm thick films[30] (closest to bulk TiN, T_c = 6.0 K[11]). At the same time, the presence of nitrogen vacancies and GBs in TiN for RRAM applications has been reported to be beneficial for oxygen incorporation at the HfO_2/TiN interface during resistive switching processes.[32]

To our knowledge, highest surface quality TiN (001) thin films were reported when grown on MgO (001) substrates due to their low lattice mismatch (0.7%). However, Narayan et al. reported the epitaxial growth of TiN (001) on Si(001) substrates by PLD, which was suggested to occur via a domain matching epitaxy.[33] This is unexpected because Si (001) as a substrate for TiN (001) thin films should not yield high epitaxial growth due the high lattice mismatch of 25%. Here, the epitaxy is induced by the common structure, which is composed of four TiN (001) unit cells matching on three Si (001) unit cells, resulting in a lattice mismatch of less than 4%. Reisinger et al. identified a recombination in the Si (001)/TiN (001) system with a “5-on-4-cube-on-cube” reconstruction (lattice mismatch 2.4%) for lower deposition temperatures.[34,35] For 100 nm thick films, Talyansky et al. reported epitaxial growth of TiN (111) film on *c*-cut sapphire substrates with resistivity as low as 13 $\mu\Omega$cm and surface roughness (RMS) of 0.6−1 nm.[36] A high lattice misfit of 8.75% was calculated considering a rhomb-on-rhomb growth on the *c*-cut sapphire substrate.

Although quasi epitaxial growth of TiN thin films was reported for both Silicon and *c*-cut sapphire substrates,[31,37] there is a lack of experimental evidence to clarify the specific nature and properties of the grown microstructures. The high relevance of microstructural effects in TiN is underpinned by studies reporting a total loss of SC for films thinner than 40 nm.[12,16] Most studies are limited by being confined to macroscopic characterization methods like resistivity and X-ray diffraction (XRD) techniques, which allow for functional assessment of the as-grown films, but provide an incomplete picture of the deposited thin films. This study aims at broadening the understanding of defect sources in TiN thin films, namely, nitrogen deficiency and grain boundary density, by combining macroscopic and microscopic investigations down to the atomic level.

2. RESULTS AND DISCUSSION

2.1. TiN_{1-x}—Nitrogen Deficiency.

Figure 1a shows the temperature-dependent resistivity measurements of the ∼25 nm thick TiN thin films. Films with increasing nitrogen deficiency are presented in the sample series number #1 to #5. The N deficiency was introduced by (a) lowering the substrate temperature and (b) increasing the Ti evaporation rate; see the Experimental Section for further details. Figure 1b shows the low-temperature regime of Figure 1a to reveal the transition temperature to the SC state. Only sample #5 does not show a critical temperature (T_c) above the lowest measurement temperature of 4.2 K. To investigate the influence of the growth temperature in more detail, out-of-plane *d*-spacing (111) values were retrieved from XRD $2\theta/\omega$-scans, as shown in Figure S1. The TiN thin film with the largest *d*-spacing (2.451 Å, #1) shows the highest T_c value (4.9 K), as shown in Figure 1c. T_c drops to 4.4 K at a *d*-spacing of 2.440 Å (#4). The film with the lowest *d*-spacing (2.438 Å, #5) shows no SC. The *d*-spacings found for the different deposition conditions can be compared to literature data of known stoichiometry, here (111) $TiN_{0.71}$[38] and $TiN_{0.9}$[39] (dashed lines, Figure 1c,d), which allows for the estimation of the nitrogen deficiency. The most stoichiometric film yields a high T_c, whereas the most nitrogen deficient sample shows no T_c. Changing nitrogen deficiency directly translates to the formation of nitrogen vacancies in the crystal lattice.[11] To investigate the defect density of the TiN thin film, the residual resistance ratio (RRR)[12] was calculated (Figure 1d). RRR is defined as the quotient of the resistivity at room temperature (RT) and at 10 K [RRR = ρ(300 K)/ρ(10 K)]. The conductivity at 10 K is an indirect measure of defect density because the (thermal) phonon scattering contribution is greatly reduced at this temperature.[40] In the present system, this defect density is primarily governed by N deficiency shown by a decrease in RRR with smaller d-spacing.

2.2. Thin Film Microstructure.

The doubling of resistivity cannot be only explained by the volume defects introduced by the increased nitrogen deficiency. Another source of defects that decreases electrical conductivity in a material is the presence of GBs. A first indication for the presence of GBs would be the existence of more than one in-plane orientation of the (111) oriented TiN grains. The out-of-plane texture that was extracted from the $2\theta/\omega$ scans is TiN (111)||Al_2O_3 (001). The in-plane alignment of the TiN grains can be achieved by azimuthal or ϕ-scan. The results are depicted in Figure S1 and show that TiN {111} peaks are separated by 60° and are offset by ± 30° to the Al_2O_3 $\{\bar{1}02\}$ peaks. This indicates the presence of two in-plane locked crystal orientations or domains, which are 60° in-plane rotated to each other. This was also previously reported for epitaxial TiN (111) thin films on c-cut Al_2O_3 and Si substrates[36,41] where the equivalent TiN $(01\bar{1})$ and $(10\bar{1})$ crystal orientations align along Al_2O_3 (100). The full epitaxial relationship can thus be summarized as follows: TiN (111)|| Al_2O_3 (001) out-of-plane and TiN$(01\bar{1})$,$(10\bar{1})$||Al_2O_3(100) in-plane.

With an electron mean free path (MFP) of ~100 nm for TiN thin films as estimated by Krockenberger et al.[9] for a 40 nm TiN (001) film on MgO (001), a supposedly grain boundary free TiN film was grown epitaxially on the low lattice mismatch substrate. In the present samples, a grain size distribution analysis provides insights into the contribution of these boundaries in the resistivity.[10] The contribution of these GBs is higher if the distance between the boundaries is the same length scale as the MFP.[42] A common method to image GBs is backscatter electron (BSE) imaging, which has been applied to the present sample series and is displayed in Figure 2.

Figure 2a shows a model for two 60° in-plane rotated TiN grains with GBs indicated by dashed lines. The GBs that are formed can be understood as twins (with boundaries of the $(\bar{1}2\bar{1})/(\bar{2}11)/(11\bar{2})$ type). Figure 2b−f shows representative top-view BSE images of the TiN films. BSE contrast is susceptible to the crystal quality, grain orientation, and RMS. With the film fully aligned in the (111) orientation, the observed contrast should only indicate GBs and roughness. GBs reduce the number of backscattered electrons due to the presence of defects in the crystal lattice, thus giving a detailed view of the thin film microstructure. For the sample with the highest nitrogen deficiency (Figure 2f), GBs are visible as meandering dark lines. For the samples grown at 620, 660, and 690 °C and the stoichiometric sample grown at 750 °C, no distinct GBs can be observed. Dark spots observed for the low growth temperature samples (Figure 2b−d) can be correlated with the increase in RMS as indicated by the X-ray reflectometry (XRR) results (Figure S3a) down to a RMS of 1.5 nm for the films grown at 750 °C. The meandering of the boundaries in the sample shown in Figure 2f does not indicate a random behavior, but it follows a set of three dominating orientations. They correspond to the twin boundaries marked by dashed lines shown in Figure 2a. Consequently, this indicates the presence of a high number of twin boundaries for the sample shown in Figure 2f.

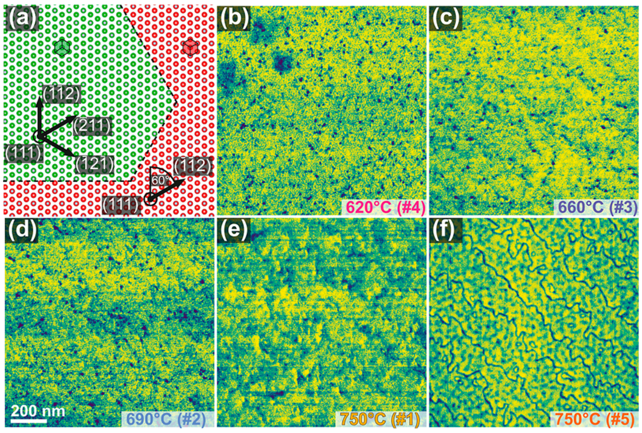

Figure 2. (a) Twin grain boundary of two 60° in-plane rotated TiN grains (red and green). (b−e) Top view BSE maps of the SC TiN thin films showing no visible GBs in contrast to the non-SC TiN thin film (f). False color is applied to enhance contrast.

With BSE imaging, no GBs could be observed for the samples grown at lower temperatures. However, XRD ϕ-scans indicate that there are two orientations of the TiN grains present in each sample. To investigate the microstructure of all samples, ion channeling contrast (iCC) imaging[43] was performed, as shown in Figure 3. The imaging conditions were selected to give the strongest iCC between the two orientations. A sample tilt of 54° from the 30 keV Ga ion beam allowed the ions to penetrate one TiN orientation at the prominent (001) zone axis, while the other grain orientation would be oriented at the same time along the $(\bar{1}22)$ zone axis. The discrepancy between the index of the zone axis directly correlates with the secondary electron (SE) yield and thus the observed contrast in the images (prominent {001} zone axis, low SE yield; $\{\bar{1}22\}$ zone axis, high SE yield).[44] With the high contrast achieved in an otherwise featureless surface, this method proved to be ideal to identify grain sizes and microstructures in this system, which can also be optimized by a ϕ/azimuth rotation series. In the iCC images, large, over 100 nm sized grains can be observed for all samples.

The anisotropy of the grain size can be attributed to a miscut of the c-cut sapphire substrate, which was used for all samples. Cuccureddu et al. found that even for nominally 0° miscut "c-cut" samples, there are still surface steps present that are homogeneously distributed on the surface.[45] For a 0.15° miscut c-Al_2O_3 sample, the step width was found to be 120 nm. In addition, annealing leads to a "bunching" of the surface steps if they are held at elevated temperatures, meaning that each resulting step height is a multiple of $c/6$ = 2.2 Å of the Al_2O_3 c-axis unit cell parameter (c = 13 Å). The step width and height converge to uniformity.[46] The (111) d-spacing value of TiN is 2.439 Å, which is a ~10% deviation of the $c/6$ Al_2O_3 = 2.2 Å (see Figure S4) lattice constant along growth direction. A

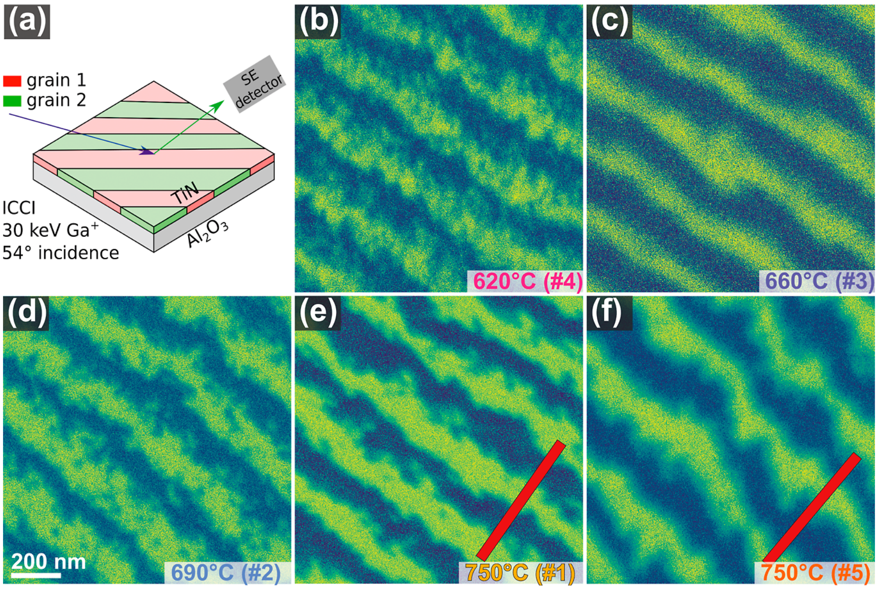

Figure 3. (a) Ion channeling contrast (iCC) imaging geometry. (b−f) iCC images of the samples revealing an elongated grain structure with comparable grain sizes for all samples. Red lines (e,f) showing the orientation of the cross sections cut in the subsequent focused ion beam lamella preparation, perpendicular to the observed GBs.

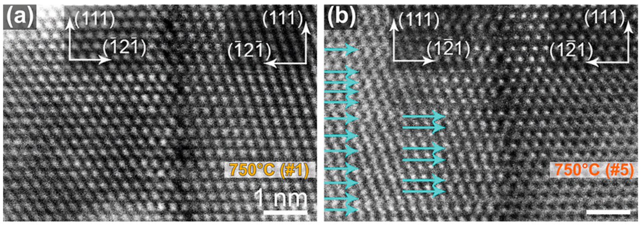

Figure 4. High-angle annular dark-field scanning transmission electron microscopy (HAADF-STEM) images of $\{\bar{1}2\bar{1}\}$ twin boundaries in the (a) SC and (b) non-SC TiN thin films. The grain boundary in (b) shows a high density of stacking faults in the atomic resolution image, indicated by blue arrows.

bunched surface step of $5^*c/6$ Al_2O_3 would introduce an overall mismatch of 56%, whereas a surface step of $9^*c/6$ Al_2O_3 would be a full TiN (111) *d*-spacing. Depending on the step height, the bonding configuration for the first adatom differ[47] and might trigger the respective TiN in-plane rotation (the out-of-plane direction fixed by the rhomb-on-rhomb epitaxy). By this high degree of ordering, the observed consistent alternation of in-plane orientations can be understood as an effect of uniform step widths and heights on the seeding conditions. The investigated TiN films have been grown on the same batch of substrates, which were heated during deposition and which will therefore yield to similar surface steps, as indicated by the uniform grain size distribution throughout the sample series. The four-point electrode geometry used in the resistivity measurement was not aligned with the observed elongation. The anisotropy, induced by the substrate miscut, dictates one crucial source for defects in the thin film: the grain boundary density. It is virtually the same for all samples and thus will have the same contribution for all samples. For the following high-resolution scanning transmission electron microscopy (HR-STEM) analysis, cross-sectional FIB lamellae have been cut from the samples grown at 750 °C. Cutting was performed perpendicular to the elongated grain structures (indicated in Figure 3e,f) to ensure that the GBs are aligned along the observation direction of the STEM.

2.3. Atomic Structure of (Dissociated) Twin GBs.

Figure 4 shows representative cross sections of GBs for the samples grown at 750 °C. The sets of neighboring grains are all oriented with (111) pointing upward along growth direction, which confirms the observations of the $2\theta/\omega$ scans (Figure 1). Both of the imaged GBs can be indexed as twin boundaries of the $\{\bar{1}2\bar{1}\}$ type. For the sample grown at a Ti evaporation rate of 0.2 Å/s (Figure 4a), atomic resolution high-angle annular dark-field (HAADF)-STEM imaging shows that the defects present at the boundary are located at the boundary itself, where the joining of the lattices of the grains form periodic recombination sites along the boundary. This is in stark contrast to the boundary of the sample grown at 0.6 Å/s (Figure 4b). Here, an extended defect structure indicated by split atomic columns (indicated by blue arrows) can be observed. These variations in contrast can be attributed to stacking faults along the (111) axis for the left grain shown in Figure 4b. Twin boundary dissociation by stacking fault emission is observed for other systems[48,49] as well as for TiN, but up until this point, only under mechanical deformation.[50] Strain induced by the lattice mismatch in the present substrate/thin film stack in combination with the growth conditions of the RMBE deposition process was reported as the cause for the occurrence of stacking faults in the Si/GaAs system.[51,52] Here, the volume affected by stacking faults extends through the full film thickness up to the surface of the film, where it gives rise to the grain boundary contrast found in the BSE images (Figure 2f), as they pose a sample volume of high defect concentration, reducing the backscatter yield.

Strongly confined geometrical conditions for the microstructure developed during the thin film growth process have a direct impact on the physical properties. A high fraction of high symmetry boundaries are generally associated with reduced resistance in conductors.[41,53] This is the case in our study because the microstructure of the TiN films contains almost solely twin boundaries. If the average grain size is in the range of the MFP, the grain boundary can be considered as a main contributor to electron scattering, increasing the resistivity.[24,54] Due to the equal average grain size in the present sample series, the impact on resistivity should therefore be equivalent. Nonetheless, the defects associated with the extended GBs play a crucial role in the contribution to the resistivity. Extended scattering regions lead to higher resistivity, which is described as a reduction of "grain boundary transparency" in terms of electrical conduction across a grain boundary.[55−57] This is directly evident in the increase of conductivity (Figure 1a). There is also a higher concentration of oxygen[12] and other contaminants[58] expected at the boundaries, which could negatively affect electronic transport properties.

In their application as bottom electrodes for valence change memory RRAM devices, the ability of the electrodes to incorporate oxygen plays a fundamental role in the resistive switching process.[59−63] Nitrogen-deficient TiN thin films lower the energy necessary to incorporate oxygen ions in the electrode material.[32] As GBs form a localized high density of defects, especially for the dissociated GBs observed in this work, they would have the potential to locally facilitate electroforming and switching processes.[3] As the microstructure of the TiN electrode also defines the growth conditions—or conditions for crystallization by annealing for ALD grown films[64]—GBs present a predefined seeding location and thus will have a direct influence on the microstructure observed in subsequent layers of a thin film stack.[3] This influence can be further addressed by nanoscale orientation mapping techniques like automated crystal orientation mapping in a plan-view geometry.[65]

3. CONCLUSIONS

The impact of nitrogen deficiency on the room and low temperature conductivity as well as on the microstructure and type of evolving GBs was studied for the c-Al_2O_3/TiN system. By combining XRD $2\theta/\omega$, ϕ-scans, BSE, iCC imaging in a multibeam FIB system and atomic resolution HR-STEM, the microstructure, grain size, and type of GBs were determined. The ∼25 nm thick TiN films exhibit a homogeneous (111) out-of-plane texture, with a set of two in-plane rotations, separated by 60°. This texture is defined by the quasi epitaxial growth of (111) TiN on c-Al_2O_3 where the large lattice mismatch of 8.75% is compensated by a rhomb-on-rhomb configuration. A fixed grain size as observed for the present sample series allowed us to separate the grain boundary density, as one contributor to defect density, from the effect of increasing nitrogen deficiency. The observed grain boundary density and the anisotropy of the grain size are directly related to the surface step density found on nominally 0° c-cut sapphire substrates. These steps also define the initial seeding conditions of the TiN grains and result in the alternating in-plane rotations observed in the thin film microstructure. Increased nitrogen deficiency has three effects on the film properties: (a) the loss of superconductivity, (b) an increase in resistivity, and (c) grain boundary dissociation by stacking fault emission. Nonetheless, the same morphological quality is achieved. Stoichiometric, ultrathin 25 nm films are achieved for the first time with a room-temperature conductivity of 10 $\mu\Omega$cm and a T_c of 4.9 K with a RMS of ∼1.5 nm. The observed properties match best in class SC epitaxially grown TiN films on MgO substrates.

4. EXPERIMENTAL SECTION

BSE imaging was performed on a Tescan Mira3 XMH at 15 kV, 320 μs dwell time and 434 pA specimen current using a Deben 4 quadrant detector. Ion beam channeling contrast (iCC) imaging and cross-sectional focused ion beam (FIB) sample preparation for scanning transmission electron microscopy (STEM) were performed on a JEOL JIB-4600F, and iCC imaging was conducted at 30 keV acceleration voltage. Atomic resolution high-angle annular dark-field (HAADF) STEM imaging was performed on a JEOL JEM-ARM200F operated at 200 kV with a semiconvergence angle of 25 mrad.

In this study, an electron-beam evaporation setup was used to evaporate elemental sources of titanium (99.99%, Chempur). Nitrogen radicals obtained using a RF plasma source (Oxford Applied Research, HD25) were used as the source of nitridation in our experiments. Mass flow controllers (MFC) allowed us to control the flow rates of nitrogen (99.995% purity) to the radical sources. The growth temperature was increased from 620 to 750 °C with a constant Ti evaporation rate of 0.2 Å/s, a nitrogen flow of 1.0 sccm, and a RF power of 200 W. For a sample with higher nitrogen deficiency, a Ti evaporation rate of 0.6 Å/s has been selected. Initial selection of the growth parameters included aspects like minimization of nitrogen deficiency[26] stoichiometry, RMS, and grain size.[17,66]

XRD and XRR were performed on a Rigaku (SmartLab) X-ray diffractometer by using Cu $K\alpha_1$ ($\lambda = 1.54057$ Å) at 45/170 kV/mA and a parallel beam geometry and on a Seifert PTS by using Cu $K\alpha_{1,2}$ ($\lambda = 1.54057$ Å) at 40/40 kV/mA and a parallel beam geometry with a graphite monochromator.

A Keithley 6221 model current source and Keithley 2182A model nanovoltmeter were used for the presented four-probe resistivity measurements, while the temperature was measured using a calibrated Lakeshore silicon diode sensor (model DT-670D-SD), placed in contact with the sample stage.

■ ASSOCIATED CONTENT

Supporting Information

The Supporting Information is available free of charge at https://pubs.acs.org/doi/10.1021/acsomega.1c05505.

> XRD 2θ scans for all samples, indicating the TiN (111) lattice parameter change due to nitrogen deficiency; XRD ϕ scans for all samples of TiN {111} and Al_2O_3 (102), showing the in-plane alignment of the film to substrate; XRR scans for all samples, indicating RMS and film density; and VESTA[67] models of the substrate and film, indicating the (001)/6 Al_2O_3 and (111) TiN lattice spacings (PDF)

■ AUTHOR INFORMATION

Corresponding Author

Leopoldo Molina-Luna − *Advanced Electron Microscopy, Institute of Materials Science, TU Darmstadt, 64287 Darmstadt, Germany;* orcid.org/0000-0002-9412-8093; Phone: +49 6151 16 20180; Email: leopoldo.molina-luna@aem.tu-darmstadt.de, molina@aem.tu-darmstadt.de

Authors

Alexander Zintler − *Advanced Electron Microscopy, Institute of Materials Science, TU Darmstadt, 64287 Darmstadt, Germany;* orcid.org/0000-0002-2272-3184

Robert Eilhardt – *Advanced Electron Microscopy, Institute of Materials Science, TU Darmstadt, 64287 Darmstadt, Germany*

Stefan Petzold – *Advanced Thin Film Technology, Institute of Materials Science, TU Darmstadt, 64287 Darmstadt, Germany*

Sankaramangalam Ulhas Sharath – *Advanced Thin Film Technology, Institute of Materials Science, TU Darmstadt, 64287 Darmstadt, Germany*

Enrico Bruder – *Physical Metallurgy, Institute of Materials Science, TU Darmstadt, 64287 Darmstadt, Germany*

Nico Kaiser – *Advanced Thin Film Technology, Institute of Materials Science, TU Darmstadt, 64287 Darmstadt, Germany;* orcid.org/0000-0002-5644-890X

Lambert Alff – *Advanced Thin Film Technology, Institute of Materials Science, TU Darmstadt, 64287 Darmstadt, Germany*

Complete contact information is available at: https://pubs.acs.org/10.1021/acsomega.1c05505

Notes

The authors declare no competing financial interest.

■ ACKNOWLEDGMENTS

This work was supported by the European Research Council (ERC) "Horizon 2020" Program under Grant no. 805359-FOXON and the Deutsche Forschungsgemeinschaft (DFG) under project 384682067 and was undertaken in the framework of the WAKeMeUP and StorAIge projects, which has received funding from the Electronic Components and Systems for European Leadership Joint Undertaking in collaboration with the European Union's H2020 Framework Programme (Grant no. H2020/2014–2020) and National Authorities, under Grant Agreement nos. 3783176 and 101007321 as well by the Federal Ministry of Education and Research (BMBF) under contract 16MEE0154. The authors thank Dr. Joachim Brötz for assisting with the $2\theta/\omega$ and ϕ XRD scans. We acknowledge support by the Deutsche Forschungsgemeinschaft (DFG – German Research Foundation) and the Open Access Publishing Fund of Technische Universität Darmstadt.

■ REFERENCES

(1) Sharath, S. U.; Vogel, S.; Molina-Luna, L.; Hildebrandt, E.; Wenger, C.; Kurian, J.; Duerrschnabel, M.; Niermann, T.; Niu, G.; Calka, P.; Lehmann, M.; Kleebe, H.-J.; Schroeder, T.; Alff, L. Control of Switching Modes and Conductance Quantization in Oxygen Engineered HfOxbased Memristive Devices. *Adv. Funct. Mater.* **2017**, *27*, 1700432.

(2) Waser, R.; Dittmann, R.; Staikov, G.; Szot, K. Redox-Based Resistive Switching Memories - Nanoionic Mechanisms, Prospects, and Challenges. *Adv. Mater.* **2009**, *21*, 2632–2663.

(3) Petzold, S.; Zintler, A.; Eilhardt, R.; Piros, E.; Kaiser, N.; Sharath, S. U.; Vogel, T.; Major, M.; McKenna, K. P.; Molina-Luna, L.; Alff, L. Forming-Free Grain Boundary Engineered Hafnium Oxide Resistive Random Access Memory Devices. *Adv. Electron. Mater.* **2019**, *5*, 1900484.

(4) Böscke, T. S.; Müller, J.; Bräuhaus, D.; Schröder, U.; Böttger, U. Ferroelectricity in Hafnium Oxide Thin Films. *Appl. Phys. Lett.* **2011**, *99*, 102903.

(5) Hyuk Park, M.; Joon Kim, H.; Jin Kim, Y.; Lee, W.; Moon, T.; Seong Hwang, C. Evolution of Phases and Ferroelectric Properties of Thin Hf0.5Zr0.5O2 Films According to the Thickness and Annealing Temperature. *Appl. Phys. Lett.* **2013**, *102*, 242905.

(6) Cao, R.; Wang, Y.; Zhao, S.; Yang, Y.; Zhao, X.; Wang, W.; Zhang, X.; Lv, H.; Liu, Q.; Liu, M. Effects of Capping Electrode on Ferroelectric Properties of Hf0.5Zr0.5O2 Thin Films. *IEEE Electron Device Lett* **2018**, *39*, 1207.

(7) Schroeder, U.; Richter, C.; Park, M. H.; Schenk, T.; Pešić, M.; Hoffmann, M.; Fengler, F. P. G.; Pohl, D.; Rellinghaus, B.; Zhou, C.; Chung, C.-C.; Jones, J. L.; Mikolajick, T. Lanthanum-Doped Hafnium Oxide: A Robust Ferroelectric Material. *Inorg. Chem.* **2018**, *57*, 2752–2765.

(8) Max, B.; Hoffmann, M.; Mulaosmanovic, H.; Slesazeck, S.; Mikolajick, T. Hafnia-Based Double-Layer Ferroelectric Tunnel Junctions as Artificial Synapses for Neuromorphic Computing. *ACS Appl. Electron. Mater.* **2020**, *2*, 4023–4033.

(9) Krockenberger, Y.; Karimoto, S.-i.; Yamamoto, H.; Semba, K. Coherent Growth of Superconducting TiN Thin Films by Plasma Enhanced Molecular Beam Epitaxy. *J. Appl. Phys.* **2012**, *112*, 083920.

(10) Ningthoujam, R. S.; Gajbhiye, N. S. Synthesis, electron transport properties of transition metal nitrides and applications. *Prog. Mater. Sci.* **2015**, *70*, 50–154.

(11) Spengler, W.; Kaiser, R.; Christensen, A. N.; Müller-Vogt, G. Raman Scattering, Superconductivity, and Phonon Density of States of Stoichiometric and Nonstoichiometric TiN. *Phys. Rev. B: Solid State* **1978**, *17*, 1095–1101.

(12) Torgovkin, A.; Chaudhuri, S.; Ruhtinas, A.; Lahtinen, M.; Sajavaara, T.; Maasilta, I. J. High Quality Superconducting Titanium Nitride Thin Film Growth Using Infrared Pulsed Laser Deposition. *Supercond. Sci. Technol.* **2018**, *31*, 055017.

(13) Vissers, M. R.; Gao, J.; Wisbey, D. S.; Hite, D. A.; Tsuei, C. C.; Corcoles, A. D.; Steffen, M.; Pappas, D. P. Low Loss Superconducting Titanium Nitride Coplanar Waveguide Resonators. *Appl. Phys. Lett.* **2010**, *97*, 232509.

(14) Ohkubo, I.; Hou, Z.; Lee, J. N.; Aizawa, T.; Lippmaa, M.; Chikyow, T.; Tsuda, K.; Mori, T. Realization of Closed-Loop Optimization of Epitaxial Titanium Nitride Thin-Film Growth via Machine Learning. *Mater. Today Phys.* **2021**, *16*, 100296.

(15) Naik, G. V.; Saha, B.; Liu, J.; Saber, S. M.; Stach, E. A.; Irudayaraj, J. M. K.; Sands, T. D.; Shalaev, V. M.; Boltasseva, A. Epitaxial Superlattices with Titanium Nitride as a Plasmonic Component for Optical Hyperbolic Metamaterials. *Proc. Natl. Acad. Sci. U.S.A.* **2014**, *111*, 7546–7551.

(16) Xiang, W.; Liu, Y.; Zhang, J. Influence of Microstructure on the Electrical Properties of Heteroepitaxial TiN Films. *Electron. Mater. Lett.* **2018**, *14*, 314–318.

(17) Savvides, N.; Window, B. Electrical Transport, Optical Properties, and Structure of TiN Films Synthesized by Low-energy Ion Assisted Deposition. *J. Appl. Phys.* **1988**, *64*, 225–234.

(18) Sun, N.; Zhou, D.; Liu, W.; Shi, S.; Tian, Z.; Liu, F.; Li, S.; Wang, J.; Ali, F. Tailoring Surface Chemistry and Morphology of Titanium Nitride Electrode for On-Chip Supercapacitors. *ACS Sustainable Chem. Eng.* **2020**, *8*, 7869–7878.

(19) Valour, A.; Higuita, M. A. U.; Guillonneau, G.; Crespo-Monteiro, N.; Jamon, D.; Hochedel, M.; Michalon, J.-Y.; Reynaud, S.; Vocanson, F.; Jiménez, C.; Langlet, M.; Donnet, C.; Jourlin, Y. Optical, Electrical and Mechanical Properties of TiN Thin Film Obtained from a TiO2 Sol-Gel Coating and Rapid Thermal Nitridation. *Surf. Coat. Technol.* **2021**, *413*, 127089.

(20) Yu, J.; Phang, P.; Samundsett, C.; Basnet, R.; Neupan, G. P.; Yang, X.; Macdonald, D. H.; Wan, Y.; Yan, D.; Ye, J. Titanium Nitride Electron-Conductive Contact for Silicon Solar Cells By Radio Frequency Sputtering from a TiN Target. *ACS Appl. Mater. Interfaces* **2020**, *12*, 26177–26183.

(21) Grosso, S.; Latu-Romain, L.; Berthomé, G.; Renou, G.; Le Coz, T.; Mantel, M. Titanium and Titanium Nitride Thin Films Grown by Dc Reactive Magnetron Sputtering Physical Vapor Deposition in a Continuous Mode on Stainless Steel Wires: Chemical, Morphological and Structural Investigations. *Surf. Coat. Technol.* **2017**, *324*, 318–327.

(22) Sun, N.; Zhou, D.; Shi, S.; Liu, W.; Zhao, X.; Liu, F.; Tian, Z.; Li, S.; Wang, J.; Ali, F. DC Substrate Bias Enables Preparation of

Superior-Performance TiN Electrode Films over a Wide Process Window. *Mater. Res. Bull.* **2019**, *119*, 110575.

(23) Xu, Z.; Zhang, Z.; Bartosik, M.; Zhang, Y.; Mayrhofer, P. H.; He, Y. Insight into the Structural Evolution during TiN Film Growth via Atomic Resolution TEM. *J. Alloys Compd.* **2018**, *754*, 257−267.

(24) Patsalas, P.; Logothetidis, S. Optical, Electronic, and Transport Properties of Nanocrystalline Titanium Nitride Thin Films. *J. Appl. Phys.* **2001**, *90*, 4725−4734.

(25) Grossi, A.; Walczyk, D.; Zambelli, C.; Miranda, E.; Olivo, P.; Stikanov, V.; Feriani, A.; Sune, J.; Schoof, G.; Kraemer, R.; Tillack, B.; Fox, A.; Schroeder, T.; Wenger, C.; Walczyk, C. Impact of Intercell and Intracell Variability on Forming and Switching Parameters in RRAM Arrays. *IEEE Trans. Electron Devices* **2015**, *62*, 2502−2509.

(26) Johansson, B. O.; Sundgren, J. E.; Greene, J. E.; Rockett, A.; Barnett, S. A. Growth and Properties of Single Crystal TiN Films Deposited by Reactive Magnetron Sputtering. *J. Vac. Sci. Technol., A* **1985**, *3*, 303−307.

(27) Bonholzer, M.; Lorenz, M.; Grundmann, M. Layer-by-Layer Growth of TiN by Pulsed Laser Deposition on in-Situ Annealed (100) MgO Substrates. *Phys. Status Solidi A* **2014**, *211*, 2621−2624.

(28) Elers, K.-E.; Winkler, J.; Weeks, K.; Marcus, S. TiCl4 as a Precursor in the TiN Deposition by ALD and PEALD. *J. Electrochem. Soc.* **2005**, *152*, G589.

(29) Kim, J.; Hong, H.; Ghosh, S.; Oh, K.-Y.; Lee, C. Physical Properties of Highly Conformal TiN Thin Films Grown by Atomic Layer Deposition. *Jpn. J. Appl. Phys.* **2003**, *42*, 1375.

(30) Olson, G. A. Growth of Titanium-Nitride Thin Films for Low-Loss Superconducting Quantum Circuits. Ph.D. Thesis, University of Illinois at Urbana-Champaign, 2015. http://hdl.handle.net/2142/87951.

(31) Chen, W.-C.; Lin, Y.-R.; Guo, X.-J.; Wu, S.-T. Heteroepitaxial TiN of Very Low Mosaic Spread on Al2O3. *Jpn. J. Appl. Phys.* **2003**, *42*, 208.

(32) Bradley, S. R.; McKenna, K. P.; Shluger, A. L. The Behaviour of Oxygen at Metal Electrodes in HfO2 Based Resistive Switching Devices. *Microelectron. Eng.* **2013**, *109*, 346−350.

(33) Narayan, J.; Tiwari, P.; Chen, X.; Singh, J.; Chowdhury, R.; Zheleva, T. Epitaxial Growth of TiN Films on (100) Silicon Substrates by Laser Physical Vapor Deposition. *Appl. Phys. Lett.* **1992**, *61*, 1290−1292.

(34) Reisinger, D.; Schonecke, M.; Brenninger, T.; Opel, M.; Erb, A.; Alff, L.; Gross, R. Epitaxy of Fe3O4 on Si(001) by Pulsed Laser Deposition Using a TiN/MgO Buffer Layer. *J. Appl. Phys.* **2003**, *94*, 1857−1863.

(35) Willmott, P. R.; Timm, R.; Huber, J. R. RHEED Analysis of Interface Growth Modes of TiN Films on Si(001) Produced by Crossed Beam Laser Ablation. *Appl. Surf. Sci.* **1998**, *127−129*, 105−110.

(36) Talyansky, V.; Choopun, S.; Downes, M. J.; Sharma, R. P.; Venkatesan, T.; Li, Y. X.; Salamanca-Riba, L. G.; Wood, M. C.; Lareau, R. T.; Jones, K. A. Pulsed Laser Deposition of Titanium Nitride Films on Sapphire. *J. Mater. Res.* **1999**, *14*, 3298−3302.

(37) Volz, K.; Stolz, W.; Dadgar, A.; Krost, A. Growth of III/Vs on Silicon. In *Handbook of Crystal Growth*; Kuech, T. F., Ed., 2nd ed.; North-Holland: Boston, 2015; pp 1249−1300.

(38) Holmberg, B.; Yhland, M.; Dahlbom, R.; Sjövall, J.; Theander, O.; Flood, H. Structural Studies on the Titanium-Nitrogen System. *Acta Chem. Scand.* **1962**, *16*, 1255−1261.

(39) Christensen, A. N.; Hämäläinen, R.; Turpeinen, U.; Andresen, A. F.; Smidsrød, O.; Pontchour, C.-O.; Phavanantha, P.; Pramatus, S.; Cyvin, B. N.; Cyvin, S. J. The Temperature Factor Parameters of Some Transition Metal Carbides and Nitrides by Single Crystal X-Ray and Neutron Diffraction. *Acta Chem. Scand.* **1978**, *32a*, 89−90.

(40) Wilson, A. H. The Second Order Electrical Effects in Metals. *Math. Proc. Cambridge Philos. Soc.* **1937**, *33*, 371−379.

(41) Hultman, L.; Ljungcrantz, H.; Hallin, C.; Janzén, E.; Sundgren, J.-E.; Pécz, B.; Wallenberg, L. R. Growth and Electronic Properties of Epitaxial TiN Thin Films on 3C-SiC(001) and 6H-SiC(0001) Substrates by Reactive Magnetron Sputtering. *J. Mater. Res.* **1996**, *11*, 2458−2462.

(42) Zhu, Y. F.; Lang, X. Y.; Zheng, W. T.; Jiang, Q. Electron Scattering and Electrical Conductance in Polycrystalline Metallic Films and Wires: Impact of Grain Boundary Scattering Related to Melting Point. *ACS Nano* **2010**, *4*, 3781−3788.

(43) Giannuzzi, L. A.; Michael, J. R. Comparison of Channeling Contrast between Ion and Electron Images. *Microsc. Microanal.* **2013**, *19*, 344−349.

(44) Silk, J. R.; Dashwood, R. J.; Chater, R. J. Determination of Lattice Orientation in Aluminium Alloy Grains by Low Energy Gallium Ion-Channelling. *Nucl. Instrum. Methods Phys. Res., Sect. B* **2010**, *268*, 2064−2068.

(45) Cuccureddu, F.; Murphy, S.; Shvets, I. V.; Porcu, M.; Zandbergen, H. W.; Sidorov, N. S.; Bozhko, S. I. Surface Morphology of C-Plane Sapphire (α-Alumina) Produced by High Temperature Anneal. *Surf. Sci.* **2010**, *604*, 1294−1299.

(46) Gossmann, H. J.; Sinden, F. W.; Feldman, L. C. Evolution of Terrace Size Distributions during Thin-film Growth by Step-mediated Epitaxy. *J. Appl. Phys.* **1990**, *67*, 745−752.

(47) Lee, H.-J.; Fujii, K.; Goto, T.; Yao, T.; Chang, J. Effects of Controlled Ambidirectional Nucleation on the Heteroepitaxial Growth of M-GaN on m-Sapphire. *Appl. Phys. Lett.* **2011**, *98*, 071904.

(48) Lucadamo, G.; Medlin, D. L. Geometric Origin of Hexagonal Close Packing at a Grain Boundary in Gold. *Science* **2003**, *300*, 1272−1275.

(49) Rittner, J. D.; Seidman, D. N.; Merkle, K. L. Grain-Boundary Dissociation by the Emission of Stacking Faults. *Phys. Rev. B: Condens. Matter Mater. Phys.* **1996**, *53*, R4241−R4244.

(50) Zhang, L.; Wu, Y.; Yu, W.; Shen, S. Response of symmetric tilt grain boundary in titanium nitride under shear. *Eng. Anal. Bound. Elem.* **2019**, *105*, 231−241.

(51) Giannini, C.; Carlino, E.; Sciacovelli, P.; Tapfer, L.; Sauvage-Simkin, M.; Garreau, Y.; Jedrecy, N.; Véron, M. B.; Pinchaux, R. Influence of the Interface Layer on the Strain Relaxation of ZnSe Epitaxial Layers Grown by MBE on (001)GaAs. *J. Phys. D: Appl. Phys.* **1999**, *32*, A51−A55.

(52) Kim, S.-D.; Harris, J. S. Stacking Fault Stability in GaAs/Si Hetero-Epitaxial Growth. *J. Cryst. Growth* **1992**, *123*, 439−444.

(53) Lu, L.; Shen, Y.; Chen, X.; Qian, L.; Lu, K. Ultrahigh Strength and High Electrical Conductivity in Copper. *Science* **2004**, *304*, 422−426.

(54) Kasap, S.; Koughia, C.; Ruda, H. E. Electrical Conduction in Metals and Semiconductors. In *Springer Handbook of Electronic and Photonic Materials*; Kasap, S., Capper, P., Eds.; Springer International Publishing: Cham, 2017; p 1.

(55) Reiss, G.; Vancea, J.; Hoffmann, H. Grain-Boundary Resistance in Polycrystalline Metals. *Phys. Rev. Lett.* **1986**, *56*, 2100−2103.

(56) Olaya, J. J.; Huerta, L.; Rodil, S. E.; Escamilla, R. Superconducting Niobium Nitride Films Deposited by Unbalanced Magnetron Sputtering. *Thin Solid Films* **2008**, *516*, 8768−8773.

(57) Bishara, H.; Lee, S.; Brink, T.; Ghidelli, M.; Dehm, G. Understanding Grain Boundary Electrical Resistivity in Cu: The Effect of Boundary Structure. *ACS Nano* **2021**, *15*, 16607−16615.

(58) Ohya, S.; Chiaro, B.; Megrant, A.; Neill, C.; Barends, R.; Chen, Y.; Kelly, J.; Low, D.; Mutus, J.; O'Malley, P. J. J.; Roushan, P.; Sank, D.; Vainsencher, A.; Wenner, J.; White, T. C.; Yin, Y.; Schultz, B. D.; Palmstrøm, C. J.; Mazin, B. A.; Cleland, A. N.; Martinis, J. M. Room Temperature Deposition of Sputtered TiN Films for Superconducting Coplanar Waveguide Resonators. *Supercond. Sci. Technol.* **2013**, *27*, 015009.

(59) Gutiérrez Moreno, J. J.; Nolan, M. Ab Initio Study of the Atomic Level Structure of the Rutile TiO2(110)−Titanium Nitride (TiN) Interface. *ACS Appl. Mater. Interfaces* **2017**, *9*, 38089−38100.

(60) McKenna, K. P. Structure, Electronic Properties, and Oxygen Incorporation/Diffusion Characteristics of the Σ 5 TiN(310)[001] Tilt Grain Boundary. *J. Appl. Phys.* **2018**, *123*, 075301.

(61) Niu, G.; Calka, P.; Huang, P.; Sharath, S. U.; Petzold, S.; Gloskovskii, A.; Fröhlich, K.; Zhao, Y.; Kang, J.; Schubert, M. A.;

Bärwolf, F.; Ren, W.; Ye, Z.-G.; Perez, E.; Wenger, C.; Alff, L.; Schroeder, T. Operando Diagnostic Detection of Interfacial Oxygen 'Breathing' of Resistive Random Access Memory by Bulk-Sensitive Hard X-Ray Photoelectron Spectroscopy. *Mater. Res. Lett.* **2019**, *7*, 117−123.

(62) Yong, Z.; Persson, K.-M.; Saketh Ram, M.; D'Acunto, G.; Liu, Y.; Benter, S.; Pan, J.; Li, Z.; Borg, M.; Mikkelsen, A.; Wernersson, L.-E.; Timm, R. Tuning Oxygen Vacancies and Resistive Switching Properties in Ultra-Thin HfO2 RRAM via TiN Bottom Electrode and Interface Engineering. *Appl. Surf. Sci.* **2021**, *551*, 149386.

(63) Starschich, S.; Menzel, S.; Böttger, U. Evidence for Oxygen Vacancies Movement during Wake-up in Ferroelectric Hafnium Oxide. *Appl. Phys. Lett.* **2016**, *108*, 032903.

(64) Eilhardt, R.; Zintler, A.; Recalde, O.; Nasiou, D.; Petzold, S.; Alff, L.; Molina-Luna, L. Birth of a Grain Boundary: In Situ TEM Observation of the Microstructure Evolution in HfO2 Based Memristors. *Microsc. Microanal.* **2021**, *27*, 1238−1239.

(65) Zintler, A.; Eilhardt, R.; Wang, S.; Krajnak, M.; Schramowski, P.; Stammer, W.; Petzold, S.; Kaiser, N.; Kersting, K.; Alff, L.; Molina-Luna, L. Machine Learning Assisted Pattern Matching: Insight into Oxide Electronic Device Performance by Phase Determination in 4D-STEM Datasets. *Microsc. Microanal.* **2020**, *26*, 1908−1909.

(66) Chowdhury, R.; Vispute, R. D.; Jagannadham, K.; Narayan, J. Characteristics of Titanium Nitride Films Grown by Pulsed Laser Deposition. *J. Mater. Res.* **1996**, *11*, 1458−1469.

(67) Momma, K.; Izumi, F. VESTA 3 for Three-Dimensional Visualization of Crystal, Volumetric and Morphology Data. *J. Appl. Crystallogr.* **2011**, *44*, 1272−1276.

https://doi.org/10.1021/acsomega.1c05505
ACS Omega 2022, 7, 2041−2048

NANO LETTERS

pubs.acs.org/NanoLett Letter

Texture Transfer in Dielectric Layers via Nanocrystalline Networks: Insights from in Situ 4D-STEM

Robert Winkler, Alexander Zintler, Oscar Recalde-Benitez, Tianshu Jiang, Déspina Nasiou, Esmaeil Adabifiroozjaei, Philipp Schreyer, Taewook Kim, Eszter Piros, Nico Kaiser, Tobias Vogel, Stefan Petzold, Lambert Alff, and Leopoldo Molina-Luna*

Cite This: *Nano Lett.* 2024, 24, 2998–3004 **Read Online**

ACCESS | Metrics & More | Article Recommendations | Supporting Information

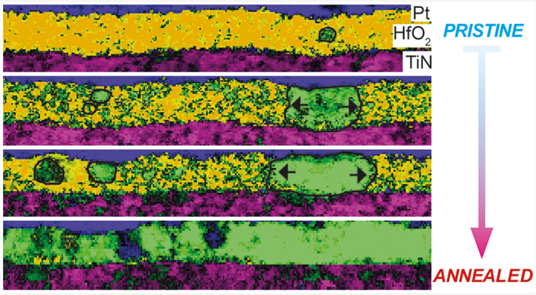

ABSTRACT: Transition metal oxide dielectric layers have emerged as promising candidates for various relevant applications, such as supercapacitors or memory applications. However, the performance and reliability of these devices can critically depend on their microstructure, which can be strongly influenced by thermal processing and substrate-induced strain. To gain a more in-depth understanding of the microstructural changes, we conducted in situ transmission electron microscopy (TEM) studies of amorphous HfO$_2$ dielectric layers grown on highly textured (111) substrates. Our results indicate that the minimum required phase transition temperature is 180 °C and that the developed crystallinity is affected by texture transfer. Using in situ TEM and 4D-STEM can provide valuable insights into the fundamental mechanisms underlying the microstructural evolution of dielectric layers and could pave the way for the development of more reliable and efficient devices for future applications.

KEYWORDS: *In situ transmission electron microscopy, scanning probe electron diffraction, automated crystal orientation mapping, annealing, dielectric layers, hafnia, microstructure evolution, four-dimensional scanning transmission electron microscopy*

Transition metal oxide (TMO) dielectric layers play a crucial role in various scientific and technological applications like field-effect transitions,[1] supercapacitors,[2] and emerging memories like resistive random access memory (RRAM).[3] The dielectric properties of TMOs, including their permittivity and dielectric constant, are influenced by factors like crystal structure, composition, and defects.[4] Nowadays, especially high-κ dielectrics like HfO$_2$ are of critical importance as they allow for thinner layers without compromising the device's performance or increasing leakage current.[5] As shown by our previous studies, performance metrics of RRAM devices can be optimized by careful oxygen[6−8] and grain boundary[9,10] engineering of the HfO$_2$ dielectric layer but also adjacent metal electrodes that sandwich the dielectric layer can impact performance.[11] These optimized dielectric layers were grown by reactive molecular beam epitaxy (RMBE) at elevated temperatures to utilize epitaxial texture transfer for successive grown layers. This, however, might be more challenging to integrate in a complementary metal oxide semiconductor (CMOS) back-end-of-line (BEOL) process.[12]

Commonly in the CMOS BEOL process, thermal annealing is used to activate dopants or remove defects.[13] In the case of RRAM, the thermal processing can strongly alter the polycrystallization of the dielectric layer.[14,15] For HfO$_2$ dielectric layers, previous reports that investigated annealing temperatures of HfO$_2$ thin films concluded similarly: typically, a temperature above 300 °C is required to crystallize HfO$_2$, while annealing temperatures increase with decreasing film thickness.[14,16−23] For high surface-to-interface ratios, studies have proven that crystallization can be suppressed and that at least a 6 nm thickness is required to crystallize into the monoclinic hafnia phase.[24] This is generally suboptimal for CMOS BEOL processes, as the goal is to fabricate the dielectric layer, in this case the high-κ HfO$_2$, as thin as possible to achieve high density and low-power operation while maintaining reliability and manufacturability.[25]

What is striking about these previous studies is that amorphous hafnia films grown by atomic layer deposition (ALD), a low-kinetic deposition technique,[26] required typically higher annealing temperatures compared to films grown by pulsed laser deposition (PLD),[27] a high-kinetic energy technique. This suggests that the growth technique might affect the atomic coordination of amorphous films, which in turn might affect the annealing temperature. In a study by Luo

Received: October 13, 2023
Revised: January 30, 2024
Accepted: January 31, 2024
Published: February 6, 2024

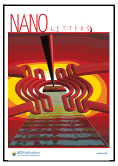

https://doi.org/10.1021/acs.nanolett.3c03941

and Demkov different atomic coordinated amorphous hafnia unit cells were investigated. They estimated the crystallization temperature for monoclinic HfO_2 to be 146 °C,[28] which is lower than experimentally determined annealing temperatures of 300 °C. In principle, this difference could be explained by the fact that HfO_2 thin films usually have a higher surface-to-interface ratio. However, HfO_2 thin films are grown on substrates and can be part of a thin film stack. As a result, the difference in Gibbs free energy and consequently the required temperature for phase transition could be altered by adjacent layers and accommodating strain.[24] Moreover, the adjacent layers might affect the crystallinity of the annealed film.

Therefore, a question arises about what the minimum required temperature would be to get a crystalline hafnia film with a microstructure (grain boundaries) that improves device performance metrics and if texture transfer via a nanocrystalline network is achievable.

To our best knowledge, time-resolved X-ray diffractometry (XRD) has been the primary tool for in situ investigation of the crystallization of HfO_2 thin films. However, due to the relatively large area of investigation in comparison to the expected grain size (a few nm), small parts that might have already crystallized cannot be measured by XRD and thus merge into the amorphous background. Hence, a precise identification of the required phase transition temperature might not be possible. In addition, the origin and dynamics of crystallization cannot be observed. Therefore, we investigate microstructural changes by conducting in situ transmission electron microscopy (TEM) heating of HfO_2 dielectric layers to determine the exact crystallization temperature and origin with nanometer resolution and correlate them to possible texture transfer mechanisms. In addition, microscopic findings are related to ex situ annealed macroscopic RRAM device performances.

30 × 30 μm^2 metal−insulator−metal (MIM) RRAM devices with the structure $Au/Pt/HfO_2/TiN/Al_2O_3$ were created by a combination of reactive molecular beam epitaxy (RMBE), optical lithography, and sputter coating. First, 50 nm TiN and 12 nm HfO_2 were grown consecutively on *c*-cut sapphire by using RMBE in a custom ultrahigh vacuum chamber (base pressure 10^{-9} mbar). Details on the RMBE chamber can be found elsewhere.[29] The TiN substrate was heated to 800 °C, and 4.5N pure Ti from Lesker was evaporated at 0.3 Å/s with in situ nitridation. Amorphous HfO_2 layers were grown at room temperature. 3N pure Hf from MaTeck was evaporated at 0.7 Å/s and in situ oxidized with 200 W RF-power. Second, following a lithography step for surface patterning, 100 nm Pt and 300 nm Au were sputtered. The RMBE-grown TiN and HfO_2 thin films were investigated by XRD with a Rigaku SmartLab diffractometer in parallel beam geometry by using a copper Kα X-ray source to verify thin film quality and amorphousness. Resistive switching for a device under test (DUT) was investigated with a Keithley 4200 semiconductor characterization system (SCS) by applying DC-negative voltage sweeps to the top electrode with the bottom electrode grounded. During electroforming, the SCS's internal current compliance (CC) was restricted to 10 and 100 μA to avoid hard dielectric breakdown. To investigate microstructural changes at the nanoscale during in situ heating, cross-sectional electron-transparent lamellae were fabricated. From the MIM devices, using the in situ lift-out focus ion beam (FIB) technique with a JEOL JIB-4600F and a Thermo Fisher Scientific Helios 5 Hydra dual beam system, the lamellae were transferred onto a microelectrical mechanical system (MEMS)-based heating chip from DENSsolutions. Details on the fabrication routine can be found elsewhere.[30] Using a JEOL ARM 200F TEM operated at 200 kV, high-resolution TEM and scanning probe electron diffraction (SPED) images were acquired with the Orius SC200D CCD from Gatan and the MerlinEM direct electron detector from Quantum Detectors, respectively. For SPED imaging, the smallest possible condenser aperture was used (10 μm), and the microscope was set to nanobeam electron diffraction (NBED) mode, yielding roughly an electron beam spot size of 1 nm. The 4D-STEM data set generated by SPED imaging was analyzed by ASTAR from Nanomegas to generate orientation and phase maps. Further information regarding the analysis procedure has been provided elsewhere.[31]

Selected high-resolution (HR) TEM images of the complete in situ heating experiment (summarized in the in situ heating TEM video in Supporting Information) are shown in Figure 1a−d. To enhance the visibility of microstructural changes, the fast Fourier transform (FFT) of the two growing grains is shown in Figure 1a1,a2−d1,d2. In its pristine state (t = 0 min), the investigated section of the dielectric layer is mostly amorphous hafnia; however, the FFT of grain I already shows nanocrystallinity. Increasing the temperature to 160 °C leads to crystallization of the hafnia layer. In this section, two grains grow from the corners of the image, parallel to the interfaces, toward each other until the formation of a grain boundary. The boundary between the crystalline and amorphous phase is indicated by colored lines. This boundary has been qualitatively determined by utilizing inverse FFTs obtained through band-pass filtering of the amorphous ring, which were subsequently overlaid on the HR TEM images depicted in Figure S1.

To investigate crystallization of the hafnia layer in more detail, a 2D waterfall plot, shown in Figure 2d, as a function of time and temperature (Figure 2f) of azimuthal integrations (AI) is retrieved from the FFT of the HR-TEM images by using the PASAD-tools from Gammer et al.[32] The FFT and corresponding AI of the pristine and crystallized hafnia layers of the investigated section are shown in Figure 2a,c and Figure 2b,e, respectively. Non-grayed-out parts of the FFTs visualize the range of the AI. To provide a more thorough comparison, azimuthal integrations are overlaid on FFTs of the pristine, crystallized, and intermediate states (after 69 min of heating) in Figure S2. The AI pattern for the pristine state shows a broad peak ranging from 3 to 4 nm^{-1}, which can be attributed to amorphous hafnia. After 60 min of continuous heating, this broad peak disappears, and two distinct peaks located at ∼3 and 4 nm^{-1} appear. The peaks at ∼4 nm^{-1} can be indexed as (200) HfO_2 and (111) TiN and the peak at ∼3 nm^{-1} as (11−1) HfO_2. Close inspection of the FFT of the annealed HR TEM sample indicates a texture relation between the (111) TiN and (200) HfO_2 crystallinity due to the close positioning of the diffraction spots (see also Figure S3).Though the peak at 3 nm^{-1} is not always visible, e.g., in the AI after 90 min of heating, inverse FFT retrieved by band-pass filtering at 3 ± 0.3 nm^{-1} (Figure S2d) reveals that this feature is related to the HfO_2 layer. However, the intensity of this feature might be affected by a loss of high resolution due to defocus as a consequence of drift during in situ heating, as shown by the feature at the TiN/HfO_2 interface.

To gain more insight into the origin and dynamics of grain growth, superimposed phase + phase reliability and orientation

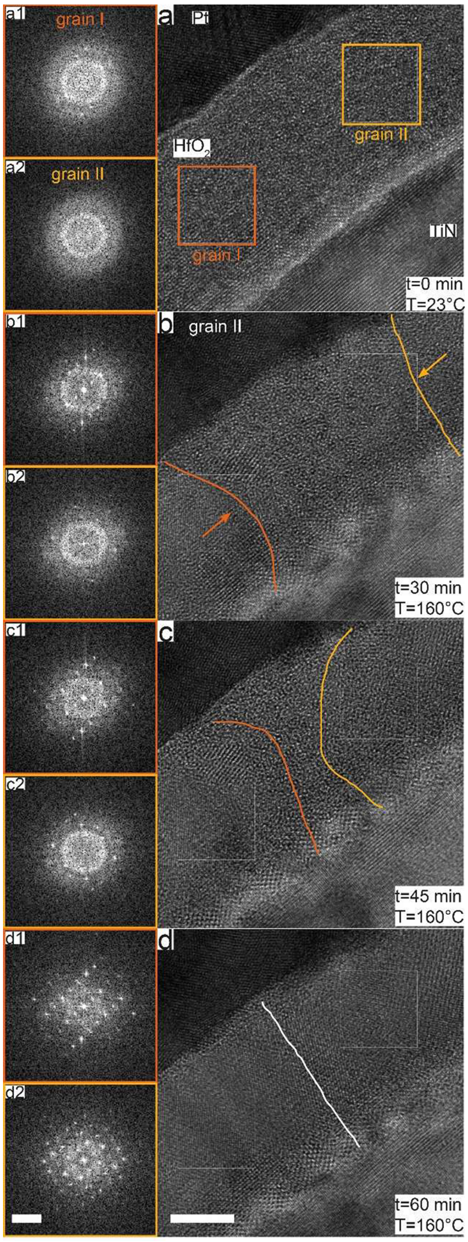

Figure 1. Image sequence for high-resolution transmission electron microscopy (HR-TEM) in situ heating. (a)−(d) Show the growth of two HfO$_2$ grains (orange and yellow) and (a1), (a2)−(d1), (d2) the corresponding fast Fourier fransforms (FFTs). The scale bar for the HR-TEM images is 5 nm and for the FFT images 5 1/nm. The colored arrows represent the direction of grain growth and are positioned on the crystalline HfO$_2$ phase directly at the boundary of the amorphous phase, which is represented by colored lines. A white line marks the grain boundary.

+index maps from a 4D-STEM data set of another in situ annealing experiment captured by SPED imaging are shown in Figure S4, respectively. This method provides a larger field of view compared to TEM imaging (Figure 1) while retaining the most important information, namely, crystallinity and grain orientation. Figure 3 shows selected orientation+index maps from this annealing experiment. The saturation of the Pt and TiN layers has been decreased to focus on the HfO$_2$ dielectric layer. In the pristine state (Figure 3a), the majority of the HfO$_2$ layer shows a yellow color, representing the amorphous phase. The yellow color is not consistent in brightness and shows some darker parts, in addition to some black pixels. The brightness change is related to the superimposed index and indicates how well the ASTAR software could assign or index a pixel to a certain phase and orientation. The presence of black pixels is a result of inadequate indexing, as the ASTAR software may not be able to assign any orientation to a pixel. The dark blue feature, encircled in white, is visible in the yellow amorphous HfO$_2$ matrix and can be attributed to a crystalline seed. As shown in Figure 3b, after applying a temperature of at least 180 °C, this initial seed grows (highlighted by black arrows) in addition to the formation of new seeds (encircled in white) that will also grow (Figure 3c) until adjoining adjacent grains, thus forming grain boundaries (Figure 3d, white lines).

To confirm our findings from the in situ TEM experiments, XRD patterns of the pristine and annealed memristive macro device are shown in Figure 4a. The pristine XRD pattern shown in orange is directly measured after RMBE thin film growth of TiN and HfO$_2$ before sputter coating and annealing and shows a low-intensity broad feature between 32° and 34° attributed to the amorphous phase. Annealing the macro device results in similar crystallization compared to the in situ annealing: according to the XRD pattern, the HfO$_2$ (11−1) is the most intense peak in addition to an unknown peak (dot) and peaks indexed as (001) and (100) HfO$_2$. The electroforming voltages (V_F) of 40 devices with amorphous and annealed HfO$_2$ are shown by the cumulative distribution function in Figure 4c. Exemplary $I-V$ curves of the electroforming of a device with annealed (pink) and amorphous (blue) HfO$_2$ are shown in Figure 4b. The corresponding XRD pattern of the device with amorphous HfO$_2$ is shown in Figure S5. Devices with amorphous HfO$_2$ have an average V_F of −6.1 V, and annealing leads to a reduction of V_F to an average of −4.2 V. The device-to-device variability, in terms of V_F spread, increases from 0.5 V for devices with amorphous HfO$_2$ to 0.6 V after annealing.

With our first annealing experiment using HR-TEM, we could determine the crystallization temperature to 160 °C, which is lower than the previously reported lowest crystallization temperatures of 200 °C[19,33] and, for the first time, for a HfO$_2$ film thickness about 10 times thinner at only 12 nm. For this small observation area, the thin HfO$_2$ layer crystallizes into monoclinic (200) and (11−1), which could previously be studied only at annealing temperatures above 400 °C. This might be caused by a pre-existing grain or seed acting as a "template" for grain growth,[34] as shown by the crystalline spots next to the amorphous ring in the FFT of grain I. However, a reduced annealing temperature to develop the (200) texture during grain growth could also be related to the adjacent layers:[35] as shown by the FFT of the entire HR-TEM image after annealing, the TiN (111) and grains I and II HfO$_2$ (200) diffraction spots are closely positioned, which can be attributed to a texture transfer. This also aligns with the findings from the annealing experiment utilizing 4D-STEM, although a temperature of 180 °C was required to crystallize amorphous HfO$_2$. Although heating by electron beam and current induction is negligible as shown by a study of Egerton and Malac,[36] and our previous study,[37] the difference in annealing temperatures might be related to the electron flux. The higher electron flux used to acquire the TEM images could facilitate bonding of the material[38] and thus, reduce the required crystallization temperature. As visible in the superimposed maps of orientation and index of the entire annealing process (Figure S4), the pre-existing seed (Figure 3a) is always

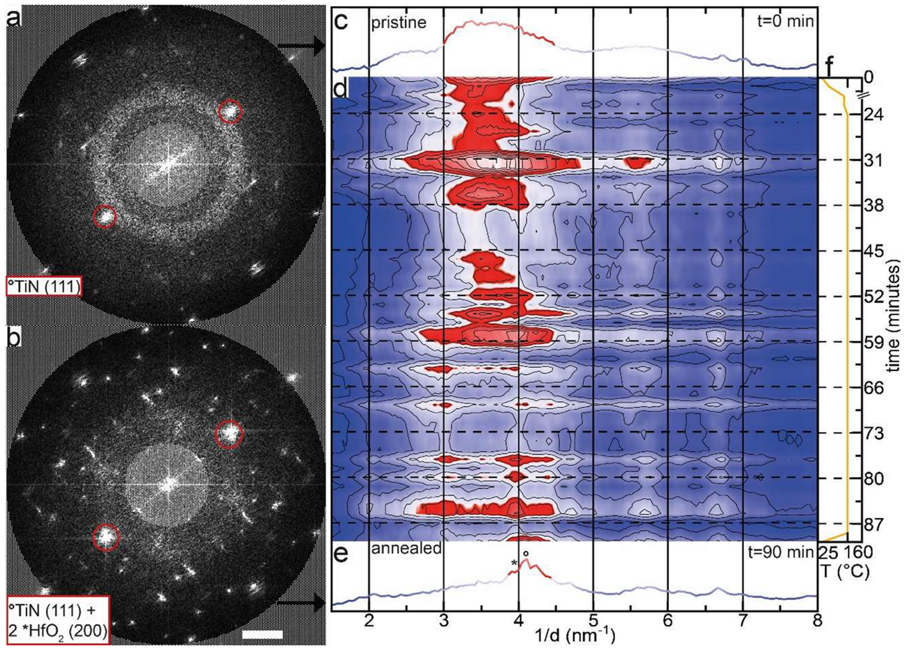

Figure 2. (a, b) Fast Fourier transform (FFT) of the high-resolution transmission electron microscopy (HR-TEM) (Figure 1a,d) before (pristine) and after annealing (annealed), respectively. Parts of the FFT are grayed out to show the selected limits of the azimuthal integration for (c) pristine and (e) annealed. The in situ annealing experiment is summarized by the 2D-waterfall plot of the azimuthal integration (d) next to the heating profile (f). The entire HR-TEM in situ heating images are shown in the video in the Supporting Information. The scale bar is 2 1/nm.

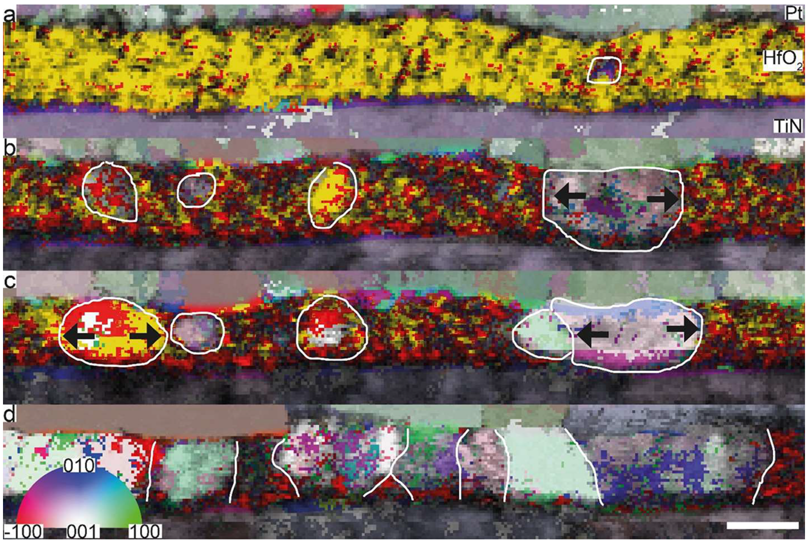

Figure 3. Superimposed maps of orientation (z-direction, viewing direction) and index from the automated crystal orientation map (ACOM) of the in situ 4D-STEM annealing data. (a−c) New and growing grains are encircled. (d) Grain boundaries are indicated by white lines. The scale bar is 10 nm.

colored nonyellow, meaning that this grain is already crystalline. The other newly developed seeds (Figure 3b) appear mainly in yellow, indicating that these seeds are amorphous. During growth, these grains will stay amorphous (Figure 3c) until they come into contact with an adjacent layer to receive some texture transfer, which might explain the low crystallization temperatures.

In the macroscopic RRAM device, the HfO$_2$ dielectric layer also crystallizes at 180 °C, and the mixed (11−1) and (001) monoclinic HfO$_2$ texture improves V_F, but not to standard operational voltages as is the case for highly textured (11−1) HfO$_2$ with high-symmetry grain boundaries.[10] Therefore, although a (11−1) texture is present, the developed threading grain boundaries (according to TEM and 4D-STEM) might not have similar properties to epitaxially grown (11−1) HfO$_2$. Or because multiple (001) peaks are present in the XRD pattern, the dominant texture might not be (11−1) but (001). According to a study by Khan et al.,[19] a dominant (001) texture might be linked to an insufficient crystallization temperature. However, a dominant (001) texture would result in low symmetry grain boundaries with an average V_F of −5.3 V, but instead the observed average V_F is located in between highly textured (001) and highly textured ((11−1) (average V_F of −1.9 V).

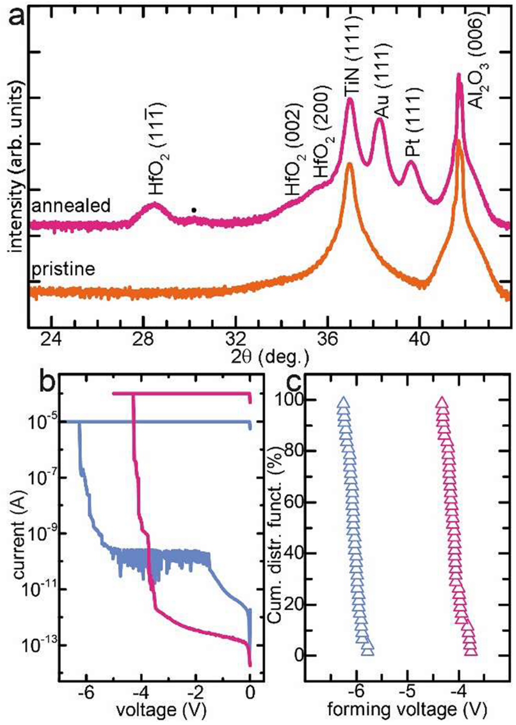

Figure 4. (a) X-ray diffraction (XRD) patterns of the pristine (orange) device, measured directly after HfO_2 and TiN thin film growth and after annealing (and sputter coating) (pink). Amorphous HfO_2, noticeable from the broad feature from 32 to 34°, crystallizes into primarily monoclinic *m*-(11−1) but also *m*-(002) and *m*-(200) HfO_2. (b) When comparing the electroforming of a device with amorphous HfO_2 (blue, XRD pattern shown in Figure S5) to the annealed device (pink), a reduction of forming voltage (V_F) can be observed. (c) On average, as shown by the cumulative distribution function of V_F for the 40 amorphous (blue) and crystalline (pink) devices, V_F is reduced by 1.9 V, while the spread of V_F is increased by 0.1 V.

In this study, we have investigated the microstructural changes of HfO_2 dielectric layers and how the crystallization impacts the device performance. Our in situ TEM and 4D-STEM experiments revealed that crystallizing amorphous hafnia into the monoclinic phase starts at 180 °C. Although grain growth appears nonadjacent to an interface, the growing grains develop texture only when reaching an adjacent textured layer. Annealing a macroscopic device confirmed the findings by TEM and resulted in a mixed monoclinic (11−1 + 001) texture. The microstructural changes in the dielectric layer improved device performance by lowering the average forming voltage from −6.1 V to −4.2 V. The results suggest that the low crystallization temperature might be attributed to texture transfer but also to pre-existing “templates” for grain growth. Altering the thin film layers adjacent to the dielectric layer and performing ab initio calculations could be crucial to further investigating why certain crystallinities (11−1/001) develop.

■ ASSOCIATED CONTENT

Supporting Information

The Supporting Information is available free of charge at https://pubs.acs.org/doi/10.1021/acs.nanolett.3c03941.

Additional XRD measurements of HfO_2 thin film stacks, all processed images of the entire in situ annealing 4D-STEM showing orientation and phase, azimuthal integration of different zone axes of monoclinic (11−1) and (020) HfO_2 (PDF)

Video of aligned TEM images of in situ annealing of HfO_2 based memristive devices (AVI)

■ AUTHOR INFORMATION

Corresponding Author

Leopoldo Molina-Luna − *Advanced Electron Microscopy Division, Institute of Materials Science, Technische Universität Darmstadt, 64287 Darmstadt, Germany*; orcid.org/0000-0002-9412-8093; Email: leopoldo.molina-luna@tu-darmstadt.de

Authors

Robert Winkler − *Advanced Electron Microscopy Division, Institute of Materials Science, Technische Universität Darmstadt, 64287 Darmstadt, Germany*; orcid.org/0000-0002-1779-1895

Alexander Zintler − *Advanced Electron Microscopy Division, Institute of Materials Science, Technische Universität Darmstadt, 64287 Darmstadt, Germany*; orcid.org/0000-0002-2272-3184

Oscar Recalde-Benitez − *Advanced Electron Microscopy Division, Institute of Materials Science, Technische Universität Darmstadt, 64287 Darmstadt, Germany*

Tianshu Jiang − *Advanced Electron Microscopy Division, Institute of Materials Science, Technische Universität Darmstadt, 64287 Darmstadt, Germany*

Déspina Nasiou − *Advanced Electron Microscopy Division, Institute of Materials Science, Technische Universität Darmstadt, 64287 Darmstadt, Germany*

Esmaeil Adabifiroozjaei − *Advanced Electron Microscopy Division, Institute of Materials Science, Technische Universität Darmstadt, 64287 Darmstadt, Germany*

Philipp Schreyer − *Advanced Thin Film Technology Division, Institute of Materials Science, Technische Universität Darmstadt, 64287 Darmstadt, Germany*; orcid.org/0000-0002-7200-3855

Taewook Kim − *Advanced Thin Film Technology Division, Institute of Materials Science, Technische Universität Darmstadt, 64287 Darmstadt, Germany*; orcid.org/0000-0002-3095-0053

Eszter Piros − *Advanced Thin Film Technology Division, Institute of Materials Science, Technische Universität Darmstadt, 64287 Darmstadt, Germany*; orcid.org/0000-0001-8714-9059

Nico Kaiser − *Advanced Thin Film Technology Division, Institute of Materials Science, Technische Universität Darmstadt, 64287 Darmstadt, Germany*; orcid.org/0000-0002-5644-890X

Tobias Vogel − *Advanced Thin Film Technology Division, Institute of Materials Science, Technische Universität Darmstadt, 64287 Darmstadt, Germany*; orcid.org/0000-0002-1519-0041

Stefan Petzold − *Advanced Thin Film Technology Division, Institute of Materials Science, Technische Universität Darmstadt, 64287 Darmstadt, Germany*

Lambert Alff − *Advanced Thin Film Technology Division, Institute of Materials Science, Technische Universität Darmstadt, 64287 Darmstadt, Germany*; orcid.org/0000-0001-8185-4275

Complete contact information is available at:

https://pubs.acs.org/10.1021/acs.nanolett.3c03941

Author Contributions

The manuscript was written through contributions of all authors. All authors have given approval to the final version of the manuscript.

Notes

The authors declare no competing financial interest.

■ ACKNOWLEDGMENTS

This research was funded by the European Research Council (ERC) through the "Horizon 2020" program under Grants 805359-FOXON and 957521-STARE, as well as by the Deutsche Forschungsgemeinschaft (DFG) through Projects MO 3010/3-1 and AL 560/21-1. The work leading to this publication has been undertaken in the framework of the projects WAKeMeUP and StorAIge, which received funding from the Electronic Components and Systems for European Leadership Joint Undertaking in collaboration with the European Union's H2020 Framework Programme (H2020/2014-2020) and National Authorities, under Grant Agreements 783176 and 101007321, respectively. Funding by the Federal Ministry of Education and Research (BMBF) under Contracts 16ESE0298 and 16MEE0154, respectively, is gratefully acknowledged. We thank Dr. Letian Li from Thermo Fisher Scientific for assistance with TEM lamella preparation.

■ ABBREVIATIONS

STEM	scanning transmission electron microscopy
TEM	transmission electron microscopy
TMO	transition metal oxide
RRAM	resistive random access memory
RMBE	reactive molecular beam epitaxy
CMOS	complementary metal oxide semiconductor
BEOL	back-end-of-line
ALD	atomic layer deposition
PLD	pulsed laser deposition
XRD	X-ray diffractometry
MIM	metal−insulator−metal
DUT	device of test
SCS	semiconductor characterization system
CC	current compliance
FIB	focused ion beam
SPED	scanning probe electron diffraction
NBED	nanobeam electron diffraction
HR	high-resolution
FFT	fast Fourier transform
AI	azimuthal integration
ACOM	automated crystal orientation mapping

■ REFERENCES

(1) Fortunato, E.; Barquinha, P.; Martins, R. Oxide Semiconductor Thin-Film Transistors: A Review of Recent Advances. *Adv. Mater.* **2012**, *24* (22), 2945−2986.

(2) Advances in the design and application of transition metal oxide-based supercapacitors. https://www.degruyter.com/document/doi/10.1515/chem-2021-0059/html?lang=dwebe (accessed Oct 12, 2023).

(3) Chen, A. A. Review of Emerging Non-Volatile Memory (NVM) Technologies and Applications. *Solid-State Electron.* **2016**, *125*, 25−38.

(4) Song, M.-K.; Kang, J.-H.; Zhang, X.; Ji, W.; Ascoli, A.; Messaris, I.; Demirkol, A. S.; Dong, B.; Aggarwal, S.; Wan, W.; Hong, S.-M.; Cardwell, S. G.; Boybat, I.; Seo, J.; Lee, J.-S.; Lanza, M.; Yeon, H.; Onen, M.; Li, J.; Yildiz, B.; del Alamo, J. A.; Kim, S.; Choi, S.; Milano, G.; Ricciardi, C.; Alff, L.; Chai, Y.; Wang, Z.; Bhaskaran, H.; Hersam, M. C.; Strukov, D.; Wong, H.-S. P.; Valov, I.; Gao, B.; Wu, H.; Tetzlaff, R.; Sebastian, A.; Lu, W.; Chua, L.; Yang, J. J.; Kim, J. Recent Advances and Future Prospects for Memristive Materials, Devices, and Systems. *ACS Nano* **2023**, *17* (13), 11994−12039.

(5) Kumar, J.; Birla, S.; Agarwal, G. A Review on Effect of Various High-k Dielectric Materials on the Performance of FinFET Device. *Materials Today: Proceedings* **2023**, *79*, 297−302.

(6) Sharath, S. U.; Kurian, J.; Komissinskiy, P.; Hildebrandt, E.; Bertaud, T.; Walczyk, C.; Calka, P.; Schroeder, T.; Alff, L. Thickness Independent Reduced Forming Voltage in Oxygen Engineered HfO2 Based Resistive Switching Memories. *Appl. Phys. Lett.* **2014**, *105* (7), 073505.

(7) Sharath, S. U.; Bertaud, T.; Kurian, J.; Hildebrandt, E.; Walczyk, C.; Calka, P.; Zaumseil, P.; Sowinska, M.; Walczyk, D.; Gloskovskii, A.; Schroeder, T.; Alff, L. Towards Forming-Free Resistive Switching in Oxygen Engineered HfO2−x. *Appl. Phys. Lett.* **2014**, *104* (6), 063502.

(8) Sharath, S. U.; Vogel, S.; Molina-Luna, L.; Hildebrandt, E.; Wenger, C.; Kurian, J.; Duerrschnabel, M.; Niermann, T.; Niu, G.; Calka, P.; Lehmann, M.; Kleebe, H.-J.; Schroeder, T.; Alff, L. Control of Switching Modes and Conductance Quantization in Oxygen Engineered HfOx Based Memristive Devices. *Adv. Funct. Mater.* **2017**, *27* (32), 1700432.

(9) Petzold, S.; Zintler, A.; Eilhardt, R.; Piros, E.; Kaiser, N.; Sharath, S. U.; Vogel, T.; Major, M.; McKenna, K. P.; Molina-Luna, L.; Alff, L. Forming-Free Grain Boundary Engineered Hafnium Oxide Resistive Random Access Memory Devices. *Advanced Electronic Materials* **2019**, *5* (10), 1900484.

(10) Winkler, R.; Zintler, A.; Petzold, S.; Piros, E.; Kaiser, N.; Vogel, T.; Nasiou, D.; McKenna, K. P.; Molina-Luna, L.; Alff, L. Controlling the Formation of Conductive Pathways in Memristive Devices. *Advanced Science* **2022**, *9* (33), 2201806.

(11) Zintler, A.; Eilhardt, R.; Petzold, S.; Sharath, S. U.; Bruder, E.; Kaiser, N.; Alff, L.; Molina-Luna, L. Enhanced Conductivity and Microstructure in Highly Textured TiN1−x/c-Al2O3 Thin Films. *ACS Omega* **2022**, *7* (2), 2041−2048.

(12) Schmitz, J. Low Temperature Thin Films for Next-Generation Microelectronics (Invited). *Surf. Coat. Technol.* **2018**, *343*, 83−88.

(13) Lanza, M. A. Review on Resistive Switching in High-k Dielectrics: A Nanoscale Point of View Using Conductive Atomic Force Microscope. *Materials* **2014**, *7* (3), 2155−2182.

(14) Gusev, E. P.; Cabral, C.; Copel, M.; D'Emic, C.; Gribelyuk, M. Ultrathin HfO2 Films Grown on Silicon by Atomic Layer Deposition for Advanced Gate Dielectrics Applications. *Microelectron. Eng.* **2003**, *69* (2), 145−151.

(15) Lanza, M.; Porti, M.; Nafria, M.; Benstetter, G.; Frammelsberger, W.; Ranzinger, H.; Lodermeier, E.; Jaschke, G. Influence of the Manufacturing Process on the Electrical Properties of Thin (<4nm) Hafnium Based High-k Stacks Observed with CAFM. *Microelectronics Reliability* **2007**, *47* (9), 1424−1428.

(16) Nishitani, K.; Yabuhara, H.; Endou, A.; Suzuki, A.; Tsuboi, H.; Hatakeyama, N.; Takaba, H.; Kubo, M.; Miyamoto, A. Prediction of Crystallization Temperature for HfO$_2$ Thin Film in High Temperature Annealing Process by Reaction Time Accelerating Molecular Dynamics. In *Extended Abstracts*, 2009 International Conference on Solid State Devices and Materials, Sendai Kokusai Hotel, Miyagi, Japan; The Japan Society of Applied Physics, 2009; DOI: 10.7567/SSDM.2009.H-3-3.

(17) Lysaght, P. S.; Woicik, J. C.; Sahiner, M. A.; Lee, B.-H.; Jammy, R. Incipient Amorphous-to-Crystalline Transition in HfO2 as a Function of Thickness Scaling and Anneal Temperature. *J. Non-Cryst. Solids* **2008**, *354* (2), 399−403.

(18) Triyoso, D.; Liu, R.; Roan, D.; Ramon, M.; Edwards, N. V.; Gregory, R.; Werho, D.; Kulik, J.; Tam, G.; Irwin, E.; Wang, X.-D.; La, L. B.; Hobbs, C.; Garcia, R.; Baker, J.; White, B. E.; Tobin, P. Impact of Deposition and Annealing Temperature on Material and Electrical

Characteristics of ALD HfO2. *J. Electrochem. Soc.* **2004**, *151* (10), F220.

(19) Khan, S. B.; Zhang, Z.; Lee, S. L. Annealing Influence on Optical Performance of HfO2 Thin Films. *J. Alloys Compd.* **2020**, *816*, 152552.

(20) Ho, M.-Y.; Gong, H.; Wilk, G. D.; Busch, B. W.; Green, M. L.; Voyles, P. M.; Muller, D. A.; Bude, M.; Lin, W. H.; See, A.; Loomans, M. E.; Lahiri, S. K.; Räisänen, P. I. Morphology and Crystallization Kinetics in HfO2 Thin Films Grown by Atomic Layer Deposition. *J. Appl. Phys.* **2003**, *93* (3), 1477−1481.

(21) Vinod, A.; Rathore, M. S.; Srinivasa Rao, N. Effects of Annealing on Quality and Stoichiometry of HfO2 Thin Films Grown by RF Magnetron Sputtering. *Vacuum* **2018**, *155*, 339−344.

(22) Park, M. H.; Chung, C.-C.; Schenk, T.; Richter, C.; Opsomer, K.; Detavernier, C.; Adelmann, C.; Jones, J. L.; Mikolajick, T.; Schroeder, U. Effect of Annealing Ferroelectric HfO2 Thin Films: In Situ, High Temperature X-Ray Diffraction. *Advanced Electronic Materials* **2018**, *4* (7), 1800091.

(23) Balogh-Michels, Z.; Stevanovic, I.; Borzi, A.; Bächli, A.; Schachtler, D.; Gischkat, T.; Neels, A.; Stuck, A.; Botha, R. Crystallization Behavior of Ion Beam Sputtered HfO2 Thin Films and Its Effect on the Laser-Induced Damage Threshold. *Journal of the European Optical Society-Rapid Publications* **2021**, *17* (1), 3.

(24) Ushakov, S. V.; Navrotsky, A.; Yang, Y.; Stemmer, S.; Kukli, K.; Ritala, M.; Leskelä, M. A.; Fejes, P.; Demkov, A.; Wang, C.; Nguyen, B.-Y.; Triyoso, D.; Tobin, P. Crystallization in Hafnia- and Zirconia-Based Systems. *physica status solidi (b)* **2004**, *241* (10), 2268−2278.

(25) Hwang, B.; Lee, J.-S. Recent Advances in Memory Devices with Hybrid Materials. *Advanced Electronic Materials* **2019**, *5* (1), 1800519.

(26) Shih, H.-Y.; Lee, W.-H.; Kao, W.-C.; Chuang, Y.-C.; Lin, R.-M.; Lin, H.-C.; Shiojiri, M.; Chen, M.-J. Low-Temperature Atomic Layer Epitaxy of AlN Ultrathin Films by Layer-by-Layer, in-Situ Atomic Layer Annealing. *Sci. Rep* **2017**, *7* (1), 39717.

(27) Aziz, M. J. Film Growth Mechanisms in Pulsed Laser Deposition. *Appl. Phys. A: Mater. Sci. Process.* **2008**, *93* (3), 579−587.

(28) Luo, X.; Demkov, A. A. Structure, Thermodynamics, and Crystallization of Amorphous Hafnia. *J. Appl. Phys.* **2015**, *118* (12), 124105.

(29) Buckow, A.; Retzlaff, R.; Kurian, J.; Alff, L. Growth of Superconducting Epitaxial LaNixBi2pnictide Thin Films with a Bi Square Net Layer by Reactive Molecular Beam Epitaxy. *Supercond. Sci. Technol.* **2013**, *26* (1), 015014.

(30) Zintler, A.; Kunz, U.; Pivak, Y.; Sharath, S. U.; Vogel, S.; Hildebrandt, E.; Kleebe, H.-J.; Alff, L.; Molina-Luna, L. FIB Based Fabrication of an Operative Pt/HfO_2/TiN Device for Resistive Switching inside a Transmission Electron Microscope. *Ultramicroscopy* **2017**, *181* (Suppl. C), 144−149.

(31) Darbal, A. D.; Gemmi, M.; Portillo, J.; Rauch, E.; Nicolopoulos, S. Nanoscale Automated Phase and Orientation Mapping in the TEM. *Microscopy Today* **2012**, *20* (6), 38−42.

(32) Gammer, C.; Mangler, C.; Rentenberger, C.; Karnthaler, H. P. Quantitative Local Profile Analysis of Nanomaterials by Electron Diffraction. *Scripta Materialia* **2010**, *63* (3), 312−315.

(33) Aguirre, B. Microstructure And Electrical Performance Of Sputter-Deposited Hafnium Oxide (Hfo2) Thin Films. Masters of Science Thesis, University of Texas at El Paso, 2009; https://scholarworks.utep.edu/open_etd/2626 (accessed Mar 20, 2023).

(34) Souza Junior, J. B.; Schleder, G. R.; Bettini, J.; Nogueira, I. C.; Fazzio, A.; Leite, E. R. Pair Distribution Function Obtained from Electron Diffraction: An Advanced Real-Space Structural Characterization Tool. *Matter* **2021**, *4* (2), 441−460.

(35) Rollett, A. D. Crystallographic Texture Change during Grain Growth. *JOM* **2004**, *56* (4), 63−68.

(36) Egerton, R. F.; Li, P.; Malac, M. Radiation Damage in the TEM and SEM. *Micron* **2004**, *35* (6), 399−409.

(37) Recalde-Benitez, O.; Jiang, T.; Winkler, R.; Ruan, Y.; Zintler, A.; Adabifiroozjaei, E.; Arzumanov, A.; Hubbard, W. A.; van Omme, T.; Pivak, Y.; Perez-Garza, H. H.; Regan, B. C.; Alff, L.; Komissinskiy, P.; Molina-Luna, L. Operando Two-Terminal Devices inside a Transmission Electron Microscope. *Commun. Eng.* **2023**, *2* (1), 1−8.

(38) Vaerst, O.; Wilde, G.; Peterlechner, M. Beam Effects on Atomic Dynamics in Metallic Glasses Studied With Electron Correlation Microscopy. *Microscopy and Microanalysis* **2023**, *29* (6), 1870−1878.

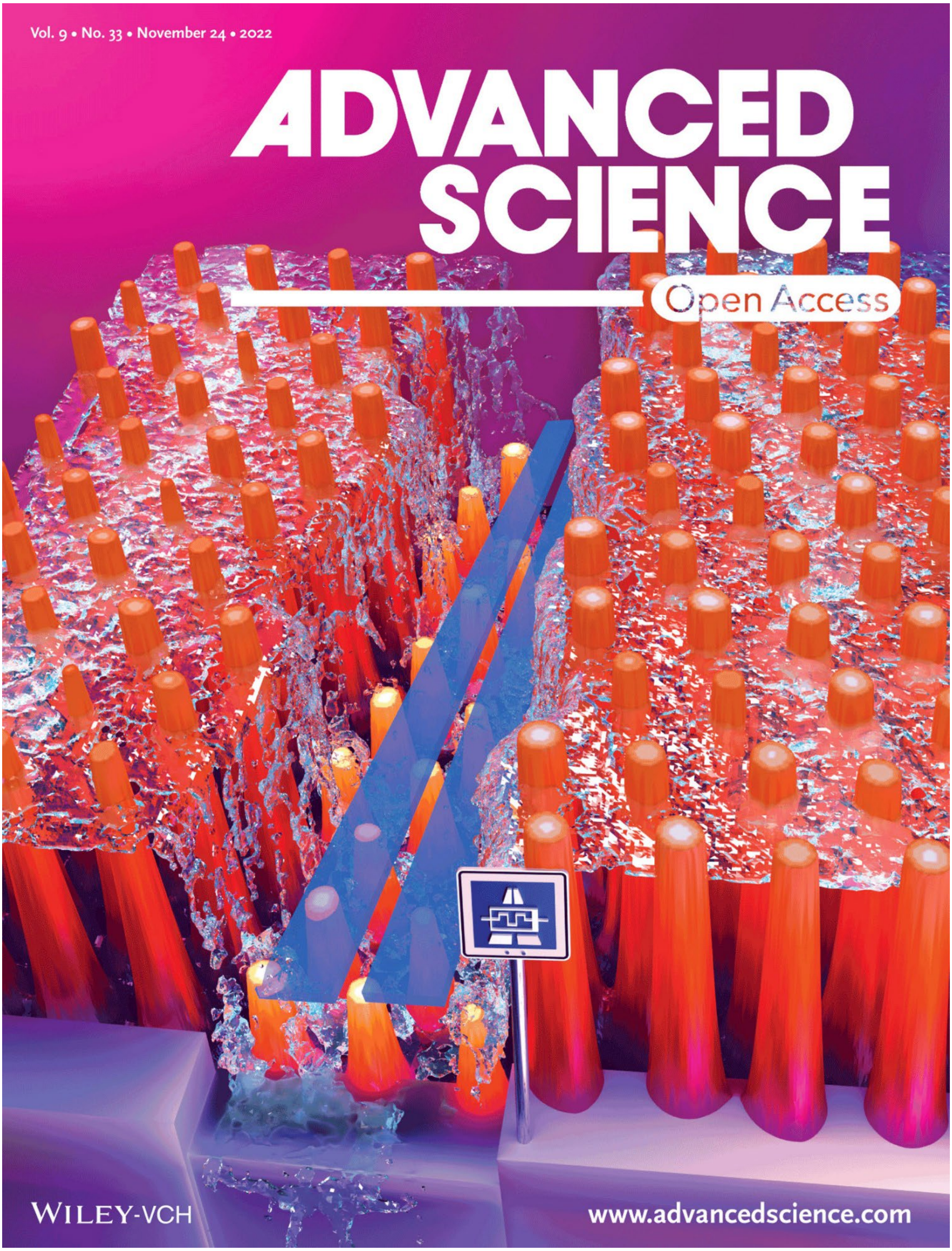

Sketch of oxygen vacancy segregation toward a specific grain boundary in a hafnia (Hf)-based memristor. The orange pillars correspond to the atomic positions of Hf calculated based on transmission electron microscopy imaging. The water symbolizes oxygen vacancies attracted (through a waterfall) to the grain boundary region (canyon), which will then form the speedway (autobahn) of the filamentary conductive current.

R. Winkler et al., Adv. Sci. 9, 2270212 (2022). https://doi.org/10.1002/advs.202270212.

NANO LETTERS

March 13, 2024
Volume 24, Number 10
pubs.acs.org/NanoLett

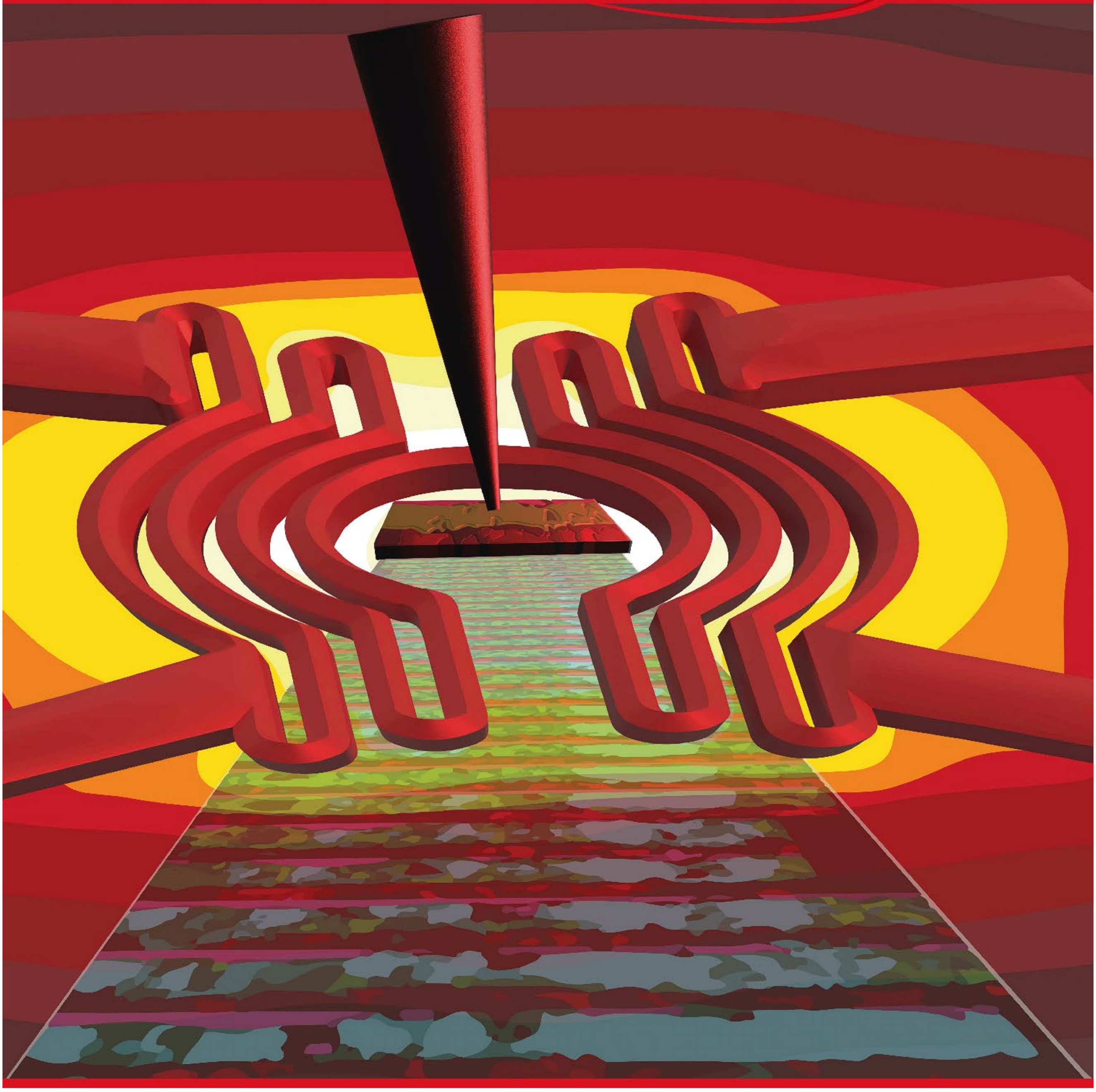

ACS Publications
Most Trusted. Most Cited. Most Read.

www.acs.org

A HfO_2-based memristive transmission electron microscope (TEM) lamella is placed on a micro-electromechanical systems (MEMS)-based heating chip. The amorphous HfO_2 layer is in situ annealed and investigated via 4D-STEM. The maps show the phase transition from amorphous to crystalline monoclinic HfO_2 starting at 180 °C.

R. Winkler et al., Nano Lett. 24, 2998 (2024). https://doi.org/10.1021/acs.nanolett.3c03941.